High Oxide-Ion Conductivity and Phase Transition of Doped Bismuth Vanadate

Department of Materials Science and Engineering,

Kyoto University

Yu-ki Taninouchi

2010

Content

Chapter 1

General Introduction

1.1. Introduction

In the recent past, the development of novel solid-state ionic conductors at intermediate temperatures between 400 and 600 °C has generated great interest. The broad objective of this thesis is to reveal the effects of doping on bismuth vanadate and to obtain a material exhibiting high oxide-ion conduction that is available for an oxygen pump. In particular, this work is devoted to uncovering the variation in electrical conductivity, phase transition behavior, and long-term phase stability induced by doping at vanadium sites.

In this chapter, a brief overview of non-doped and doped bismuth vanadate is provided first. Then, the outline of this thesis as well as the method of analysis is provided. After that, the concept of an oxygen pump and a phonological review of oxide-ion conductivity are described.

1.2. Bismuth vanadate

Bismuth vanadate $Bi_2VO_{5.5-\delta}$ (δ: oxygen loss due to partial reduction of vanadium [98Abr,03Pir]), which was firstly identified in 1988 by Abraham *et al.* [88Abr], shows a Aurivillius-type structure [49Aur1,49Aur2,50Aur], complex polymorphs, and favorable oxide-ion conduction. Generally speaking, three main phases are obtained in $Bi_2VO_{5.5-\delta}$: a low-temperature phase of α (below 445 °C), an intermediate-temperature phase of β (between 445 and 570 °C), and a high-temperature phase of γ (at around 700 °C). Figure 1.1 shows the ideal structure of the γ-phase, which is often called a single-layer Aurivillius structure.

$Bi_2VO_{5.5-\delta}$ consists of alternate bismuth-oxygen (Bi-O) and vanadium-oxygen (V-O) layers. The Bi-O layer, formulated as $(Bi_2O_2)^{2+}$, exhibits Bi in a square pyramidal coordination. The asymmetric coordination geometry of Bi results from the stereochemical activity of the non-bonding Bi $6s^2$ lone pairs. The V-O layer is composed of VO_6 octahedrons that contain oxygen vacancies to preserve electroneutrality. Thus, the V-O layer of ideal γ-phase can be described as $(VO_{3.5}\square_{0.5})^{2-}$, where vanadium is pentavalent and □ denotes a randomly distributed oxygen vacancy. The β- and α-phases are characterized by the ordering of oxygen vacancies in the V-O layer. In the β-phase, the V-O layer still contains oxygen vacancies. Besides α-, β-, and γ-phases, several phases that deviate from the three main phases are also observed. The details of structural differences in each phase will be given in Chapter 2.

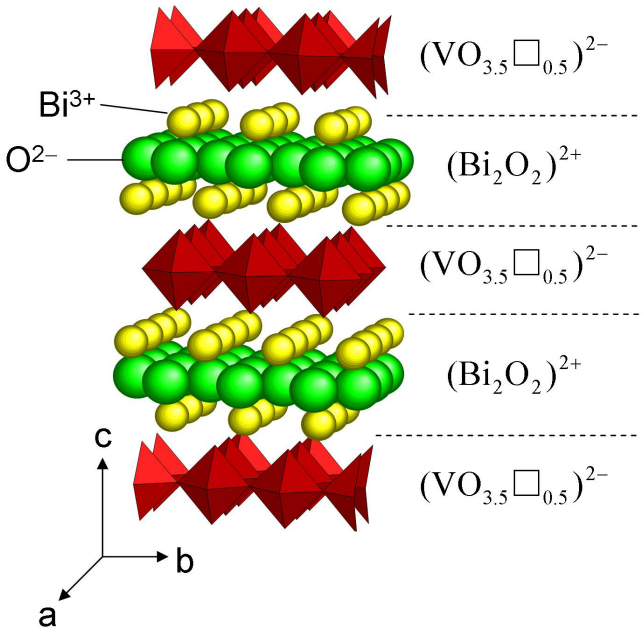

Figure 1.1 Ideal structure of γ-phase that consists of alternating Bi-O and V-O layers. This structure is often called a single-layer Aurivillius structure.

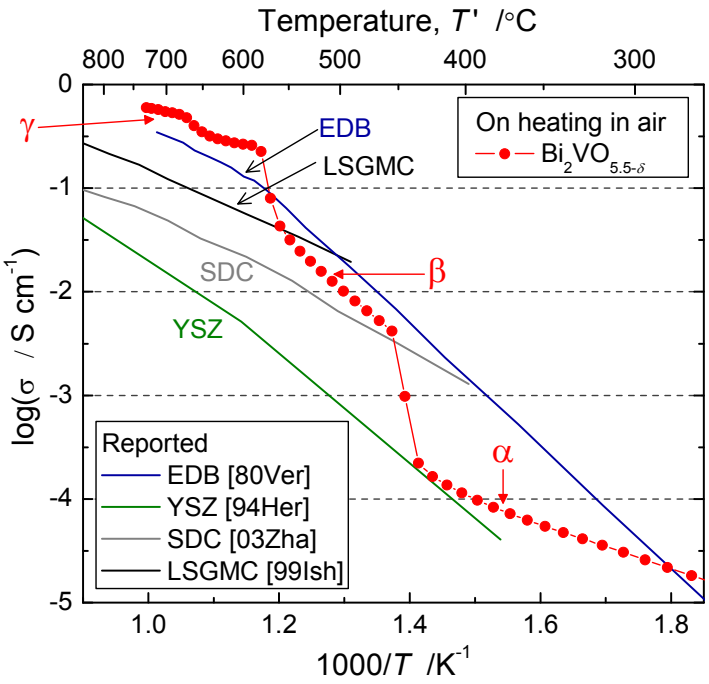

Figure 1.2 Electrical conductivities of $Bi_2VO_{5.5-\delta}$, $(Bi_2O_3)_{0.8}(Er_2O_3)_{0.2}$ (EDB) [80Ver], $(ZrO_2)_{0.92}(Y_2O_3)_{0.08}$ (YSZ) [94Her], $(CeO_2)_{0.85}(SmO_{1.5})_{0.15}$ (SDC) [03Zha], and $La_{0.8}Sr_{0.2}Ga_{0.8}Mg_{0.115}Co_{0.085}O_3$ (LSGMC) [99Ish]. The data for $Bi_2VO_{5.5-\delta}$ were obtained in air at a heating rate of 1 K min^{-1}.

Figure 1.2 shows the electrical conductivity of $Bi_2VO_{5.5-\delta}$ on heating. Two large conductivity jumps at about 445 and 570 °C correspond to the transitions from α to β and from β to γ (strictly speaking, ε-phase appears from 570 to 650 °C [05Abr], which is further described in Chapter 2), respectively. α-$Bi_2VO_{5.5-\delta}$ is a semiconductor, but β- and γ-$Bi_2VO_{5.5-\delta}$ exhibit pure oxide-ion conduction [88Abr,93Lee]. The oxide-ion conductivity exceeds 10^{-2} S cm^{-1} above 500 °C in the β-phase and approaches 5×10^{-1} S cm^{-1} at 700 °C in the γ-phase. Figure 1.2 also shows the oxide-ion conductivities of $(Bi_2O_3)_{0.8}(Er_2O_3)_{0.2}$ (EDB) [80Ver], $(ZrO_2)_{0.92}(Y_2O_3)_{0.08}$ (YSZ) [94Her], $(CeO_2)_{0.85}(SmO_{1.5})_{0.15}$ (SDC) [03Zha], and $La_{0.8}Sr_{0.2}Ga_{0.8}Mg_{0.115}Co_{0.085}O_3$ (LSGMC) [99Ish], which are well known as novel oxide-ion

conductors. EDB, YSZ, and SDC have fluorite-type structures where high temperature phases of parent compounds are stabilized by doping. LSGMC has a perovskite-type structure where Sr is doped on the A-site and Mg and Co are doped on the B-site. Currently, YSZ is most commonly used as the oxide-ion conductive membrane of various solid-state ionic devices such as solid oxide fuel cells and oxygen sensors. β- and γ- $Bi_2VO_{5.5-\delta}$ exhibit good oxide-ion conduction in comparison with other famous oxides. In particular, γ-$Bi_2VO_{5.5-\delta}$ exhibits higher oxide-ion conductivities than EDB, YSZ, SDC, and LSGMC at a given temperature. For the development of solid-state ionic devices at intermediate temperatures, especially oxygen pumps described in Section 1.5, it is strongly required to stabilize γ-phases below 570 °C and increase oxide-ion conductivity around 10^{-1} S cm^{-1} at around 500 °C.

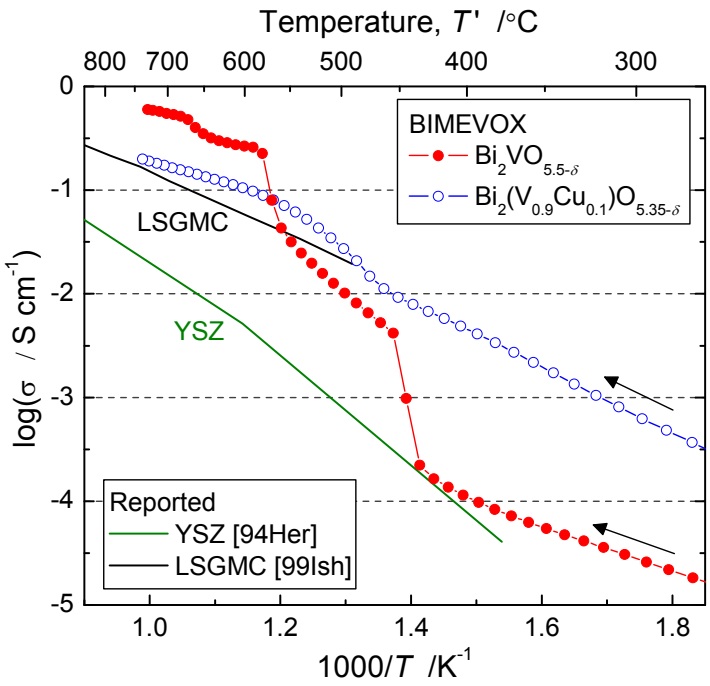

Figure 1.3 Electrical conductivities of $Bi_2(V_{0.9}Cu_{0.1})O_{5.35-\delta}$, $Bi_2VO_{5.5-\delta}$, $(ZrO_2)_{0.92}(Y_2O_3)_{0.08}$ (YSZ) [94Her], and $La_{0.8}Sr_{0.2}Ga_{0.8}Mg_{0.115}Co_{0.085}O_3$ (LSGMC) [99Ish]. The data for $Bi_2(V_{0.9}Cu_{0.1})O_{5.35-\delta}$ and $Bi_2VO_{5.5-\delta}$ were obtained in air at a heating rate of 1 K min^{-1}. γ-phase was stabilized by Cu doping.

It is known that the doping of vanadium sites changes the phase transformation behavior and electrical conductivity of $Bi_2VO_{5.5-\delta}$ [98Boi,99Sam]. Such doped bismuth vanadate, $Bi_2(V_{1-x}ME_x)O_{5.5+\Delta}$ (ME: doped metal, x: dopant concentration, and $\Delta \equiv d - \delta$, where Δ is total oxygen deviation, d is oxygen deviation due to aliovalent doping, and δ is oxygen loss due to partial reduction), is denoted by the acronym BIMEVOX. In 1990, Abrahams *et al.* were the first to carry out doping with divalent Cu [90Abr]. Figure 1.3 shows the conductivities of $Bi_2(V_{0.9}Cu_{0.1})O_{5.35-\delta}$ obtained in this study. Abrahams *et al.* reported that γ-$Bi_2(V_{0.9}Cu_{0.1})O_{5.35-\delta}$ was stabilized down to room temperature (strictly speaking, the phase at room temperature slightly deviates from the γ-phase [94Per]) and exhibited high oxide-ion conductivity below 570 °C. After the publishing of their first report, many studies have been carried out, especially on Cu- and Co-doped $Bi_2VO_{5.5-\delta}$. Various kinds of metal with different sizes and valences can partially substitute for vanadium, as summarized in Figure 1.4, and certain properties of BIMEVOX have been reported. However, the roles of each dopant involve complicated mechanisms and have yet to be well understood. Thus, systematic research with various dopants and concentrations is important to comprehensively understand the effect of doping on polymorphs and electrical conductivity, which should allow us to design a more favorable BIMEVOX.

It is also notable that $Bi_2VO_{5.5-\delta}$ and BIMEVOX have limitations in terms of long-term phase stability. In 2001, Watanabe reported that $Bi_2VO_{5.5-\delta}$ is metastable below 550 °C and it thermally decomposes into $BiVO_4$ and $Bi_{3.5}V_{1.2}O_{8.25}$ after 300 hr or more [01Wat]. In 2005, Steil *et al.* reconfirmed the decomposition of β-$Bi_2VO_{5.5-\delta}$ into $BiVO_4$ and $Bi_{3.5}V_{1.2}O_{8.25}$ by annealing at 500 °C for 7 weeks [05Ste]. For BIMEVOX, Dygas *et al.* reported in 1995 that γ-$Bi_2(V_{0.9}Cu_{0.1})O_{5.35-\delta}$ exhibits considerable degradation in oxide-ion conductivity upon

prolonged annealing at 423 °C [95Dyg]. In 2002, Watanabe and Das revealed that the time-dependent degradations in conductivity of $Bi_2(V_{0.9}Cu_{0.1})O_{5.35-\delta}$ and $Bi_2(V_{0.9}Co_{0.1})O_{5.35-\delta}$ are caused by gradual ordering from the γ- to the α-phase. In 2005, Steil *et al.* reported that γ-$Bi_2(V_{0.9}Mg_{0.1})O_{5.35-\delta}$ and γ-$Bi_2(V_{0.9}Ni_{0.1})O_{5.35-\delta}$ exhibited ordering at 450–500 °C for 3 weeks, but γ-$Bi_2(V_{0.9}Mg_{0.1})O_{5.5\ 5-\delta}$, γ-$Bi_2(V_{0.9}Mg_{0.1})O_{5.5-\delta}$, and γ-$Bi_2(V_{0.9}Mg_{0.1})O_{5.5-\delta}$ were stable at 450 °C for 10 weeks and 500 °C for 7 weeks [05Ste]. Long-term phase stability against thermal decomposition and ordering is key for the practical use of BIMEVOX. However, very little is known about the long-term phase stability of other BIMEVOX variants.

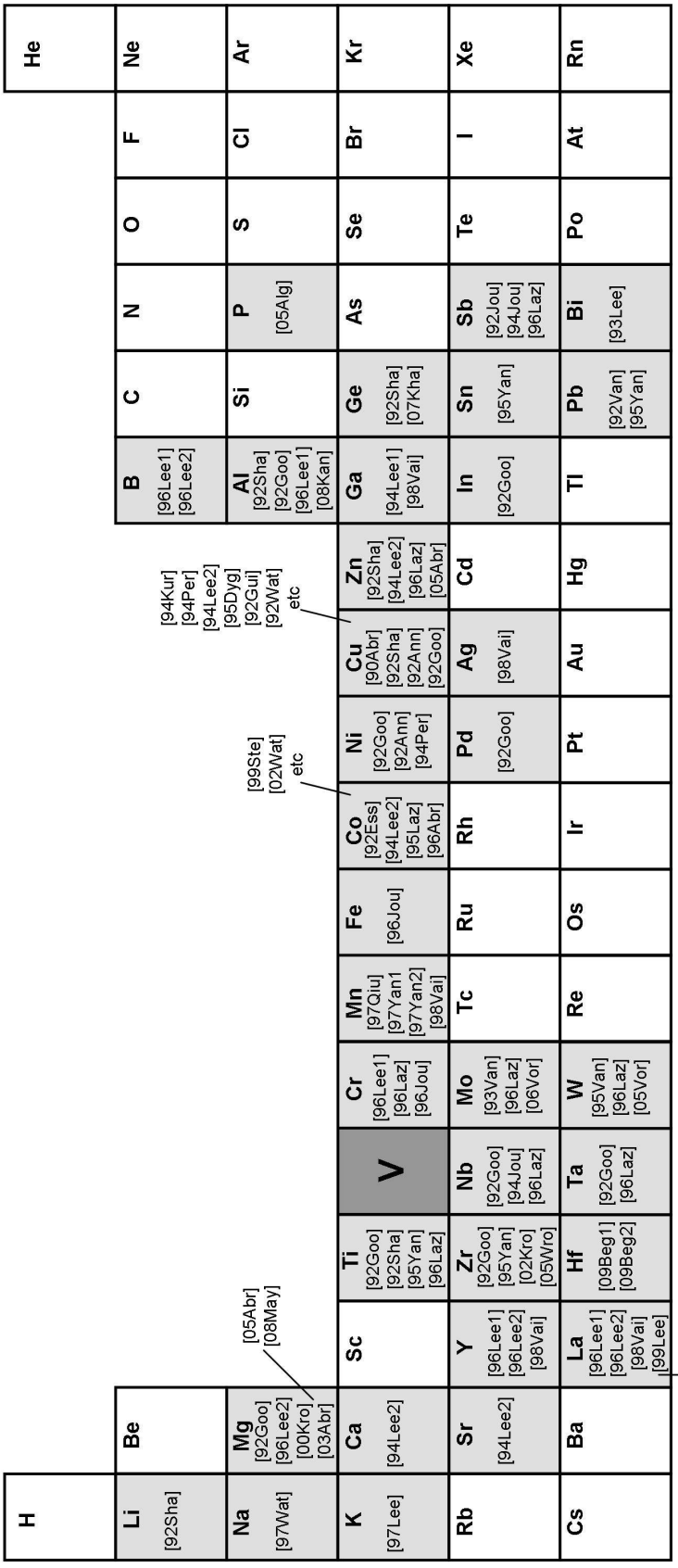

Figure 1.4 Elements that have been reported to substitute for vanadium sites in $Bi_2VO_{5.5-\delta}$.

1.3. Outline of this study

On the background as mentioned in the previous section, the electrical properties and phase stabilities (polymorphic transition as well as thermal decomposition) of various $Bi_2(V_{1-x}ME_x)O_{5.5+\Delta}$ have been investigated depending on temperature and time. Based on the empirical facts, the guideline to realize high-performance BIMEVOX has been considered.

In Chapter 2, a new phase classification system is established for convenience in the following discussions on polymorphs and electrical conductivity of BIMEVOX. Complex structural phases in BIMEVOX are classified into three phase groups of α_f, β_f, and γ_f in terms of the network structures in the V-O layer without strict determination of crystalline structures.

Figure 1.5 shows the dopants selected in Chapters 3–7. Table 1.1 lists some characters of each dopant, *i.e.*, valences in BIMEVOX (experimentally verified in each chapter), Shannon ionic radii in 6-fold coordination [76Sha], lattice energies of binary oxides (Q), and preferable oxygen coordinations of dopants and V. Aliovalent doping is expected to change the amount of oxygen vacancy to preserve electroneutrality, *i.e.*, doping with mono-, tri-, and tetravalent metals should increase the oxygen vacancy concentration in each phase, but doping with hexavalent metal decreases the oxygen vacancy concentration in β_f and γ_f. The difference in size between dopant and V should induce lattice strain in BIMEVOX structures. The lattice energy Q, which corresponds to the trend of affinity between dopant and oxide-ion, is the negative value of the enthalpy change of following reaction: $ME^{x+}(g) + x/2\ O^{2-}(g) \rightarrow ME_1O_{x/2}(s)$. Table 1.2 lists the thermodynamical data used for the evaluation of Q. Comparing at the same valence of dopant, dopant with larger Q is expected to bind more strongly with oxide-ion in BIMEVOX. Such affinity between dopant and oxide-ion might also play important role to change some properties such as oxide-ion conductivity and phase stability

against thermal decomposition. The oxygen coordinations of V are significantly changed in each phase, which will be further described in Chapter 2. Thus, the preferable oxygen coordinations of dopants might be important for determining polymorphs.

For the elements in Chapter 3, the solid solution of BIMEVOX was examined in Bi_2O_3-V_2O_5 pseudo-binary system. The electrical conductivities, polymorphs, and thermal decompositions behavior of $Bi_2(V_{1-x}Bi_x)O_{5.5+\Delta}$ was revealed in this chapter.

For elements in Chapter 4, doping with monovalent metals of Li and Ag is carried out. As shown in Figure 1.5 and Table 1.1, the valences, sizes, and preferable oxygen coordinations of Li and Ag markedly deviate from those of V. Thus, doping with alkaline metal Li and transition metal Ag probably causes notable changes in physical properties and might provide us some insight how to design more favorable BIMEVOX.

For elements in Chapters 5–7, doping with various transition metals (TM = Ti, Zr, Hf, Nb, Ta, Cr, Mo, and W), which locate close to V in the periodic table and have various characters, is performed. For elements in Chapter 4, where dopant concentration is fixed at 5 mol%, the variation in temperature dependence of electrical conductivity and long-term phase stability are revealed. From the results in Chapter 4, it was found that the electrical conductivities and phase transitions vary significantly with not only the dopant but also the thermal history of the sample. In Chapter 5, to understand this phenomenon, the phase transition behavior of $Bi_2(V_{0.95}Ti_{0.05})O_{5.475-\delta}$, which has various thermal histories and sample forms, is carefully studied. For elements in Chapter 7, where dopants are tetravalent transition metals of Ti, Zr, and Hf, the influences of dopant concentration are carefully investigated.

In Chapter 8, based on the empirical facts in Chapter 3–7, co-doping with monovalent metal (Li and Ag) and Ti is performed to further improve the oxide-ion conductivity at intermediate temperatures. Doping with Li and Ag most effectively stabilized γ_f against β_f and

α_f (expand temperature region of γ_f at low temperatures) but did not suppress thermal decomposition. On the other hand, doping with Ti effectively suppressed thermal decomposition and stabilized γ_f against β_f and α_f. Finally, Chapter 9 sums up the findings of each chapter.

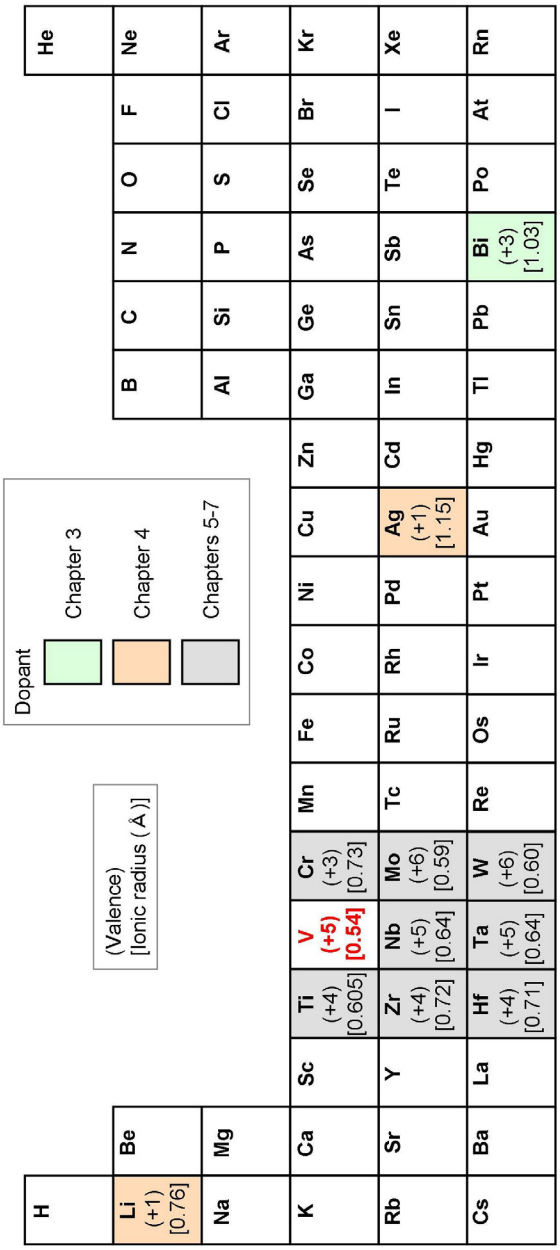

Figure 1.5 Valences in BIMEVOX and Shannon ionic radii in 6-fold coordination [76Sha] of selected dopants.

Table 1.1 Valences, Shannon ionic radii in 6-fold coordination [76Sha], and lattice energies (Q) of binary oxide (trend of affinity with oxide-ion in BIMEVOX), and preferable oxygen coordinations of dopants and V. Valence of dopant changes the amount of oxygen vacancies. Lattice energy Q is the negative value of the enthalpy change of following reaction: $ME^{x+}(g) + x/2\ O^{2-}(g) \rightarrow ME_1O_{x/2}(s)$. Comparing at the same valence of dopant, dopant with larger Q is expected to bind more strongly with oxide-ion in BIMEVOX. Oxygen coordinations in Bi_2O_3 (α-type-structure which is stable below 710 °C), Li_2O (anti-fluorite structure), Ag_2O (cuprite structure), TiO_2 (rutile structure), ZrO_2 (fluorite structure), HfO_2 (fluorite structure), Nb_2O_5 (high-temperature form [76Kat]), Ta_2O_5 (low-temperature form [71Ste]), Cr_2O_3 (corundum structure), MoO_3 (layer structure consisting of distorted MoO_6 octahedron [50And]), WO_3 (distorted ReO_3 structure [53And]), and V_2O_5 (ReO_3-related one-dimensional shear structure [76Hul,86Enj]) are regarded as preferable.

	Valence	Ionic radius (nm)	Lattice energy, Q (MJ mol^{-1})	Preferable oxygen coordination
Bi	+3	0.103	6.623	5-fold (square pyramid)
Li	+1	0.076	1.429	4-fold (tetrahedron)
Ag	+1	0.115	1.481	2-fold (linear)
Ti	+4	0.0605	12.009	6-fold (octahedron)
Zr	+4	0.072	9.811	8-fold (hexahedron)
Hf	+4	0.071	11.113	8-fold (hexahedron)
Nb	+5	0.064	16.927	6-fold (octahedron) and 4-fold (tetrahedron)
Ta	+5	0.064	17.134	7-fold (pentagonal bipyramid)
Cr	+3	0.073	7.551	6-fold (octahedron)
Mo	+6	0.059	25.916	6-fold (octahedron)
W	+6	0.060	26.252	6-fold (octahedron)
V	+5	0.054	19.236	5-fold (square pyramid)

Table 1.2 Thermodynamical data used for the evaluation of lattice energies (Q).

Chemical species	$\Delta_f H°$ (kJ mol^{-1})	Source	Chemical species	$\Delta_f H°$ (kJ mol^{-1})	Source
$V^{5+}(g)$	16241.0	[82Wag]	$V_2O_5(s)$	−1550.6	[82Wag]
$Bi^{3+}(g)$	5004		$Bi_2O_3(s)$	−573.88	
$Li^{+}(g)$	685.783		$Li_2O(s)$	−597.94	
$Ag^{+}(g)$	1021.73		$Ag_2O(s)$	−31.05	
$Ti^{4+}(g)$	9289		$TiO_2(s)$	−944.7	
$Zr^{4+}(g)$	6934		$ZrO_2(s)$	−1100.56	
$Hf^{4+}(g)$	8192		$HfO_2(s)$	−1144.7	
$Nb^{5+}(g)$	13757		$Nb_2O_5(s)$	−1899.5	
$Ta^{5+}(g)$	13891*		$Ta_2O_5(s)$	−2046.0	
$Cr^{3+}(g)$	5648.4		$Cr_2O_3(s)$	−1139.7	
$Mo^{6+}(g)$	22506		$MoO_3(s)$	−745.09	
$W^{6+}(g)$	22745**		$WO_3(s)$	−842.87	
$O^{2-}(g)$	888.17	[82Wag, 93Huh]			

* Estimated under the assumption that enthalpy change from $Ta^{+}(g)$ to $Ta^{5+}(g)$ is same with that from $Nb^{+}(g)$ to $Nb^{5+}(g)$.

** Estimated under the assumption that enthalpy change from $W^{+}(g)$ to $W^{6+}(g)$ is same with that from $Mo^{+}(g)$ to $Mo^{6+}(g)$.

1.4. Methods of analysis

Table 1.3 lists the methods of analysis employed in this study. X-ray diffraction (XRD) analysis, high-temperature X-ray diffraction (HT-XRD) analysis, inductively coupled plasma atomic emission spectroscopy (ICP-AES), energy dispersive X-ray spectroscopy (EDX), field-emission scanning electron microscopy (FE-SEM), optical microscopy, AC impedance spectroscopy, DC polarization measurement, differential scanning calorimetry (DSC), differential thermal analysis (DTA), and thermogravimetric analysis (TGA) were employed. Analytical equipment and analytical conditions are shown in Table 1.3. Figure 1.6 shows the

experimental apparatus used for the electrical conductivity measurements [07Tan,07MT].

Table 1.3 Methods of analysis and equipment. Analytical conditions and/or comments are also shown.

Property	Method of analysis	Equipment	Condition/comment
Structure	X-ray diffraction (XRD) analysis	X'Pert PRO MPD (PANalytical), RINT 2200 (Rigaku)	Cu-Kα radiation
	High-temperature X-ray diffraction (HT-XRD) analysis	X'Pert PRO MPD (PANalytical) with an HTK-1200N oven chamber (Anton Paar)	Cu-Kα radiation
Composition	Inductively coupled plasma atomic emission spectroscopy (ICP-AES)	ICPS-8000 (Shimadzu)	Samples were dissolved in nitric acid
	Energy dispersive X-ray spectroscopy (EDX)	JED-2300 (Jeol) attached to JSM-6500F (Jeol)	–
Microstructure	Field-emission scanning electron microscopy (FE-SEM)	JSM-6500F (Jeol) equipped with JED-2300 (Jeol)	–
	Optical microscopy	VHX-900 (Keyence)	–
Electrical conductivity	AC impedance spectroscopy	Solartron 1260 (Solartron) with a custom-built apparatus in Figure 1.8	Voltage amplitude of 50 mV. In artificial air (Ar-21%O_2 at 80 ml min^{-1}), pure O_2 (at 80 ml min^{-1}), or pure Ar (at 80 ml min^{-1})
	DC polarization measurement	Solartron 1287 (Solartron) or VersaSTAT 3 (Princeton Applied Research) with a custom-built apparatus in Figure 1.8	Direct voltage of 50–100 mV for ~10 min. In artificial air (Ar-21%O_2 at 80 ml min^{-1})
Thermal reaction	Differential scanning calorimetry (DSC)	Diamond DSC (PerkinElmer) with platinum container	In stagnant air or in artificial air (Ar-21%O_2 at 50 ml min^{-1})
	Differential thermal analysis (DTA)	DTG-60H (Shimadzu) with aluminum container (when heated above 900 °C) or platinum container	In artificial air (Ar-21%O_2 at 50 ml min^{-1})
Weight change	Thermogravimetric analysis (TGA)	DTG-60H (Shimadzu) with platinum container	In artificial air (Ar-21%O_2 at 50 ml min^{-1})

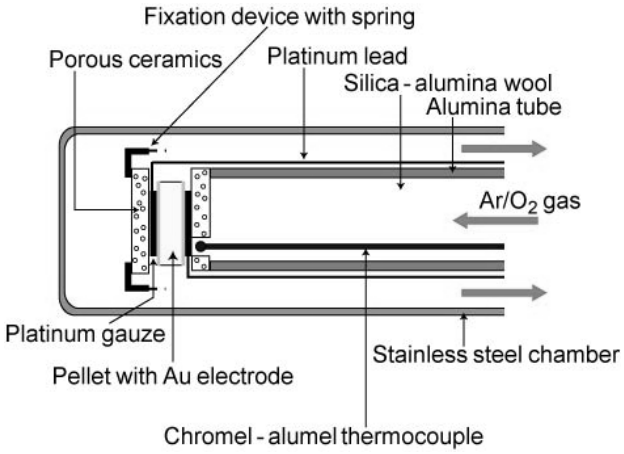

Figure 1.6 Schematic diagram of the experimental apparatus used for the conductivity measurements [07Tan,07MT].

1.5. Oxygen pump

Highly concentrated oxygen is widely used in various fields, such as for medical treatment of lung conditions, thermal processes in burner reactors, and gas-to-liquid technologies (GLT technology: synthesizing liquid fuels such as gasoline or kerosene from natural gas). Currently, the pressure swing absorption (PSA) method, which utilizes the gas absorption characteristics of zeolite, is commonly used to obtain highly concentrated oxygen. The PSA method is an almost mature technology and needs a gas compressor, which constricts potential reductions in size and weight. Thus, the development of electrochemical oxygen concentration devices that can undergo reductions in size and weight has received much attention as an important economic challenge.

Although several types of electrochemical devices using solid-state electrolytes can be considered, the most attractive one is an oxygen pump whose performance is the under control of an external power source [98Boi2,99Mai,06Pay]. Figure 1.7 shows the concept of an oxygen pump. The dissociation of oxygen gas occurs at the cathode of the cell according to

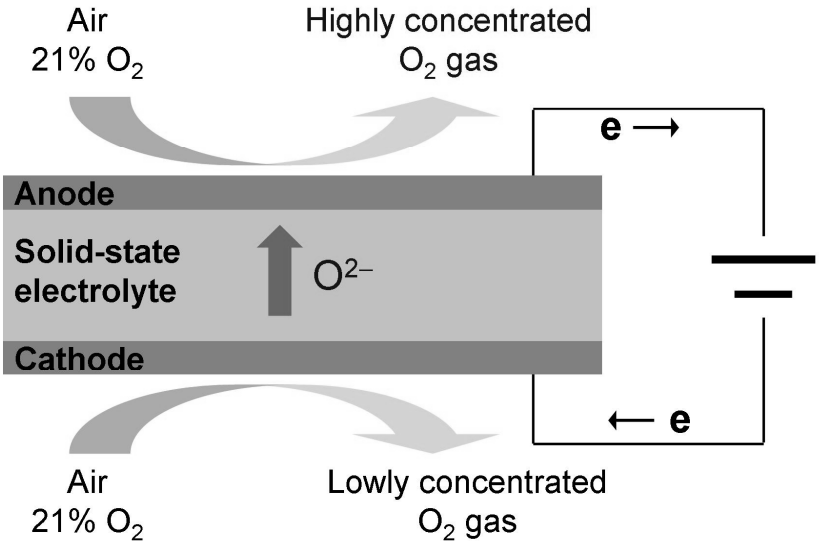

Figure 1.7 Concept of oxygen pump using solid-state oxide-ion conductor.

the reaction $O^2 + 4e^- \rightarrow 2O^{2-}$. The electrons flow exclusively through the external circuit. After the migration of oxide ions through the electrolyte, the reconstituting reaction of oxygen gas, *i.e.*, $2O^{2-} \rightarrow O^2 + 4e^-$, occurs at the anode side and oxygen gas is released into the surrounding gas phase. In this system, the oxygen flux is fully adjustable by varying the intensity through the electrolyte, and oxygen can be transferred from air towards the high-oxygen-pressure compartment. The electric power required depends mainly on the oxide-ion conductivity of the electrolyte, the mixed conductivity and catalytic activity of the electrodes, and the operating temperature. Considering the operability and economical cost for construction and operation, the oxygen pump is desired to operate at intermediate temperatures of around 500 °C.

Generally speaking, BIMEVOX is reduced by hydrogen at elevated temperatures [03Pia,Chapter4] and its practical use has been restricted. However, BIMEVOX is expected to be stable under the operation conditions of an oxygen pump. In addition, bismuth-based oxides were reported as catalytically active phases towards oxygen dissociation

[86Ste,00Bou]. There is a possibility that high-performance electrodes are easily formed on the BIMEVOX membrane by slight surface modification. BIMEVOX is, therefore, a promising candidate as a membrane of oxygen pumps.

1.6. Phenomenological review of oxide-ion conductivity

This section contains a phenomenological review of oxide-ion conduction as well as the appearance of electron or hole conduction in solid oxides [84Sub,04Boy].

A pure ionic conductor with only one type of charge carrier is assumed. According to Ohm's law, the ionic conductivity σ_{ion} in isotropic material (including the polycrystalline body of anisotropic crystals) relates the current density $\vec{i}$ to the applied electric field $\vec{\varepsilon}$ as follows:

$$\vec{i} = \sigma_{\text{ion}} \vec{\varepsilon} . \tag{1.1}$$

The current density $\vec{i}$ can be expressed using concentration n, charge q, and average velocity $\langle \vec{v} \rangle$ of the charge carrier as follows:

$$\vec{i} = n q \langle \vec{v} \rangle . \tag{1.2}$$

The mobility of charge carrier u is defined as

$$u \equiv \frac{\langle \vec{v} \rangle}{\vec{\varepsilon}} . \tag{1.3}$$

Combining eqs. (1.1.), (1.2), and (1.3),

$$\sigma_{\text{ion}} = n q u \tag{1.4}$$

can be obtained.

When the charge carrier concentration and electric potential ϕ vary along the *x*-direction, the mean force for ion diffusion $\langle F \rangle$ is

$$\langle F \rangle = \frac{\partial \mu}{\partial x} + q\frac{\partial \phi}{\partial x}, \tag{1.5}$$

where μ (= $\partial G / \partial n$) is the chemical potential of the charge carrier. Thus, the charge carrier flux J, which corresponds to the number of charge carriers passing through an area per unit time, is expressed using the mobility per charge u/q as follows:

$$J = \frac{-nu}{q}\left(\frac{\partial \mu}{\partial x} + q\frac{\partial \phi}{\partial x}\right). \tag{1.6}$$

When the electric field $\partial \phi / \partial x$ is zero, eq. (1.6) reduces to

$$J = \frac{-nu}{q}\left(\frac{\partial \mu}{\partial x}\right). \tag{1.7}$$

The flux J is also expressed in terms of a charge carrier diffusion coefficient D according to Fick's first law:

$$J = -D\left(\frac{\partial n}{\partial x}\right). \tag{1.8}$$

In dilute solutions, the chemical potential μ is expressed as

$$\mu = \mu_0 + \mathrm{k_B} T \ln n, \tag{1.9}$$

where μ_0 is standard chemical potential, $\mathrm{k_B}$ is the Boltzmann constant, and T is temperature in Kelvin. The differentiation of eq. (1.9) with respect to *x* yields

$$\frac{\partial \mu}{\partial x} = \frac{\mathrm{k_B} T}{n}\left(\frac{\partial n}{\partial x}\right). \tag{1.10}$$

From eqs. (1.6), (1.7), and (1.10), the relationship between the diffusion coefficient and the charge carrier mobility, *i.e.*, the Nernst-Einstein equation,

$$u = \frac{qD}{k_B T} \tag{1.11}$$

is obtained. The substitution of eq. (1.11) into eq. (1.4) yields

$$\sigma_{\text{ion}} = \frac{nq^2 D}{\mathrm{k_B} T} . \tag{1.12}$$

When a random walk model is applied to the motion of a charge carrier, the charge carrier diffusion coefficient D can be described as

$$D = \kappa a_0^2 f , \tag{1.13}$$

where κ is a geometric factor depending on the structure of the solid electrolyte, a_0 is the jump distance of the mobile charge carrier, and f is the frequency at which the charge carrier jumps. The jumping of charge carriers between crystallographic sites is a thermally activated process. This thermally activated process can be described by the Arrhenius-type temperature dependence,

$$f = f_0 \exp\left(\frac{-\Delta G_a}{\mathrm{k_B} T} \right), \tag{1.14}$$

where f_0 is the attempt frequency and ΔG_a is the Gibbs free energy for activation of this process. The substitution of eq. (1.14) into eq. (1.13) yields

$$D = \kappa a_0^2 f_0 \exp\left(\frac{-\Delta G a}{\mathrm{k_B} T} \right) \tag{1.15}$$

$$\leftrightarrow D = D_0 \exp\left(\frac{-\Delta G_a}{\mathrm{k_B} T} \right), \tag{1.16}$$

where the pre-exponential factor is $D_0 = \kappa a_0^2 f_0$. The Gibbs free energy of activation can be expressed using activation enthalpy ΔH_a and entropy ΔS_a as follows:

$$\Delta G_a = \Delta H_a - T\Delta S_a . \tag{1.17}$$

Similarly, the activation enthalpy can be expressed using activation energy ΔE_a and volume ΔV_a as follows:

$$\Delta H_a = \Delta E_a + P\Delta V_a . \tag{1.18}$$

The activation volume ΔV_a can be neglected for the ion diffusion at ambient pressure. Combining eqs. (1.12) and (1.13) and thermodynamic relationships, the Arrhenius relationship of ionic conductivity can be described as

$$\sigma_{\text{ion}} T = A \exp\left(\frac{-\Delta E_a}{\mathrm{k_B} T} \right), \tag{1.19}$$

where the pre-exponential factor A is

$$A = \frac{D_0 n q^2}{\mathrm{k_B}} \exp\left(\frac{\Delta S_a}{\mathrm{k_B}} \right) = \frac{\gamma a_0^2 f_0 n q^2}{\mathrm{k_B}} \exp\left(\frac{\Delta S_a}{\mathrm{k_B}} \right). \tag{1.20}$$

Now, an expression for the ionic conductivity in terms of intrinsic material properties as a function of temperature has been obtained. This expression closely models the bulk behavior of real ionic solids. When the oxide ions isotropically diffuse via oxygen vacancies, n means the concentration of mobile oxygen vacancies and $q = -2$.

In solid-state oxide-ion conductors, there is a possibility that electron or hole conduction appears, which depends on oxygen partial pressure ($p\mathrm{O_2}$). At low $p\mathrm{O_2}$, oxide ions can decompose into oxygen gas, oxygen vacancies, and electrons as follows:

$$\mathrm{O_O^\times} = \frac{1}{2}\mathrm{O_2}(g) + \mathrm{V_O^{\bullet\bullet}} + 2\mathrm{e'} \quad (\text{low } p\mathrm{O_2}), \tag{1.21}$$

where Kröger-Vink notation is used, *i.e.*, $\mathrm{O_O^\times}$ indicates an oxide-ion in solid oxide that is relatively electroneutral and $\mathrm{V_O^{\bullet\bullet}}$ indicates an oxygen vacancy whose relative valence is +2 in solid oxide. On the other hand, at high $p\mathrm{O_2}$, oxygen gas reacts with an oxygen vacancy, which produces a hole in solid oxide as follows:

$$\frac{1}{2}\mathrm{O_2}(g) + \mathrm{V_O^{\bullet\bullet}} = \mathrm{O_O^\times} + 2\mathrm{h^\bullet} \quad (\text{high } p\mathrm{O_2}). \tag{1.22}$$

The law of mass action for eqs. (1.21) and (1.22) gives

$$\left[\mathrm{e'}\right] = \mathrm{K}_1^{1/2}\left[\mathrm{V}_\mathrm{O}^{\bullet\bullet}\right]^{-1/2}\left(p\mathrm{O}_2\right)^{-1/4} \quad (\text{low } p\mathrm{O}_2) \tag{1.23}$$

and

$$\left[\mathrm{h}^{\bullet}\right] = \mathrm{K}_2^{1/2}\left[\mathrm{V}_\mathrm{O}^{\bullet\bullet}\right]^{1/2}\left(p\mathrm{O}_2\right)^{1/4} \quad (\text{high } p\mathrm{O}_2)\,, \tag{1.24}$$

respectively, where K_1 is the equilibrium constant of eq. (1.21), K_2 is the equilibrium constant of eq. (1.22), $\left[\mathrm{V}_\mathrm{O}^{\bullet\bullet}\right]$ is the concentration of $\mathrm{V}_\mathrm{O}^{\bullet\bullet}$, $\left[\mathrm{e'}\right]$ is the concentration of electrons, and $\left[\mathrm{h}^{\bullet}\right]$ is the concentration of holes. Generally, the mobilities of electrons and holes are much higher than that of oxide-ions. Thus, there is a possibility that the dominant charge carrier changes from oxide-ions to electrons and holes at low and high $p\mathrm{O}_2$, respectively. Figure 1.8 schematically shows the $p\mathrm{O}_2$ dependence of electrical conductivity at a given temperature. It is assume that the mobilities of all charge carriers are independent of $p\mathrm{O}_2$ and the variation in oxygen vacancy concentration due to reactions (1.21) and (1.22) is negligible. In general, oxide-ion conductivity is independent of $p\mathrm{O}_2$. Meanwhile, electron conduction that is proportional to $\left(p\mathrm{O}_2\right)^{-1/4}$ becomes dominant at low $p\mathrm{O}_2$, and hole conduction that is proportional to $\left(p\mathrm{O}_2\right)^{1/4}$ becomes dominant at high $p\mathrm{O}_2$.

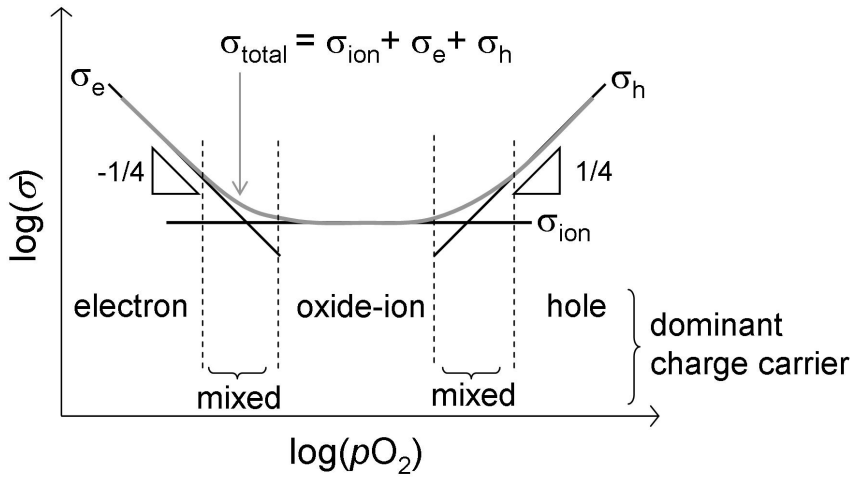

Figure 1.8 Schematic diagram of the $p\mathrm{O}_2$ dependence of the electrical conductivity of solid oxide.

References

[49Aur1] B. Aurivillius, Arkiv för Kemi 1 (1949) 463.

[49Aur2] B. Aurivillius, Arkiv för Kemi 1 (1949) 499.

[50Aur] B. Aurivillius, Arkiv för Kemi 2 (1950) 519.

[50And] G. Andersson and A. Magnéli, Acta Chem. Scand. 4 (1950) 793.

[53And] G. Andersson, Acta Chem. Scand. 7 (1953) 154.

[71Ste] N.C. Stephenson, R.S. Roth, Acta Crystallogr. Sect. B 27 (1971) 1037.

[76Sha] R.D. Shannon, Acta Crystallogr. Sect. A 32 (1976) 767.

[76Kat] K. Kato, Acta Crystallogr. Sect. B 32 (1976) 764.

[76Hul] F. Hulliger, *Structural chemistry of layer-type phases*, D. Reidel Publishing Company, Boston (1976).

[80Ver] M.J. Verkerk, K. Keizer, and A.J. Burggraaf, J. Appl. Electrochem. 10 (1980) 81.

[82Wag] D.D. Wagman, W.H. Evans, V.B. Parker, R.H. Schumm, I Halow, S.M. Bailey, K.L. Churney, and R.L. Nuttall, J. Phys. Chem. Ref. Data, Suppl. 11(2) (1982).

[84Sub] E.C. Subbarao and H.S. Maiti, Solid State Ionics 11 (1984) 317.

[86Enj] R. Enjalbert and J. Galy, Acta Cryst. C42 (1986) 1467.

[86Ste] B.C.H. Steele, J.A. Kilner, P.F. Dennis, and A.E. McHale, Solid State Ionics 18-19 (1986) 1038.

[88Abr] F. Abraham, M.F. Debreuille-Gresse, G. Mairesse, and G. Nowogrocki, Solid State Ionics 28-30 (1988) 529.

[90Abr] F. Abraham, J.C. Boivin, G. Mairesse, and G. Nowogrocki, Solid State Ionics 40-41 (1990) 934.

[92Van] R.N. Vannier, G. Mairesse, G. Nowogrocki, F. Abraham, and J.C. Boivin, Solid State Ionics 53-56 (1992) 713.

[92Sha] V. Sharma, A.K. Shukla, and J. Gopalakrishnan, Solid State Ionics 58 (1992) 359.

[92Goo] J.B. Goodenough, A. Manthiram, M. Paranthaman and Y.S. Zhen, Mater. Sci. Eng. B12 (1992) 357.

[92Ess] R. Essalim, B. Tanouti, J.P. Bonnet, and J.M. Réau, Mater. Lett. 13 (1992) 382.

[92Ann] M. Anne, M. Bacmann, E. Pernot, F. Abraham, G. Mairesse, and P. Strobel, Physica B 180-181 (1992) 621.

[92Jou] O. Joubert, A. Jouanneaux, M. Ganne, and M. Tourmoux, Mat. Res. Bull. 27 (1992) 1235.

[93Van] R.N. Vannier, G. mairesse, F. Abraham, and G. Nowogrocki, J. Solid State Chem. 103 (1993) 441.

[93Rei] K. Reiselhuber, G. Dorner, and M.W. Breiter, Electrochim. Acta 38(7) (1993) 969.

[93Lee] C.K. Lee, D.C. Sinclair, and A.R. West, Solid State Ionics 62 (1993) 193.

[93Huh] J.E. Huheey, E.A. Keiter, and R.L. Keiter, *Inorganic chemistry: principles of structure and reactivity*, 4th ed., (Hapere Collins, New York, 1993).

[94Her] J. Van Herle, A.J. Mcevoy, and K.R. Thampi, J. Mater. Sci. 29 (1994) 3691.

[94Per] E. Pernot, M. Anne, M. Bacmann, and P. Strobel, Solid State Ionics 70-71 (1994) 259.

[94Jou] O. Joubert, A. Jouanneaux, M. Ganne, R.N. Vannier, and G. Mairesse, Solid State Ionics 73 (1994) 309.

[94Lee1] C.R. Lee, G.S. Lim, and A.R. West, J. Mater. Chem. 4(9) (1994) 1441.

[94Lee2] C.R. Lee, M.P. Tan, and A.R. West, J. Mater. Chem. 4(4) (1994) 525.

[94Kur] P. Kurek, J.R. Dygas, and M.W. Breiter, J. Electroanal. Chem. 378 (1994) 77.

[95Van] R.N. Vannier, G. mairesse, F. Abraham, and G. Nowogrocki, Solid State Ionics 80 (1995) 11.

[95Yan] J. Yan and M. Greenblatt, Solid State Ionics 81 (1995) 225.

[95Dyg] J.R. Dygas, P. Kurek, and M.W. Breiter, Electrochim. Acta 40(10) (1995) 1545.

[95Laz] S. Lazure, R.N. Vannier, G. Nowogrocki, G. Mairesse, C. Muller, M. Anne, and P. Strobel, J. Mater. Chem. 5(9) (1995) 1395.

[96Lee1] C.K. Lee, B.H. Bay, and A.R. West, J. Mater. Chem. 6(3) (1996) 331.

[96Lee2] C.K. Lee and A.R. West, Solid State Ionics 86-88 (1996) 235.

[96Abr] I. Abrahams, F. Kork, and J.A.G. Nelstrop, Solid State Ionics 90 (1996) 57.

[96Laz] S. Lazure, Ch. Vernochet, R.N. Vannier, G. Nowogrocki, and G. Mairesse, Solid State Ionics 90 (1996) 117.

[96Jou] O. Joubert, M. Ganne, R.N. Vannier, and G. Mairesse, Solid State Ionics 93 (1996) 199.

[97Yan1] Y.L. Yang, L. Qui, W.T.A. Harrison, R. Christoffersen, and A.J. Jacobson, J. Mater. Chem. 7(2) (1997) 243.

[97Yan2] Y.L. Yang, L. Qui, and A.J. Jacobson, J. Mater. Chem. 7(6) (1997) 937.

[97Qui] L. Qui, Y.L. Yang, and A.J. Jacobson, J. Mater. Chem. 7(2) (1997) 249.

[97Lee] C.K. Lee, A.M. Coats, and A.R. West, Powder Diffraction 12(4) (1997) 245.

[97Wat] C.J. Watson, A. Coats, and D.C. Sinclair, J. Mater. Chem. 7(10) (1997) 2091.

[98Boi1] J.C. Boivin and G. Mairesse, Chem. Mater. 10 (1998) 2870.

[98Boi2] J.C. Boivin, C. Pirovano, G. Nowogrocki, G. Mairesse, Ph. Labrune, and G. Lagrange, Solid State Ionics 113-115 (1998) 639.

[98Vai] B. Vaidhyanathan, K. Balaji, and K.J. Rao, Chem. Mater. 10 (1998) 3400.

[98Abr] I. Abrahams, A.J. Bush, F. Krok, G.E. Hawkes, K.D. Sales, P. Thornton, and W. Bogusz, J. Mater. Chem. 8(5) (1998) 1213.

[99Ish] T. Ishihara, H. Furutani, M. Honda, T. Yamada. T. Shibayama, T. Akbay. N. Sakai, H. Yokokawa, and Y. Takita, Chem. Mater. 11 (1999) 2081.

[99Lee] C.K. Lee and C.S. Ong, Solid State Ionics 117 (1999) 301.

[99Mai] G. Mairesse, C.R. Acad. Sci. Paris, Ser. IIc 2 (1999) 651.

[99Ste] M.C. Steil, J. Fouletier, M. Kleitz, and P. Labrune, J. Eur. Ceram. Soc. 19 (1999) 815.

[99Sam] N.M. Sammes, G.A. Tompsett, H. Näfe, and F. Aldinger, J. Eur. Ceram. Soc. 19 (1999) 1801.

[00Bou] B.A. Boukamp, Solid State Ionics 136-137 (2000) 75.

[00Kro] F. Krok, I. Abrahams. M. Malys, W. Bogusz, J.R. Dygas, J.A.G. Nelstrop, and A.J. Bush, Solid State Ionics 136-137 (2000) 119.

[01Wat] A. Watanabe, J. Solid State Chem. 161 (2001) 410.

[02Kro] F. Krok, I. Abrahams, W. Wrobel, S.C.M. Chan, M. Malys, W. Bogusz, and J.R. Dygas, Solid State Ionics 154-155 (2002) 511.

[02Wat] A. Watanabe and K. Das, J. Solid State Chem. 163 (2002) 224.

[02Gui] M. Guillodo, J. Fouletier, L. Dessemond, and P. Del Gallo, J. Electrochem. Soc. 149(12) (2002) J93.

[03Mai1] G. Mairesse, P. Roussel, R.N. Vannier, M. Anne, C. Pirovano, and G. Nowogrocki, Solid State Science 5 (2003) 851.

[03Mai2] G. Mairesse, P. Roussel, R.N. Vannier, M. Anne, and G. Nowogrocki, Solid State Science 5 (2003) 861.

[03Zha] S. Zha, C. Xia, and G. Meng, J. Power Sources 115 (2003) 44.

[03Abr] I. Abrahams, F. Krok, M. Malys, W. Wrobel, S.C.M. Chan, W. Bogusz, and J.R. Dygas, Solid State Ionics 157 (2003) 155.

[03Pir] C. Pirovano, R.N. Vannier, G. Nowogrocki, J.C. Boivin, and G. Mairesse, Solid State Ionics 159 (2003) 181.

[04Boy] D.A. Boysen, *Superprotonic Solid Acids: Structure, Properties, and Applications.*, PhD thesis, California Institute of Technology, 2004.

[05Alg] M. Alga, A. Ammar, R. Essalim, B. Tanouti, F. Mauvy, and R. Decourt, Solid State Science 7 (2005) 1173.

[05Wro] W. Wrobel, I. Abrahams, F. Krok, A. Kozanecka, S.C.M. Chan, M. Malys, W. Bogusz, and J.R. Dygas, Solid State Ionics 176 (2005) 1731.

[05Abr] I. Abrahams, F. Krok, M. Malys, and W. Wrobel, Solid State Ionics 176 (2005) 2053.

[05Ste] M.C. Steil, F. Ratajczak, E. Capoen, C. Pirovano, R.N. Vannier, and G. Mairesse, Solid State Ionics 176 (2005) 2305.

[05Vor] V.I. Voronkova, V.K. Yanovskii, E.P. Kharitonova, and O.G. Rudnitskaya, Inorg. Mater. 41(7) (2005) 866.

[06Vor] V.I. Voronkova, E.P. Kharitonova, and O.G. Rudnitskaya, Inorg. Mater. 42 (2006) 1255.

[06Pay] M.H. Paydar, A.M. Hadian, and G. Fafilek, J. Mater. Sci. 41 (2006) 1953.

[07Kha] E.P. Kharitonova and V.I. Voronkova, Inorg. Mater. 43(1) (2007) 55.

[07Tan] Y. Taninouchi, T. Uda, Y. Awakura, A. Ikeda and S.M. Haile, J. Mater. Chem. 17 (2007) 3182.

[07MT] Y. Taninouchi, *Dehydration Behavior of Superprotonic Conductor CsH_2PO_4*, Master thesis, Kyoto University, 2007.

[08Kan] R. Kant, K. Singh, and O.P. Panday, Int. J. Hydrogen Energy 33 (2008) 455.

[08May] M. Malys, I. Abrahams, F. Krok, W. Wrobel, and J.R. Dygas, Solid State Ionics 179 (2008) 82.

[08Chm] J. Chmielowiec, G. Paściak, and P. Bujło, J. Alloys Compd. 451 (2008) 676.

[09Beg1] S. Beg, N.A.S. Al-Areqi, and A. Al-Alas, J. Alloys Compd. 479 (2009) 107.

[09Beg2] S. Beg, N.A.S. Al-Areqi, A. Al-Alas, and S. Hafeez, Physica B 404 (2009) 2072.

Chapter 2

Phase Classification

2.1. Introduction

The parent compound $Bi_2VO_{5.5}$ and BIMEVOX have a characteristic layered structure and exhibit the three main polymorphs of α, β, and γ, as shown in Chapter 1. However, besides the α-, β- and γ-phases, several phases that deviate from the three main phases are exhibited. In this chapter, a new phase classification system for BIMEVOX is established in terms of the network structures in V-O layer. Practical phase classification system described in this chapter is convenient to comprehensively understand the electrical conductivities and phase transitions in BIMEVOX.

2.2. Description of three main phases of α, β, and γ

The structure of $Bi_2VO_{5.5}$ consists of alternating layers of $(Bi_2O_2)^{2+}$, referred to as the Bi-O layer, and $(VO_{3.5})^{2-}$, referred to as the V-O layer. Figure 2.1(a) shows the atomic arrangements in Bi-O and V-O layers of α-, β-, and γ-$Bi_2VO_{5.5}$, which are drawn based on the crystalline data of α-, β-, and γ-$Bi_2VO_{5.5}$ obtained by Mairesse *et al.* [03Mai1,03Mai2]. Three main phases are characterized the polyhedron network structures in V-O layer. In γ-phase, V-O layer is made up of corner-sharing oxygen octahedrons that contain oxygen vacancies. Meanwhile, the complex network structures are observed in the α- and β-phases due to the ordering of oxygen vacancies. The crystalline structures of the three main phases are described by considering a subcell of $a_m = 0.55$, $b_m = 0.56$, and $c_m = 1.53$ nm. The α-phase is

(a) Atomic arrangements

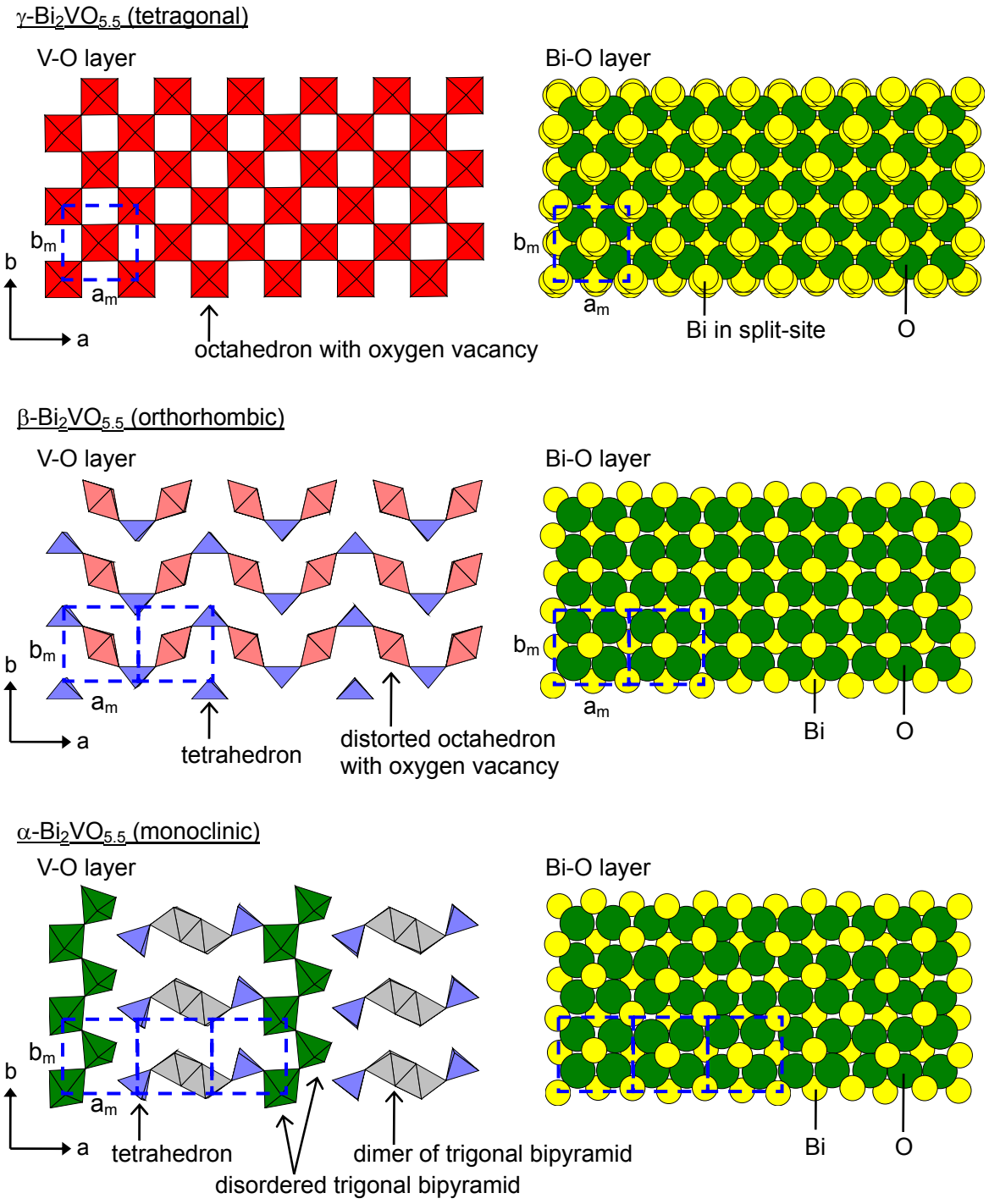

(b) XRD patterns

(c) Electrical conductivity

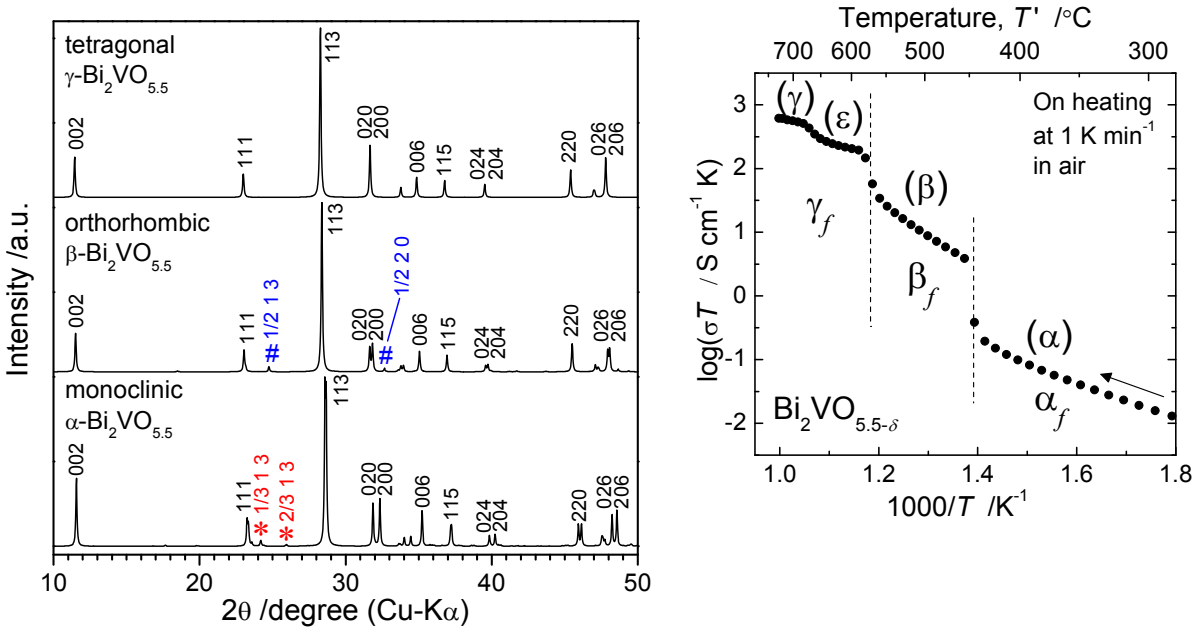

Figure 2.1 (a) Polyhedron network structures in the V-O layers and atomic arrangement in the Bi-O layers of monoclinic α-, orthorhombic β-, and tetragonal γ-$Bi_2VO_{5.5}$. The crystalline data reported by Mairesse *et al.* [03Mai1,03Mai2] were used. Blue boxes represent the subcells to characterize each phase, *i.e.*, a ≅ $3a_m$, b ≅ b_m, c ≅ c_m, and γ = 90.26° for the α-phase, a ≅ $2a_m$, b ≅ b_m, and c ≅ c_m for the β-phase, and a = b ≅ $a_m/\sqrt{2}$ and c ≅ c_m for the γ-phase. (b) XRD patterns for α-, β-, and γ-$Bi_2VO_{5.5}$ calculated from Cu-Kα_1 radiation. The asterisks (∗) and hash marks (#) indicate the typical superlattice diffraction peaks of α- and β-$Bi_2VO_{5.5}$, respectively. The plane indices are marked assuming the mean orthorhombic subcell. (c) Electrical conductivity of $Bi_2VO_{5.5-\delta}$ in air at a heating rate of 1 K min^{-1}. $Bi_2VO_{5.5-\delta}$ pellet was sintered at 800 °C and slowly cooled at 1 K min^{-1} to room temperature.

a monoclinic cell of $a \cong 3a_m$, $b \cong b_m$, $c \cong c_m$, and $\gamma = 90.26°$, the β-phase is an orthorhombic cell of $a \cong 2a_m$, $b \cong b_m$, and $c \cong c_m$, and the γ-phase is a tetragonal cell of $a = b \cong a_m/\sqrt{2}$ and $c \cong c_m$. Figure 2.1(b) shows the XRD patterns calculated from Cu-Kα_1 radiation. The diffraction peaks are indexed on the orthorhombic subcell of a_m, b_m, and c_m. The three phases show similar profiles except for split peaks such as 2 2 0 at about 46° and characteristic superlattice diffraction peaks (*e.g.*, 1/3 1 3 at about 24° for α-phase, 2/3 1 3 at about 26° for the β-phase). In the γ-phase, some diffraction peaks, *e.g.*, 0 2 0 and 2 0 0 at about 32°, merge and no superlattice diffraction peaks are observed. Figure 2.1(c) shows typical changes in the electrical conductivity of $Bi_2VO_{5.5-\delta}$ upon heating. The electrical conductivities markedly vary among three phases [88Abr,93Lee]. The α-phase is an n-type semiconductor. Meanwhile, β-phase exhibits the oxide-ion conductivity as high as 10^{-2} S cm^{-1} at 500 °C, and γ-$Bi_2VO_{5.5}$ exhibit the oxide-ion conductivity 6×10^{-1} S cm^{-1} at 700 °C.

2.3. Description of the phases deviating from α, β, and γ

Even in $Bi_2VO_{5.5-\delta}$, there are two additional phases that deviate slightly from the α- and γ-phases. Figure 2.2(a) shows the XRD patterns of $Bi_2VO_{5.5-\delta}$ powders that were quenched in air or cooled at 1 K min^{-1} from 800 °C to room temperature. Both of the samples showed the characteristic superlattice diffractions for the α-phase. In contrast, the monoclinic distortion at 2 2 0 disappeared in the quenched sample. This indicates that an orthorhombic phase which has an atomic configuration similar to that of the α-phase (denoted as orthorhombic α-like-phase) can be obtained by rapid cooling. In conductivity change on heating shown in Figure 2.1(c), two conductivity jumps were mainly observed at about 450 and 570 °C, which are generally explained by transitions from α to β and from β to γ, respectively. However,

another small jump exists at about 650 °C. Abrahams *et al.* reported that the ε-phase, which shows an orthorhombic phase slightly distorted from the γ-phase, can be detected from 570 to 650 °C by high-resolution powder neutron diffraction [05Abr]. It is quite difficult to identify the ε-phase by thermal analysis and conventional XRD analysis.

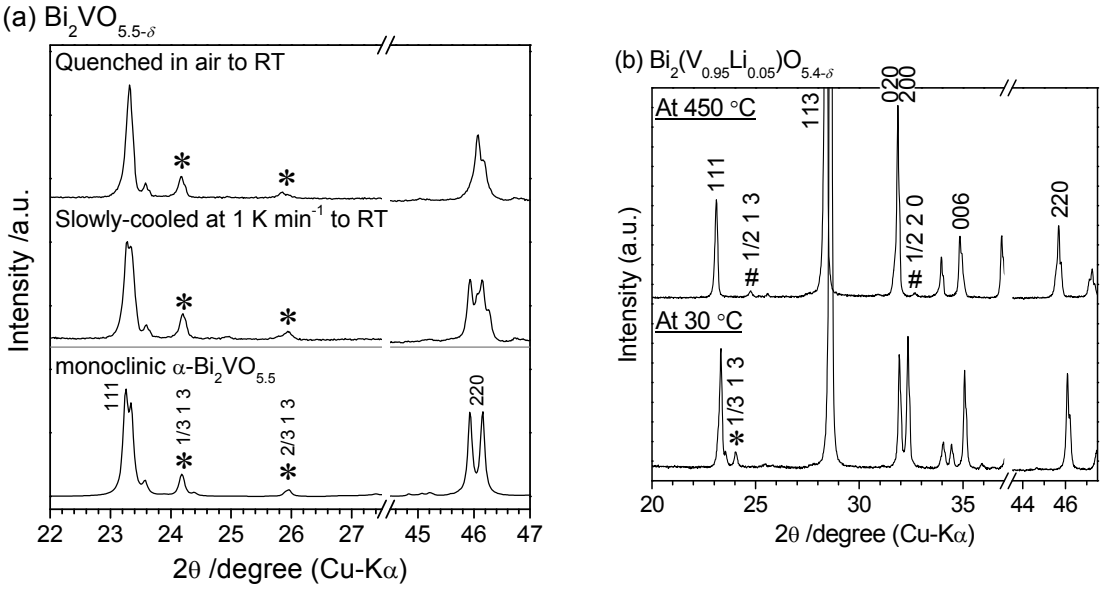

Figure 2.2 (a) XRD pattern of $Bi_2VO_{5.5-\delta}$ powders quenched and slowly-cooled at 1 K min^{-1} from 800 °C. Reference pattern of monoclinic α-$Bi_2VO_{5.5}$ calculated from Cu-Kα$_1$ radiation is also shown. Orthorhombic α-like-phase was obtained in quenched powder. (b) HT-XRD patterns of $Bi_2(V_{0.95}Li_{0.05})O_{5.4-\delta}$ at 30 and 450 °C on heating [Chapter4]. Orthorhombic α-like-phase and tetragonal β-like-phase was observed at 30 and 450 °C, respectively.

In BIMEVOX, polymorphs are more complexes. Huve *et al.* reported that a small amount of impurity or dopant often causes the orthorhombic α-like-phase [96Huv]. It was found that orthorhombic α-like-phase as well as tetragonal phase showing superlattice diffractions for orthorhombic β-phase (denoted as β-like-phase) can be obtained in $Bi_2(V_{0.95}Li_{0.05})O_{5.4-\delta}$ and $Bi_2(V_{0.95}Ag_{0.05})O_{5.4-\delta}$, as shown in Figure 2.2(b) [Chapter4]. Furthermore, a γ'-phase was reported in some forms of BIMEVOX, such as $Bi_2(V_{0.9}Cu_{0.1})O_{5.35-\delta}$ [90Abr,02Wat]. Figure

2.3 shows the electrical conductivities of $Bi_2(V_{0.9}Cu_{0.1})O_{5.35-\delta}$ measured in the present study and that reported by Watanabe and Das [02Wat]. A slight conductivity jump is observed at around 480 °C. It is quite difficult to identify the difference between γ'- and γ-phases by conventional XRD analysis. By careful XRD analysis on single crystal, Pernot *et al.* revealed that γ'-$Bi_2(V_{0.9}Cu_{0.1})O_{5.35-\delta}$ has some weak and highly complex incommensurate superstructures [94Per]. The conductivity changes for the γ'/γ transition are observed in $Bi_2(V_{0.9}Li_{0.1})O_{5.3-\delta}$ and $Bi_2(V_{0.9}Ag_{0.1})O_{5.3-\delta}$, as described in Chapter 4.

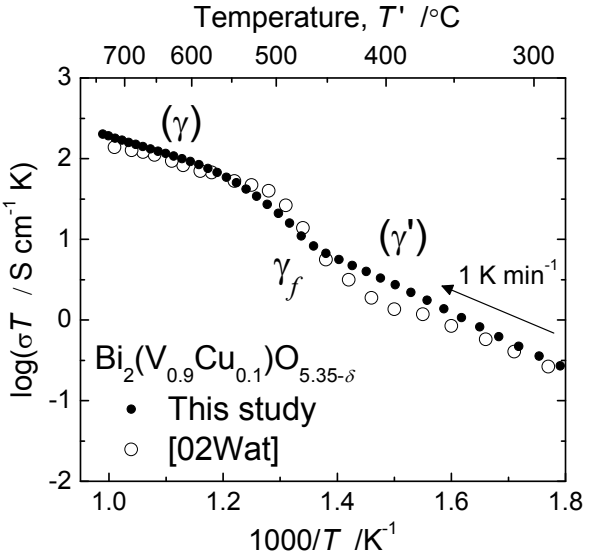

Figure 2.3 Electrical conductivity of $Bi_2(V_{0.9}Cu_{0.1})O_{5.35-\delta}$ on heating. Pellet with Au electrodes were quenched from 800 °C and then heated at 1 K min^{-1} in air. The conductivity reported by Watanabe and Das [02Wat] is also shown.

2.4. Establishment of practical phase classification system

For convenience in the following discussions on BIMEVOX, a practical phase classification system is established based on the network structure of the V-O layers without considering strict crystalline symmetries. Table 2.1 shows the three phase groups of α_f, β_f, and γ_f defined by the superlattice diffraction peaks and electrical conductivities. The phases

exhibiting the characteristic superlattice diffraction peaks of α- and β-$Bi_2VO_{5.5}$ are called α_f and β_f defined as families of α and β, respectively. Phases without the characteristic superlattice diffraction peaks of α and β are called γ_f and defined as the γ family. The polyhedron network structures in the V-O layer of α_f, β_f, and γ_f must resemble those of α-, β-, and γ-$Bi_2VO_{5.5}$ in Figure 2.1(a), respectively. That is, α_f corresponds to subcell of $3a_m \times b_m \times c_m$, β_f to that of $2a_m \times b_m \times c_m$, and γ_f to that of $a_m \times b_m \times c_m$. Because the main difference among the three groups is the extent of order/disorder of oxygen vacancies, the oxide-ion conductivity is highest for γ_f, intermediate for β_f, and lowest for α_f at a given composition. Consequently, this phase classification of α_f, β_f, and γ_f, by ignoring strict crystalline symmetries, is more convenient for explaining the characteristic conductivities of BIMEVOX.

Table 2.1 Classification of various phases of $Bi_2VO_{5.5}$ and BIMEVOX.

Phase group	Feature
α_f	Typical superlattice diffraction peaks of α-$Bi_2VO_{5.5}$, such as 1/3 1 3 and 2/3 1 3, appear in the XRD profile. The polyhedron network structure in the V-O layer resembles that of α-$Bi_2VO_{5.5}$. High-level order and low-conductive phases. Includes monoclinic α-phase and orthorhombic α-like-phase.
β_f	Typical superlattice diffraction peaks of β-$Bi_2VO_{5.5}$, such as 1/2 1 3 and 1/2 2 0, appear in the XRD profile. The polyhedron network structure in the V-O layer resembles that of β-$Bi_2VO_{5.5}$. Intermediate-level disorder and intermediate-conductive phases. Includes orthorhombic β-phase and tetragonal β-like-phase.
γ_f	Typical superlattice diffraction peaks of α- and β-$Bi_2VO_{5.5}$ are not observed in the XRD profile. The polyhedron network structure in the V-O layer resembles that of γ-$Bi_2VO_{5.5}$. High-level disorder and high-conductive phases. Includes tetragonal γ-phase as well as ε- and γ'-phases.

2.5. Conclusion

In this chapter, a practical phase classification system has established. Many structural phases, *i.e.*, three main phases of α, β, and γ as well as α-like-phase, β-like-phase, ε-phase, and γ'-phase, were exhibited depending on the composition, temperature, and thermal history. The structural phases of $Bi_2VO_{5.5-\delta}$ and BIMEVOX were classified into the three groups of α_f, β_f, and γ_f on the basis of characteristic superlattice diffractions and trends of oxide-ion conductivities in each group, without strictly determining crystalline symmetries.

References

[88Abr] F. Abraham, M.F. Debreuille-Gresse, G. Mairesse, and G. Nowogrocki, Solid State Ionics 28-30 (1988) 529.

[90Abr] F. Abraham, J.C. Boivin, G. Mairesse, and G. Nowogrocki, Solid State Ionic 40-41 (1990) 934.

[93Lee] C.K. Lee, D.C. Sinclair, and A.R. West, Solid State Ionics 62 (1993) 193.

[94Per] E. Pernot, M. Anne, M. Bacmann, P. Strobel, J. Fouletier, R.N. Vannier, G. Mairesse, F. Abraham, and G. Nowogrocki, Solid State Ionics 70-71 (1994) 259.

[96Huv] M. Huve, R.N. Vannier, G. Nowogrocki, G. Mairesse, and G.V. Tendeloo, J. Mater. Chem. 6(8) (1996) 1339.

[02Wat] A. Watanabe and K. Das, J. Solid State Chem. 163 (2002) 224.

[03Mai1] G. Mairesse, P. Roussel, R.N. Vannier, M. Anne, C. Pirovano, and G. Nowogrocki, Solid State Science 5 (2003) 851.

[03Mai2] G. Mairesse, P. Roussel, R.N. Vannier, M. Anne, and G. Nowogrocki, Solid State Science 5 (2003) 861.

[05Abr] I. Abrahams, F. Krok, M. Malys, and W. Wrobel, Solid State Ionics 176 (2005) 2053.

Chapter 3

Doping with Bi:

"Oxide-Ion Conductivity and Phase Stability of $Bi_2(V_{1-x}Bi_x)O_{5.5+\Delta}$ ($0 \le x \le 0.08$)"

3.1. Introduction

The first objective is to determine the electrical conductivity and phase transition behavior of $Bi_2(V_{1-x}Bi_x)O_{5.5+\Delta}$ ($\Delta \equiv d - \delta$, where Δ is total oxygen deviation, d is deviation due to aliovalent doping, and δ is loss due to partial reduction). Bi is expected to have smaller valence and a larger size than V (ionic radii in 6-fold coordination; Bi^{3+}: 0.103 nm and V^{5+}: 0.054 nm [76Sha]). Thus, Bi content should change the physical properties of BIMEVOX. In 1993, Lee *et al.* reported the phase diagram of the Bi_2O_3-V_2O_5 system at around $Bi_2VO_{5.5}$ (66.7 mol% Bi_2O_3) [93Lee]. In 2001, however, Watanabe reported that BIMEVOX phases, whose compositions are 66.7 and 68.5 mol% Bi_2O_3, are metastable below 550 °C and decompose to $BiVO_4$ and $Bi_{3.5}V_{1.2}O_{8.25}$ after 300 hr or more [01Wat]. In 2005, Steil *et al.* also confirmed that β-$Bi_2VO_{5.5-\delta}$ completely decomposes into $BiVO_4$ and $Bi_{3.5}V_{1.2}O_{8.25}$ at 500 °C after 7 weeks [05Ste]. Thus, the second objective is to further investigate the thermal decomposition of $Bi_2(V_{1-x}Bi_x)O_{5.5+\Delta}$ and describe the phase diagram. The partial reduction phenomenon of $Bi_2VO_{5.5-\delta}$ is also described in this chapter.

3.2. Sample preparation

Table 3.1 shows the abbreviations used to denote the prepared samples. Figure 3.1 shows

plots of the compositions of prepared samples in the pseudo-binary phase diagram reported by Lee *et al.* [93Lee]. Polycrystalline powders were synthesized by solid-state reaction in air using a platinum crucible. The starting materials were Bi_2O_3 (99.99%, Furuuchi chemical) and V_2O_5 (99.9%, Furuuchi chemical), which were dried at 600 °C and 300 °C, respectively. The final calcination temperatures were 800 °C (BiP, Bi0, Bi2, Bi5, Bi8, and BiR) and 750 °C ($BiVO_4$). The molar ratio of Bi to V in Bi0 was determined to be 2.03 ± 0.05 by ICP-AES, which allows us to regard the composition of Bi0 as $Bi_2VO_{5.5}$.

Table 3.1 Abbreviations and compositions of prepared samples, and phases at room temperature. The chemical formulas of Bi0 and Bi8 are expressed ignoring the existence of small amounts of secondary phase. XRD analysis was performed for the powders quenched from 800 °C.

Abbreviation	Composition		Phase at room temperature
	Mol% Bi_2O_3	Chemical formula	
$BiVO_4$	50.0	$BiVO_4$	$BiVO_4$
BiP	64.0	-	α_f (orthorhombic) + $BiVO_4$
Bi0	66.7	$Bi_2VO_{5.5-\delta}$	α_f (orthorhombic) + $BiVO_4$
Bi2	67.3	$Bi_2(V_{0.98}Bi_{0.02})O_{5.48-\delta}$	α_f (orthorhombic)
Bi5	68.3	$Bi_2(V_{0.95}Bi_{0.05})O_{5.45-\delta}$	α_f (orthorhombic)
Bi8	69.3	$Bi_2(V_{0.92}Bi_{0.08})O_{5.42-\delta}$	α_f (orthorhombic) + unidentified phase
BiR	71.0	-	Unidentified phases

Bi0, Bi2, Bi5, and Bi8 powders were sintered for conductivity measurements. The synthesized powders were mixed with an organic binder solution and compressed uniaxially at 3 ton cm^{-2} for 15 min. Shaped samples were placed on a platinum plate and kept at 500 °C for 5 hr to dry/burn the binder solution. Then, pellets were sintered at 800 °C for 24 hr in air. The surfaces of sintered pellets (diameter: ~10 mm, thickness: ~1.2 mm) were mirror-polished

using SiC polishing paper and Au electrodes were applied with gold paint (No.8560, Tokuriki Chemical Research). We also prepared a rectangular bar of Bi0 (1.57×3.17×7.65 mm^3) by cutting a sintered pellet using a diamond saw.

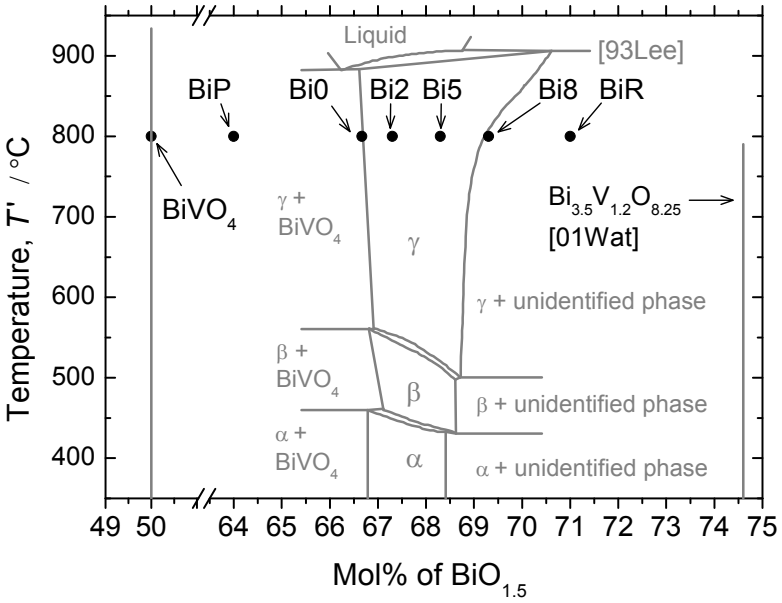

Figure 3.1 Compositions of prepared samples plotted in the Bi_2O_3-V_2O_5 phase diagram. Phase relationships reported by Lee *et al.* [93Lee] are also shown in gray. The melting temperature of $BiVO_4$ is about 934 °C. Watanabe reported that $Bi_{3.5}V_{1.2}O_{8.25}$ exists as a stable phase in the Bi_2O_3-V_2O_5 system but decomposes into two unidentified phases above 790 °C [01Wat].

3.3. Variations in XRD pattern of Bi_2O_3-V_2O_5 system

Figure 3.2 shows the XRD patterns of powders quenched from 800 °C in a logarithmic scale. Observed phases are listed in Table 3.1. In quenched Bi0 powder, orthorhombic α_f was obtained. In addition, Bi0 contained a small amount of $BiVO_4$ because the true stoichiometry of $Bi_2VO_{5.5-\delta}$ is slightly Bi-rich. This agrees with the reports by Lee *et al.* [93Lee] and Watanabe [01Wat]. Single-phase orthorhombic α_f was obtained in quenched powders of Bi2 and Bi5. In Bi8, an unidentified phase appeared as a small amount of secondary phase, which

means that the solid solution of Bi-doped $Bi_2VO_{5.5}$, *i.e.*, x in $Bi_2(V_{1-x}Bi_x)O_{5.5+\Delta}$, is $0 < x < 8$ at 800 °C. The solid solution in this study matches that reported by Lee *et al.* [93Lee], as shown in Figure 3.1. Details of phase relationships at higher Bi_2O_3 concentrations are still unclear. In quenched BiR powder, the BIMEVOX phase was not observed and unidentified phases appeared. The unidentified phases in Bi8 and BiR were not $Bi_{3.5}V_{1.2}O_{8.25}$ because $Bi_{3.5}V_{1.2}O_{8.25}$ decomposes into two unidentified phases above 790 °C [01Wat]. We believe that the stable solid phase, whose composition is about 71 mol% Bi_2O_3, exists above 790 °C.

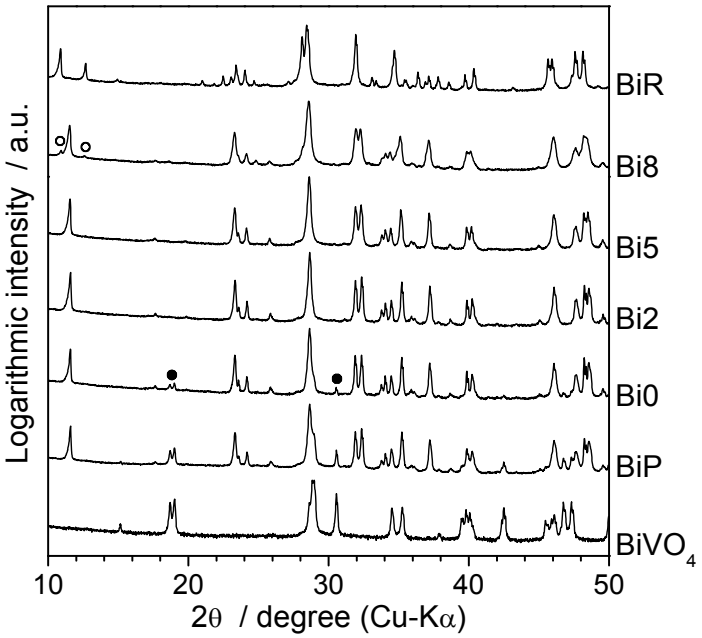

Figure 3.2 XRD patterns of powders quenched from 800 °C. The intensities are plotted in logarithmic scale. Bi0 contains a small amount of $BiVO_4$, whose typical peaks are indicated by closed circles (•). Bi8 contains a small amount of unidentified phase, whose typical peaks are indicated by open circles (o). The detected phases are summarized in Table 3.1

3.4. Electrical conductivities and phase transitions determined by AC impedance spectroscopy, DSC, and HT-XRD analysis

The sintered pellets exhibited relative densities as high as 95%. The grains grew substantially larger than 10 μm. AC impedance spectroscopy was performed during heating at

1 K min^{-1} in air. Just before conductivity measurements, the pellets with Au-electrodes were heated to 800 °C and then quenched to room temperature. It should be noted that Ag cannot be used for electrodes of BIMEVOX because Ag reacts with Bi0 at high temperatures in air, as shown in Figure 3.3.

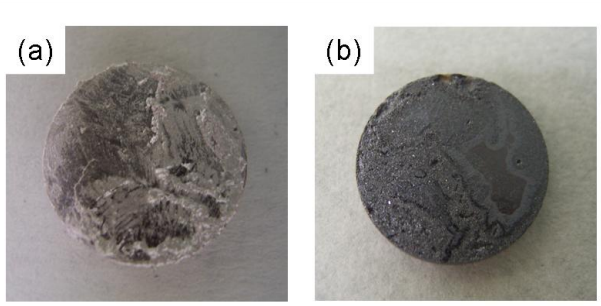

Figure 3.3 Bi0 pellet with Ag electrode (a) before and (b) after heating at 700 °C for 24 hr in air. Ag reacted with $Bi_2VO_{5.5-\delta}$ at 700 °C in air. After annealing, the color of electrode changed from silver to black, and XRD indicated the disappearance of metal Ag.

Figure 3.4(a) shows the typical impedance spectra for α_f of Bi0, obtained with a pellet and a rectangular bar. At α_f of Bi0, which is an n-type semiconductor, two semicircles appeared in the high frequency region (Arc-1) and the low frequency region (Arc-2). When two parallel RQ circuits in series ($Q \equiv (i\omega)^p Y_0$, Q: constant phase element, ω: angular frequency, p: deviation from ideal semicircle, Y_0: capacitance) are assumed for the spectrum obtained with the pellet sample, the simulated values for Arc-1 were R = 5597 Ω, $Y_0 = 1.1\times10^{-8}$ F, and p = 0.69, and those for Arc-2 were R = 8199 Ω, $Y_0 = 6.8\times10^{-6}$ F, and p = 0.50. The geometrical factors of the rectangular bar (S: electrode area, L: distance between two electrodes, S/L = 6.51×10^{-2} cm, S = 4.98×10^{-2} cm^2) differ substantially from those of the pellet (S/L = 4.94 cm, S = 7.76×10^{-1} cm^2). However, the resistivities of Arc-1 and Arc-2 normalized by S/L were sufficiently similar for the pellet and the rectangular bar. Thus, neither Arc-1 nor Arc-2 originates from the interface between electrolyte and electrode. By considering the

capacitance in each component, we conclude that Arc-1 originates from the bulk, and that Arc-2 originates from the grain boundary. The resistivity of the Bi0 electrolyte, *i.e.*, the total of bulk and grain boundary, was evaluated from the right edge of Arc-2. Figures 3.4(b) and (c)

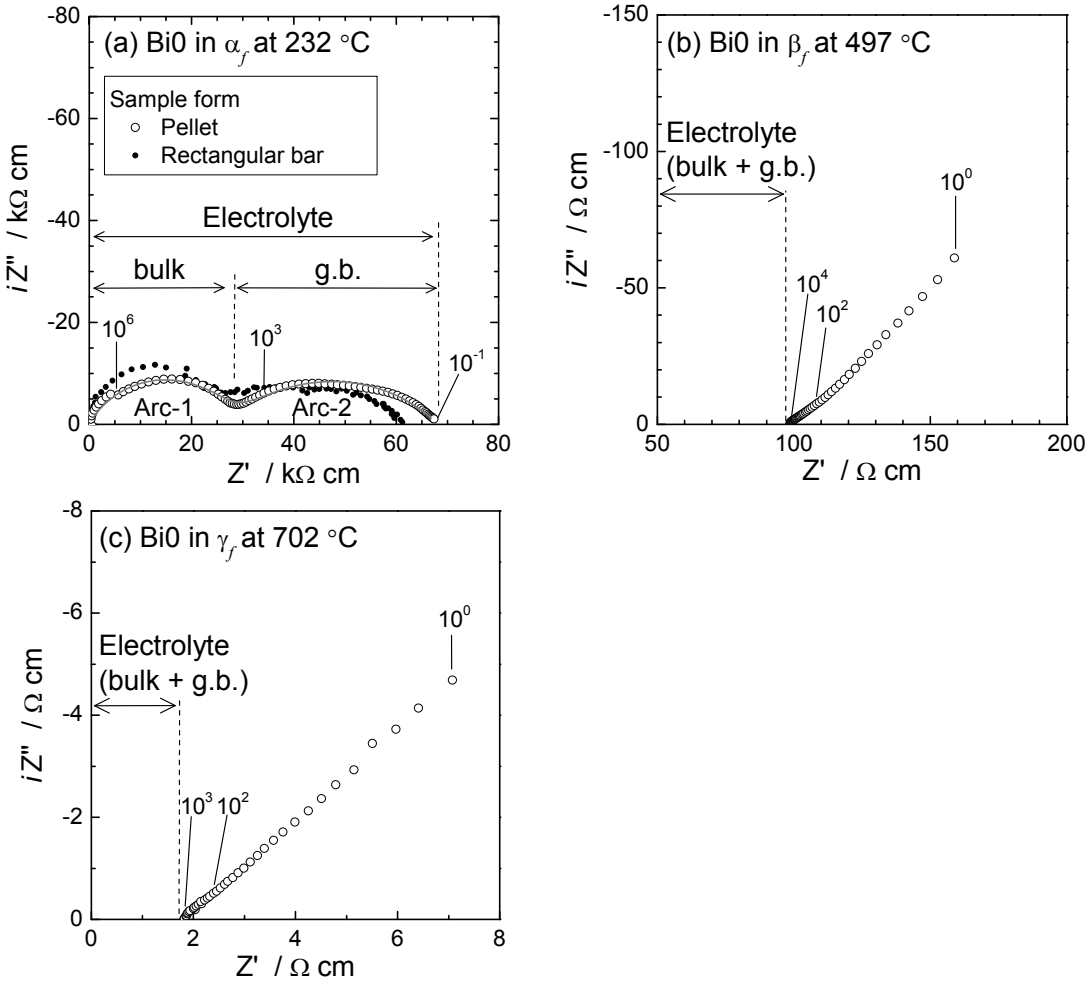

Figure 3.4 Typical impedance spectra of Bi0 pellet (a) in α_f at 232 °C, (b) in β_f at 497 °C, and (c) in γ_f at 702 °C. The gray line in (a) indicates the fitting curve with two parallel *RQ* circuits in series. The data collected for the rectangular bar is also shown in (a). The geometrical factors of the rectangular bar (S/L = 6.51×10^{-2} cm, S = 4.98×10^{-2} cm^2) differ substantially from those of the pellet (S/L = 4.94 cm, S = 7.76×10^{-1} cm^2).

show the typical impedance spectra for β_f and γ_f of Bi0, respectively. β_f and γ_f of Bi0 are oxide ion conductors. The spectra appear as almost straight lines inclined at an angle of ~45° to the real axis, which can be explained by the Warburg impedance, *i.e.*, the ionic diffusion-limited

process in the electrode reaction [97Jia]. The highly ionic conductors attached with blocking electrodes for ion diffusion exhibited similar spectra [07Tan,08Tan]. The resistivity of the Bi0 electrolyte was evaluated from the intercept of the spectrum with the real axis.

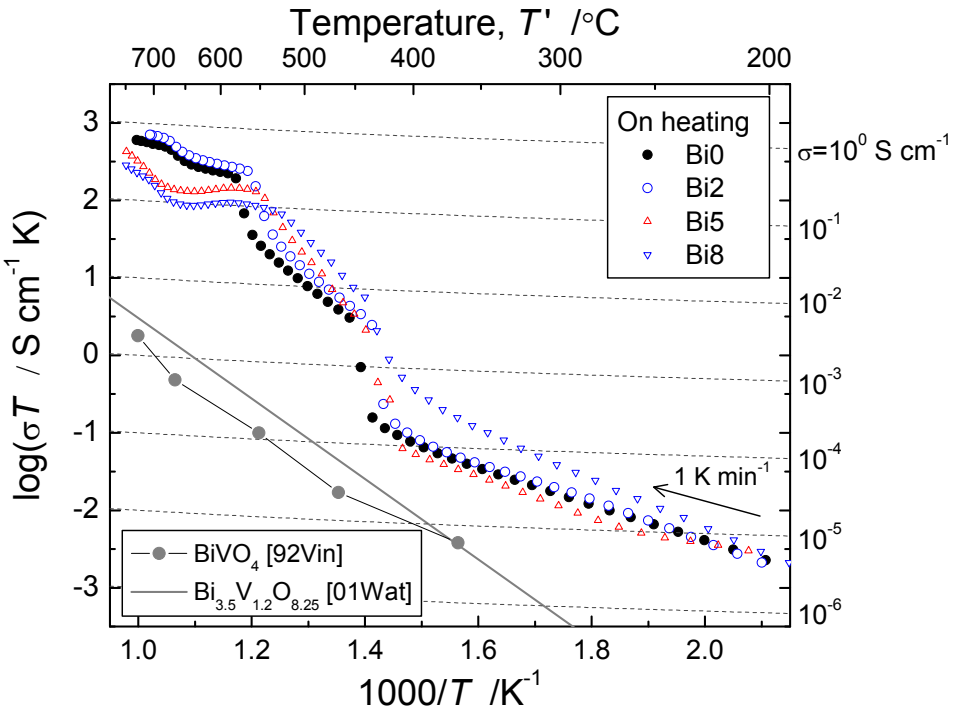

Figure 3.5 Temperature dependence of electrical conductivities of Bi0, Bi2, Bi5, and Bi8. Pellets quenched from 800 °C were heated at 1 K min^{-1} in air. The electrical conductivities of $BiVO_4$ [92Vin] and $Bi_{3.5}V_{1.2}O_{8.25}$ [01Wat] are also shown.

Figure 3.5 shows Arrhenius plots of the electrical conductivities of Bi0, Bi2, Bi5, and Bi8. Reported conductivities of $BiVO_4$ [92Vin] and $Bi_{3.5}V_{1.2}O_{8.25}$ [01Wat] are also plotted. $BiVO_4$ is a mixed conductor of electrons and oxide ions [92Vin], but the charge carrier in $Bi_{3.5}V_{1.2}O_{8.25}$ is unknown. Bi-doping stabilizes β_f and γ_f at lower temperatures, which agrees with the phase diagram in Figure 3.2 reported by Lee *et al.* [93Lee]. Additionally, for Bi5 and Bi8, the conductivity jump at the transition from β_f to γ_f (β_f/γ_f transition) almost disappeared and only a slope change was observed. Substitution of trivalent Bi for pentavalent V sites is expected to increase the amount of oxygen vacancies (decrease oxygen content per chemical

formula) to preserve electroneutrality. At 500 °C, at which β_f were stable in all samples, conductivity increased with an increase in Bi content. On the other hand, the conductivity of γ_f largely decreased in Bi5 and Bi8.

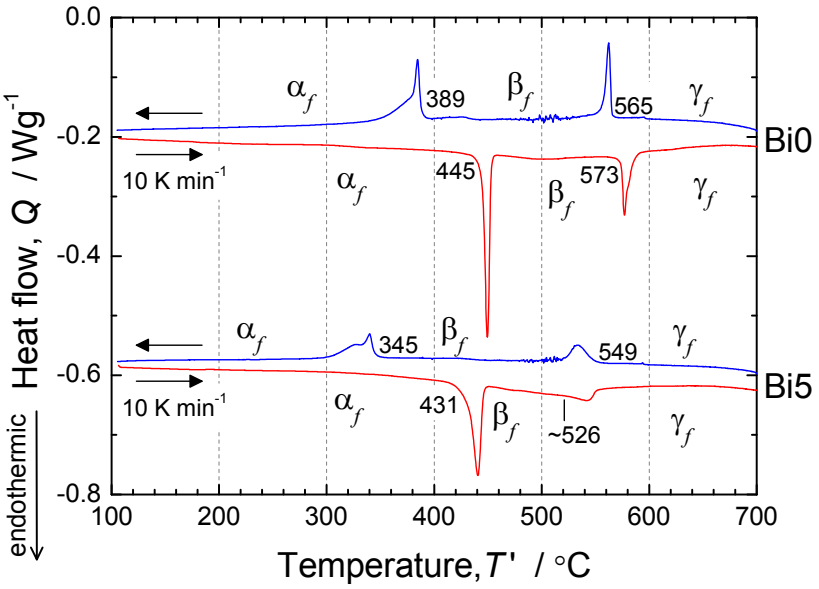

Figure 3.6 DSC profiles of Bi0 and Bi5. Powder samples quenched from 800 °C were heated and cooled at 10 K min^{-1} in air. Numbers denote onset temperatures of each endothermic and exothermic peak.

Figure 3.6 shows the DSC profiles of Bi0 and Bi5. Powders quenched from 800 °C were heated and cooled at 10 K min^{-1} between 100 and 700 °C in stagnant air. Bi0 exhibits two endothermic peaks on heating and two exothermic peaks on cooling, corresponding to the transitions between α_f, β_f, and γ_f. The transition temperature from α_f to β_f ($T_{\alpha/\gamma}$) and that from β_f to γ_f ($T_{\beta/\gamma}$) are evaluated from the onset temperatures of endothermic peaks. For Bi5, the endothermic peak of the β_f/γ_f transition was broad and small, which corresponds to the continuous conductivity change at the β_f/γ_f transition in Figure 3.5. For Bi5, $T_{\alpha/\gamma}$ decreased from 445 to 431 °C, and $T_{\beta/\gamma}$ decreased from 573 to about 526 °C.

HT-XRD analysis was carried out for Bi0 powder quenched from 800 °C. The scan rate of the sample temperature was 10 K min^{-1}. The sample temperatures were maintained for 5 min at 50 °C intervals, and diffraction patterns were collected within 10 min at each temperature.

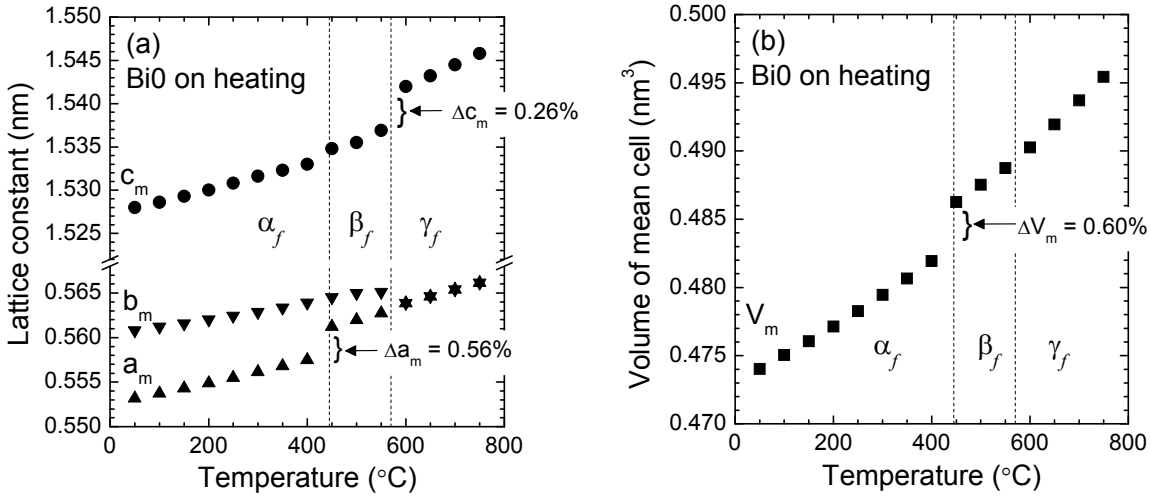

Figure 3.7 Lattice parameters as a function of temperature on heating. HT-XRD analysis was performed for Bi0 powder quenched from 800 °C. (a) Lattice constants of a_m, b_m, and c_m. (b) Volume of subcell, V_m.

α_f, β_f, and γ_f can be characterized using a orthorhombic subcell of a_m, b_m, and c_m, as described in Chapter 2. Figure 3.7 shows the parameters of the subcell, *i.e.*, a_m, b_m, c_m, and the cell volume V_m, as a function of temperature. Orthorhombic α_f was transformed to orthorhombic β_f and then to tetragonal γ_f with increasing temperature. In terms of lattice constants, the α_f/β_f transition was mainly related to the jump in a_m (0.56%), and the $\beta_f/\gamma f$ transition to the jump in c_m (0.26%). At the α_f/β_f transition, V_m jumps about 0.60%. Meanwhile, the volume jump was very small at the β_f/γ_f transition.

3.5. Long-term phase stabilities

3.5.1 Thermal decomposition and phase diagram determined by XRD analysis of annealed powders and DTA

Figure 3.8 shows the XRD patterns of Bi0 and Bi5 powders annealed for 200 hr in air. The BIMEVOX phase in Bi0 was stable at 700 °C for 200 hr, when we neglect small amount of $BiVO_4$ in as-prepared sample. However, thermal decomposition proceeded at 600 and 500 °C.

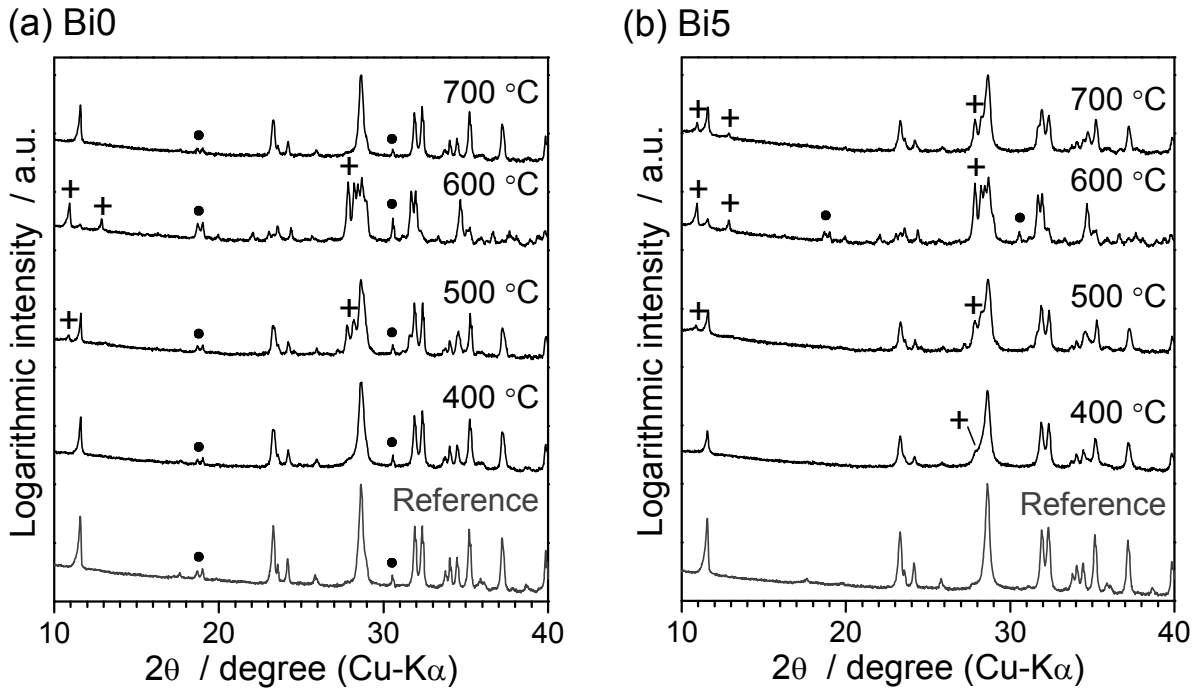

Figure 3.8 XRD patterns of (a) Bi0 powders and (b) Bi5 powders that were annealed for 200 hr in air. The XRD patterns of powders quenched from 800 °C are also shown as references. Crosses (+) indicate typical peaks of $Bi_{3.5}V_{1.2}O_{8.25}$ caused by the thermal decomposition of BIMEVOX phase. Closed circles (•) indicate typical peaks of $BiVO_4$.

In particular, BIMEVOX phase almost-totally decomposed into $BiVO_4$ and $Bi_{3.5}V_{1.2}O_{8.25}$ at 600 °C, which means that γ_f of $Bi_2(V_{1-x}Bi_x)O_{5.5+\Delta}$ is metastable at around 600 °C. At 400 °C, the thermal decomposition of Bi0 was kinetically suppressed. Figure 3.8(b) indicates that decomposition of Bi5 proceeded at all annealing temperatures of 700, 600, 500, and 400 °C.

This clearly indicates that Bi-doping does not effectively suppress the thermal decomposition at intermediate temperatures. The decomposition of Bi5 was prominent at 600 °C. Bi5 annealed at 600 °C contained $BiVO_4$ and $Bi_{3.5}V_{1.2}O_{8.25}$ besides small amount of BIMEVOX phase. Meanwhile, Bi5 annealed at 400, 500, 700 °C did not contain $BiVO_4$ as a decomposition product. Because Bi0 was stable at 700 °C, Bi5 exists in the two-phase region of BIMEVOX phase and $Bi_{3.5}V_{1.2}O_{8.25}$ at 700 °C. This means that the solubility limit of Bi at 700 °C is smaller than that at the synthesis temperature of 800 °C. At 400 and 500 °C, at which Bi5 should exist in the two-phase region of $BiVO_4$ and $Bi_{3.5}V_{1.2}O_{8.25}$, decomposition of Bi5 into BIMEVOX phase and $Bi_{3.5}V_{1.2}O_{8.25}$ proceeded for 200 hr, but production of $BiVO_4$ was kinetically suppressed. Annealing at 750 °C for 12 hr returned the decomposed Bi5 to a single phase of BIMEVOX. Thus, Bi5 is thermodynamically stable above 750 °C.

The results of XRD analysis are summarized as a pseudo-binary phase diagram in Figure 3.9(a). The upper limit of the stable region of the BIMEVOX phase was evaluated by DTA. Quenched powders in an alumina container were heated at 10 K min^{-1} in air until the liquid phase appeared. Figure 3.9(b) shows the DTA profiles of Bi0, Bi2, and Bi5. Large endothermic reactions started at T_1 and ended at T_2. For regions (i) and (ii) in Figures 3.9(a) and (b), we assume the following phases: (i) solid + liquid, from T_1 to T_2, and (ii) liquid, above T_2. The shaded area in Figure 3.9(a) indicates the thermodynamically stable region of the BIMEVOX phase. In this area, single phase of γ_f can be obtained even after prolonged annealing. The phase diagram clarifies that Bi-doping reduces the size of the thermodynamically stable region of the BIMEVOX phase below 800 °C, although T_1 somewhat increases.

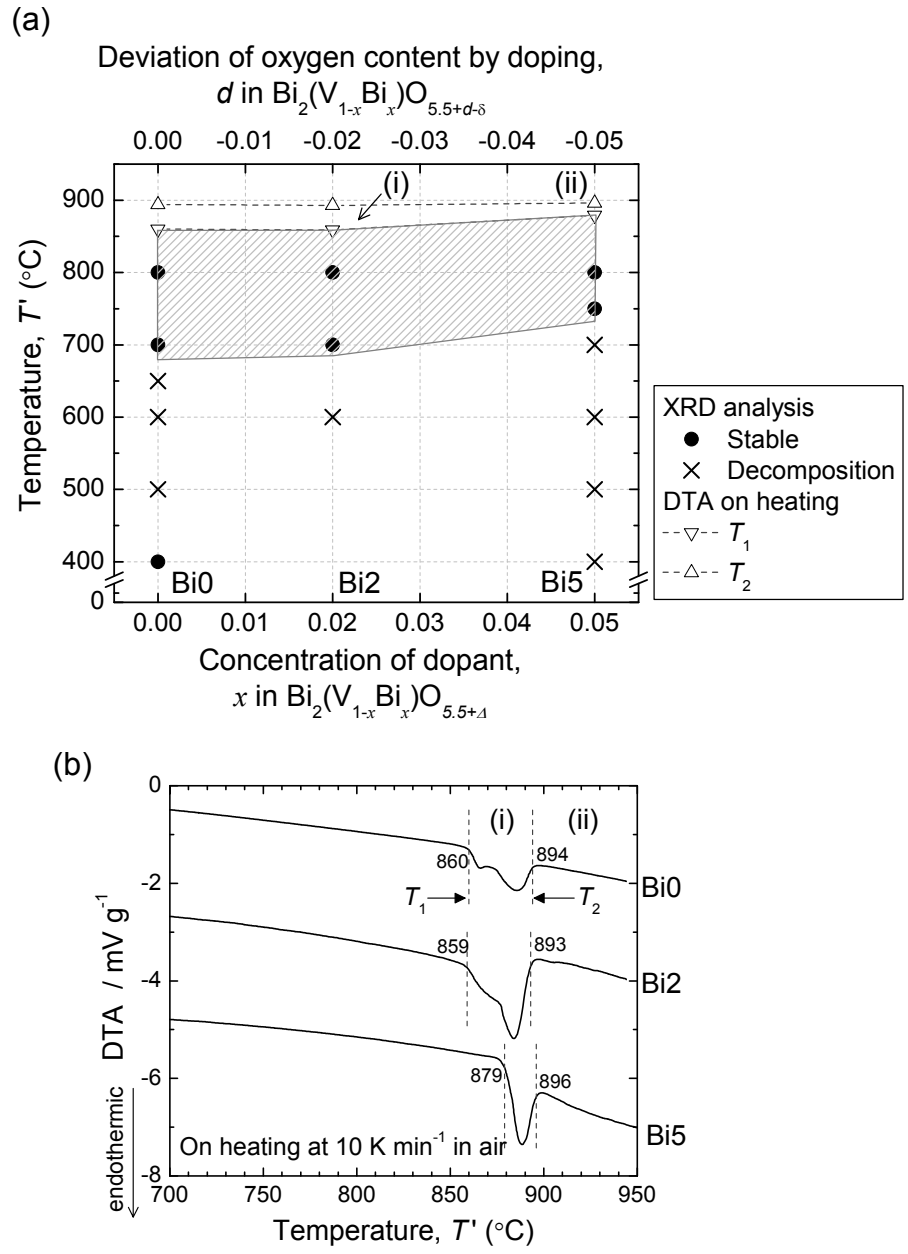

Figure 3.9 (a) Pseudo-binary phase diagram of $Bi_2(V_{1-x}Bi_x)O_{5.5+\Delta}$, generated by XRD analysis and DTA. As-prepared Bi0 contains a small amount of $BiVO_4$. The solid solution of $Bi_2(V_{1-x}Bi_x)O_{5.5+\Delta}$ at 800 °C is $0 < x < 8$. The shaded area indicates the thermodynamically stable region of the γf phase, where γ_f is stable. (b) DTA profiles of Bi0, Bi2, and Bi5 obtained at a heating rate of 10 K min^{-1} in air. The following phases are assumed: (i) solid + liquid, from T_1 to T_2, (ii) liquid, above T_2.

3.5.2 Time dependence of electrical conductivities determined by AC impedance spectroscopy

Figure 3.10 shows the time-dependent degradation of the conductivity of Bi0 at 600 °C in air. The conductivity after annealing for *n* hours is denoted as $\sigma_{n\mathrm{hr}}$ (*n*: annealing time). The $\sigma_{n\mathrm{hr}}$ and the ratio of $\sigma_{n\mathrm{hr}}$ to $\sigma_{0\mathrm{hr}}$, *i.e.*, $\sigma_{n\mathrm{hr}}/\sigma_{0\mathrm{hr}}$, are summarized in Table 3.2. Before annealing, γ_f of Bi0 exhibited high oxide-ion conductivity of 2.67×10^{-1} S cm^{-1} ($\sigma_{0\mathrm{hr}}$) at 600 °C. The conductivity declined exponentially with annealing time due to the progression of thermal decomposition into $BiVO_4$ and $Bi_{3.5}V_{1.2}O_{8.25}$. The electrical conductivity reached a steady state after 150 hr, corresponding to the completion of decomposition reaction. By fitting the data with an exponential decay function, we evaluated the conductivity in the steady-state as 2.01×10^{-2} S cm^{-1}, which is denoted as $\sigma_{\infty\mathrm{hr}}$. For Bi0 at 600 °C, $\sigma_{\infty\mathrm{hr}}/\sigma_{0\mathrm{hr}}$ was evaluated as 0.075. It should be noted that the $\sigma_{\infty\mathrm{hr}}$ of Bi0 at 600 °C, *i.e.*, conductivity of the composite of $BiVO_4$ and $Bi_{3.5}V_{1.2}O_{8.25}$, was about 2 orders of magnitude higher than the conductivities of $BiVO_4$ [92Vin] and $Bi_{3.5}V_{1.2}O_{8.25}$ [01Wat] at 600 °C, which are indicated in Figure 3.5. This fact suggests that grain boundaries formed by the decomposition are relatively high-conductive.

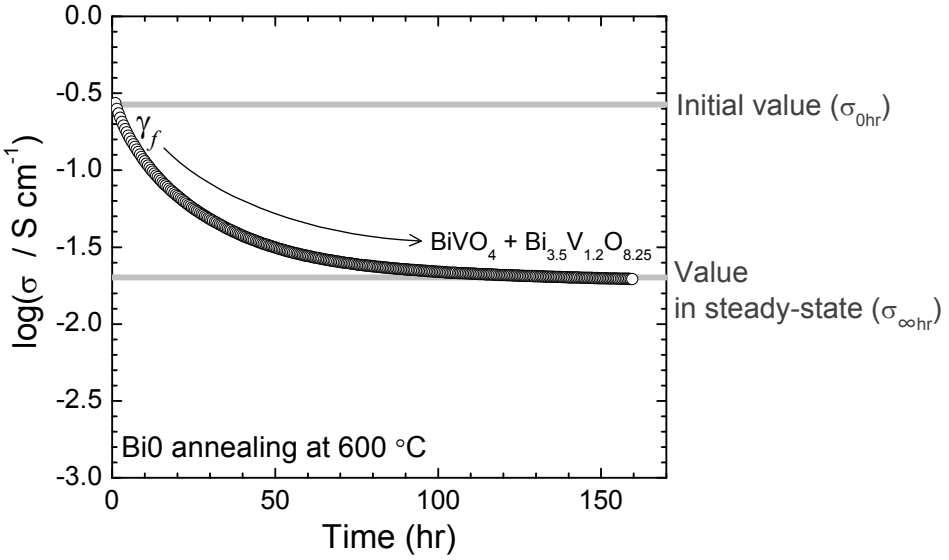

Figure 3.10 Time-dependent degradation of electrical conductivity of Bi0 at 600 °C in air.

Table 3.2 Electrical conductivities after annealing for n hr ($\sigma_{n\mathrm{hr}}$) and the ratios of $\sigma_{n\mathrm{hr}}$ to $\sigma_{0\mathrm{hr}}$ ($\sigma_{n\mathrm{hr}}/\sigma_{0\mathrm{hr}}$). The values of $\sigma_{200\mathrm{hr}}$ and $\sigma_{\infty\mathrm{hr}}$ at 600 °C were extrapolated by fitting the data in Figure 3.10 with an exponential decay function.

Temperature (°C)	Phase before annealing	Annealing time, n (hr)	Conductivity, $\sigma_{n\mathrm{hr}}$ (S cm^{-1})	$\sigma_{n\mathrm{hr}}/\sigma_{0\mathrm{hr}}$
500	β_f	0	1.08×10^{-2}	-
		200	7.70×10^{-3}	0.71
		400	6.78×10^{-3}	0.63
600	γ_f	0	2.67×10^{-1}	-
		50	3.14×10^{-2}	0.12
		100	2.19×10^{-2}	0.082
		150	1.99×10^{-2}	0.074
		200	2.01×10^{-2}	0.075
		∞	2.01×10^{-2}	0.075

Table 3.2 also lists the values of $\sigma_{n\mathrm{hr}}$ and $\sigma_{n\mathrm{hr}}/\sigma_{0\mathrm{hr}}$ for Bi0 at 500 °C, at which β_f was present before annealing. At 500 °C, β_f of Bi0 essentially decomposes into into $BiVO_4$ and $Bi_{3.5}V_{1.2}O_{8.25}$. However, the rate of decomposition is slow, as shown in Figure 3.8. Thus, the degradation of conductivity was small, compared with the results at 600 °C.

3.6. Partial reduction in $Bi_2VO_{5.5-\delta}$ determined by TGA

Before TGA, Bi0 powders were kept at 800 °C for a few hours, and then cooled to room temperature at 0.5 K min^{-1} in air. We regarded the chemical formula of this slowly cooled Bi0 as fully oxidized $Bi_2VO_{5.5}$, *i.e.*, $\delta = 0$, by ignoring the small amount of secondary phase. The slowly cooled Bi0 powders of ~320 mg were kept at 150 °C for 2 hr for drying, and then heated at 5 K min^{-1} to 800 °C in air. To calculate the oxygen content per compositional formula, we assumed that weight change is attributable only to the change in oxygen content.

Figure 3.11 shows the evaluated oxygen content and the DTA profile measured simultaneously. Partial reduction started at around 580 °C, which is just above $T_{\beta/\gamma}$. At 800

°C, the oxygen content of Bi0 decreased to 5.495 ± 0.002 (δ = 0.005 ± 0.002). This means that about 0.09% of oxygen was lost from 580 to 800 °C, and the composition at 800 °C can be described as $Bi_2(V^{+5}_{0.99}V^{+4}_{0.01})O_{5.495}$. Pirovano *et al.* reported that the δ of $Bi_2VO_{5.5-\delta}$ at 800 °C is 0.010 ± 0.002 [03Pir], which is in good agreement with our results.

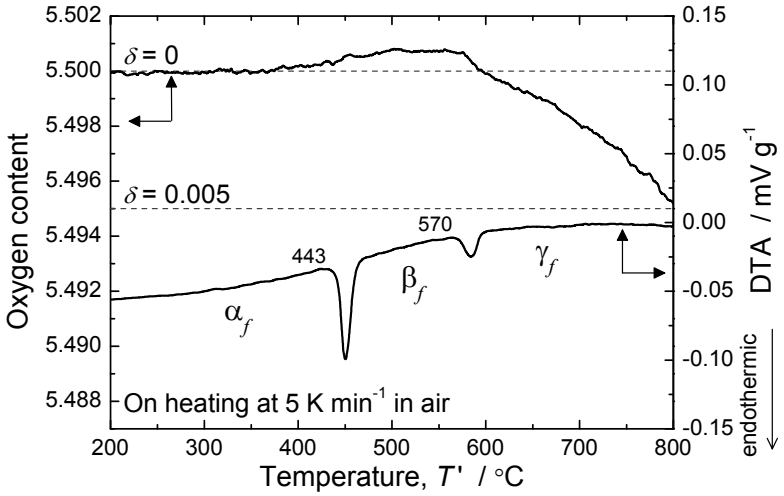

Figure 3.11 Temperature dependence of oxygen content and DTA profile of Bi0 powder. Before analysis, Bi0 powder was cooled from 800 °C at 0.5 K min^{-1}. TGA and DTA were obtained at a heating rate of 5 K min^{-1} in air. For the evaluation of oxygen content, the composition of slowly cooled Bi0 was regarded as $Bi_2VO_{5.5}$, *i.e.*, δ in $Bi_2VO_{5.5-\delta}$ was zero.

3.7. Empirical knowledge about doping effects

This section briefly describes the effects of Bi-doping on oxide-ion conductivity in γ_f, phase stability of γ_f against β_f and α_f (widening of temperature region for γ_f at low temperatures), and phase stability against thermal decomposition. Table 3.3 lists valences in BIMEVOX, ionic radius in 6-fold coordination, and preferable oxygen coordinations of Bi and V.

Oxide-ion conductivity in γ_f

Conductivity in γ_f decreases with an increase in Bi content, although doping with trivalent Bi should increase the amount of oxygen vacancies to preserve electroneutrality. This

suggests the some kind of association occurs between Bi and oxygen vacancy in the V-O layer of γ_f. Association areas (disarray in local structure) disturb the diffusion of oxide ions, and some oxygen vacancies can not diffuse independently and freely.

Phase stability of γ_f against β_f and α_f

Transition temperature from β_f to γ_f ($T_{\beta/\gamma}$) decreases with an increase in Bi content. Compared with high-level disorder γ_f, the binding between V and O should be stronger in intermediate-level disorder β_f and high-level order α_f. Thus, the oxygen vacancies induced by Bi-doping probably tend to destabilize the structures of β_f against that of γ_f, which qualitatively explains the reduction of $T_{\beta/\gamma}$ by Bi-doping.

Phase stability against thermal decomposition

Bi-doping does not suppress thermal decomposition of BIMEVOX phase. Bi has much larger size than V as shown in Table 3.3. Such large deviation in size should cause notable lattice distortions. The strain energy caused by Bi-doping destabilizes BIMEVOX phases (α_f, β_f, and γ_f) against decomposition products, which qualitatively explains the poor phase stability of $Bi_2(V_{1-x}Bi_x)O_{5.5+\Delta}$ as well as relatively small solid solution ($0 < x < 8$ at 800 °C).

Table 3.3 Valences, Shannon ionic radii in 6-fold coordination [76Sha], and preferable oxygen coordinations of Bi and V. Valence of dopant changes the amount of oxygen vacancies. Oxygen coordinations in Bi_2O_3 (α-type-structure which is stable below 710 °C) and V_2O_5 (ReO_3-related one-dimensional shear structure [76Hul,86Enj]) are regarded as preferable.

	Valence	Ionic radius (nm)	Preferable oxygen coordination
Bi	+3	0.103	5-fold (square pyramid)
V	+5	0.054	5-fold (square pyramid)

3.8. Conclusion

The solid solution of $Bi_2(V_{1-x}Bi_x)O_{5.5+\Delta}$ was $0 < x < 8$ at 800 °C. Bi-doping decreased the transition temperature from α_f to β_f and from β_f to γ_f. At around 500 °C, the conductivity of β_f increased by doping with Bi. Meanwhile, the conductivity of γ_f decreased with doping at a given temperature.

Bi-doping did not suppress thermal decomposition at intermediate temperatures. The established phase diagram indicates that the thermodynamically stable region of the BIMEVOX phase was reduced in size below 800 °C. High oxide-ion conductivity in $Bi_2(V_{1-x}Bi_x)O_{5.5+\Delta}$ exponentially decreased with time corresponding to the progression of thermal decomposition. At 600 °C, where γ_f of $Bi_2VO_{5.5-\delta}$ exhibited an oxide-ion conductivity of 2.67×10^{-1} S cm^{-1} initially, the conductivity decreased to 2.01×10^{-2} S cm^{-1} in a steady state.

References

[76Sha] R.D. Shannon, Acta Crystallogr. A 32 (1976) 767.

[76Hul] F. Hulliger, *Structural chemistry of layer-type phases*, D. Reidel Publishing Company, Boston (1976).

[86Enj] R. Enjalbert and J. Galy, Acta Cryst. C42 (1986) 1467.

[92Vin] I. C. Vinke, J. Diepgrond, B. A. Boukamp, K. J. de Vries, and A. J. Burggraaf, Solid State Ionics 57 (1992) 83.

[93Lee] C. K. Lee, D. C. Sinclair, and A. R. West, Solid State Ionics 62 (1993) 193.

[97Jia] S. P. Jiang, J. G. Love, and S. P. S. Badwal, Key Eng. Mater. 125-126, (1997) 81.

[01Wat] A. Watanabe, J. Solid State Chem. 161 (2001) 410.

[03Pir] C. Pirovano, R. N. Vannier, G. Nowogrocki, J. C. Boivin, and G. Mairesse, Solid State Ionics 159 (2003) 181.

[05Ste] M. C. Steil, F. Ratajczak, E. Capoen, C. Pirovano, R. N. Vannier, and G. Mairesse, Solid State Ionics 176 (2005) 2305.

[07Tan] Y. Taninouchi, T. Uda, Y. Awakura, A. Ikeda and S.M. Haile, J. Mater. Chem. 17 (2007) 3182.
[08Tan] Y. Taninouchi, T. Uda, and Y. Awakura, Solid State Ionics 178 (2008) 1648.

Chapter 4

Doping with Monovalent Metal:

"Oxide-Ion Conductivity and Phase Stability of $Bi_2(V_{1-x}MM_x)O_{5.5+\Delta}$ (MM = Li and Ag, x = 0.05 and 0.1)"

4.1. Introduction

Both alkali metal Li and transition metal Ag are expected to be monovalent form in BIMEVOX, although Li and Ag have different size and preferable oxygen coordination. Substitution of monovalent metal for pentavalent V sites should produce large amount of oxygen vacancies (decrease oxygen content per chemical formula) to preserve electroneutrality. Moreover, Li and Ag have larger sizes than V (ionic radii in 6-fold coordination; Li^+: 0.076 nm, Ag^+: 0.115 nm, and V^{5+}: 0.054 nm [76Sha]). Thus, Li- and Ag-doping are expected to largely change some physical properties of $Bi_2VO_{5.5-\delta}$ and provide us an insight into the design of favorable BIMEVOX.

However, only a few properties of Li- and Ag-doping have been reported. Sharma *et al.* [92Sha] reported the temperature dependence of the electrical conductivities of $Bi_2(V_{0.95}Li_{0.05})O_{5.4-\delta}$ and $Bi_2(V_{0.9}Li_{0.1})O_{5.3-\delta}$, although conductivities in the present study are about 2 orders of magnitude higher than their values. Vaidhyanathan *et al.* [98Vai] synthesized $Bi_2(V_{0.9}Ag_{0.1})O_{5.3-\delta}$ by the microwave-assisted method. They reported that the γ_f of $Bi_2(V_{0.9}Ag_{0.1})O_{5.3-\delta}$ was stabilized at room temperature and it exhibited an oxide-ion conductivity of 3.06×10^{-5} S cm^{-1} at 300 °C.

The objective of this chapter is to determine the effects of Li- and Ag-doping, *i.e.*,

electrical conductivities, polymorphs, and long-term phase stabilities of $Bi_2(V_{1-x}MM_x)O_{5.5+\Delta}$ (MM = Li and Ag, x = 0.05 and 0.1, $\Delta \equiv d - \delta$, where Δ is total oxygen deviation, d is oxygen deviation due to aliovalent doping, and δ is oxygen loss due to partial reduction).

4.2. Sample preparation

Prepared samples of $Bi_2(V_{0.95}Li_{0.05})O_{5.4-\delta}$, $Bi_2(V_{0.9}Li_{0.1})O_{5.3-\delta}$, $Bi_2(V_{0.95}Ag_{0.05})O_{5.4-\delta}$, and $Bi_2(V_{0.9}Ag_{0.1})O_{5.3-\delta}$ are abbreviated as Li5, Li10, Ag5, and Ag10, respectively. Polycrystalline powders were synthesized by a solid-state reaction in air using platinum containers. Table 4.1 lists the staring materials, and Figure 4.1(a) shows the flowchart of the solid-state reaction. Appropriate amounts of constituents were mixed and then heated at 600 °C for 12 hr. The ground powders were pelletized at 0.2 ton cm^{-2}, heated again at 800 °C (Li5, Ag5, and Ag10) or 700 °C (Li10) for 12 hr, and then grinded. Before analysis, powders were kept at 700 °C (Li5, Li10, and Ag5) or 750 °C (Ag10) for several hours and then quenched in air.

Figure 4.1(b) shows the sintering procedure. Powders were pelletized at 3 ton cm^{-2} for 15 min and then sintered in air at 700 °C for 24 hr (Li5 and Ag5), at 700 °C for 12 hr (Li10), or at 750 °C for 12 hr (Ag10).

Table 4.1 Purity and Source of starting materials

Starting material	Chemical formula	Purity (mass %)	Source
Bismuth oxide	Bi_2O_3	99.99	Furuuchi chemical
Vanadium oxide	V_2O_5	99.9	Furuuchi chemical
Lithium carbonate	Li_2CO_3	99.9	Furuuchi chemical
Silver oxide	Ag_2O	99+	Wako

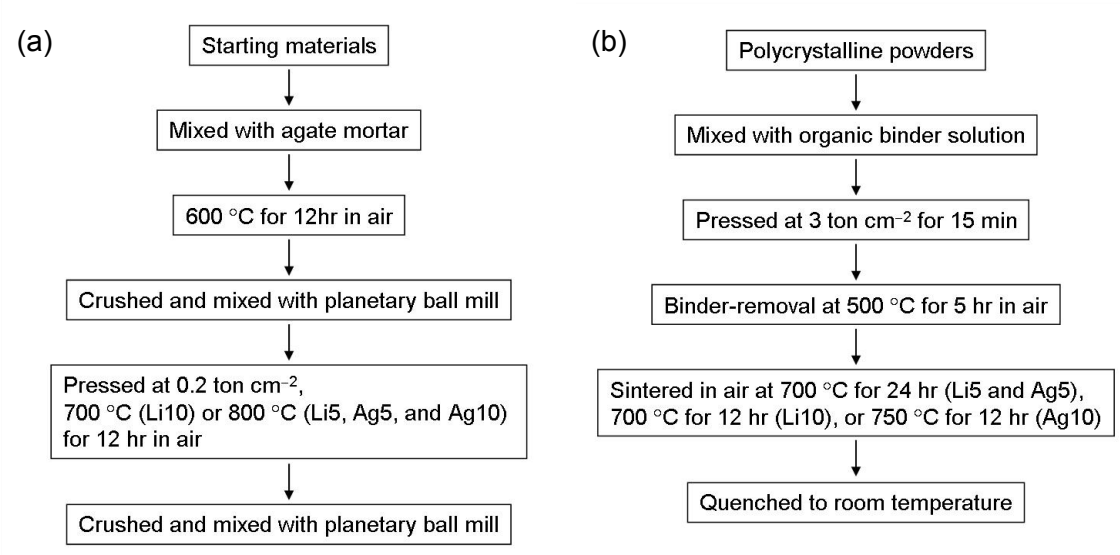

Figure 4.1 Flowchart for (a) preparing of polycrystalline powder and (b) sintering of pellet

4.3. Phases at room temperature identified by XRD analysis

Figure 4.2 shows the XRD patterns of quenched powders in logarithmic intensity scale. All diffraction peaks came from BIMEVOX phase. Orthorhombic α_f was obtained in Li5 and Ag5. Meanwhile, tetragonal γ_f was stabilized in Li10 and Ag10 even at room temperature. Figure 4.3 shows the lattice constants of a_m, b_m, and c_m. Li- and Ag-doping decreased the difference between a_m and b_m, and increased the c_m.

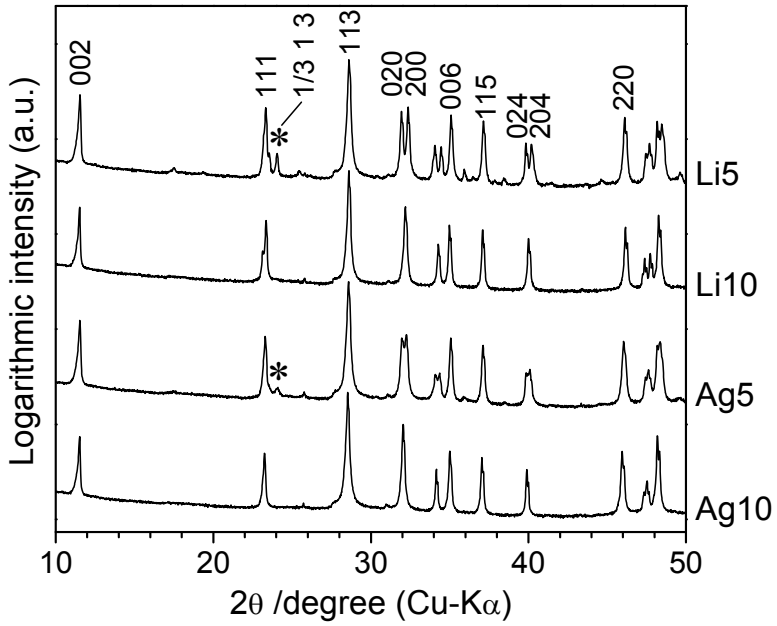

Figure 4.2 XRD patterns of powders quenched from 700 °C (Li5, Li10, and Ag5) or 750 °C (Ag10) in logarithmic intensity scale. The plane indices are marked assuming the orthorhombic subcell of a_m, b_m, and c_m. Asterisks (∗) indicate typical superlattice diffraction peak of α_f.

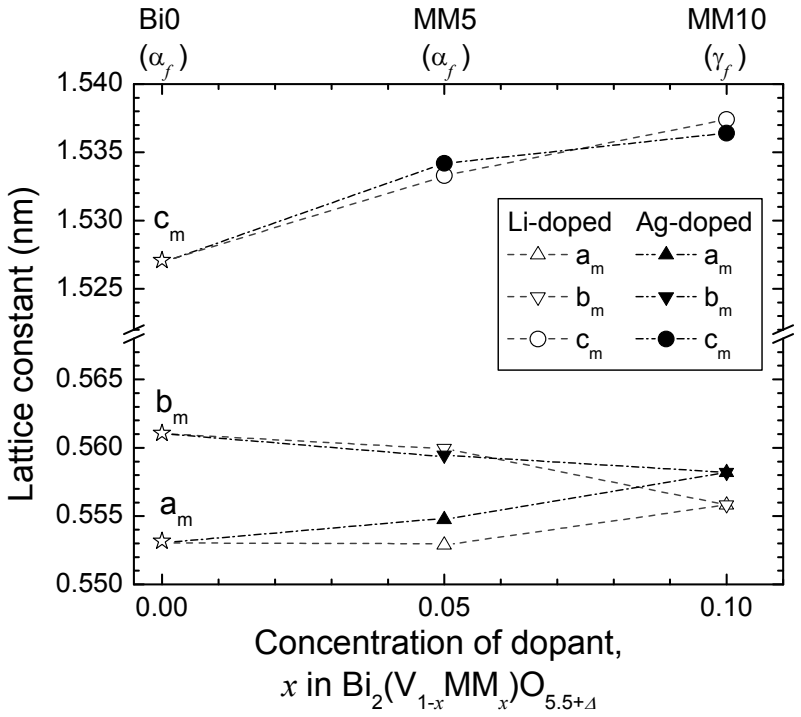

Figure 4.3 Lattice constant of a_m, b_m, and c_m as a function of dopant concentration.

4.4. Composition checks by weight change under H_2 atmosphere and XPS

Li10 powder in ceramic crucible (SiO_2: 63%, Al_2O_3:31%) was heated in pure H_2 at 500 °C for 12 hr. Weight change by this thermal treatment was −11.4%. XRD analysis indicated that BIMEVOX phase completely disappeared and Bi(*s*) and V_2O_3(*s*) were present. From the identified phases, the progress of the following reduction reaction is expected:

$$Bi_2(V_{0.9}Li_{0.1})O_{5.3-\delta}(s) \rightarrow 2Bi(l) + 0.45V_2O_3(s) + 0.05Li_2O(s) + (1.95-\delta/2)O_2(g) \qquad (4.1)$$

The theoretical weight change of reaction (4.1) is −11.36% when the oxygen loss due to the partial reduction δ is ignored. This theoretical value of −11.36% sufficiently agrees with the measured weight change, −11.4%. Thus, the composition of Li10 was confirmed to be $Bi_2(V_{0.9}Li_{0.1})O_{5.3-\delta}$.

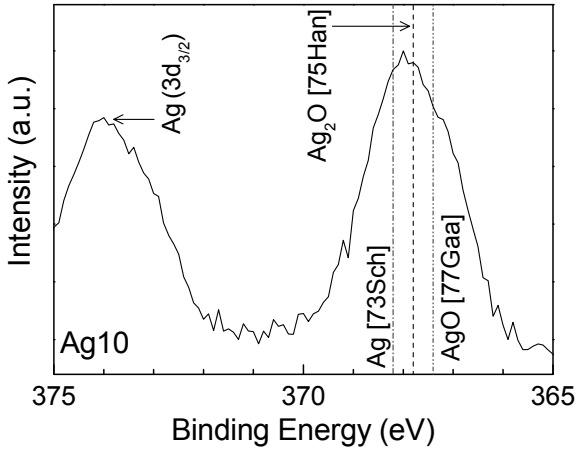

Figure 4.4 XPS spectrum of Ag $3d_{5/2}$ component collected for Ag10. Dotted line shows the reference peak position reported for Ag [73Sch], Ag_2O [75Han], and AgO [77Gaa].

Figure 4.4 shows XPS spectrum of Ag $3d_{5/2}$ component collected for Ag10 pellet after Ar-sputtering for 20 min. The peak positions reported for Ag (valence of Ag: 0, binding energy: 368.2 eV) [73Sch], Ag_2O (valence of Ag: +1, binding energy: 367.8 eV) [75Han], and AgO (valence of Ag: mixture of +1 and +3, binding energy: 367.4 eV) [77Gaa] are indicated

as references. The peak position of Ag $3d_{5/2}$ in Ag10 was evaluated as 367.9 eV, which is in good agreement with that reported for Ag_2O. In addition, the peak positions of Bi and V in Ag10 (159.0 and 516.9 eV, respectively) sufficiently agree with those in $Bi_2VO_{5.5-\delta}$ (159.1 and 516.5 eV, respectively). In Ag10, therefore, the valances of Ag, Bi, V can be regarded as monovalent, trivalent, and pentavalent, respectively, which means that the composition of Ag10 is $Bi_2(V_{0.9}Li_{0.1})O_{5.3-\delta}$.

4.5. Microstructures and relative densities of sintered pellets

Figure 4.5 shows cross-sectional FE-SEM images of sintered pellets. As shown in Figure 4.5(a), grain boundaries were unclear due to the transgranular cracking in the samples as crushed. Thermal etching was carried out at the sintering temperatures for 3 hr to determine the grain sizes, as shown in Figure 4.5(b). Grain sizes were larger than 10 μm in all sintered pellets.

Table 4.2 shows the relative densities of sintered pellets with the phases at room temperature and sintering conditions. The relative densities were evaluated from the densities which were calculated from the nominal composition and the cell volume derived from XRD analysis. All sintered pellets exhibited the high relative densities of 93−95%.

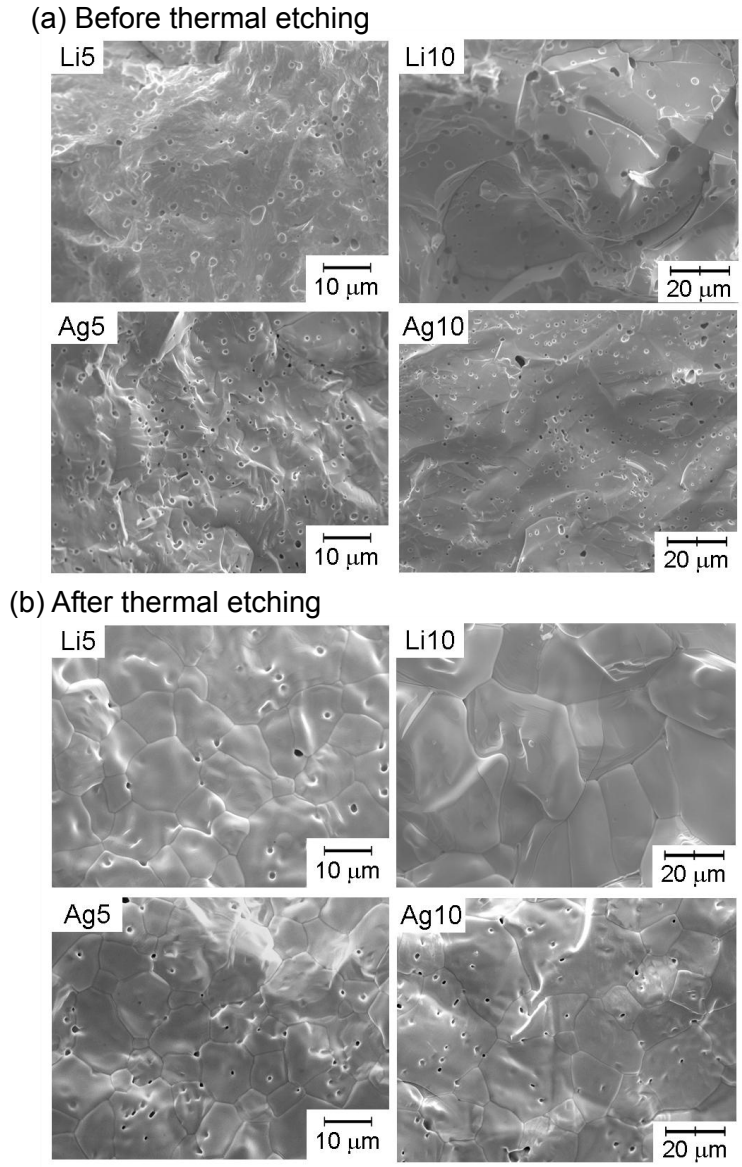

Figure 4.5 Cross-sectional FE-SEM images of sintered pellets (a) before and (b) after thermal etching at the sintering temperatures for 3 hr.

Table 4.2 Phases in quenched powders at room temperature, sintering conditions, and relative densities of sintered pellets.

	Composition	Phase at room temperature	Pellet	
			Sintering condition	Relative density (%)
Li5	$Bi_2(V_{0.95}Li_{0.05})O_{5.4-\delta}$	α_f (orthorhombic)	700 °C, 24 hr	93
Li10	$Bi_2(V_{0.9}Li_{0.1})O_{5.3-\delta}$	γ_f (tetragonal)	700 °C, 12 hr	93
Ag5	$Bi_2(V_{0.95}Ag_{0.05})O_{5.4-\delta}$	α_f (orthorhombic)	700 °C, 24 hr	95
Ag10	$Bi_2(V_{0.9}Ag_{0.1})O_{5.3-\delta}$	γ_f (tetragonal)	750 °C, 12 hr	95

4.6. Electrical conductivities determined by AC impedance spectroscopy and DC polarization measurement

Figure 4.6 shows the Arrhenius plots of electrical conductivities on heating at 1 K min^{-1} in air. Just before measurements, the pellets with Au electrodes, which are applied with gold paint, were quenched from the sintering temperatures. The conductivities of Bi0 and Cu10 quenched from 800 °C measured at the same condition and reported conductivities of YSZ [94Her] and LSGMC [99Ish] are also shown for comparison.

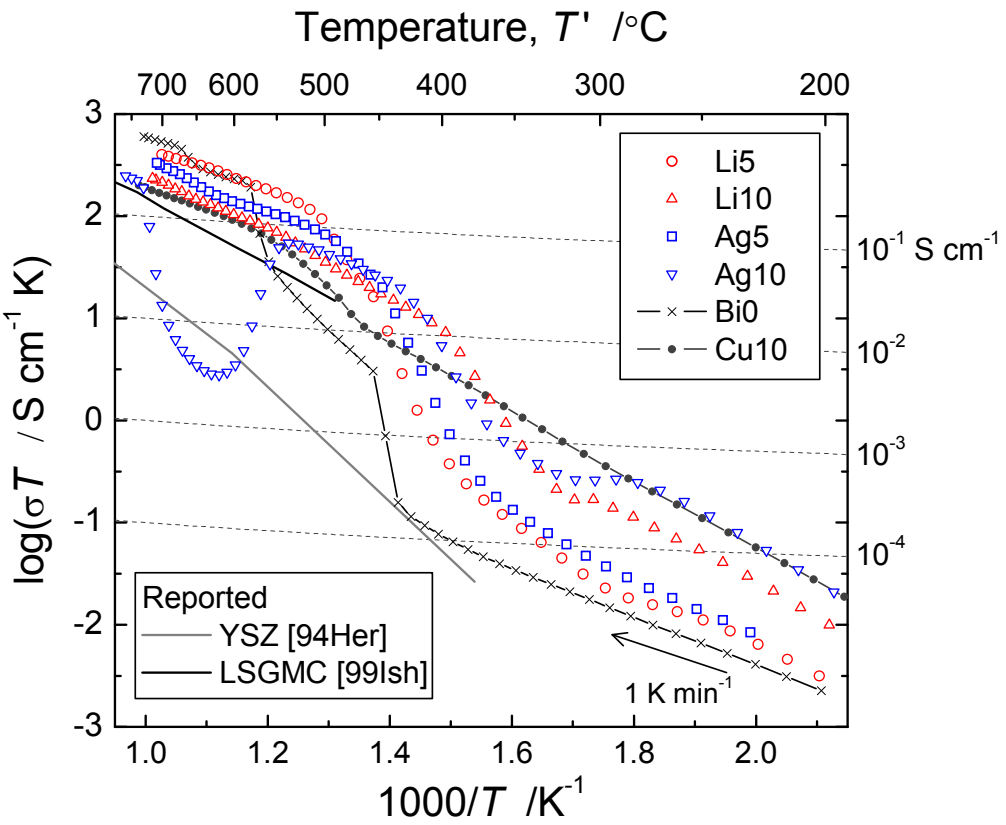

Figure 4.6 Temperature dependence of electrical conductivities at a heating rate of 1 K min^{-1} in air. The conductivities of Bi0 and Cu10 quenched from 800 °C and reported conductivities of YSZ [94Her] and LSGMC [99Ish] are also shown.

Table 4.3 Activation energies (E_a), and pre-exponential terms (A) of the electrical conductivities in γ_f. We employed $\sigma T = A\exp\left[-(E_a / kT)\right]$, where k is the Boltzmann constant.

	E_a (eV)	A (S cm^{-1} K)	Temperature range (°C)
Li5	0.45 (±0.02)	9.3 (±0.2) ×10^4	500–700
Li10	0.60 (±0.02)	3.2 (±0.4) ×10^5	410–720
Ag5	0.47 (±0.02)	7.7 (±0.2) ×10^4	500–700
Ag10	0.47 (±0.02)	4.5 (±0.5) ×10^4	430–750*
Bi0	0.43 (±0.03)	7.1 (±0.4) ×10^4	580–650
	0.38 (±0.03)	5.0 (±0.2) ×10^4	670–730
Cu10	0.47 (±0.02)	4.4 (±0.5) ×10^4	550–740

* The data between 540 and 730 °C were not used.

For Li5 and Ag5, the slopes of the conductivity increased markedly at around 400 °C. This change corresponds to the transition from α_f to γ_f passing through the β_f, as verified in the following section. In Li5 and Ag5, the γ_f was stabilized at ~500 °C, which was 70 °C lower than the transition temperature from β_f to γ_f of Bi0. Table 4.3 lists the activation energies (E_a) and pre-exponential terms (A) of electrical conductivity of γ_f. Li- an Ag-doping increased the E_a of γ_f. In Li10 and Ag10, the γ_f was stabilized down to room temperature. However, slow conductivity jumps from lowly conductive to highly conductive states were observed between 300 and 400 °C for Li10 and between 280 and 420 °C for Ag10. The highly conductive states of γ_f exhibited conductivities higher than 10^{-2} S cm^{-1} at temperatures as low as 400 °C for Li10 and 420 °C for Ag10. The E_a of highly conductive γ_f of Li10 and Ag10 were 0.60 and 0.47 eV, respectively, as shown in Table 4.3. Similar slow conductivity jump from lowly conductive to highly conductive states, which is qualitatively explained by slight modification of oxygen vacancies, was observed in γ_f of Cu10 from 465 to 550 °C and often called as γ' to γ transition [02Wat]. Recently, Pirovana *et al.* reported that the reducing the grain sizes of

Cu10 suppressed the formation of lowly conductive γ_f and improved the conductivity at lower temperatures [05Pir]. Thus, the conductivities of Li10 and Ag10 below ~400 °C might be further improved by the optimization of preparation process (*e.g.*, powders are prepared by combustion synthesis [09Roy] or sol-gel method [98Pel], and the sintering conditions are optimized). It is also notable that unusual conductivity drop was observed in Ag10 between 540 and 730 °C. This change is due to the decomposition reaction into BIMEVOX phase and secondary phases from 540 to 630 °C and the recomposition reaction to Ag10 from 630 to 730 °C, which is clarified in Section 4.7.

The most notable feature in Figure 4.6 is that Li- and Ag-doping significantly improve the electrical conductivities of $Bi_2VO_{5.5}$ below 570 °C. In Figure 4.7, the conductivities at 500 °C shown in Figure 4.6 are re-plotted as a function of dopant concentration. At 500 °C, β_f was obtained in Bi0 but γ_f was stabilized in $Bi_2(V_{1-x}MM_x)O_{5.5+\Delta}$ (progress in thermal decomposition can be negligible for all samples). γ_f of $Bi_2(V_{1-x}MM_x)O_{5.5+\Delta}$ exhibited high conductivities of $0.5–1 \times 10^{-1}$ S cm^{-1} at 500 °C, which are ~2 orders of magnitude higher than that of YSZ, 2–5 times higher than that of LSGMC, and 1.5–4 times higher than that of Cu10. It is also notable in Figure 4.7 that Li10 and Ag10 exhibited lower conductivity than Li5 and Ag5, respectively, although oxygen vacancy concentration should increase with dopant concentration. Figure 4.8 shows the typical impedance spectra at 500 °C. The spectra were almost straight lines inclined at an angle of ~45° to the real axis. Similar spectra are often observed for the highly ionic conductors attached to the blocking electrodes for ion migration [07Tan]. The straight lines are explained by the Warburg impedance, *i.e.*, the ionic diffusion-limited process in the electrode reaction [97Jia]. Thus, even after doping, the charge carriers are still considered to be oxide ions at about 500 °C.

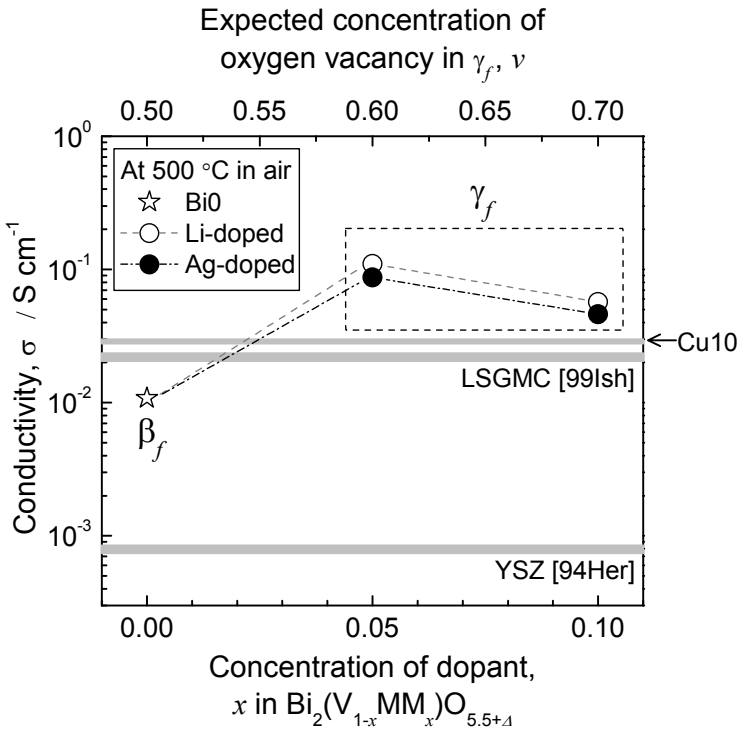

Figure 4.7 The oxide-ion conductivity at 500 °C as a function of dopant concentration. Data in Figure 4.6 are re-plotted. Those of Cu10, YSZ [94Her] and LSGMC [99Ish] are also indicated as gray lines. Concentration of oxygen vacancies in γ_f, *i.e.*, v in $Bi_2(V_{1-x}MM_x)O_{6-v}\square_v$, was evaluated assuming ideal Aurivillius structure (V-O layer consists of VO_6 octahedron including dopant and oxygen vacancies) and by preserving electroneutrality via oxygen content.

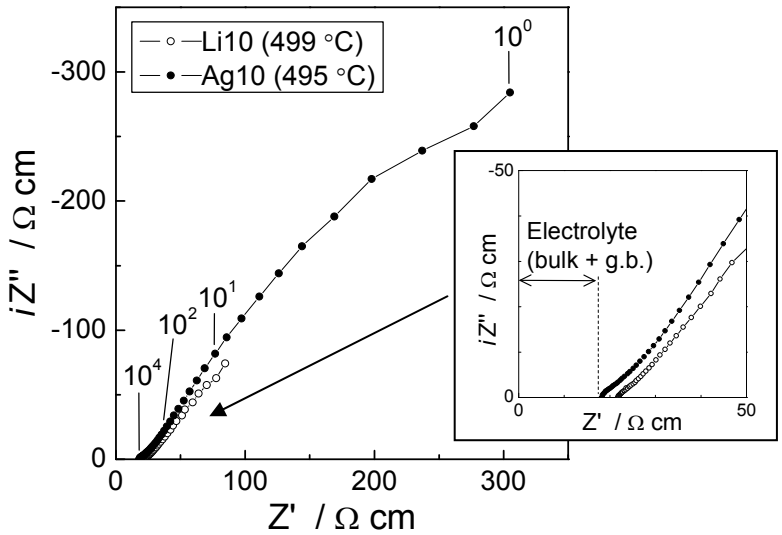

Figure 4.8 Impedance spectra of Li10 at 499 °C and Ag10 at 495 °C. Au electrodes were attached to form blocking electrodes for oxide-ion diffusion. The inset is a magnified image of the high-frequency region.

We further checked the oxide-ion conduction by DC polarization measurements using the pellets with vacuum-deposited Au electrodes. As a blocking electrode is used, the current in a steady state is derived from only electron/hole diffusion. We can evaluate the transference numbers of electrons/holes (t_e) and oxide ions (t_O) by comparing with the conductivities evaluated by AC impedance spectroscopy where the conductivity is the total of that due to all charge carriers [09Tan]. Table 4.4 shows the summary of the values evaluated for Li10 and Ag10. Evaluated values were preliminary because blocking electrodes were used in the present measurement instead of a reversible anode for oxygen gas and a blocking cathode in the Hebb-Wagner method [52Heb,56Wag]. However, σ_e was evidently quite small compared with the oxide-ion conductivities in Li10 and Ag10. Furthermore, Figure 4.9 shows the conductivities of Li5 and Li10 at oxygen partial pressures (pO_2) of 1, 0.21, and 8×10^{-4} atm. The data were determined by AC impedance spectroscopy on cooling from 700 °C at 1 K min^{-1}. In general, electron conductivity decreases with pO_2, and hole conductivity increases with pO_2, as described in Chapter 1. On the other hand, ionic conductivity is independent of pO_2. The conductivity of Li10 did not change with pO_2 between 400 and 700 °C. Thus, Li10 is an oxide-ion conductor at the temperatures of interest, which is consistent with the results of DC polarization measurements. In Li5, the conductivity did not change with pO_2 between 500 and 700 °C but decreased with pO_2 at 400 °C. The slope of conductivity change in the pO_2 range from 8×10^{-4} to 0.21 atm was close to the expected value for electron conduction, *i.e.*, $pO_2^{-1/4}$. At 400 °C on cooling, the phase of Li5 is β_f. Thus, β_f of Li5 exhibits oxide-ion conduction in O_2 and Air, but electron conduction appears in Ar.

Table 4.4 Electron/hole conductivities (σ_e), and calculated transference numbers for oxide-ion conduction (t_O) and electron/hole conduction (t_e). Transference numbers are preliminary because we employed a simplified version of the Hebb-Wagner method [52Heb,56Wag].

	Temperature (°C)	σ_e (S cm^{-1})	t_O	t_e
Li10	401	3.35×10^{-5}	0.99	0.01
	504	6.72×10^{-5}	1.00	0.00
	604	4.91×10^{-4}	1.00	0.00
	695	2.05×10^{-3}	0.99	0.01
Ag10	484	6.61×10^{-5}	1.00	0.00
	755	8.07×10^{-3}	0.97	0.03

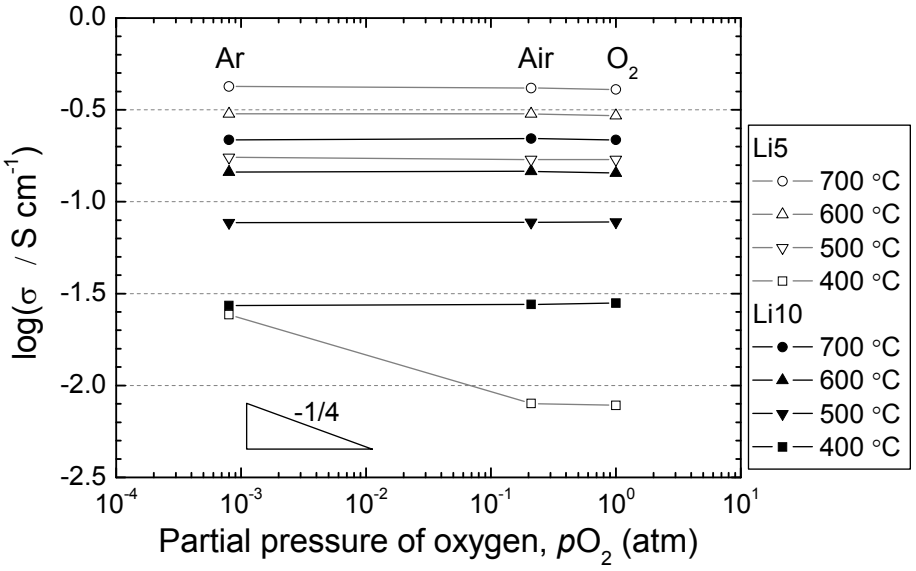

Figure 4.9 Electrical conductivities of Li5 and Li10 at various pO_2. Electron conductivity is expected to be proportional to $pO_2^{-1/4}$.

4.7. Phase transitions and phase decompositions determined by DSC and HT-XRD analysis

Figure 4.10 shows the (a,b) DSC profiles of quenched powders collected at a scan rate of 10 K min^{-1} in flowing air and (c) reprinted data of electrical conductivities. In HT-XRD analysis, the scan rate of the sample temperature was 10 K min^{-1}. The sample temperatures were maintained for 5 min at 50 °C intervals, and diffraction patterns were collected within 10 min at each temperature. Figure 4.11 shows the HT-XRD patterns on heating in logarithmic intensity scale, and Figure 4.12 shows a summary of the phases confirmed by HT-XRD analysis.

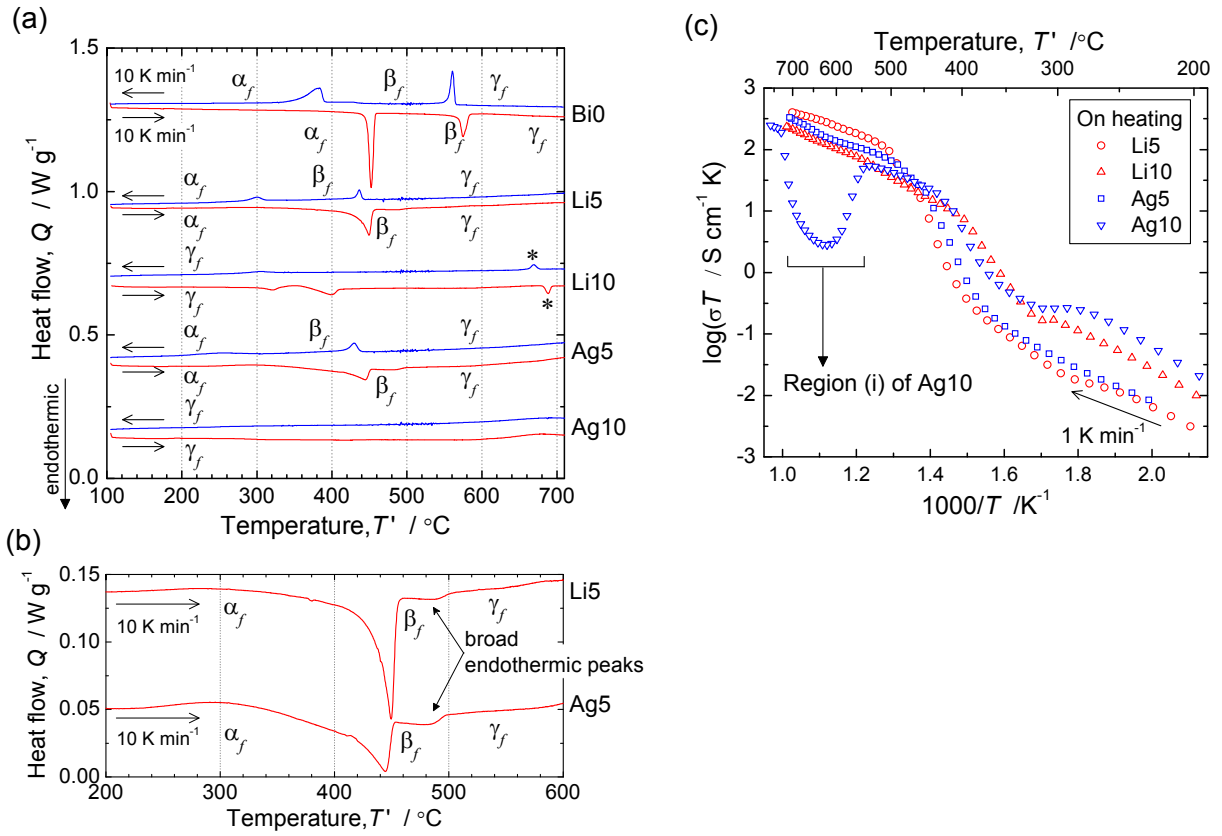

Figure 4.10 (a) DSC profiles collected in air at a scan rate of 10 K min^{-1}. In Li10, the peaks marked by asterisks correspond to the reaction: Li10 ↔ BIMEVOX phase + small amount of liquid. (b) Magnified profiles of Li5 and Ag5 on heating. (c) Reprinted data in Figure 4.6: electrical conductivity on heating at 1 K min^{-1} in air. A distinct conductivity drop was observed in region (i) for Ag10.

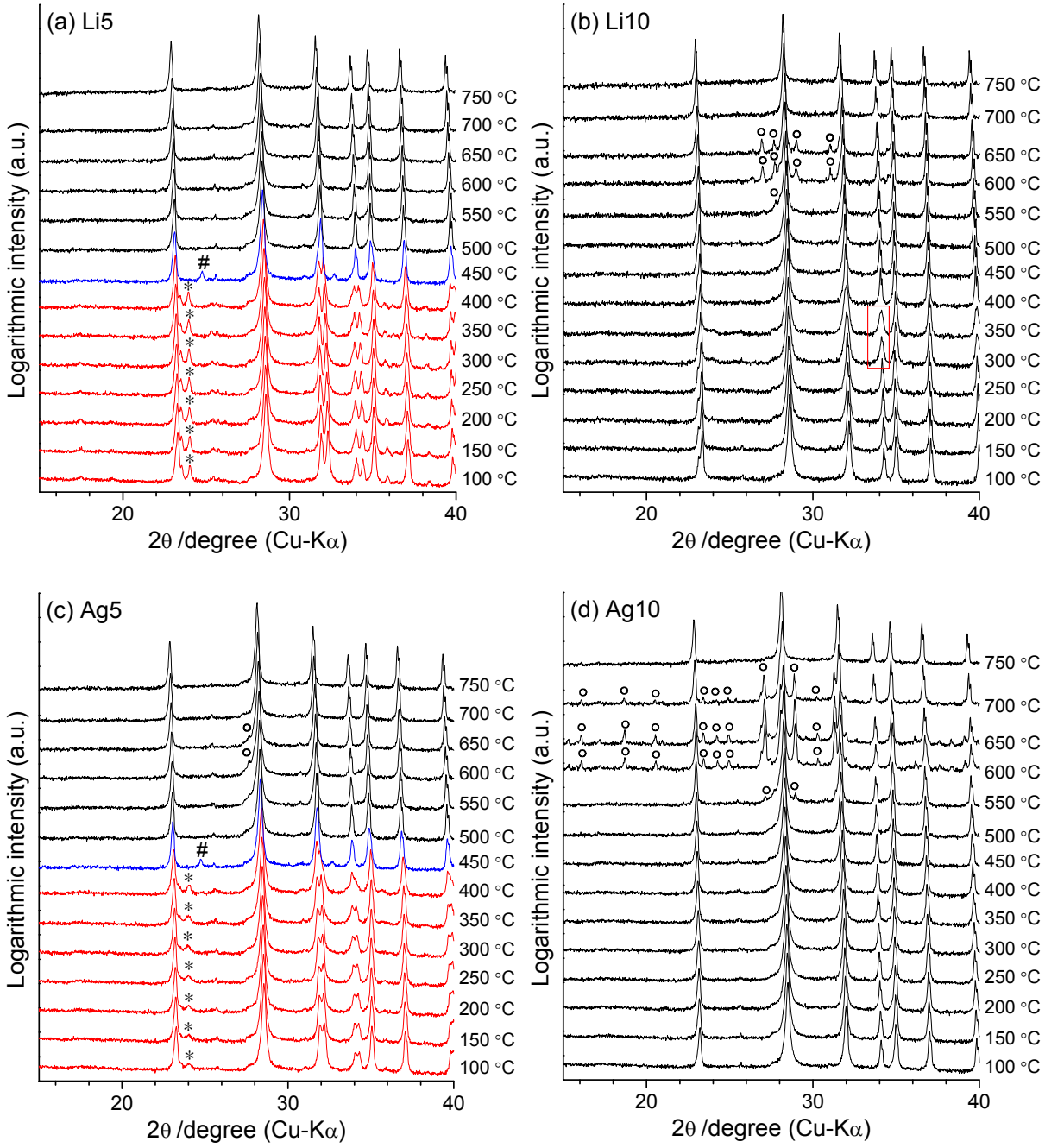

Figure 4.11 HT-XRD profiles of (a) Li5, (b) Li10, (c) Ag5, and (d) Ag10 on heating in air. In (a) Li5 and (c) Ag5, typical superlattice diffractions of α_f and β_f are marked by asterisks (∗) and hashes (#), respectively. The peak broadening observed at 300 and 350 °C in (b) Li10 is indicated by a red box. The secondary phases that appeared in (b) Li10, (c) Ag5, and (d) Ag10 are indicated by open circles (o).

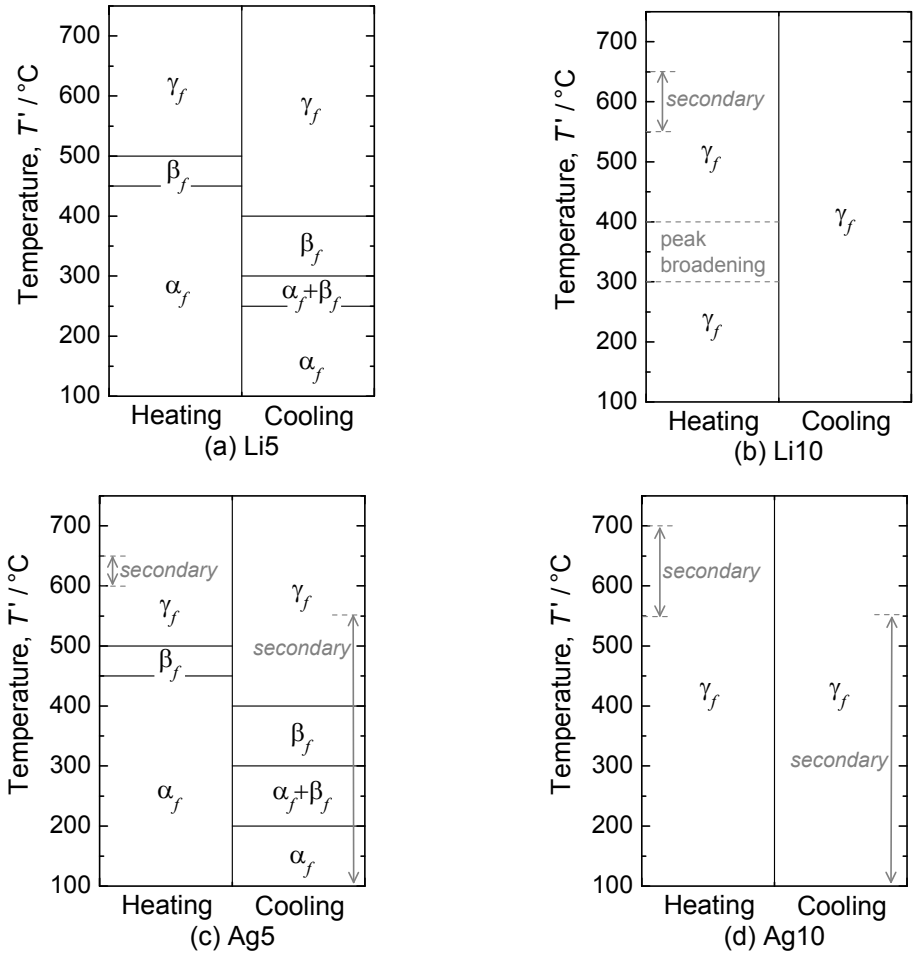

Figure 4.12 Summary of the phases in (a) Li5, (b) Li10, (c) Ag5, and (d) Ag10 determined by HT-XRD analysis. The ranges in which secondary phases appeared are indicated by arrows.

In Li5 and Ag5, the transition between α_f and γ_f passes through the β_f. In the DSC profiles of Li5 and Ag5 on heating, clear endothermic peaks appeared from 400 to 450 °C, corresponding to the transition from α_f to β_f (α_f/β_f transition). β_f of Li5 and Ag5 have tetragonal symmetry at 450 °C on heating, as shown in Figures 4.11(a) and (c). Very broad and small endothermic peaks were observed for the β_f/γ_f transition at approximately 480 °C in DSC profiles, as shown in Figure 4.10(b). The broad peak can be explained on the basis of the nature of the second-order β_f/γ_f transition in Li5 and Ag5. DSC profiles are consistent with continuous conductivity changes at the β_f/γ_f transition in Figure 4.10(c). In the DSC profiles

of Li5 and Ag5 on cooling, the exothermic peaks at around 420 °C correspond to the γ_f/β_f transition. The exothermic peaks corresponding to the β_f/α_f transition are very small and broad, which indicates that the β_f/α_f transitions in Li5 and Ag5 proceed gradually.

In Li10 and Ag10, the fundamental diffraction peaks were attributed to the γ_f. In the DSC profile of Li10, two endothermic peaks are exhibited in the temperature range from 300 to 420 °C. In the same temperature range, the conductivity increased (γ_f changed from lowly conductive to highly conductive state) in Figure 4.10(c), and the diffraction peaks were broadened in Figure 4.11(b). The broadening of the diffraction peaks at 300 and 350 °C should be attributed to some structural relaxation induced by the rearrangement of oxygen vacancies and/or dopant Li. A pair of endothermic and exothermic peaks was observed at around 680 °C in the DSC profile of Li10, as indicated by asterisks. These peaks correspond to a partial melting of Li10, as explained in Section 4.8. In the case of Ag10, a slow conductivity jump from lowly conductive to highly conductive γ_f was exhibited from 280 to 420 °C in Figure 4.10(c). However, DSC and HT-XRD analysis did not indicate some reaction and notable structural change, respectively.

Results of the HT-XRD analysis also showed the progress of thermal decompositions in Li10, Ag5, and Ag10 during the temperature scan. In Li10, a very small amount of the secondary phase appeared from 550 to 650 °C on heating; the ratio of the maximum peak of the secondary phase at ~27.1° to that of BIMEVOX at ~28.2°, I_{SP}/I_{BVO}, was ~3.8 %. Similarly, a small amount of the secondary phase (I_{SP}/I_{BVO}, ~2.1 %) appeared in Ag5. The results are summarized in Figure 4.12. In Ag10, a relatively large amount of the secondary phase appeared from 550 to 700 °C on heating, as shown in Figure 4.11(d). The secondary phase is estimated to be $Bi_{14}V_5AgO_{34}$ based on the diffraction peaks and EDX. Figure 4.13 shows the I_{SP}/I_{BVO} in Ag10 as a function of temperature. The amount of secondary phase increased from

550 to 650 °C and then decreased from 650 to 700 °C. Thus, the unusual drop in the conductivity of Ag10 from 540 to 730 °C, which is shown in region (i) of Figure 4.10(c), is explained by the decomposition reaction from 540 to 630 °C,

$$\gamma_f \text{ of Ag10} \rightarrow \text{BIMEVOX phase + secondary phases} \quad (4.2)$$

and the recomposition reaction from 630 to 730 °C,

$$\text{BIMEVOX phase + secondary phases} \rightarrow \gamma_f \text{ of Ag10.} \quad (4.3)$$

On cooling, a small amount of the secondary phase (I_{SP}/I_{BVO}, ~1.5 %) appeared below 550 °C in Ag10.

The appearance of secondary phases during the HT-XRD analysis indicates the instability of Li- and Ag-doped $Bi_2VO_{5.5-\delta}$ at intermediate temperatures. Thus, Li- and Ag-doping do not effectively suppress thermal decomposition, which is further confirmed in Section 4.8. It is also important finding that the transition behavior does not show a large difference between Li- and Ag-doped $Bi_2VO_{5.5-\delta}$ at the same dopant concentration.

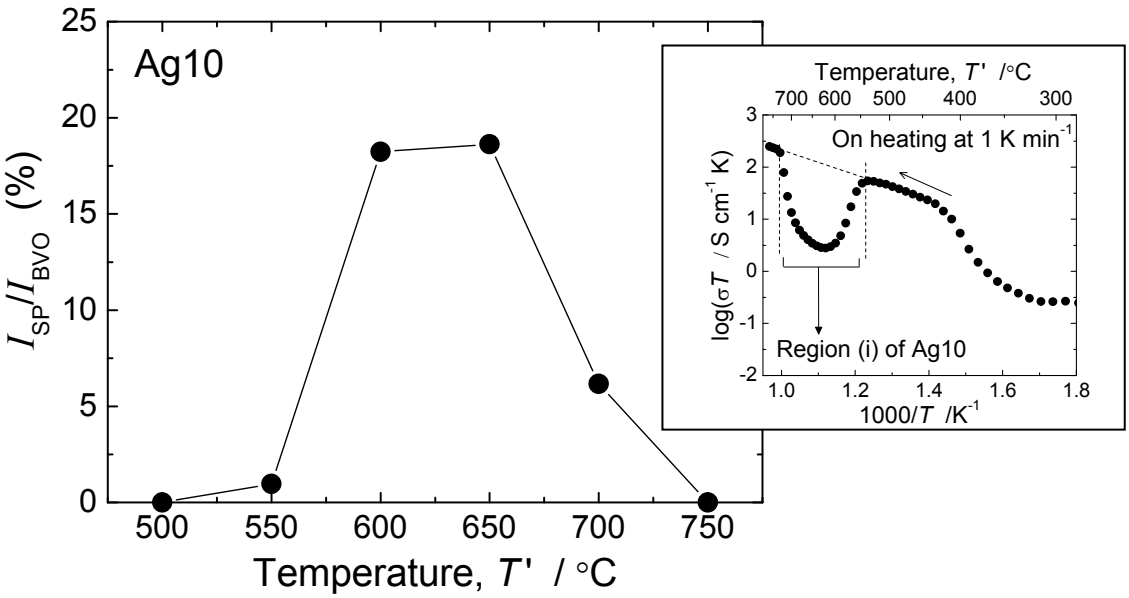

Figure 4.13 The variation in the amount of secondary phase in Ag10. I_{SP}/I_{BVO} in Figure 4.12(d) is plotted as a function of temperature. The inset is the conductivity change of Ag10.

4.8. Long-term phase stabilities

4.8.1. Phase stabilities and phase diagrams determined by XRD analysis of annealed powders and DTA

Figure 4.14(a) shows the XRD patterns of powders after annealing at 500 or 700 °C for 200 hr in air. At 500 °C, Bi0 is partially decomposed during annealing. The decomposition was also confirmed in Li- and Ag-doped $Bi_2VO_{5.5-\delta}$ at 500 °C. In particular, the BIMEVOX phase almost disappeared in annealed Li5. Ag10 annealed at 500 °C contained the BIMEVOX phase, $BiVO_4$, and two other phases whose compositions are roughly evaluated as $Bi_{14}V_5AgO_{34}$ and $Bi_3V_2AgO_{10}$ by EDX on the assumption that oxygen content follows the stoichiometry evaluated from the valences of the metallic ions. In Ag10 annealed at 700 °C, a

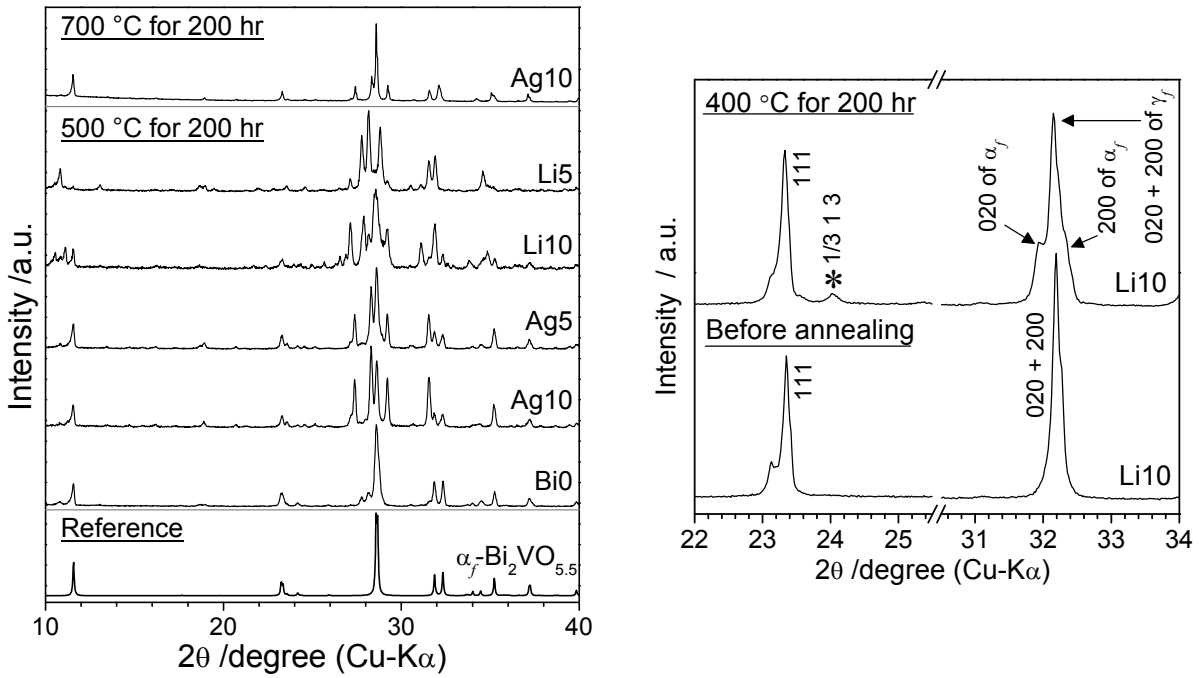

Figure 4.14 (a) XRD patterns of powders after annealing at 500 or 700 °C for 200hr. The reference pattern of α_f-$Bi_2VO_{5.5}$ is calculated at Cu-Kα_1 radiation [03Mai2]. (b) XRD patterns of Li10 before and after annealing at 400 °C for 200 hr. The asterisk (∗) indicate typical superlattice diffractions of α_f. After annealing at 400 °C, a mixture of α_f and γ_f was obtained.

secondary phase existed although the BIMEVOX phase remained as the main phase. Composition of the secondary phase was $Bi_{14}V_5AgO_{34}$, and the composition of the BIMEVOX phase remained largely unchanged as $Bi_2(V_{0.9}Ag_{0.1})O_{5.3-\delta}$. Because Ag5 was stable sat 700 °C for 200 hr, Ag10 exists in the two-phase region of BIMEVOX phase and $Bi_{14}V_5AgO_{34}$ at 700 °C. Figure 4.14(b) shows the XRD patterns of Li10 after annealing at 400 °C for 200 hr. In Li10, BIMEVOX phase was kinetically stable at 400 °C, but the ordering from γ_f to α_f partially proceeded.

Similar measurements were performed at various temperatures. The results are summarized as pseudo-binary phase diagrams in Figure 4.15. Li- and Ag-doped $Bi_2VO_{5.5-\delta}$ are metastable at intermediate temperatures. The upper limit of the stable region of the BIMEVOX phase was evaluated by DTA at 10 K min^{-1} in air using alumina containers. Figure 4.16 show the DTA profile of Li10 as an example. A slight endothermic reaction started at T_1 = 680 °C. At the same temperature, an endothermic peak was observed in the DSC profile, as shown in Figure 4.10(a). The DTA profile also exhibits a large endothermic peak, which appeared at T_2 = 855 °C, and disappeared at T_3 = 887 °C. Only the BIMEVOX phase was observed in the HT-XRD patterns at 700 and 750 °C, as shown in Figure 4.11(b). We confirmed the abnormal grain growth reaching 0.1 mm in grain size by maintaining a Li10 pellet at 800 °C for 9 hr. Therefore, a small amount of liquid phase should appear between T_1 and T_2. The estimated phase in each region shown in Figures 4.15 and 4.16 are summarized as follows: (i) BIMEVOX phase + small amount of liquid between T_1 and T_2, (ii) solid + liquid between T_2 and T_3, and (iii) liquid above T_3. The thermodynamically stable region of the BIMEVOX phase, which is indicated by the shaded area in Figure 4.15, is reduced by Li- and Ag-doping.

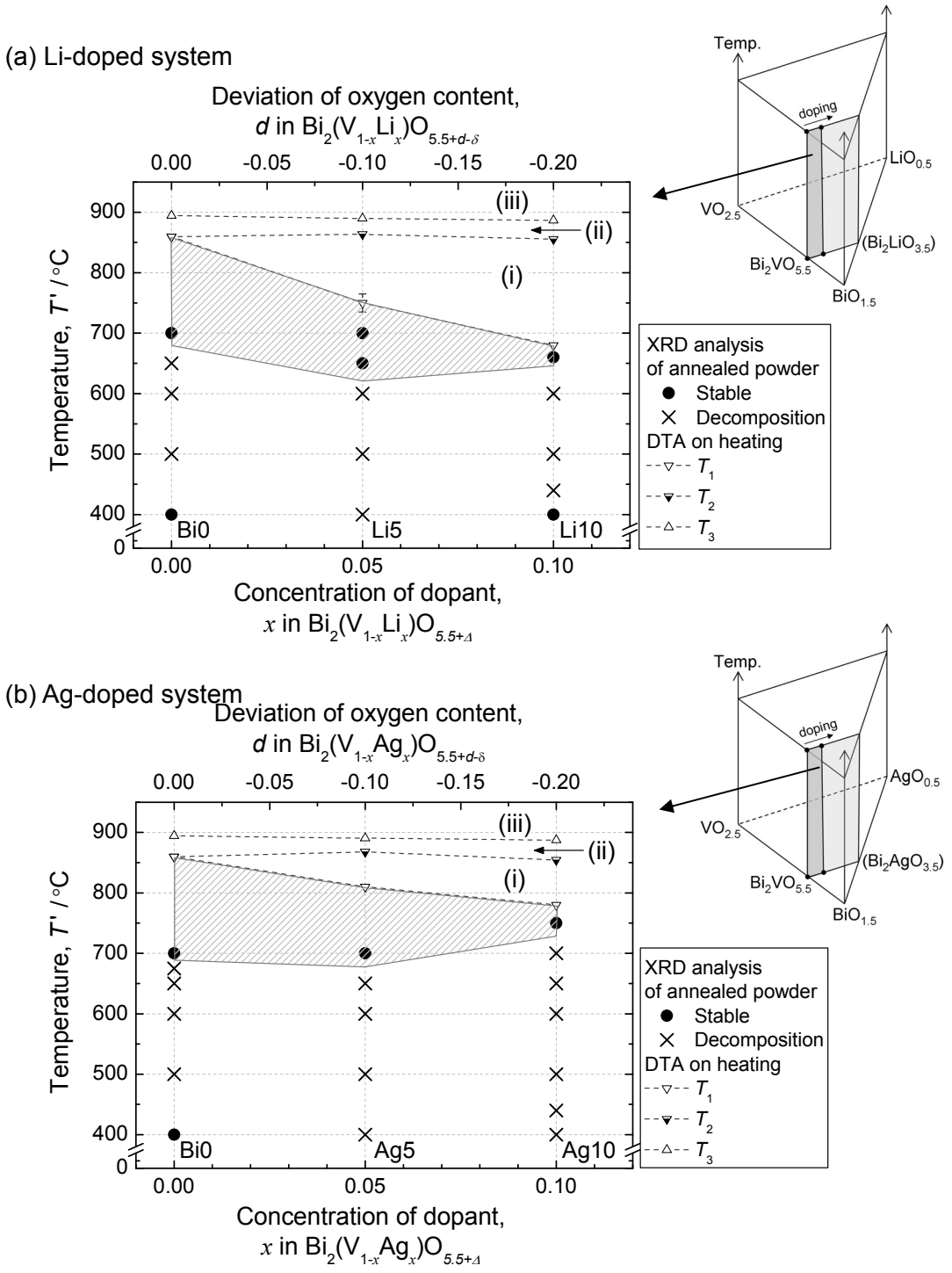

Figure 4.15 Pseudo-binary phase diagrams, generated by the XRD analysis as well as DTA. The shaded areas indicate the thermodynamically stable region of the γ_f of BIMEVOX. An example of a DTA profile is shown in Figure 4.16. The following phases were estimated: (i) BIMEVOX phase + small amount of liquid, from T_1 to T_2, (ii) solid + liquid, from T_2 to T_3, and (iii) liquid, above T_3.

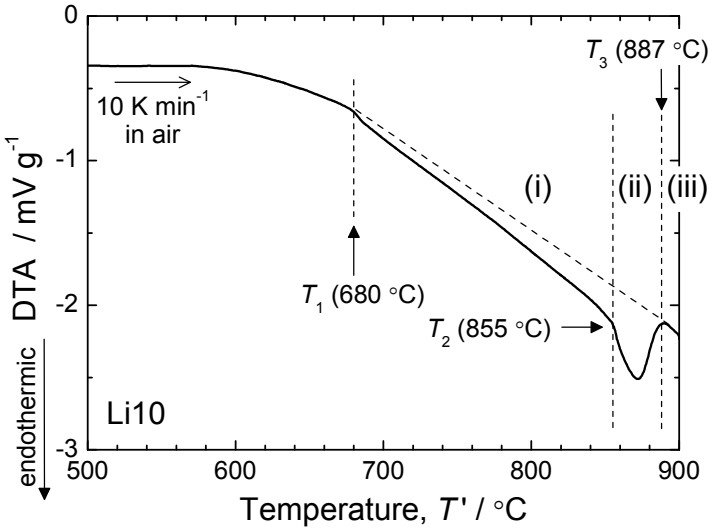

Figure 4.16 DTA profile of Li10 on heating at 10 K min^{-1} in air. Estimated phases are as follows: (i) BIMEVOX phase + small amount of liquid, from T_1 to T_2, (ii) solid + liquid, from T_2 to T_3, and (iii) liquid, above T_3.

4.8.2. Time dependence of electrical conductivities determined by AC impedance spectroscopy

Figure 4.17(a) and (b) show the time-dependent degradation of conductivities of Li10 and Ag10 at 500 and 600 °C, respectively. "$\sigma_{n\mathrm{hr}}/\sigma_{0\mathrm{hr}}$" denotes the ratio of conductivity after annealing for n hr to that before annealing. The data of Bi0 obtained in Chapter 3 are also shown for comparison. As shown in Figure 4.17(a), prolonged annealing at 500 °C markedly decreased the conductivities of Li10 and Ag10 due to the progress in thermal decomposition from γ_f, and $\sigma_{n\mathrm{hr}}/\sigma_{0\mathrm{hr}}$ of Li10 and Ag10 were much lower than that of Bi0 at each annealing time. In particular, the degradation of conductivity was prominent in Ag10. When L10 and Ag10 were annealed at 600 °C, thermal decomposition also decreased the oxide-ion conductivities, as shown in Figure 4.17(b). However, the decrease in conductivity was relatively small for Li10. The degradation of conductivity shown in Figure 4.17 further verifies the poor phase stability of Li- and Ag-doped $Bi_2VO_{5.5}$ with time.

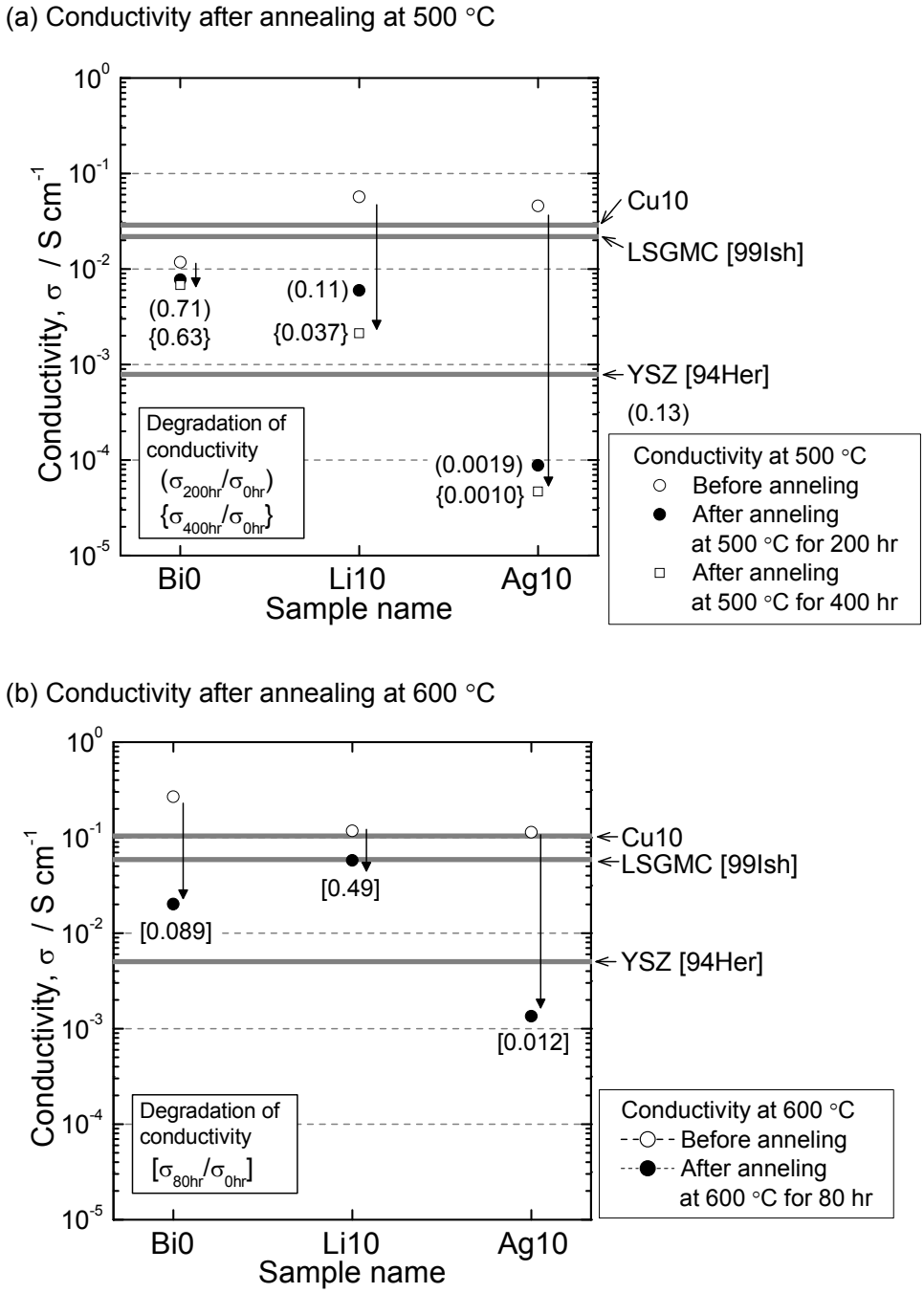

Figure 4.17 Conductivity changes of Bi0, Li10, and Ag10 (a) at 500 °C before and after annealing at 500 °C for 200 and 400 hr and (b) at 600 °C before and after annealing at 600 °C for 80 hr. "$\sigma_{n\text{hr}}/\sigma_{0\text{hr}}$" denotes the ratio of conductivity after annealing for *n* hr to that before annealing. $\sigma_{0\text{hr}}$ of Ag10 at 600 °C was interpolated value based on the electrical conductivities from 430 to 540 °C and from 730 to 750 °C in Figure 4.6. Gray lines indicate the conductivities of Cu10, YSZ [94Her], and LSGMC [99Ish] at 500 °C without prolonged annealing.

4.9. Empirical knowledge about doping effects

This section briefly describes the effects of monovalent-metal-doping on oxide-ion conductivity in γ_f, phase stability of γ_f against β_f and α_f (widening of temperature region for γ_f at low temperatures), and phase stability against thermal decomposition. Table 4.5 lists some characters of dopants with those of V, *i.e.*, valences, ionic radius in 6-fold coordination, lattice energies of binary oxide "*Q*" (trend of affinity with oxide-ion in BIMEVOX), and preferable oxygen coordinations. There is little difference in the affinity with oxide ion, represented by *Q*, between Li and Ag.

Table 4.5 Valences, Shannon ionic radii in 6-fold coordination [76Sha], lattice energies (*Q*) of binary oxide (trend of affinity with oxide ion in BIMEVOX), and preferable oxygen coordinations of Li, Ag, and V. Doping with Li and Ag increases the amount of oxygen vacancies due to smaller valence of dopants than V. As described in Chapter 1, lattice energy *Q* is the negative value of the enthalpy change of following reaction: $MM^+(g) + 0.5O^{2-}(g) \rightarrow MM_1O_{0.5}(s)$, where MM^+ is Li^+ and Ag^+. Comparing at the same valence of dopant, dopant with larger *Q* is expected to bind more strongly with oxide-ion in BIMEVOX. Oxygen coordinations in Li_2O (anti-fluorite structure), Ag_2O (cuprite structure), and V_2O_5 (ReO_3-related one-dimensional shear structure [76Hul,86Enj]) are regarded as preferable.

	Valence	Ionic radius (nm)	Lattice energy, *Q* (MJ mol^{-1})	Preferable oxygen coordination
Li	+1	0.076	1.429	4-fold (tetrahedron)
Ag	+1	0.115	1.481	2-fold (linear)
V	+5	0.054	–	5-fold (square pyramid)

Oxide-ion conductivity in γ_f

Oxide-ion conductivity in γ_f decreases with an increase in dopant concentration although doping with monovalent metal should largely increase the oxygen vacancy concentration. As shown in Table 4.3, highly conductive γ_f of Li10 and Ag10 exhibited larger E_a than γ_f of Bi0.

This fact strongly suggests that Li and Ag associate with oxygen vacancies in γ_f, *i.e.*, association areas (disarray in local structure) disturb the diffusion of oxide ions, and some oxygen vacancies can not diffuse independently and freely. HT-XRD analysis for Li10 and Ag10 did not reveal the difference in average structures between highly conductive and lowly conductive state of γ_f. The difference between two states of γ_f probably derives from the small difference in local structure around dopant, *i.e.*, association state.

Phase stability of γ_f against β_f and α_f

Li- and Ag-doping effectively stabilize γ_f against β_f and α_f. 5 mol% doping decreased $T_{\beta/\gamma}$ down to ~500 °C, and the transition behavior did not show a large difference between Li- and Ag-doped samples. This fact suggests that large amount of oxygen vacancies destabilize β_f and α_f against that of γ_f because oxygen atoms bind stronger with V in β_f and α_f rather than in γ_f. In 10 mol% doped samples, γ_f was obtained at room temperature. However, the γ_f of Li10 was kinetically stabilized phase below ~400 °C, because α_f appeared after annealing at 400 °C for 200 hr. This suggests that large amounts of oxygen vacancies and dopant in V-O layer of γ_f effectively retard the ordering from γ_f to β_f and/or α_f.

Phase stability against thermal decomposition

Li- and Ag-doped $Bi_2VO_{5.5}$ show poor phase stability against thermal decomposition. In particular, progress in thermal decomposition was prominent in Ag-doped samples. As shown in Table 4.5, Li and Ag have larger size than V. The difference in size from V is quite large for Ag. This strongly suggests that large lattice distortions around dopants decrease the phase stability against thermal decomposition. That is, the dopant, whose size is much larger than that of V, tends to destabilize BIMEVOX against thermal decomposition in terms of strain energy.

4.10. Conclusion

In this chapter, the electrical conductivities, phase transitions, and long-term phase stabilities of $Bi_2(V_{1-x}MM_x)O_{5.5+\Delta}$ (MM = Li and Ag, x = 0.05 and 0.1) have been determined. The findings are summarized as follows:

(1) $Bi_2(V_{0.95}Li_{0.05})O_{5.4}$ and $Bi_2(V_{0.95}Ag_{0.05})O_{5.4}$ showed transitions from α_f to β_f and β_f to γ_f, and γ_f was obtained above ~500 °C. Both types of 5 mol% doped sample showed the similar phase transitions. For $Bi_2(V_{0.9}Li_{0.1})O_{5.3-\delta}$ and $Bi_2(V_{0.9}Ag_{0.1})O_{5.3-\delta}$, lowly conductive state of γ_f was stabilized down to room temperature and transformed to highly conductive states from 300 and 400 °C and from 280 and 420 °C, respectively.

(2) $Bi_2(V_{1-x}MM_x)O_{5.5+\Delta}$ exhibited quite high oxide-ion conductivities of 0.5–1 × 10^{-1} S cm^{-1} at around 500 °C.

(3) The Li- and Ag-doping did not suppress thermal decomposition. $Bi_2(V_{1-x}MM_x)O_{5.5+\Delta}$ was metastable at intermediate temperatures, and prolonged annealing markedly decreased its oxide-ion conductivity. In particular, poor phase stability was prominent for $Bi_2(V_{0.9}Ag_{0.1})O_{5.3-\delta}$.

(4) The pseudo-binary phase diagram of $Bi_2(V_{1-x}MM_x)O_{5.5+\Delta}$ was generated as a function of dopant concentration. The thermodynamically stable region of the BIMEVOX phase was reduced by Li- and Ag-doping.

References

[52Heb] M. Hebb, J. Chem. Phys. 20 (1952) 185.

[56Wag] C. Wagner, Electrochemistry 60 (1956) 4.

[73Sch] G. Schoen, Acta. Chem. Scand. 27 (1973) 2623.

[75Ham] J.S. Hammond, S.W. Gaarenstroom, and N. Winograd, Anal. Chem. 47 (1975)

2194.

[76Sha] R.D. Shannon, Acta Crystallogr. A 32 (1976) 767.

[76Hul] F. Hulliger, *Structural chemistry of layer-type phases*, D. Reidel Publishing Company, Boston (1976).

[77Gaa] S.W. Gaarenstroom and N. Winograd, J. Chem. Phys. 67 (1977) 3500.

[86Enj] R. Enjalbert and J. Galy, Acta Cryst. C42 (1986) 1467.

[92Sha] V. Sharma, A.K. Shukla, and J. Gopalakrishnan, Solid State Ionics 58 (1992) 359.

[94Her] J. Van Herle, A.J. Mcevoy, and K.R. Thampi, J. Mater. Sci. 29 (1994) 3691.

[97Jia] S.P. Jiang, J.G. Love, and S.P.S. Badwal, Key Eng. Mater. 125-126 (1997) 81.

[98Pel] J. W. Pell, K. M. Delak, and H. C. zur Loye, Chem. Mater. 10 (1998) 1764.

[98Vai] B. Vaidhyanathan, K. Balaji, and K.J. Rao, Chem. Mater. 10 (1998) 3400.

[99Ish] T. Ishihara, H. Furutani, M. Honda, T. Yamada. T. Shibayama, T. Akbay. N. Sakai, H. Yokokawa, and Y. Takita, Chem. Mater. 11 (1999) 2081.

[02Wat] A. Watanabe and K. Das, J. Solid State Chem. 163 (2002) 224.

[03Mai1] G. Mairesse, P. Roussel, R.N. Vannier, M. Anne, C. Pirovano, and G. Nowogrocki, Solid State Science 5 (2003) 851.

[03Mai2] G. Mairesse, P. Roussel, R.N. Vannier, M. Anne, and G. Nowogrocki, Solid State Science 5 (2003) 861.

[05Ste] M.C. Steil, F. Ratajczak, E. Capoen, C. Pirovano, R.N. Vannier, and G. Mairesse, Solid State Ionics 176 (2005) 2305.

[07Tan] Y. Taninouchi, T. Uda, Y. Awakura, A. Ikeda and S.M. Haile, J. Mater. Chem. 17 (2007) 3182.

[09Tan] Y. Taninouchi, N. Hatada, T. Uda, and Y. Awakura, J. Electrochem. Soc. 156(5) (2009) B572.

[05Pir] C. Pirovano, M. C. Steil, E. Capoen, G. Nowogrocki, and R. N. Vannier, Solid State Ionics 176 (2005) 2079.

[09Roy] B. Roy and P. A Fuierer, J. Mater. Res. 24(10) (2009) 3078.

Chapter 5

Doping with Transition Metal (i):

"Oxide-Ion Conductivity and Phase Stability of

$Bi_2(V_{0.95}TM_{0.05})O_{5.5+\Delta}$ (TM = Ti, Zr, Hf, Nb, Ta, Cr, Mo, and W)"

5.1. Introduction

In this chapter, 5 mol% vanadium sites are substituted by various transition metals (TM = Ti, Zr, Hf, Nb, Ta, Cr, Mo, and W) that locate close to V in the periodic table and have different valences and sizes as shown in Figure 5.1. The doping effects on temperature dependence of electrical conductivities and long-tern phase stabilities are investigated.

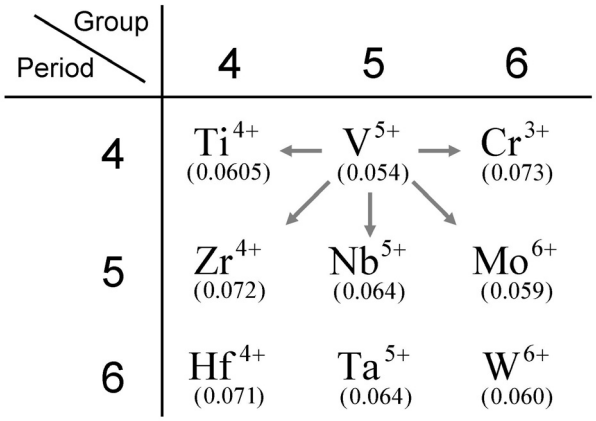

Figure 5.1 Transition metals (TM) selected as dopant cation. $TM^{a}_{(b)}$: *a* is expected valence in BIMEVOX. (*b*) is ionic radius in nm unit assuming 6-fold coordination [76Sha].

Certain properties of doping of Ti [92Goo,92Sha,95Yan,96Laz], Zr [92Goo,95Yan,02Kro,05Wro], Hf [09Beg1,09Beg2], Nb [92Goo,94Jou,96Laz], Ta [92Goo,96Laz], Cr [96Lee1,96Laz,96Jou], Mo [93Van,96Laz,06Vor], and W [95Van,96Laz,05Vor] have been reported. However, it is noted in the present study that the

electrical conductivity and transition behavior of BIMEVOX are markedly affected by thermal history.

5.2. Sample preparation

$Bi_2(V_{0.95}TM_{0.05})O_{5.5+\Delta}$ ($\Delta \equiv d - \delta$, where Δ is total oxygen deviation, d is oxygen deviation due to aliovalent doping, and δ is oxygen loss due to partial reduction) are abbreviated as TM5 (where TM is the chemical symbol of the dopant). Polycrystalline powders were synthesized by a solid-state reaction in air using platinum containers. Table 5.1 lists the staring materials. Mixtures of appropriate amounts of constituents were heated at 650 °C for 12 hr. The ground powders were formed into pellets at 0.2 ton cm^{-2} and then heated again at 800 °C for 12 hr. This heat treatment was repeated after intermediate grinding. In the case of Zr5 and Hf5, the heat treatment at 850 °C for 12 hr was repeated several times.

Table 5.1 Purity and Source of starting materials

Starting material	Chemical formula	Purity (mass %)	Source
Bismuth oxide	Bi_2O_3	99.99	Furuuchi chemical
Vanadium oxide	V_2O_5	99.9	Furuuchi chemical
Titanium oxide	TiO_2	99.9	Wako
Zirconium oxide	ZrO_2	99.5 Hf < 100 ppm	Alfa aesar
Hafnium oxide	HfO_2	99.9	Mitsuwa chemicals
Niobium oxide	Nb_2O_5	99.9	Wako
Tantalum oxide	Ta_2O_5	99.9	Wako
Chromium oxide	Cr_2O_3	99.9	Furuuchi chemical
Molybdenum oxide	MoO_3	99.99	Kojundo chemical laboratory
Tungsten oxide	WO_3	99.99	Kojundo chemical laboratory

Figure 5.2(a) shows the sintering procedure to obtain dense pellets. Powders were uniaxially compressed at 3 ton cm^{-2} for 15 min and then sintered at 800 °C for 24 hr or 850 °C for 24 hr (only in Zr5 and Hf5). Surfaces of pellets were mirror-polished using SiC polishing papers. The diameter and thickness of the sintered pellets were about 10 and 1.2 mm, respectively, as shown in Figure 5.2(b). For conductivity measurements, Au electrodes were applied with gold paint.

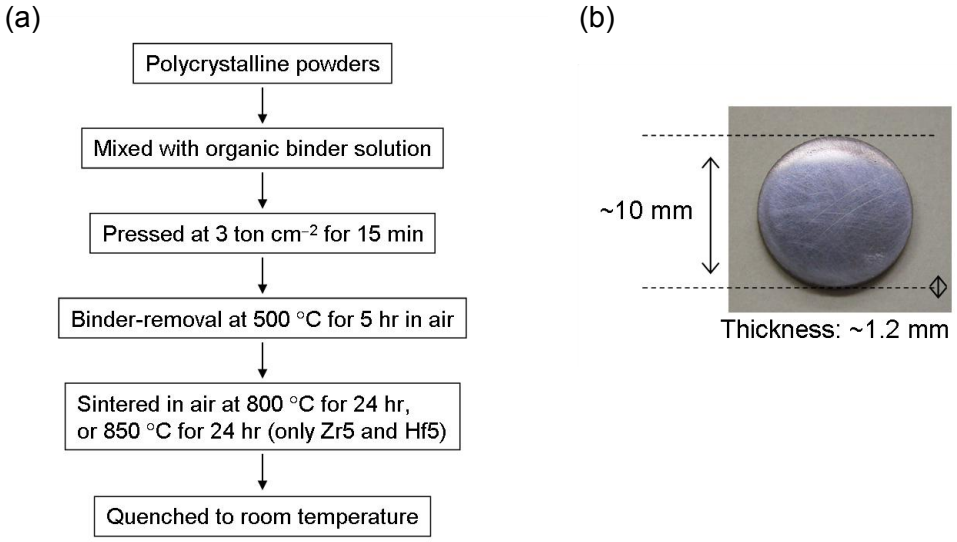

Figure 5.2 (a) Flowchart for sintering of pellet. (b) An entire image of the sintered pellet of Nb5.

5.3. Valences of dopants determined by XPS

XPS spectra of pellets quenched from 800 °C were collected before and after surface cleaning by Ar-sputtering for 20 min. The calibration of binding energy was performed for Bi0 using absorbed carbon species before Ar-sputtering and mixed Au after Ar-sputtering. As the result, the binding energy of Bi did not change with Ar-sputtering. Thus, for the calibration in TM5, we assumed that the binding energy of Bi does not change by Ar-sputtering.

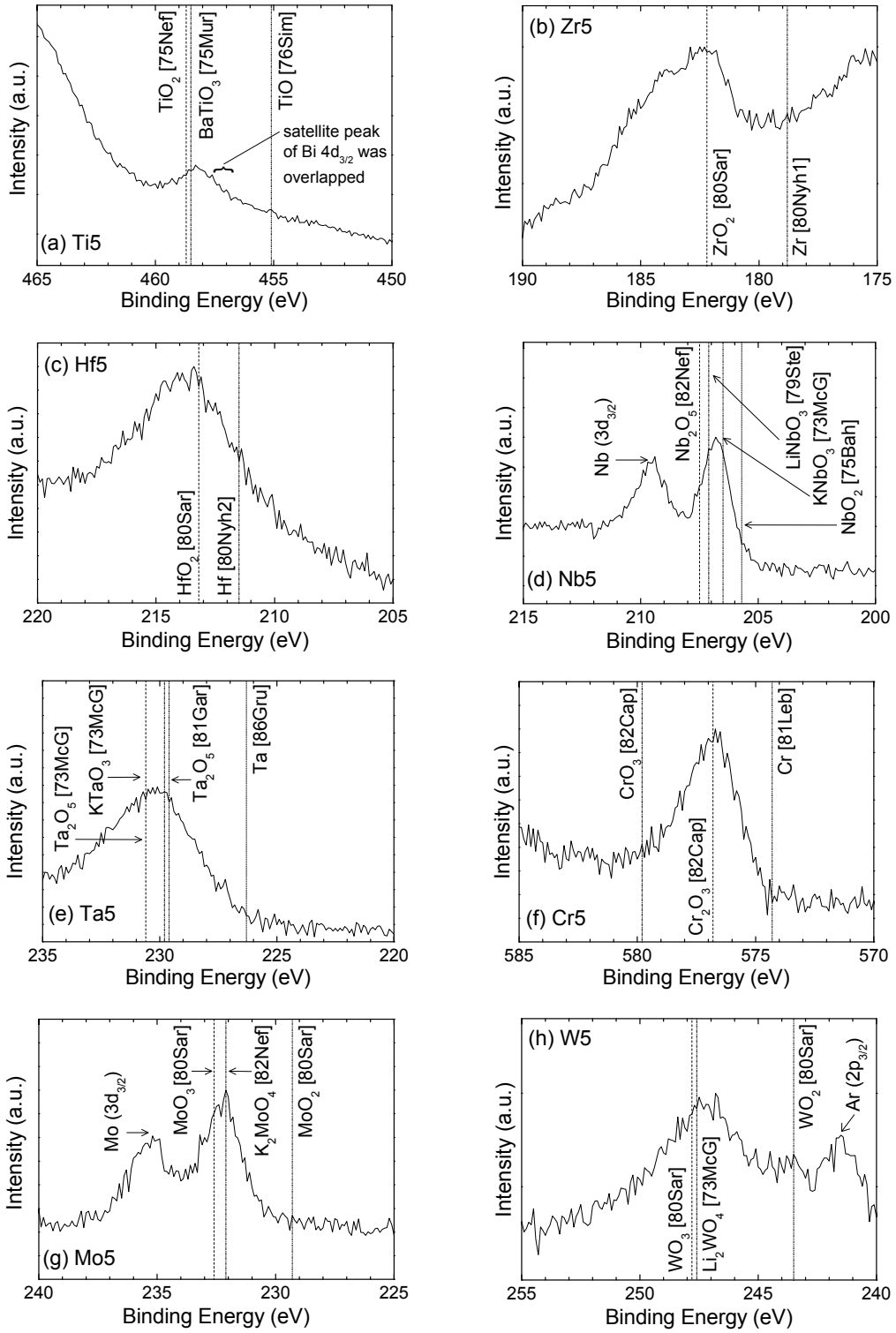

Figure 5.3 XPS spectra of dopant components. (a) Ti $2p_{3/2}$ component in Ti5. (b) Zr $3d_{5/2}$ component in Zr5. (c) Hf $4d_{5/2}$ component in Hf5. (d) Nb $3d_{5/2}$ component in Nb5. (e) Ta $4d_{5/2}$ component in Ta5. (f) Cr $2p_{3/2}$ component in Cr5. (g) Mo $3d_{5/2}$ component in Mo5. (h) W component $4d_{5/2}$ in W5.

Table 5.2 Peak positions and valences of dopant evaluated by XPS.

	Peak position (eV)		Dopant		
	Bi $4f_{7/2}$	V $2p_{3/2}$	Component	Peak position (eV)	Valence of dopant
Bi0	159.1	516.5	-	-	-
Ti5	159.0	516.4	Ti $2p_{3/2}$	458.3	+4
Zr5	159.1	516.6	Zr $3d_{5/2}$	333.5	+4
Hf5	159.1	516.6	Hf $4d_{5/2}$	213.9	+4
Nb5	159.1	516.7	Nb $3d_{5/2}$	206.8	+5
Ta5	159.1	516.6	Ta $4d_{5/2}$	230.2	+5
Cr5	159.0	516.8	Cr $2p_{3/2}$	576.8	+3
Mo5	159.0	516.5	Mo $3d_{5/2}$	232.4	+6
W5	159.0	516.7	W $4d_{5/2}$	247.3	+6

Figure 5.3 shows the XPS spectra of dopant component after Ar-sputtering. The peak positions of Bi, V, and TM are summarized in Table 5.2. In Bi0, the valences of Bi and V can be regarded as trivalent and pentavalent, respectively, because the partial reduction of Bi0 at 800 °C is small ($\delta = 0.005 \pm 0.002$), as described in Chaper3. The peak positions of Bi $4f_{7/2}$ and V $2p_{3/2}$ for all TM5 sufficiently coincided with those for Bi0. The peak position of Ti $2p_{3/2}$ in Ti5 was somewhat lower than that of TiO_2 [75Nef] but closer to that of $BaTiO_3$ [75Mur], as shown in Figure 5.3(a). It is acceptable that Ti in Ti5 is tetravalent with considering chemical shift. Zr and Hf shown in Figures 5.3(b) and (c) are also regard as tetravalent. The peak position of Nb $3d_{3/2}$ was intermediate between that of Nb_2O_5 [82Nef] and that of NbO_2 [75Bah], as shown in Figure 5.3(d). Nb is estimated as pentavalent because similar peak shift to lower binding energy can be seen in complex oxide such as $LiNbO_3$ [79Ste], and KNb_2O_6 [73McG]. The valence of Ta is also estimated to be pentavalent, as shown in Figure 5.3(e). The peak position of Cr $2p_{3/2}$ was in excellent agreement with that reported for Cr_2O_3 [82Cap], as shown in Figure 5.3(f). Cr in Cr5 is, therefore, trivalent. The peak position of Mo $3d_{5/2}$, and

W $4d_{5/2}$ shown Figures 5.3(g) and (h) were somewhat lower than that of MoO_3 [80Sar] and WO_3 [80Sar] but almost coincided that of K_2MoO_4 [82Nef] and $LiWO_4$ [73McG], respectively. Thus, we regard the valence of Mo in Mo5 and W in W5 as hexavalent.

5.4. Phases at room temperature identified by XRD analysis

Figure 5.4 shows the XRD patterns of powders quenched or slowly cooling at 1 K min^{-1} from 800 °C in logarithmic intensity scale. Table 5.3 lists the phase group of each TM5 sample at room temperature. For Bi0, orthorhombic α_f was stabilized by quenching. Despite the cooling, excluding Cr5 and W5, orthorhombic α_f was obtained in all TM5. In Cr5, β_f was stabilized by quenching. In W5, monoclinic α_f was obtained by quenching but orthorhombic

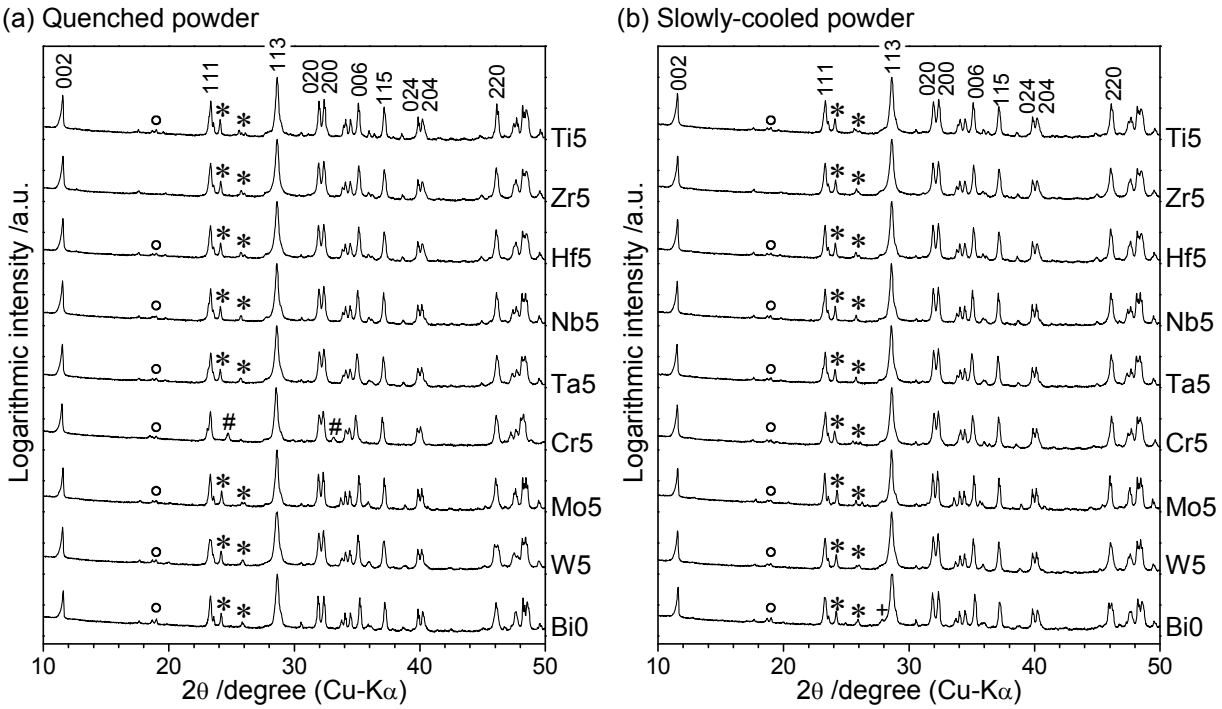

Figure 5.4 XRD patterns of powders quenched from 800 °C in logarithmic intensity scale. The plane indices are marked assuming the mean orthorhombic subcell. Asterisks (∗) and hashes (#) indicate typical superlattice diffractions of α_f and β_f, respectively. Open circles (o) indicate the typical peak of $BiVO_4$. Cross (+) indicates the peak of the secondary phase (estimated to be $Bi_{3.5}V_{1.2}O_{8.25}$) caused by thermal decomposition.

Table 5.3 Chemical formulas, phases at room temperature, and contained secondary phases. Sintering conditions and relative densities of pellet are also shown.

	Chemical formula	XRD analysis*		Pellet	
		Quenched	Cooled at 1 K min^{-1}	Sintering condition	Relative density (%)
Bi0	$Bi_2VO_{5.5-\delta}$	α_f(orth)	α_f (mono)	800 °C, 24 hr	94
Ti5	$Bi_2(V_{0.95}Ti_{0.05})O_{5.475-\delta}$	α_f(orth)	α_f (orth)	800 °C, 24 hr	95
Zr5	$Bi_2(V_{0.95}Zr_{0.05})O_{5.475-\delta}$	α_f(orth)	α_f (orth)	850 °C, 24 hr	94
Hf5	$Bi_2(V_{0.95}Hf_{0.05})O_{5.475-\delta}$	α_f(orth)	α_f (orth)	850 °C, 24 hr	95
Nb5	$Bi_2(V_{0.95}Nb_{0.05})O_{5.5-\delta}$	α_f(orth)	α_f (orth)	800 °C, 24 hr	95
Ta5	$Bi_2(V_{0.95}Ta_{0.05})O_{5.5-\delta}$	α_f(orth)	α_f (orth)	800 °C, 24 hr	95
Cr5	$Bi_2(V_{0.95}Cr_{0.05})O_{5.45-\delta}$	β_f(orth)	α_f (orth)	800 °C, 24 hr	95
Mo5	$Bi_2(V_{0.95}Mo_{0.05})O_{5.525-\delta}$	α_f (orth)	α_f (orth)	800 °C, 24 hr	95
W5	$Bi_2(V_{0.95}W_{0.05})O_{5.525-\delta}$	α_f (mono)	α_f (orth)	800 °C, 24 hr	95

* (symmetry of subcell) “mono” and “orth” refer to monoclinic and orthorhombic, respectively.

α_f appeared in the slowly cooled sample. Small amounts of $BiVO_4$ were detected as a secondary phase in Bi0, Ti5, Nb5, Ta5, Cr5, Mo5, and W5. This can be explained by the fact that the true stoichiometry of $Bi_2VO_{5.5-\delta}$ is slightly Bi-rich ($Bi_2(V_{1-n}Bi_n)O_{5.5+\Delta}$, n: 0–0.02), as shown in Chapter 3. Additionally, thermal decomposition slightly proceeded in slowly-cooled powder of Bi0.

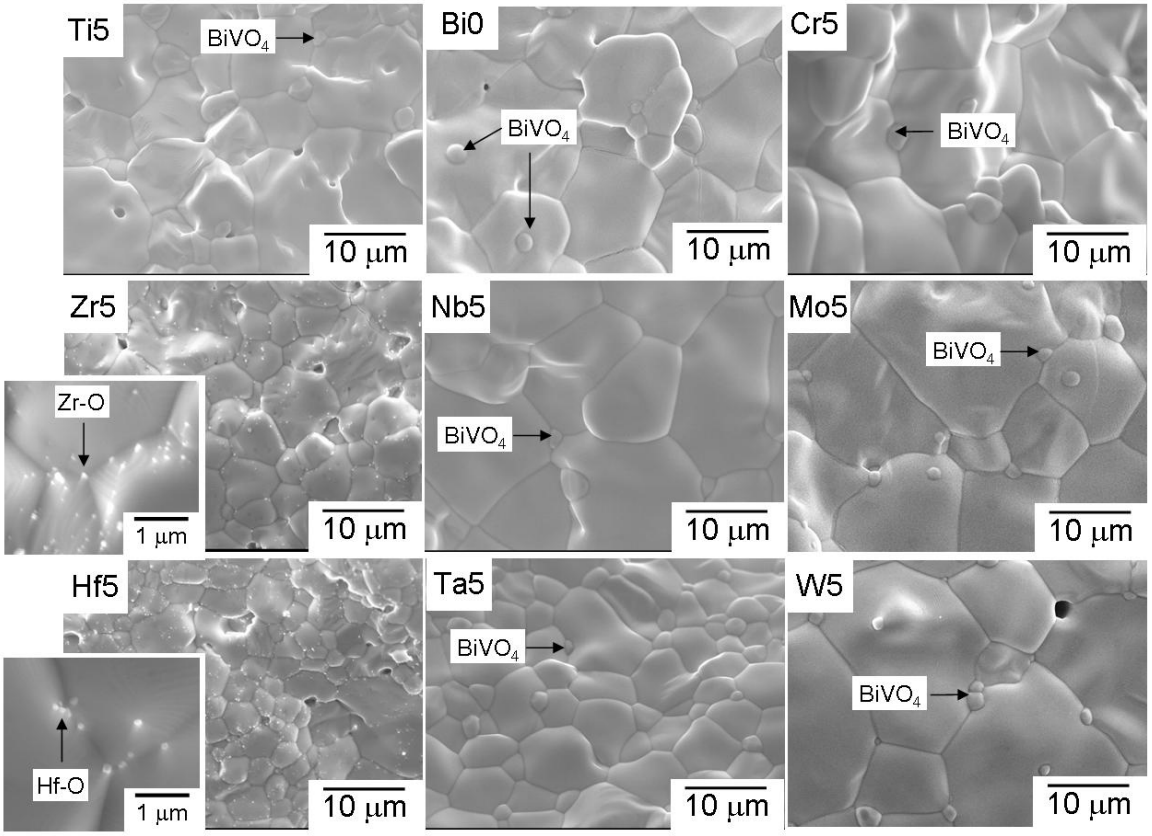

Figure 5.5 Cross-sectional FE-SEM images after thermal etching. The grains of secondary phases, *i.e.*, $BiVO_4$, zirconium-rich oxide, and hafnium-rich oxide, are indicated by arrows.

5.5. Microstructures and relative densities of sintered pellets

Figure 5.5 shows the cross-sectional FE-SEM images of sintered pellets. Samples were thermally etched at the sintering temperatures for several hours to clarify the grain boundaries. Large grains, whose sizes exceeded 5 μm, were observed in all pellets. In Nb5, Cr5, Mo5, and W5, the grain sizes were over 10 μm. Uniformity of the composition was confirmed for large grains by EDX. However, small $BiVO_4$ grains, whose sizes were ~1 μm, existed in all samples except for Zr5 and Hf5. In Zr5 and Hf5, very small grains of zirconium-rich oxide and hafnium-rich oxide, whose sizes were ~100 nm, were detected, respectively. We believe that the reason for residual oxide is the results of slow reaction/diffusion rates of ZrO_2 and HfO_2. Despite this, we set the mixing ratio at $Bi_2(V_{0.95}TM_{0.05})O_{5.5+\Delta}$. This is because the

presence of such small amount of secondary phases is unlikely to affect electrical conductivities and phase transition behavior.

The relative densities of sintered pellets were evaluated form the densities which were calculated from the nominal composition and the cell volume derived from XRD analysis. TM5 pellets showed the high relative densities of 94–95 %, as listed in Table 5.3.

5.6. Temperature dependence of electrical conductivities determined by AC impedance spectroscopy

Just before measurements, the pellets with Au electrodes were heated to 800 °C and then quenched to room temperature to produce the thermal history. Samples were heated and cooled at a rate of 1 K min^{-1} between 200 and 730 °C for more than two cycles in air. Figure 5.6 shows, as a typical example, the impedance spectra for Nb5 on the 1st heating. At a low temperature of 255 °C, Nb5 belongs to α_f. As shown in Figure 5.6(a), the spectrum consisted of a semicircle and arc in the high-, and low-frequency regions, respectively. We fitted the experimental spectrum with two parallel *RQ* circuits in series where *R* is resistance and *Q* is constant phase element ($Q \equiv (i\omega)^p Y_0$, ω: angular frequency, *p*: deviation from ideal semicircle, Y_0: capacitance). The evaluated electrical conductivity parameters were R = 1420 Ω, Y_0 = 6.1 × 10^{-9} F, and p = 0.78 in the high-frequency region, and R = 3456 Ω, Y_0 = 8.4 × 10^{-5} F, and p = 0.53 in the low-frequency region. The values of the capacitance in the low- and high-frequency regions corresponded to the bulk and grain boundary, respectively. The resistivity of the bulk was evaluated by the intersection between the semicircle and the arc, as indicated in Figure 5.6(a). The arcs disappeared and linear components were observed at an intermediate temperature of 449 °C and a high temperature of 696 °C, as shown in Figures 5.6(b) and (c), respectively. In these cases, the resistivity of the bulk was evaluated by the

intercept of the spectrum with the real axis. Similar spectra are often observed for good ionic conductors attached to blocking electrodes for ion migration [07Tan]. The spectrum is explained by the ionic diffusion-limited process in the electrode reaction, *i.e.*, the Warburg impedance [97Jia]. Nb5 is β_f at 449 °C and γ_f at 696 °C. Consequently, this suggests that the dominant charge carrier in β_f and γ_f of Nb5 is an oxide ion, which is further confirmed in Section 5.7.

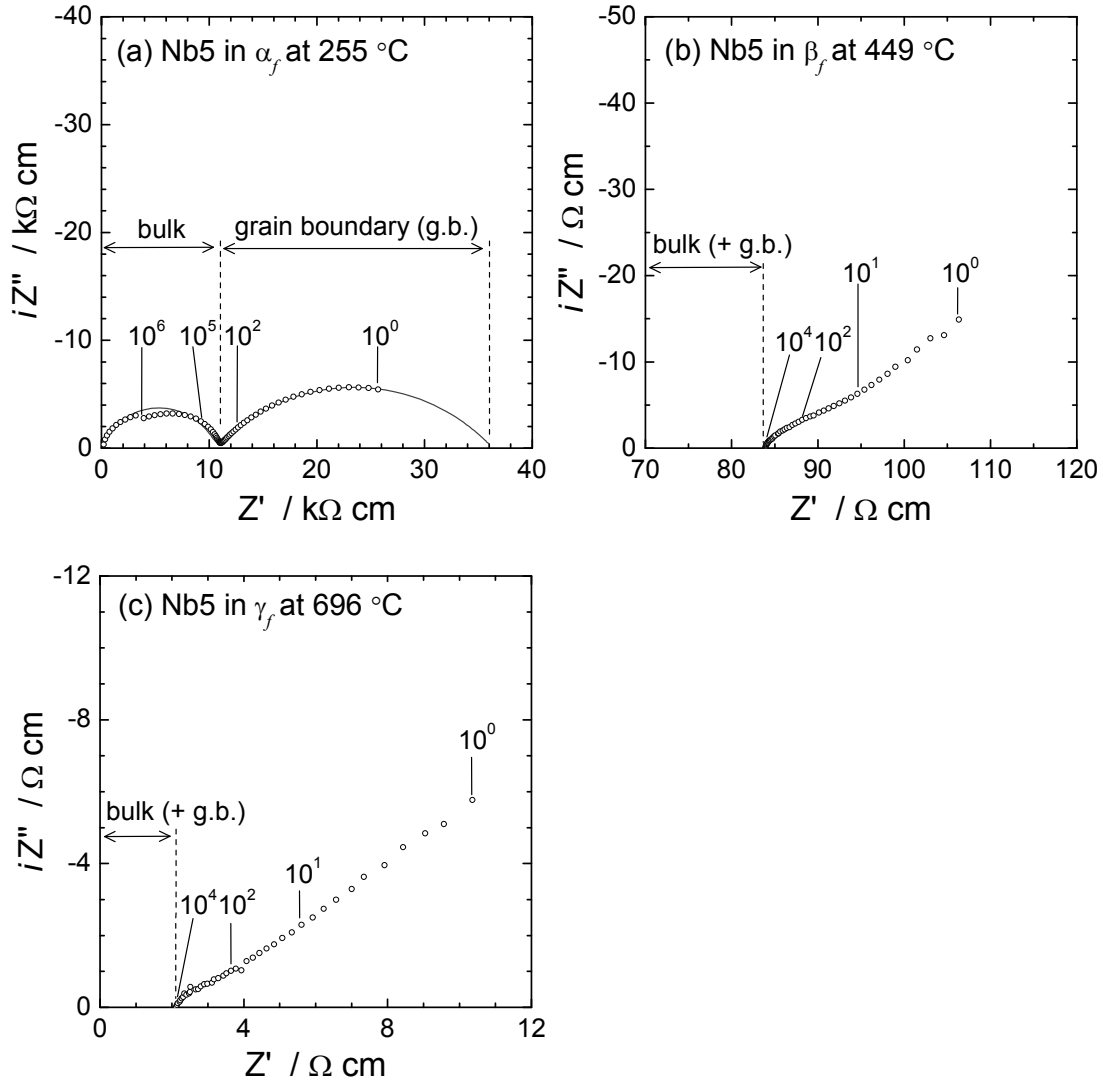

Figure 5.6 Typical impedance spectra at low, intermediate, and high temperatures. Spectra were collected for Nb5 on the 1st heating. (a) α_f at a low temperature of 255 °C. Gray line indicates the fitted result assuming two parallel *RQ* circuits in series. (b) β_f at an intermediate temperature of 449 °C. (c) γ_f at a high temperature of 696 °C.

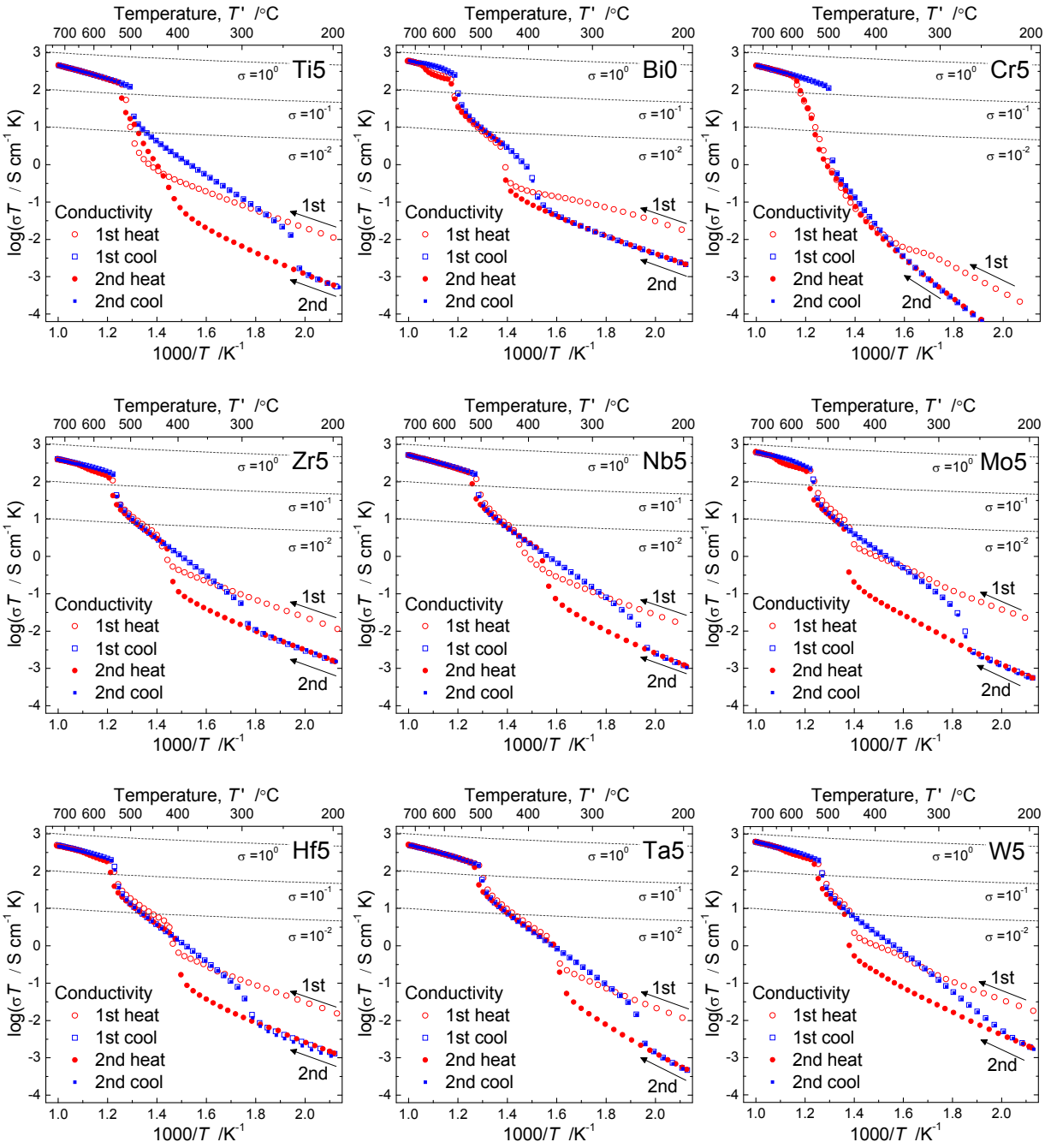

Figure 5.7 Arrhenius plots of bulk conductivities in air at a scan rate of 1 K min^{-1}. Before measurements, pellets were quenched from 800 °C to room temperature.

Figure 5.7 shows the Arrhenius plots of bulk conductivity for two heating/cooling cycles in air. Since there was no obvious change in conductivity between the 2nd and 3rd cycles, only the data in the 1st and 2nd cycles are shown. In heating Bi0, there is a large conductivity

jump at 445 °C corresponding to the transition from α_f to β_f (α_f/β_f transition), and another at 570 °C corresponding to the transition from β_f to γ_f (β_f/γ_f transition). Supercooling by as much as 50 °C was required for the β_f/α_f transition during subsequent cooling. Furthermore, α_f showed a significantly higher conductivity on the 1st heating where the sample was a quenched pellet than on the 2nd heating after the pellet was slowly cooled at 1 K min^{-1}, because the orthorhombic cell was stabilized by quenching.

The temperature dependence of conductivity in TM5 showed a trend similar to that of Bi0. Upon heating and cooling, Zr5, Hf5, Nb5, Ta5, Mo5, and W5 showed two large conductivity jumps corresponding to the transitions between α_f and β_f and between β_f and γ_f. In addition, a large hysteresis was exhibited at β_f/α_f transition. In Ti5, the β_f region was not clearly observed on heating although it appeared between 250 and 500 °C on cooling. In Cr5, the phase transition was markedly different from that of others. The quenched Cr5 powder maintained the β_f phase. This quenched powder of Cr5 was reheated to 225 or 400 °C at 1 K min^{-1} and then XRD analysis was employed after quenching. β_f was exhibited in the Cr5 reheated to 225 °C, but α_f was observed in the Cr5 reheated to 400 °C. Therefore, the change in the slope of conductivity at around 315 °C on the 1st heating was attributed to the phase transition from β_f to α_f. Another change in conductivity between 500 and 600 °C corresponded to the transition between α_f and γ_f.

Conductivities in γ_f showed almost no difference among the cycles. With the exception of Cr5, in TM5, the conductivities of α_f on the 1st heating were about an order of magnitude higher than those on the 2nd heating. Transition temperatures for the α_f/β_f ($T_{\alpha/\beta}$) and β_f/γ_f transitions ($T_{\beta/\gamma}$) are summarized in Figure 5.8. Since $T_{\beta/\gamma}$ of Ti5 and $T_{\alpha/\gamma}$ of Cr5 were difficult to evaluate from temperatures at the onset of conductivity jumps, temperatures at the

end of conductivity jumps for the transition to γ_f were used instead. In TM5, transition behavior also varied with cycles. In particular, we observed large variations due to the thermal history of the pellet in Ti5 and Nb5. For example, in Nb5, $T_{\alpha/\beta}$ on the 1st heating was markedly higher than that on the 2nd heating. Meanwhile, $T_{\beta/\gamma}$ on the 1st heating was slightly lower than that on the 2nd heating. When focus is placed on the transition temperatures on the 2nd heating, $T_{\alpha/\beta}$ became lower in Zr5, Hf5, Nb5, and Ta5 than in Bi0, while it was almost unchanged in Mo5 and W5. On the other hands, with the exception of Cr5, $T_{\beta/\gamma}$ was lower in all TM5 samples. In particular, Nb- and Ta-doping effectively stabilized γ_f at low temperatures.

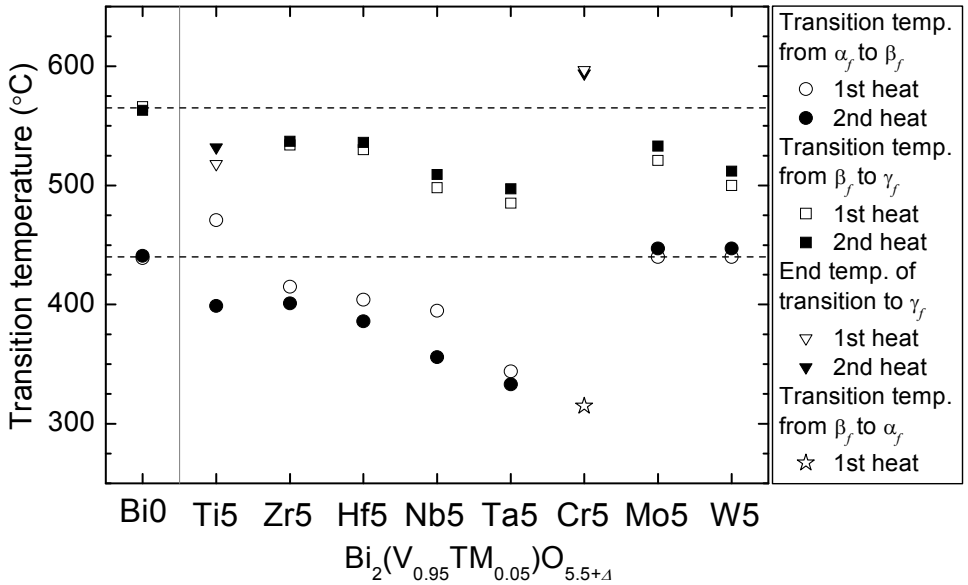

Figure 5.8 Summary of the transition temperatures determined by changes in conductivity upon heating. Dotted lines represent $T_{\alpha/\beta}$ and $T_{\beta/\gamma}$ of Bi0.

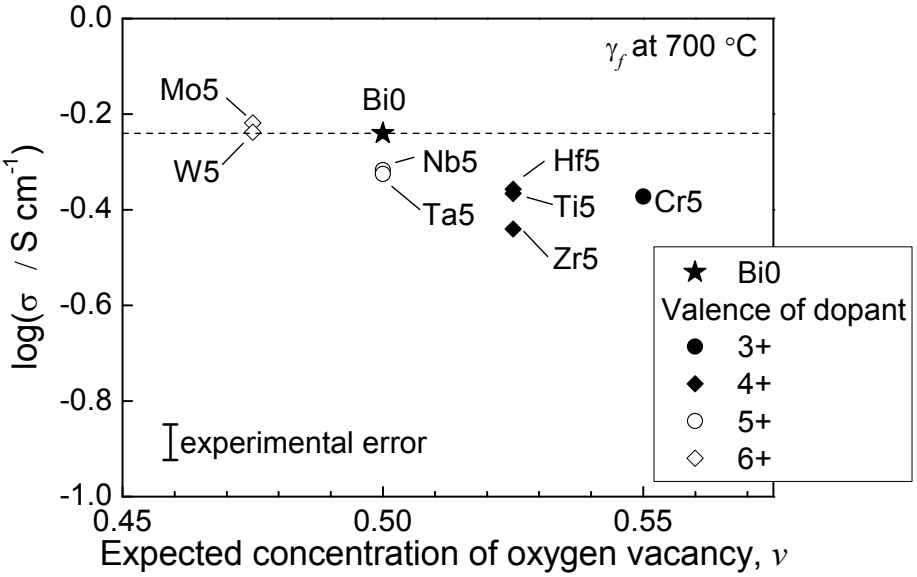

Figure 5.9 Comparison of the oxide-ion conductivities of γ_f at 700 °C. Concentration of oxygen vacancies, *i.e.*, v in $Bi_2(V_{0.95}TM_{0.05})O_{6-v}\square_v$, was estimated by assuming ideal Aurivillius structure and by preserving electroneutrality via oxygen content.

In Figure 5.9, conductivities of γ_f at 700 °C are plotted as a function of the concentration of oxygen vacancies. Oxygen vacancy concentrations were calculated by assuming the ideal Aurivillius structure (where V-O layer is composed of VO_6 octahedrons containing oxygen vacancies) and by preserving electroneutrality via the creation/annihilation of oxygen vacancies. The concentration of oxygen vacancies is denoted as v in $Bi_2(V_{0.95}TM_{0.05})O_{6-v}\square_v$, where □ refers to oxygen vacancy. It is noted that the conductivities did not increase with an increase in oxygen vacancy concentration, but maintained high values above 3×10^{-1} S cm^{-1}.

5.7. Charge carriers determined by DC polarization measurement and AC impedance spectroscopy

Figure 5.10 shows, as a typical example, the current change with time when DC voltage of 50 mV was applied to γ_f and β_f of Nb5 in air. The current at a steady state was derived from only electron/hole diffusion because Au electrodes are expected to work as blocking electrode against oxide ions. Meanwhile, the electrical conduction in AC impedance spectroscopy is sum of all mobile carriers. Table 5.4 shows the transference numbers of electrons/holes (t_e) and oxide ions (t_O), which were calculated by comparing the conductivities determined by DC polarization measurement with those determined by AC impedance spectroscopy. The obtained transference numbers are preliminary because our DC polarization measurement is a simplified version of the Hebb-Wagner method [52Heb,56Wag], where a reversible anode for oxygen gas and a blocking cathode are attached to fix the chemical potential of oxide-ions at the interface between the electrolyte and anode. However, the t_e values of γ_f and β_f were quite small in Bi0, consistent with the previous studies [88Abr,93Lee]. On the other hand, the t_e value of γ_f in TM5 was evidently as small as that for Bi0. Consequently, γ_f exhibited oxide-ion conduction even after doping with the transition metals. The dominant charge carriers of β_f were also oxide ions, although slightly higher t_e values were obtained for Zr5, Nb5, and Ta5.

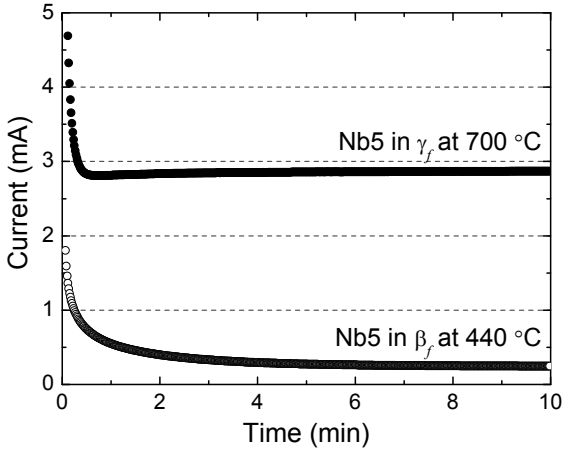

Figure 5.10 Changes of current when DC voltage of 50 mV was applied to γ_f and β_f of Nb5.

Table 5.4 Electron/hole conductivities (σ_e), and calculated transference numbers for oxide-ion conduction (t_O) and electron/hole conduction (t_e). The transference numbers are preliminary because we employed a simplified version of the Hebb-Wagner method [52Heb,56Wag]. Only data for β_f of Ti5 was obtained on cooling from 700 °C.

Phase	Sample	Temperature (°C)	σ_e (S cm^{-1})	t_O	t_e
γ_f	Bi0	700	9.89×10^{-3}	0.98	0.02
	Ti5	704	1.08×10^{-2}	0.98	0.02
	Zr5	700	7.70×10^{-3}	0.98	0.02
	Hf5	699	9.54×10^{-3}	0.98	0.02
	Nb5	700	9.56×10^{-3}	0.98	0.02
	Ta5	700	8.57×10^{-3}	0.98	0.02
	Cr5	700	7.65×10^{-3}	0.98	0.02
	Mo5	701	1.21×10^{-2}	0.98	0.02
β_f	Bi0	500	4.09×10^{-4}	0.97	0.03
	Ti5	428	1.22×10^{-4}	0.98	0.02
	Zr5	452	3.99×10^{-4}	0.94	0.06
	Hf5	450	2.84×10^{-4}	0.96	0.04
	Nb5	438	6.90×10^{-4}	0.93	0.07
	Ta5	438	7.19×10^{-4}	0.94	0.06
	Mo5	494	1.70×10^{-4}	0.99	0.01
	W5	491	3.24×10^{-4}	0.98	0.02
	Bi0	500	4.09×10^{-4}	0.97	0.03

Figure 5.11 shows the electrical conductivities at the oxygen partial pressures (pO_2) of 1 atm (in O_2), 0.21 atm (in air), and 8×10^{-4} atm (in Ar). The data were evaluated by AC impedance spectroscopy on cooling at 1 K min^{-1} from 730 °C. Generally, electron conductivity decreases with pO_2, hole conductivity increases with pO_2, but ionic conductivity is independent of pO_2, as described in Chapter 1. The electrical conductivities of γ_f in Bi0 and TM5 at 700 °C were almost unchanged when pO_2 were varied from 1 to 8×10^{-4} atm. This

supports the view that γ_f of TM5 is a primary oxide-ion conductor. In the β_f phases of $Bi_2VO_{5.5}$ as well as TM5 (with the exception of Cr5), the electrical conductivities in Ar were 2.5–4 times higher than those in air and O_2. This indicates that in generally, electron conduction appeared in Ar in the β_f phase of TM5.

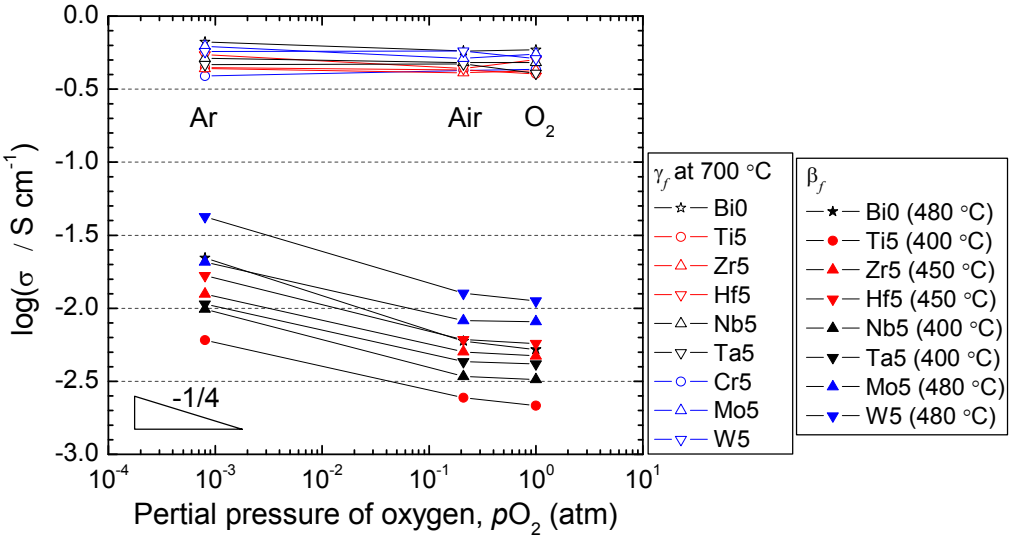

Figure 5.11 Electrical conductivities as a function of pO_2. Electron conductivity is expected to be proportional to $pO_2^{-1/4}$, as described in Chapter 1.

5.8. Long-term phase stabilities against thermal decomposition determined by XRD analysis of annealed powders

Powder samples were annealed at 700, 600, and 500 °C for 200 hr in air, and then XRD analysis was carried out. After annealing at 700 °C for 200 hr, thermal decomposition did not proceed for Bi0 or for any TM5 samples. Figure 5.12 shows the XRD patterns after annealing at 600 and 500 °C. Bi0 showed decomposition at both temperatures, almost disappearing after annealing at 600 °C. Meanwhile, thermal decomposition was markedly suppressed by TM doping. At 600 °C, the BIMEVOX phase remained in all TM5 samples, although partial decomposition was detected. The ratio of the maximum peak of the secondary phase at about 27.8° to that of BIMEVOX at about 28.6°, I_{SP}/I_{BVO}, indicated that the amount of the

secondary phase was smallest in Ti5 at 600 °C in Figure 5.12(a). After annealing at 500 °C, thermal decomposition had not progressed in Ti5, Nb5, and Ta5, as shown in Figure 5.12(b) The progression of thermal decomposition reduces oxide-ion conductivity. Thus, it is very important for the practical use of BIMEVOX that TM doping, in particular with Ti, effectively suppresses thermal decomposition.

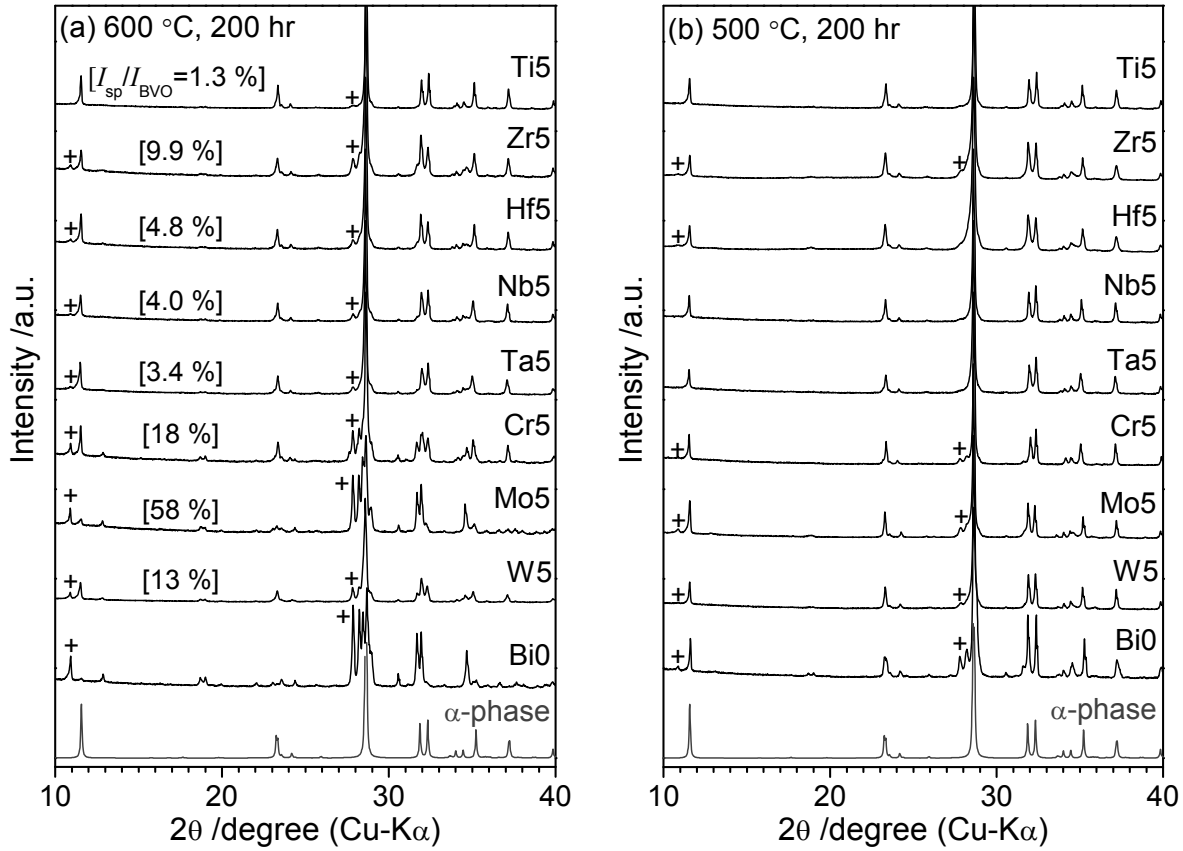

Figure 5.12 XRD patterns after annealing for 200 hr at (a) 600 °C and (b) 500 °C. The calculated pattern for α-$Bi_2VO_{5.5}$ [03Mai2] from Cu-Kα is also shown. Crosses (+) indicate typical peaks of the secondary phase caused by thermal decomposition. I_{SP}/I_{BVO} in (a) indicates the ratio of the maximum peak of the secondary phase at ~27.8° to that of BIMEVOX at ~28.6°.

5.9. Empirical knowledge about doping effects

This section briefly describes the doping effects on oxide-ion conductivity in γ_f, phase stability of γ_f against β_f and α_f (widening of temperature region for γ_f at low temperatures),

and phase stability against thermal decomposition. Table 5.5 lists some characters of dopants with those of V, *i.e.*, valences, ionic radius in 6-fold coordination, lattice energies of binary oxide "*Q*" (trend of affinity with oxide ion in BIMEVOX), and preferable oxygen coordinations. For γ_f and β_f, doping with trivalent Cr and tetravalent Ti, Zr, and Hf should increase, doping with pentavalent Nb and Ta should not change, and hexavalent Mo and W should decrease the oxygen vacancy concentration to preserve electroneutrality.

Oxide-ion conductivity in γ_f

Oxide-ion conductivity in γ_f does not increase with an increase in oxygen vacancy concentration, as shown in Figure 5.9. This suggests that the amount of oxygen vacancy, which varies according to 5 mol% doping, is not a dominant factor to determine oxide-ion conductivity in γ_f.

Phase stability of γ_f against β_f and α_f

5 mol% doping with all TM except for Cr stabilizes γ_f against β_f and α_f. In Chapters 3 and 4, it was empirically suggested that increase in oxygen vacancy concentration tends to stabilize γ_f. Figure 5.8 indicates that doping with Nb, Ta, Mo, and W also reduces $T_{\beta/\gamma}$ although it does not increase oxygen vacancy concentration. There should be other important factor to stabilize γ_f. For example, doping on V sites might increase the configurational entropy of γ_f because the disorder structure of γ_f has larger amount of crystallographic equivalent sits for V. Increase in configurational entropy of γ_f has an advantage to thermodynamically stabilize γ_f against β_f and α_f. The oxygen polyhedron network structure in the V-O layer markedly differs among γ_f, β_f, and α_f, as described in Chapter 2. Thus, preferable oxygen coordination of dopant should also affect the stability of γ_f.

Table 5.5 Valences, Shannon ionic radii in 6-fold coordination [76Sha], lattice energies of binary oxide "*Q*" (trend of affinity with oxide-ion in BIMEVOX), and preferable oxygen coordinations of dopants and V. As described in Chapter 1, lattice energy *Q* is the negative value of the enthalpy change of following reaction: $ME^{x+}(g) + x/2\ O^{2-}(g) \rightarrow ME_1O_{x/2}(s)$, where ME^{x+} is Ti^{4+}, Zr^{4+}, Hf^{4+}, Nb^{5+}, Ta^{5+}, Cr^{3+}, Mo^{6+}, and W^{6+}. Comparing at the same valence of dopant, dopant with larger *Q* is expected to bind more strongly with oxide-ion in BIMEVOX. Oxygen coordinations in TiO_2 (rutile structure), ZrO_2 (fluorite structure), HfO_2 (fluorite structure), Nb_2O_5 (high-temperature form [76Kat]), Ta_2O_5 (low-temperature form [71Ste]), Cr_2O_3 (corundum structure), MoO_3 (layer structure consisting of distorted MoO_6 octahedron [50And]), WO_3 (distorted ReO_3 structure [53And]), and V_2O_5 (ReO_3-related one-dimensional shear structure [76Hul,86Enj]) are regarded as preferable.

	Valence	Ionic radius (nm)	Lattice energy, *Q* (MJ mol^{-1})	Preferable oxygen coordination
Ti	+4	0.0605	12.009	6-fold (octahedron)
Zr	+4	0.072	9.811	8-fold (hexahedron)
Hf	+4	0.071	11.113	8-fold (hexahedron)
Nb	+5	0.064	16.927	6-fold (octahedron) and 4-fold (tetrahedron)
Ta	+5	0.064	17.134	7-fold (pentagonal bipyramid)
Cr	+3	0.073	7.551	6-fold (octahedron)
Mo	+6	0.059	25.916	6-fold (octahedron)
W	+6	0.060	26.252	6-fold (octahedron)
V	+5	0.054	19.236	5-fold (square pyramid)

Phase stability against thermal decomposition

5 mol% doping with TM tends to suppress thermal decomposition. In particular, doping with Ti, whose size is close to that of V, was effective to improve the phase stability. This fact shows no discrepancy with the empirical knowledge obtained in Chapters 3 and 4; the dopant, whose size largely deviates from that of V, has a disadvantage to suppress thermal decomposition in terms of strain energy. Mo doping was less effective for stabilization of BIMEVOX although the size of Mo is also close to that of V. This suggests that other factors,

such as diffusion rates of dopants, are also important.

5.10. Conclusion

In this chapter, the electrical conductivities, phase transitions, and phase stabilities of $Bi_2(V_{0.95}TM_{0.05})O_{5.5+\Delta}$ (TM = Ti^{4+}, Zr^{4+}, Hf^{4+}, Nb^{5+}, Ta^{5+}, Cr^{3+}, Mo^{6+}, and W^{6+}) have been determined. The findings are summarized as follows:

(1) The conductivities of α_f and β_f, as well as the transition temperatures, varied significantly with not only the dopant but also the thermal history of a sample. This became prominent in Ti- and Nb-doped samples. 5 mol% doping with TM, except for Cr, decreased the transition temperature from β_f to γ_f, although γ_f was not stabilized below ~500 °C.

(2) Despite doping with various transition metals, the dominant charge carriers in γ_f and β_f in air were oxide ions in air. The γ_f of $Bi_2(V_{0.95}TM_{0.05})O_{5.5+\Delta}$ maintained a high oxide-ion conductivity above 3×10^{-1} S cm^{-1} at 700 °C.

(3) 5 mol% doping with TM tended to improve long-term phase stability against thermal decomposition. In particular, Ti doping effectively suppressed thermal decomposition.

References

[50And] G. Andersson and A. Magnéli, Acta Chem. Scand. 4 (1950) 793.
[52Heb] M. Hebb, J. Chem. Phys. 20 (1952) 185.
[53And] G. Andersson, Acta Chem. Scand. 7 (1953) 154.
[56Wag] C. Wagner, Electrochemistry 60 (1956) 4.
[71Ste] N.C. Stephenson, R.S. Roth, Acta Crystallogr. Sect. B 27 (1971) 1037.
[73McG] G.E. McGuire, G.K.K. Schweitzer, and T.A. Carlson, Inorg. Chem. 12 (1973) 2451.
[75Nef] V.I. Nefedov, D. Gati, B.F. Dzhurinskii, N.P. Sergushin, and Y.V. Salyn, Zh. Neorg. Khim. 20 (1975) 2307.

[75Mur] M. Murata, K. Wakino, and S. Ikeda, J. Electron Spectrosc. Relat. Phenom. 6 (1975) 459.

[75Bah] M.K. Bahl, J. Phys. Chem. Solids. 36 (1975) 485.

[76Kat] K. Kato, Acta Crystallogr. Sect. B 32 (1976) 764.

[76Hul] F. Hulliger, *Structural chemistry of layer-type phases*, D. Reidel Publishing Company, Boston (1976).

[76Sha] R.D. Shannon, Acta Crystallogr. A 32 (1976) 767.

[76Sim] D. Simon, C. Perrin, and J. Bardolle, J. Microsc. Spectrosc. Electrn. 1 (1976) 175.

[79Ste] P. Steiner and H. Hochst, Z. Phys. B. 35 (1979) 51.

[80Sar] D.D. Sarma and C.N.R. Rao, J. Electron Spectrosc. Relat. Phenom. 20 (1980) 25.

[80Nyh1] R. Nyholm and N. Martensson, J. Phys. C. 13 (1980) L279.

[80Nyh2] R. Nyholm, A. Berndtsson, and N. Martensson, J. Phys. C. 13 (1980) L1091.

[81Gar] F. Garbassi, J.C.J. Bart, and G. Petrini, J. Electron Spectrosc. Relat. Phenom. 22 (1981) 95.

[81Leb] A. Lebugle, U. Axelsson, R. Nyholm, and N. Martensson, Phys. Scr. 23 (1981) 825.

[82Nef] V.I. Nefedov, M.N. Firsov, and I.S. Shaplygin, J. Electron Spectrosc. Pelat. Phenom. 26 (1982) 62.

[82Cap] F.M. Capece, V. Dicastro, C. Furlani, G. Mattogno, C. Fragale, M. Gargano, and M. Rossi, J. Electron Spectrosc. Relat. Phenom. 27 (1982) 119.

[86Gru] G.R. Gruzalski and D.M. Zehner, Phys. Rev. B 34 (1986) 3841.

[86Enj] R. Enjalbert and J. Galy, Acta Cryst. C42 (1986) 1467.

[88Abr] F. Abraham, M.F. Debreuille-Gresse, G. Mairesse, and G. Nowogrocki, Solid State Ionics 28-30 (1988) 529.

[92Sha] V. Sharma, A.K. Shukla, and J. Gopalakrishnan, Solid State Ionics 58 (1992) 359.

[92Goo] J.B. Goodenough, A. Manthiram, M. Paranthaman, and Y.S. Zhen, Mater. Sci. Eng. B 12 (1992) 357.

[93Lee] C.K. Lee, D.C. Sinclair, and A.R. West, Solid State Ionics 62 (1993) 193.

[93Van] R.N. Vannier, G. mairesse, F. Abraham, and G. Nowogrocki, J. Solid State Chem. 103 (1993) 441.

[94Jou] O. Joubert, A. Jouanneaux, M. Ganne. R.N. Vannier, and G. Mairesse Solid State Ionics 73 (1994) 309.

[95Van] R.N. Vannier, G. mairesse, F. Abraham, and G. Nowogrocki, Solid State Ionics 80

(1995) 11.

[95Yan] J. Yan and M. Greenblatt, Solid State Ionics 81 (1995) 225.

[96Lee1] C.K. Lee, B.H. Bay, and A.R. West, J. Mater. Chem. 6(3) (1996) 331.

[96Laz] S. Lazure, Ch. Vernochet, R.N. Vannier, G. Nowogrocki, and G. Mairesse, Solid State Ionics 90 (1996) 117.

[96Jou] O. Joubert, M. Ganne. R.N. Vannier, and G. Mairesse, Solid State Ionics 93 (1996) 199.

[97Jia] S.P. Jiang, J.G. Love, and S.P.S. Badwal, Key Eng. Mater. 125-126 (1997) 81.

[01Wat] A. Watanabe, J. Solid State Chem. 161 (2001) 410.

[02Kro] F. Krok, I. Abrahams, W. Wrobel, S.C.M. Chan, M. Malys, W. Bogusz, and J.R. Dygas, Solid State Ionics 154-155 (2002) 511.

[03Mai2] G. Mairesse, P. Roussel, R.N. Vannier, M. Anne, and G. Nowogrocki, Solid State Science 5 (2003) 861.

[05Wro] W. Wrobel, I. Abrahams, F. Krok, A. Kozanecka, S.C.M. Chan, M. Malys, W. Bogusz, and J.R. Dygas, Solid State Ionics 176 (2005) 1731.

[05Vor] V.I. Voronkova, V.K. Yanovskii, E.P. Kharitonova, and O.G. Rudnitskaya, Inorg. Mater. 41(7) (2005) 866.

[06Vor] V.I. Voronkova, E.P. Kharitonova, and O.G. Rudnitskaya, Inorg. Mater. 42 (2006) 1255.

[07Tan] Y. Taninouchi, T. Uda, Y. Awakura, A. Ikeda and S.M. Haile, J. Mater. Chem. 17 (2007) 3182.

[09Beg1] S. Beg, N.A.S. Al-Areqi, and A. Al-Alas, J. Alloys Compd. 479 (2009) 107.

[09Beg2] S. Beg, N.A.S. Al-Areqi, A. Al-Alas, and S. Hafeez, Physica B 404 (2009) 2072.

Chapter 6

Doping with Transition Metal (ii):

"Variation in Phase Transition Behavior of $Bi_2(V_{0.95}Ti_{0.05})O_{5.475-\delta}$"

6.1. Introduction

As shown in Chapter 4, the electrical conductivity and phase transition behavior of $Bi_2(V_{0.95}TM_{0.05})O_{5.5+\Delta}$ ($\Delta = d - \delta$, Δ: total deviation of oxygen content, d: oxygen deviation due to aliovalent doping, δ: oxygen loss due to partial reduction) varies with the thermal history of samples even though the samples have the same dopant composition. This characteristic phenomenon is not only scientifically interesting but also practically important as an insight into the design of more favorable BIMEVOX.

In this chapter, the phase transition behavior in $Bi_2(V_{0.95}Ti_{0.05})O_{5.475-\delta}$ (Ti is tetravalent, $d = -0.025$, *i.e.*, oxygen vacancy concentration should increase to preserve electroneutrality) is carefully investigated by means of DSC. This is because $Bi_2(V_{0.95}Ti_{0.05})O_{5.475-\delta}$ exhibited the highest stability against thermal decomposition and a strong effect of thermal history on electrical conductivity. First, DSC is employed at a fixed heating rate of 10 K min^{-1} for samples with various thermal histories and two different physical forms. Second, DSC is carried out at various heating rates for the specified samples.

6.2. Sample preparation

$Bi_2(V_{0.95}Ti_{0.05})O_{5.475-\delta}$, denoted as Ti5, was prepared in powder and bulk forms. The Ti5 powder sample is abbreviated as Ti5/P and the Ti5 bulk sample as Ti5/B, as listed in Table

6.1(a). Figure 6.1(a) shows a FE-SEM image of the powder sample: it was synthesized by a conventional solid-state reaction at 800 °C, as described in Chapter 4. The powder particle size of ranged from 0.2 to 5 μm. In this study, the presence of slight amount of $BiVO_4$ in Ti5 is ignored. Figure 6.1(b) shows an optical microscope image of the surface of the bulk sample with entire image with an entire image of sample. The bulk sample was a pellet fragment sintered at 800 °C. Its relative density of bulk sample was 95%. The grains were well grown and were as large as 20 μm in size.

Table 6.1(b) gives the abbreviations for the applied thermal treatments before analysis. The powder and bulk samples were cooled at various rates from 800 °C, where γ_f of Ti5 is stable. The partial pressure of oxygen, pO_2, during the cooling was 0.025, 0.21, or 1 atm. Some quenched powders were annealed at 495 °C for 12 hr in air and then cooled at 10 K min^{-1}. The various samples can be expressed by combining abbreviations from Table 6.1. For example, the powder sample that was cooled in air from 800 °C at 0.5 K min^{-1} is denoted as Ti5/P/C05.

Table 6.1 Abbreviations for (a) sample forms and (b) thermal treatments of $Bi_2(V_{0.95}Ti_{0.05})O_{5.475-\delta}$ (δ: oxygen loss induced by the partial reduction of transition metals). The surrounding gas during cooling was stagnant air (CQ, C1, and C05), Ar-0.21%O_2 at 50 ml min^{-1} (C10 and the following thermal treatment of CQA), pure O_2 at 50 ml min^{-1} (C10H), or Ar-0.025%O_2 at 200 ml min^{-1} (C10L). Below 300 °C, the true cooling rate in the experiments aiming for 10 K min^{-1} was slightly slower than 10 K min^{-1} because of the limitations of the electric furnace (DTG-60H, Shimadzu). Samples can be named by combining abbreviations. For example, the powder sample cooled in air from 800 °C at 10 K min^{-1} is termed Ti5/P/C10.

(a)	Abbreviation	Composition	Sample form
	Ti5/P	$Bi_2(V_{0.95}Ti_{0.05})O_{5.475-\delta}$	Powder
	Ti5/B	$Bi_2(V_{0.95}Ti_{0.05})O_{5.475-\delta}$	Bulk

(b)	Abbreviation	Thermal treatment		
		Cooling rate from 800 °C	pO_2 (atm)	Following thermal treatment
	CQ	Quench to room temperature	0.21	–
	C10	10 K min^{-1}	0.21	–
	C1	1 K min^{-1}	0.21	–
	C05	0.5 K min^{-1}	0.21	–
	C10H	10 K min^{-1}	1	–
	C10L	10 K min^{-1}	0.025	–
	CQA	Quench to room temperature	0.21	Annealed at 495 °C for 12 h and then cooled at 10 K min^{-1}

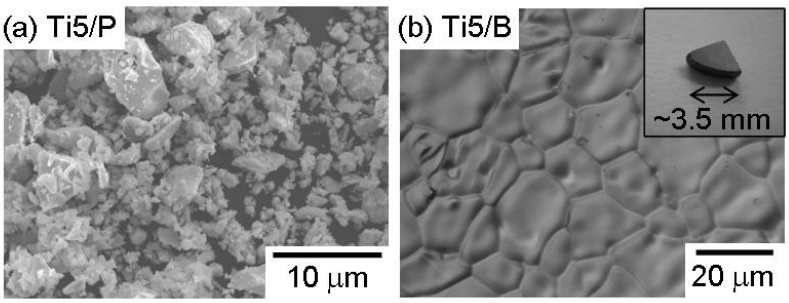

Figure 6.1 (a) FE-SEM image of powder sample, Ti5/P. (b) Optical microscope image of surface of bulk sample, Ti5/B. An image of the entire bulk sample is shown in the inset.

6.3. Structural differences due to cooling rate determined by XRD analysis

Figure 6.2(a) shows the XRD patterns of Ti5/P cooled at various rates. The calculated pattern of monoclinic α_f-$Bi_2VO_{5.5}$ at Cu-Kα_1 radiation [03Mai2] is also given as a reference. The diffraction indices are marked assuming the orthorhombic subcell of a_m, b_m, and c_m. Figure 6.2(b) summarizes the lattice constants of the subcell.

Ideal α_f-$Bi_2VO_{5.5}$ exhibits superlattice diffractions, such as the 1/3 1 3 peak at ~24.2°, and has monoclinic symmetry, as verified by the splitting of the 2 2 0 peak at ~46°. Meanwhile, orthorhombic α_f was stabilized in Ti5/P/CQ, C10, C1, and C05, as shown in Figure 6.2(a). However, there was little change in the lattice constants with the cooling rate, as shown in Figure 6.2(b).

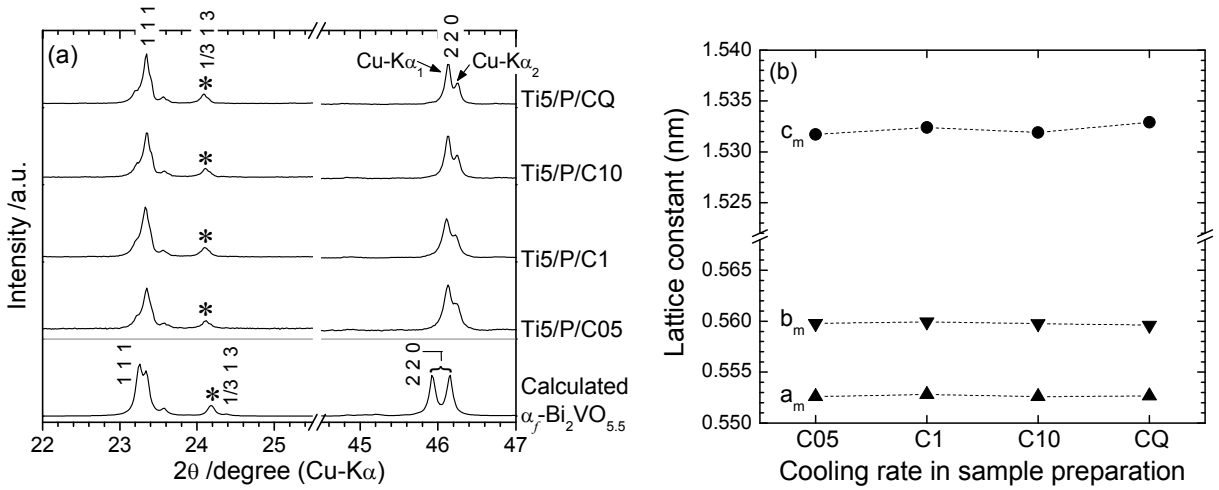

Figure 6.2 (a) XRD patterns of Ti5/P cooled at various rates. The pattern of monoclinic α_f of $Bi_2VO_{5.5}$ calculated at Cu-Kα_1 radiation is also shown as a reference [03Mai2]. Plane indices are marked assuming the orthorhombic subcell of a_m, b_m, and c_m. Asterisks (∗) indicate typical superlattice diffractions of α_f. (b) Lattice constants of a_m, b_m, and c_m.

6.4. Variations in oxygen content determined by TGA

In TGA, powder samples of ~320 mg were kept at 150 °C for 2 hr for drying and then heated at 5 K min^{-1} to 800 °C in air. To calculate the oxygen content per compositional formula, we assume that weight changes could be attributed only to the uptake and loss of oxygen, which is caused by the partial reduction or oxidation of the transition metals. The slowly cooled powder of Ti5/P/C05 were considered to be fully oxidized ($\delta = 0$), *i.e.*, the composition of as-prepared Ti5/P/C05 was $Bi_2(V_{0.95}Ti_{0.05})O_{5.475}$. To evaluate the oxygen contents of the quenched powder Ti5/P/CQ, we assumed that Ti5/P/CQ after re-heating to 800 °C has the same oxygen content with Ti5/P/C05 at 800 °C.

Figure 6.3 shows the oxygen content of Ti5/P/CQ and Ti5/P/C05 as a function of temperature. Partial reduction proceeded in the fully-oxidized sample of Ti5/P/C05 above ~540 °C. The onset temperature of the partial reduction is immediately above the temperature of the β_f/γ_f transition determined by DSC. The oxygen content decreased to 5.469 ± 0.002 (δ = 0.006 ± 0.002) at 800 °C. Meanwhile, the quenched powder Ti5/P/CQ exhibited the oxygen uptake from 300 to 500 °C, and oxygen loss above ~540 °C. The oxygen content of Ti5/P/CQ at 200 °C was evaluated as 5.470 ± 0.002 (δ = 0.005 ± 0.002). Assuming that the vanadium was partially reduced from V^{+5} to V^{+4}, the composition of as-prepared Ti5/P/CQ can be described as $Bi_2(V^{+5}_{0.94}V^{+4}_{0.01}Ti^{+4}_{0.05})O_{5.470}$. The difference in oxygen content between Ti5/P/C05 and Ti5/P/CQ gradually decreased above 300 °C.

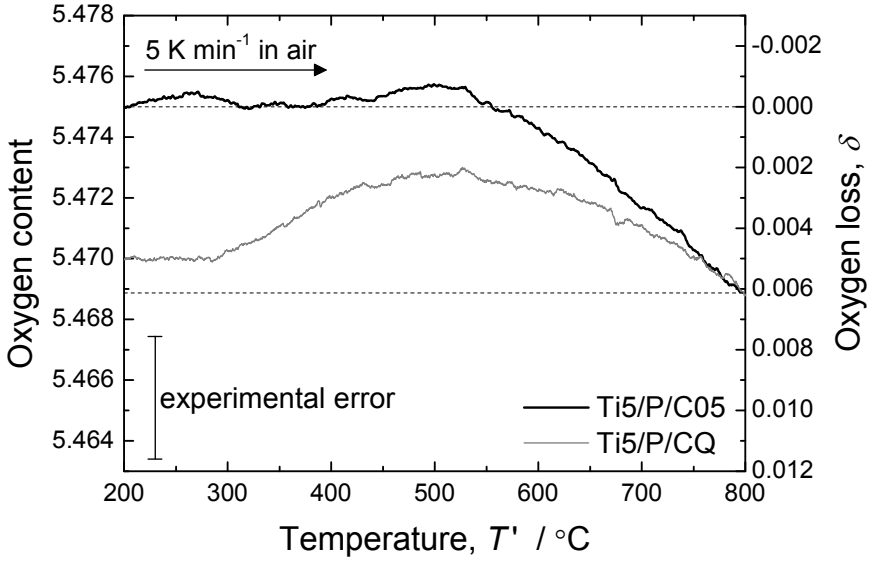

Figure 6.3 Temperature dependence of oxygen content of Ti5/P/C05 and Ti5/P/CQ. TGA was performed in air at a heating rate of 5 K min^{-1}. The oxygen content of as-prepared Ti5/P/C05 was regarded to be the fully oxidized value of 5.475. We assumed that at 800 °C the oxygen content of Ti5/P/CQ coincided with that of Ti5/P/C05.

6.5. Variations in phase transition behavior at a fixed DSC heating rate induced by the sample preparation

6.5.1. Effects of cooling rate in sample preparation

DSC was carried out in stagnant air at the same heating rate of 10 K min^{-1}. The onset temperature of each endothermic peak was evaluated by the intersection point method with an error of approximately ±2 °C. Figure 6.4 shows the DSC profiles of the powder samples cooled in air at various rates. In the DSC profiles of Ti5/P/CQ, two endothermic peaks appeared at around 400 and 530 °C. When Ti5/P/CQ was heated to 450 °C at 10 K min^{-1}, β_f was obtained, as indicated by the HT-XRD pattern (a) in Figure 6.5. Thus, the endothermic peak at around 400 °C corresponds to the α_f/β_f transition, and that at around 530 °C corresponds to the β_f/γ_f transition. We call the endothermic peak for the α_f/β_f transition $P_{\alpha/\beta}$

and that for the β_f/γ_f transition $P_{\beta/\gamma}$. In addition, the onset temperatures of the α_f/β_f and β_f/γ_f transitions are termed $T_{\alpha/\beta}$ and $T_{\beta/\gamma}$, respectively.

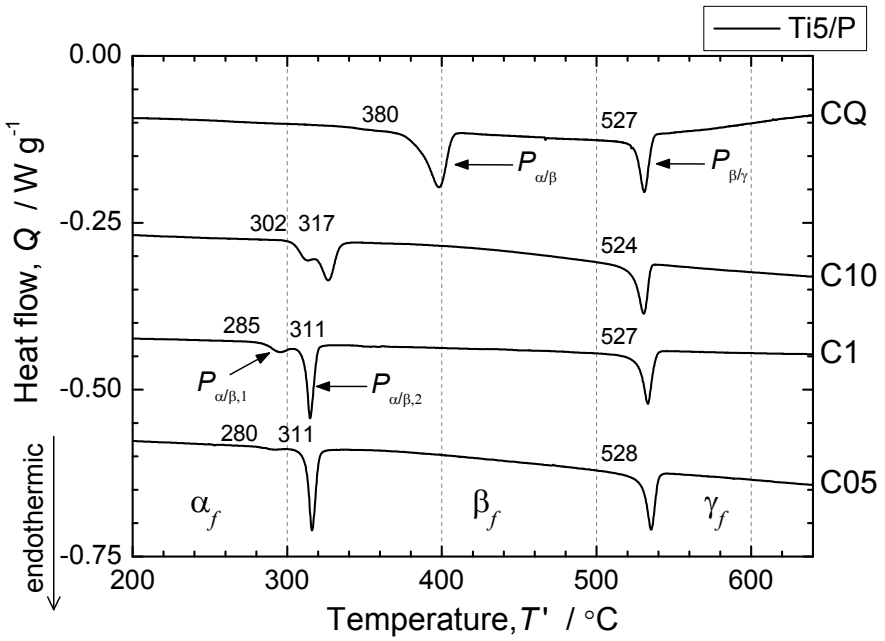

Figure 6.4 DSC profiles of Ti5/P cooled in air at various rates. All profiles were collected in air at a heating rate of 10 K min^{-1}. Numerical values are onset temperatures of endothermic peaks. $P_{\alpha/\beta}$ and $P_{\beta/\gamma}$ refer to endothermic peaks corresponding to α_f/β_f and β_f/γ_f transitions, respectively. Slowly cooled samples exhibited the splitting of $P_{\alpha/\beta}$ into $P_{\alpha/\beta,1}$ and $P_{\alpha/\beta,2}$

The DSC profiles of Ti5/P varied markedly with the cooling rate. $P_{\alpha/\beta}$ shifted from 400 to 320 °C with a decrease in the cooling rate, although $P_{\beta/\gamma}$ remained unchanged. In the DSC profiles of Ti5/P/C10, C1, and C05, $P_{\alpha/\beta}$ split into two peaks, *i.e.*, a minor peak (termed $P_{\alpha/\beta,1}$) was observed at a lower temperature than that of the major peak (termed $P_{\alpha/\beta,2}$). $P_{\alpha/\beta,1}$ decreased with the cooling rate. The onset temperatures of $P_{\alpha/\beta,1}$ and $P_{\alpha/\beta,2}$ are termed $T_{\alpha/\beta,1}$ and $T_{\alpha/\beta,2}$, respectively. HT-XRD patterns of Ti5/P/C05 heated to 300 and 350 °C at 10 K min^{-1} are shown as patterns (b) and (c) in Figure 6.5. At 300 °C, which is

between $T_{\alpha/\beta,1}$ and $T_{\alpha/\beta,2}$, the main phase is α_f, but a small amount of β_f also existed. Meanwhile, only β_f was obtained at 350 °C, which is above $T_{\alpha/\beta,2}$. These results indicate that two different types of α_f existed in as-prepared Ti5/P/C05 and they exhibited transitions at $T_{\alpha/\beta,1}$ and $T_{\alpha/\beta,2}$, respectively.

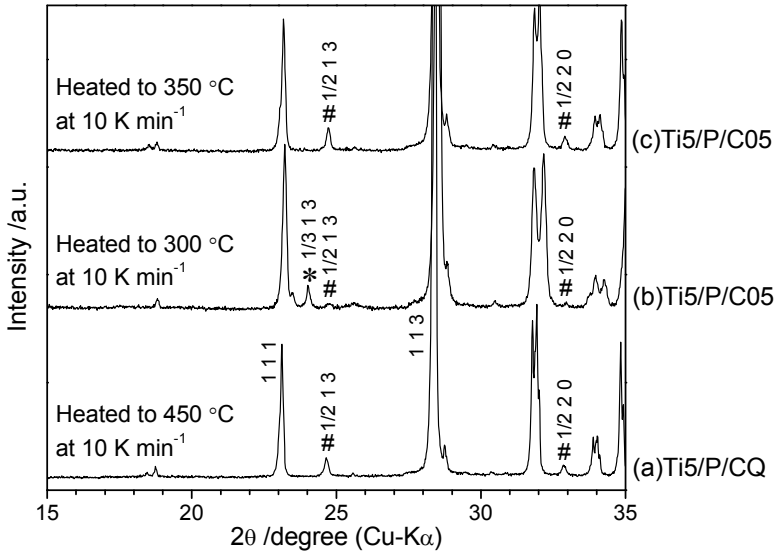

Figure 6.5 HT-XRD patterns of (a) Ti5/P/CQ heated to 450 °C at 10 K min^{-1}, (b) Ti5/P/C05 heated to 300 °C at 10 K min^{-1}, and (c) Ti5/P/C05 heated to 350 °C at 10 K min^{-1}. Diffraction patterns were collected for 10 min immediately after the samples were heated to the target temperatures. Plane indices are marked assuming a mean orthorhombic subcell. Asterisks (∗) and hashes (#) indicate typical superlattice diffractions of α_f and β_f, respectively.

6.5.2. Effects of sample form

Figure 6.6 shows the DSC profiles of both bulk and powder samples cooled at various rates; black and gray profiles correspond to powder and bulk sample, respectively. Phase transition behavior of Ti5/B was markedly affected by the cooling rate. In the DSC profile of Ti5/B/CQ, $P_{\alpha/\beta}$ appeared at around 500 °C and the temperature region of β_f was narrow. $P_{\alpha/\beta}$ for Ti5/B/C1 and C05 was split into $P_{\alpha/\beta,1}$ and $P_{\alpha/\beta,2}$ because slow cooling caused a formation of slight amount of the polymorphs of α_f. For Ti5/B, $P_{\alpha/\beta}$ shifted to a lower temperature

with a decrease in the cooling rate. This trend agrees with that observed for Ti5/P. However, $T_{\beta/\gamma}$ for Ti5/B increased with a decrease in the cooling rate. Comparing the DSC profile of Ti5/B to that of Ti5/P at a given cooling rate indicated that $P_{\alpha/\beta}$ for Ti5/B appeared at a higher temperature than that for Ti5/P. $T_{\beta/\gamma}$ for Ti5/B was lower than that for Ti5/P at a given cooling rate. The difference between the transition behaviors of Ti5/B and Ti5/P became small in slowly cooled samples.

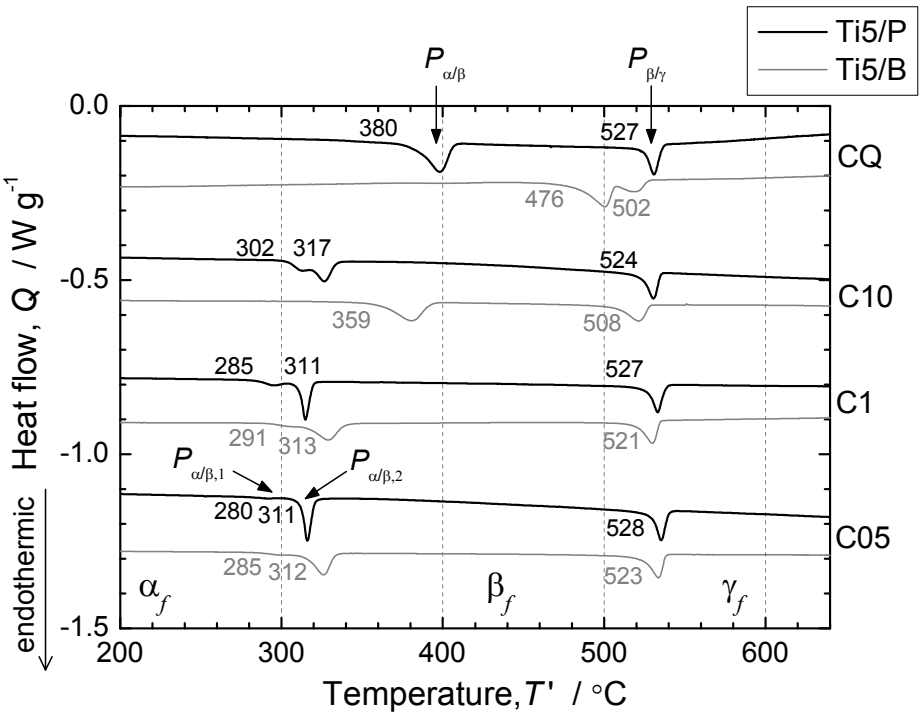

Figure 6.6 DSC profiles of Ti5/P and Ti5/B cooled in air at various rates. All profiles were collected in air at a heating rate of 10 K min^{-1}. Numerical values are onset temperatures of endothermic peaks. $P_{\alpha/\beta}$ and $P_{\beta/\gamma}$ refer to endothermic peaks corresponding to α_f/β_f and β_f/γ_f transitions, respectively. Slowly cooled samples exhibited the splitting of $P_{\alpha/\beta}$ into $P_{\alpha/\beta,1}$ and $P_{\alpha/\beta,2}$

6.5.3. Effects of pO_2 in sample preparation

Figure 6.7 shows the DSC profiles of Ti5/P/C10H and C10L with that of Ti5/P/C10. Ti5/P/C10H, which was cooled at pO_2 = 1 atm, exhibited the same DSC profile as Ti5/P/C10. However, Ti5/P/C10L, which was cooled at pO_2 = 0.025 atm, exhibited $P_{\alpha/\beta}$ at a somewhat higher temperature.

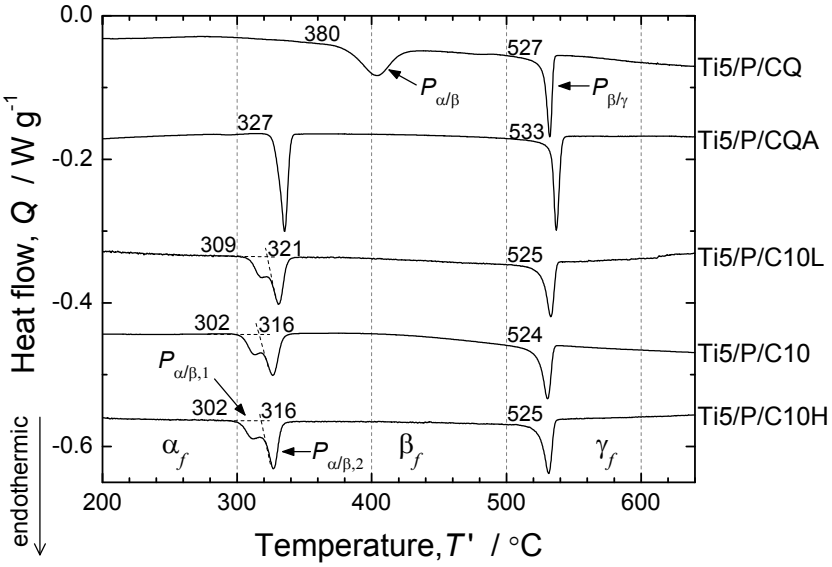

Figure 6.7 DSC profiles of Ti5/P/C10H, C10, C10L, CQA, and CQ. All profiles were collected in air at a heating rate of 10 K min^{-1}. Ti5/P/C10H, C10, and C10L were cooled at 10 K min^{-1} under various pO_2 conditions, *i.e.*, pO_2 = 1 atm for C10H, pO_2 = 0.21 atm for C10, and pO_2 = 0.025 atm for C10L. Ti5/P/CQA was powder sample annealed at 495 °C for 12 hr after quenching.

6.5.4. Effects of annealing at 495 °C

The DSC profiles of Ti5/P/CQA and Ti5/P/CQ are also shown in Figure 6.7. Ti5/P/CQA, which was annealed at 495 °C after quenching and then cooled at 10 K min^{-1}, did not exhibit the peak split of $P_{\alpha/\beta}$. $T_{\alpha/\beta}$ for Ti5/P/CQA was much lower than that for Ti5/P/CQ, but it was higher than $T_{\alpha/\beta,1}$ and $T_{\alpha/\beta,2}$ for Ti5/P/C10. In addition, $T_{\beta/\gamma}$ for Ti5/P/CQA was somewhat higher than that for Ti5/P/CQ and C10.

6.5.5. Discussion about the variation in phase transition temperatures induced by the sample preparation

The difference in the sample preparation drastically changed the phase transition behavior of Ti5. It was quite difficult to completely understand its mechanism. However, the variation of transition temperatures can be qualitatively explained in terms of the oxygen content, which corresponds to oxygen vacancy concentration, in each sample.

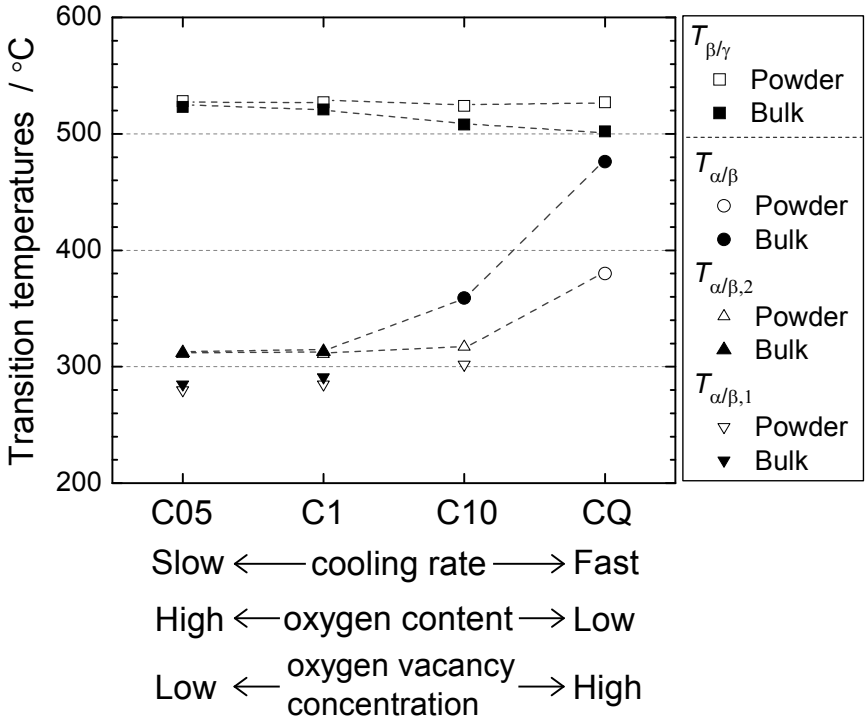

Figure 6.8 Variation of transition temperatures evaluated by DSC at the same heating rate of 10 K min^{-1}. $T_{\alpha/\beta}$, $T_{\alpha/\beta,1}$, $T_{\alpha/\beta,2}$, and $T_{\beta/\gamma}$ determined in Figures 6.4 and 6.6 are plotted. Samples cooled at faster rates should have less oxygen content (more oxygen vacancy concentration) before analysis. When cooled at the same rate, the bulk sample should have less oxygen content (more oxygen vacancy concentration) than the powder sample.

Figure 6.8 summarizes the transition temperatures evaluated by the DSC profiles at a heating rate of 10 K min^{-1} in Figures 6.4 and 6.6. As verified by TGA in Figure 6.3, the quenched samples has the less oxygen content (more oxygen vacancy concentration). This is

because Ti5 exhibited partial reduction at 800 °C and the oxygen supply during the cooling process is not enough. That is, samples cooled at faster rates should have less oxygen content than the thermally equilibrated value. Even if cooled at the same rate, the bulk sample should have less oxygen content than the powder sample due to the low specific surface area of bulk sample and the required longer-range diffusion of oxygen. According to Figure 6.8, Ti5 with less oxygen content (more oxygen vacancy concentration) exhibits the α_f/β_f transition at a higher temperature (we call this empirical knowledge (i)). In addition, Ti5 with less oxygen content (more oxygen vacancy concentration) exhibits the β_f/γ_f transition at a lower temperature (we call this empirical knowledge (ii)), although the latter trend is seen only in the bulk sample. The empirical knowledge (ii) agrees with the empirical knowledge obtained in Chapters 3 and 4: the increase in oxygen vacancy concentration tends to stabilize γ_f against β_f and α_f. The TGA profile of Ti5/P/CQ in Figure 6.3 indicates that the oxidation gradually proceeds above 300 °C in the partially reduced sample. The oxygen supply in bulk sample on the DSC heating is expected to be much lower. As a results, in the bulk sample, the oxygen content is maintained to be lower than the equilibrium value even at a higher-temperature of β_f/γ_f transition, which leads to the variation in $T_{\beta/\gamma}$.

The oxygen supply during the cooling process should be suppressed under low pO_2 conditions. Ti5/P/C10, C10H, and C10L were cooled at the same rate of 10 K min^{-1}. However, Ti5/P/C10L, which was cooled at pO_2 = 0.025 atm, should have somewhat less oxygen content than Ti5/P/C10 and C10H. As shown in Figure 6.7, $T_{\alpha/\beta,1}$ and $T_{\alpha/\beta,2}$ for Ti/P/C10L were higher than those for Ti5/P/C10 and C10H, which confirms empirical knowledge (i). The oxygen content of Ti5/P/CQA should be close to the fully oxidized value of 5.475 by annealing at 495 °C for 12 hr. That is, Ti5/P/CQA has more oxygen content than Ti5/P/CQ

and C10. As shown in Figure 6.7, $T_{\alpha/\beta}$ for Ti5/P/CQA was lower than that for Ti5/P/CQ, which agrees with empirical knowledge (i). However, $T_{\alpha/\beta}$ for Ti5/P/CQA was clearly higher than $T_{\alpha/\beta,2}$ for Ti/P/C10. This exceptional case suggests that a small difference in atomic arrangement also associates with a variation in the phase transition behavior in Ti5.

As described in Chapter 2, the network structure of oxygen polyhedra in the V-O layer differs among α_f, β_f, and γ_f. Furthermore, vanadium takes multiple crystallographic positions in α_f and β_f, but its crystallographic position is unique in γ_f, according to the crystalline structure of $Bi_2VO_{5.5}$ reported by Mairesse *et al.* [03Mai1,03Mai2]. It is, therefore, possible that Ti and oxygen vacancies induced by aliovalent doping take preferential sites in thermally equilibrated α_f and β_f. All the Ti5 samples, with the exception of Ti5/P/CQA, were cooled from γ_f to α_f at finite rates. Thus, a small difference in the atomic arrangement of the V-O layer (*e.g.* different occupancy of preferential sites) should exist depending on cooling rate. This structural difference should also affect the variation in phase transition behavior, particularly transition between α_f and β_f, although it was quite difficult to identify it by the conventional XRD analysis in this study. Only Ti5/P/CQA was cooled from β_f to α_f after annealing. Thus, Ti5/P/CQA is expected to have another characteristic atomic arrangement, which probably explains its exceptional variation in phase transition behavior.

6.6. Variations in phase transitions induced by the DSC heating rate

6.6.1. Effects of heating rate in DSC

Figure 6.9(a) shows the DSC profiles of Ti5/P/CQ collected at heating rates of 2, 5, 10, and 40 K min^{-1}. At the slower heating rates of 5 and 2 K min^{-1}, $P_{\alpha/\beta}$ apparently split into two broad peaks, *i.e.*, a large endothermic peak appeared at around 500 °C in addition to the

endothermic peak at around 400 °C. Endothermic reaction occurred successively between two endothermic peaks at the heating rate of 5 K min^{-1}. For the split $P_{\alpha/\beta}$, we term the endothermic peaks at lower and higher temperatures $P_{\alpha/\beta,L}$ and $P_{\alpha/\beta,H}$, respectively. The onset temperature of $P_{\alpha/\beta,L}$ is termed $T_{\alpha/\beta,L}$, and that of $P_{\alpha/\beta,H}$ is termed $T_{\alpha/\beta,H}$. The HT-XRD pattern of Ti5/P/CQ heated to 450 °C at 2 K min^{-1} is shown as pattern (a) in Figure 6.10. When Ti5/P/CQ was heated at 2 K min^{-1}, a mixture of α_f and β_f was obtained at 450 °C which is an intermediate temperature between $T_{\alpha/\beta,L}$ and $T_{\alpha/\beta,H}$.

Figure 6.9(b) shows the DSC profiles of Ti5/P/C05 at the various heating rates. $P_{\alpha/\beta,1}$ and $P_{\alpha/\beta,2}$ appeared in the DSC profiles at the higher heating rates of 5, 10, and 40 K min^{-1}, because as-prepared Ti5/P/C05 contained slightly amount of polymorphic α_f. $T_{\alpha/\beta,1}$ and $T_{\alpha/\beta,2}$ did not change with heating rate for 5, 10, and 40 K min^{-1}. Meanwhile, the DSC profile at the slower heating rate of 2 K min^{-1} was very different. The trace of $P_{\alpha/\beta,1}$ remained at around 290 °C. However, the major endothermic peak $P_{\alpha/\beta,2}$ apparently split into two broad peaks $P_{\alpha/\beta,L}$ and $P_{\alpha/\beta,H}$, which appeared from 318 to 403 °C

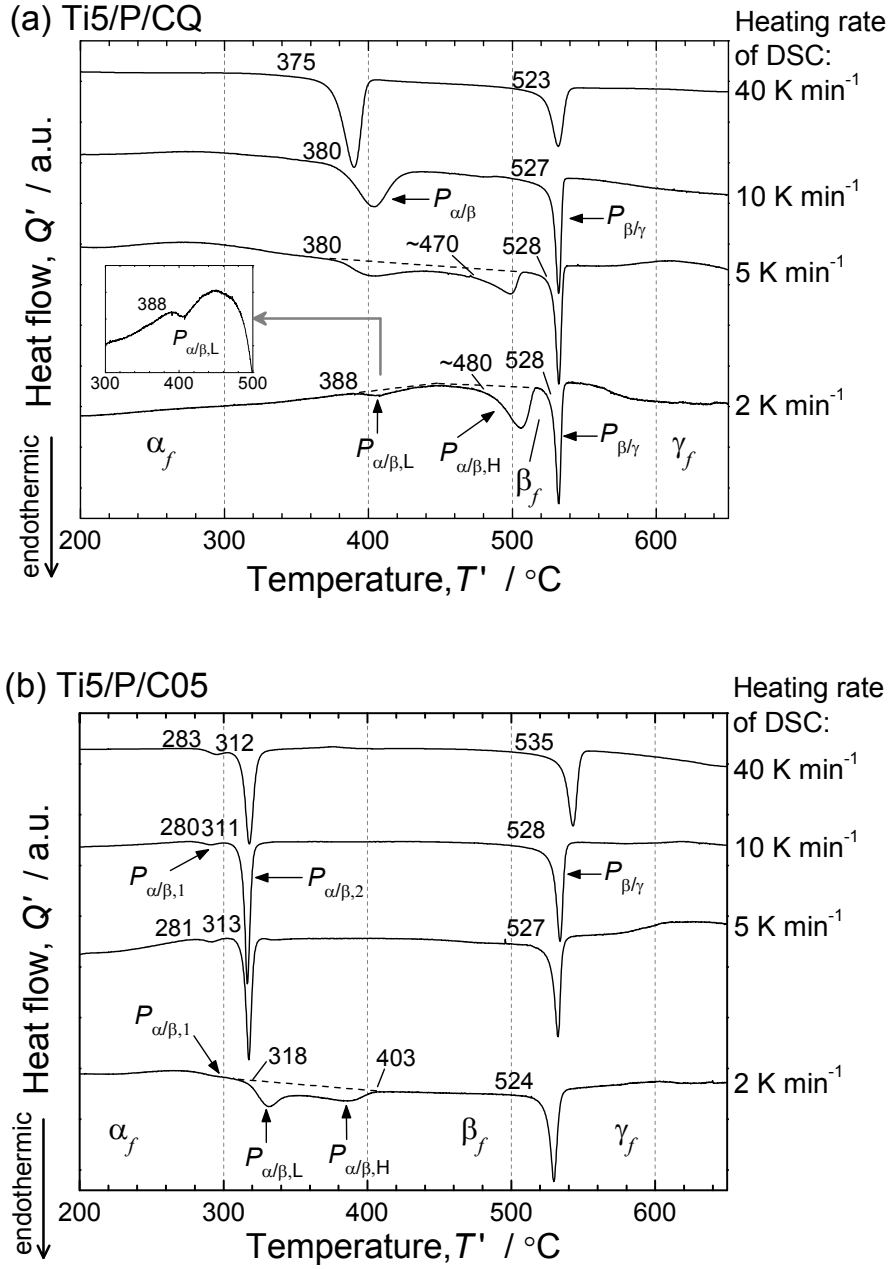

Figure 6.9 DSC profiles of (a) Ti5/P/CQ and (b) Ti5/P/C05 collected in air at heating rates of 2, 5, 10, and 40 K min^{-1}. The represented heat flow is the value divided by the heating rate. At slow heating rates, $T_{\alpha/\beta}$ for Ti5/P/CQ and $T_{\alpha/\beta,2}$ for Ti5/P/C05 exhibited splitting into $P_{\alpha/\beta,L}$ and $P_{\alpha/\beta,H}$.

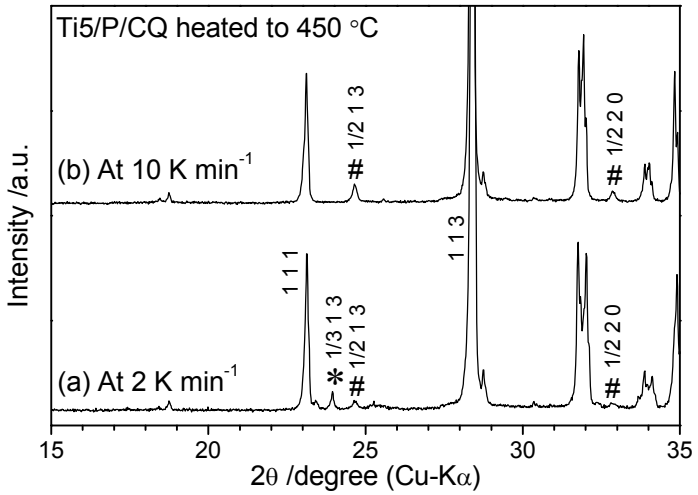

Figure 6.10 HT-XRD patterns of Ti5/P/CQ heated to 450 °C (a) at 2 K min^{-1} and (b) at 10 K min^{-1}. Diffraction patterns were collected for 10 min immediately after the samples were heated to 450 °C. Plane indices are marked assuming a mean orthorhombic subcell. Asterisks (∗) and hashes (#) indicate typical superlattice diffractions of α_f and β_f, respectively. α_f and β_f co-existed at a heating rate of 2 K min^{-1}. Meanwhile, only β_f was obtained at a heating rate of 10 K min^{-1}.

6.6.2. Discussion about the effect of DSC heating rate on phase transitions

Slow DSC heating rates caused a peak split and continuous endothermic reaction of $P_{\alpha/\beta}$ for Ti5/P/CQ and C05, as shown in Figure 6.9. The difference in oxygen content cannot simply account for this behavior because Ti5/P/C05 did not exhibit the uptake and loss of oxygen below 540 °C as seen in Figure 6.3.

HT-XRD patterns (a) and (d) in Figure 6.9 verify that, after Ti5/P/CQ was heated to 450 °C, only β_f was obtained at a heating rate of 10 K min^{-1}, but a mixture of α_f and β_f was obtained at a heating rate of 2 K min^{-1}. In the DSC profile of Ti5/P/CQ shown in Figure 6.9(a), 450 °C was above the temperature range of $P_{\alpha/\beta}$ at a heating rate of 10 K min^{-1}, but it was between the temperature range of $P_{\alpha/\beta,L}$ and $P_{\alpha/\beta,H}$ at a heating rate of 2 K min^{-1}. This

suggests that, during slow heating, the rearrangement of Ti and oxygen vacancies proceed to take more favorable structure at a given temperature, and various different types of α_f appear in samples just below $T_{\alpha/\beta,L}$. Because different types of α_f transform to β_f at different temperatures, a mixture of α_f and β_f is observed in the temperature region of $P_{\alpha/\beta,L}$ and $P_{\alpha/\beta,H}$.

As far as as-prepared Ti5/P/CQ concerned, Ti and oxygen vacancies should be randomly distributed in the V-O layer of α_f at room temperature. On heating at faster rates, such as 40 K min^{-1}, the rearrangement of Ti and oxygen vacancies did not progress, and homogeneous α_f transformed to β_f at $P_{\alpha/\beta}$. Meanwhile, on heating at slower rates, such as 2 and 5 K min^{-1}, α_f became inhomogeneous below about 370 °C corresponding to the sufficient diffusion of Ti and oxygen vacancies. Roughly speaking, two different types of α_f appeared in slowly heated Ti5/P/CQ, and transformed to β_f at $P_{\alpha/\beta,L}$ and $P_{\alpha/\beta,H}$, respectively.

This discussion further indicates that Ti and oxygen vacancies have the preferential crystallographic sites in the V-O layer of α_f and β_f. For Ti5, wide variations in transition behavior, particularly transition between α_f and β_f, are strongly related with the small differences in not only oxygen content (oxygen vacancy concentration) but also the positions of dopant and oxygen vacancies. To comprehensively understand the effect of each dopant on polymorphs, careful researches on the local structures around dopant and oxygen vacancies in the V-O layer will be required.

6.7. Conclusion

The phase transition behavior of $Bi_2(V_{0.95}Ti_{0.05})O_{5.475-\delta}$ from α_f to β_f and from β_f to γ_f varies markedly with sample preparation as well as heating rate. The findings are summarized

as follows:

(1) The variation in transition temperatures at the same heating rate of 10 K min^{-1} is qualitatively explained in terms of oxygen content (oxygen vacancy concentration), which depends on thermal history and physical form of sample. Following empirical knowledge was obtained: $Bi_2(V_{0.95}Ti_{0.05})O_{5.475-\delta}$ with less oxygen content (more oxygen vacancy concentration) exhibits transition from α_f to β_f at a higher temperature and the transition from β_f to γ_f at a lower temperature. In particular, the transition temperature from α_f to β_f shows large variation; powder sample cooled at 0.5 K min^{-1} from 800 °C, whose oxygen content was 5.475, transformed to β_f at 311 °C. Meanwhile, powder sample quenched from 800 °C, whose oxygen content was 5.470 ± 0.002 at room temperature, transformed to β_f at 380 °C.

(2) Two types of phase transition behavior from α_f to β_f are confirmed depending on the heating rate. α_f directly transformed to β_f at fast rates of 10 and 40 K min^{-1}. Meanwhile, at a slower heating rate of 2 K min^{-1}, β_f continuously precipitated and the co-existence of α_f and β_f was confirmed. This phenomenon is qualitatively explained in terms of the positions of dopant and oxygen vacancies in the V-O layer. That is, during slow heating, the rearrangement of Ti and oxygen vacancies progressed to take more favorable structure, and different types of α_f appeared in samples.

References

[03Mai1] G. Mairesse, P. Roussel, R.N. Vannier, M. Anne, C. Pirovano, and G. Nowogrocki, Solid State Science 5 (2003) 851.

[03Mai2] G. Mairesse, P. Roussel, R.N. Vannier, M. Anne, and G. Nowogrocki, Solid State Science 5 (2003) 861.

Chapter 7

Doping of Transition Metal (iii):

"Oxide-Ion Conductivity and Phase Stability of $Bi_2(V_{1-x}TM_x)O_{5.5+\Delta}$ (TM = Ti, Zr, and Hf, $0 \le x \le 0.15$)"

7.1. Introduction

The objective of this chapter is to investigate the electrical conductivities, phase transitions, and long-term phase stability of $Bi_2(V_{1-x}TM_x)O_{5.5+\Delta}$ (TM = Ti, Zr, and Hf, $\Delta \equiv d - \delta$, Δ: total deviation of oxygen content, d: oxygen deviation due to aliovalent doping, δ: oxygen loss due to partial reduction) with increasing the dopant concentration from 5 mol% (x = 0.05) to 10 mol% (x = 0.10) and 15 mol% (x = 0.15). As described in Chapter 5, Ti was most effective dopant to suppress thermal decomposition among various transition metals. All dopants selected in this chapter exist in tetravalent form, although they have different ionic radius, affinity with oxygen atom, and preferable oxygen coordination. Substitution of Ti, Zr, and Hf on pentavalent V sites induces the oxygen vacancies (decreases oxygen content per chemical formula) to preserve electroneutrality, and oxygen vacancies increase with an increase in dopant concentration.

Sharma *et al.* [92Sha], Goodenough [92Goo], and Yan and Greenbatt [95Yan] reported that γ-phase was stabilized in $Bi_2(V_{1-x}Ti_x)O_{5.5+\Delta}$ for x = 0.10 at room temperature. However, Lazure *et al.* [96Laz] reported that γ-phase was stabilized in $Bi_2(V_{1-x}Ti_x)O_{5.5+\Delta}$ for $0.125 \le x \le 0.25$. The phases obtained in this study are in good agreement with those by Lazure *et al.* [96Laz].

The compositional dependence of polymorphs in $Bi_2(V_{1-x}Zr_x)O_{5.5+\Delta}$ was reported by three groups. Goodenough [92Goo] and Yan and Greenbatt [95Yan] reported that γ-phase was stabilized in $Bi_2(V_{1-x}Zr_x)O_{5.5+\Delta}$ for $0.10 \leq x \leq 0.15$ at room temperature, but the group of Dygas [02Kro,05Wro] reported that β-phase was stabilized at $x = 0.10$ and 0.16. Our results basically agree with the findings reported by the Dygas group.

Beg *et al.* synthesized $Bi_2(V_{1-x}Hf_x)O_{5.5+\Delta}$ ($x \leq 0.20$) by a solid-state reaction at 800 °C and reported their polymorphs and electrical conductivities [09Beg1,09Beg2]. However, their data have large discrepancies with our results. For example, they reported that γ-phase of $Bi_2(V_{0.85}Hf_{0.15})O_{5.425-\delta}$ was stabilized at room temperature. However, we found that $Bi_2(V_{0.85}Hf_{0.15})O_{5.425-\delta}$ contained β_f and a small amount of secondary phase when synthesized at 800 °C. Furthermore, conductivities reported by Beg *et al.* were about one order of magnitude lower than our results. This is probably because Beg *et al.* used Ag electrodes for conductivity measurements despite the fact that Ag reacts with $Bi_2VO_{5.5-\delta}$, as described in Chapter 3.

7.2. Sample preparation

Table 7.1 shows the abbreviations and compositions of prepared samples. Polycrystalline powders were synthesized by a solid-state reaction in air using binary oxides shown in Chapter 5. Mixtures of appropriate amounts of constituents were heated at 650 °C for 12 hr. The ground powders were formed into pellets at 0.2 ton cm^{-2} and then heated at 800 °C (Ti-doped $Bi_2VO_{5.5-\delta}$) or 850 °C (Zr- and Hf-doped $Bi_2VO_{5.5-\delta}$) for 12 hr. This thermal treatment was repeated several times with intermediate grinding.

The synthesized powders were uniaxially compressed at 3 ton cm^{-2} for 15 min and then

sintered at 800–850 °C for 12–24 hr in air. For conductivity measurements, Au electrodes were applied on mirror-polished pellets using gold paint.

Table 7.1 Abbreviations, compositions, and synthesizing temperatures of powder samples, and sintering conditions of pellet samples.

Abbreviation	Composition	Source
Bi0	$Bi_2VO_{5.5-\delta}$	Chapter 3
Ti5	$Bi_2(V_{0.95}Ti_{0.05})O_{5.475-\delta}$	Chapter 5
Ti10	$Bi_2(V_{0.9}Ti_{0.1})O_{5.45-\delta}$	This study
Ti15	$Bi_2(V_{0.85}Ti_{0.15})O_{5.425-\delta}$	This study
Zr5	$Bi_2(V_{0.95}Zr_{0.05})O_{5.475-\delta}$	Chapter 5
Zr10	$Bi_2(V_{0.9}Zr_{0.1})O_{5.45-\delta}$	This study
Zr15	$Bi_2(V_{0.85}Zr_{0.15})O_{5.425-\delta}$	This study
Hf5	$Bi_2(V_{0.95}Hf_{0.05})O_{5.475-\delta}$	Chapter 5
Hf10	$Bi_2(V_{0.9}Hf_{0.1})O_{5.45-\delta}$	This study
Hf15	$Bi_2(V_{0.85}Hf_{0.15})O_{5.425-\delta}$	This study

7.3. Phases at room temperature identified by XRD analysis

Figure 7.1(a) shows the XRD patterns of powders quenched from 800 °C or 850 °C (only in Zr15 and Hf15) in logarithmic intensity scale, and Figure 7.1(b) shows the lattice constants of a_m, b_m, and c_m. The phases obtained are listed in Table 7.2. Orthorhombic α_f was obtained in Ti5 and Ti10. Meanwhile, tetragonal γ_f was stabilized down to room temperature in Ti15. Ti doping effectively changes c_m among three lattice constants, *i.e.*, c_m increased with an increase in Ti concentration. On the other hand, β_f was stabilized in Zr10, Zr15, Hf10, and Hf15, accompanied by a marked increase in c_m. In Zr15 and Hf15, the subcell became almost tetragonal, and superlattice diffraction peaks of β_f, such as 1/2 1 3 peak at around 25°, were broad and small. XRD analysis indicates that Ti5, Ti10, and Hf5 contained small amounts of

$BiVO_4$ as a secondary phase. However, we neglect the presence of $BiVO_4$ in quenched samples.

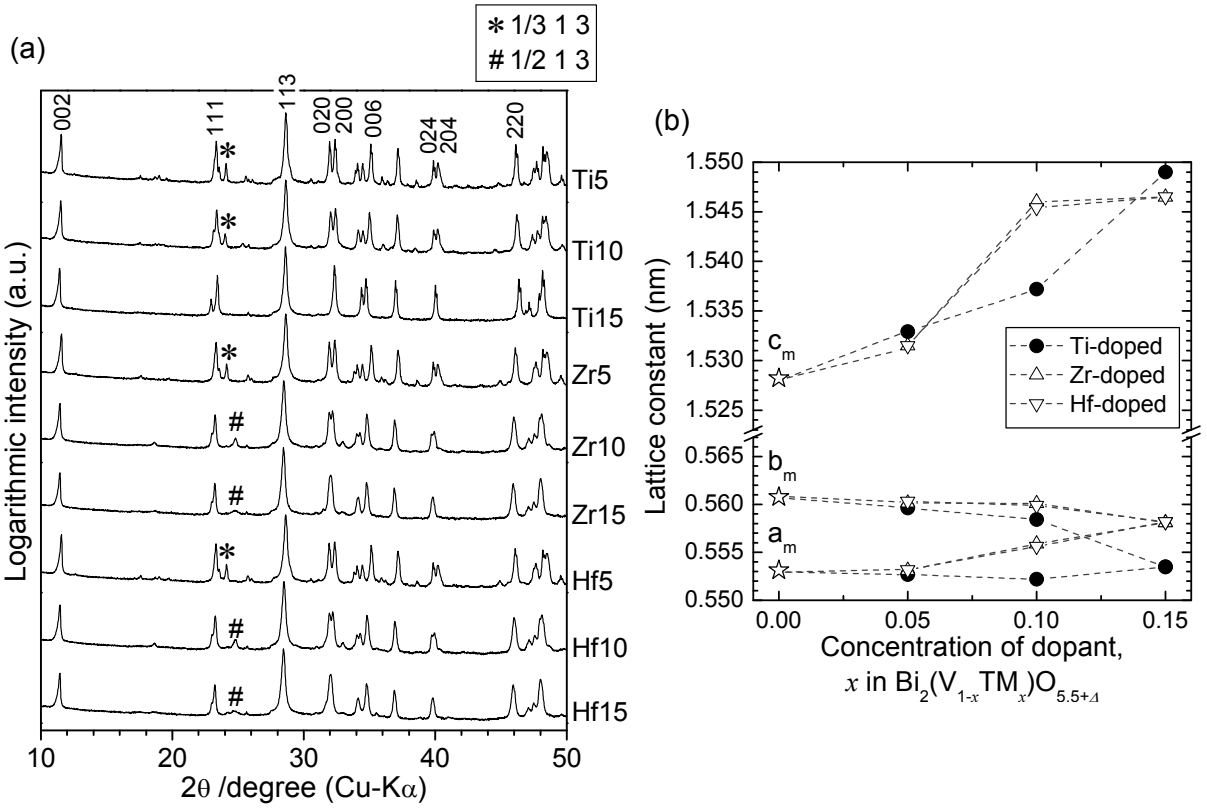

Figure 7.1 (a) XRD patterns of powders quenched from 800 °C or 850 °C (only in Zr15 and Hf15) in logarithmic intensity scale. The plane indices are marked assuming the orthorhombic subcell of a_m, b_m, and c_m. Asterisks (∗) and hashes (#) indicate typical superlattice diffractions of α_f and β_f, respectively. (b) Lattice constants of a_m, b_m, and c_m.

Table 7.2 Phases obtained at room temperature, sintering conditions, and relative densities of pellets. Before XRD analysis, powder samples, except for Zr15 and Hf15, were quenched and slowly cooled at 1 K min^{-1} from 800 °C. Only Zr15 and Hf15 were cooled from 850 °C.

	Chemical formula	XRD analysis*		Pellet	
		Quenched	Cooled at 1 K min^{-1}	Sintering condition	Relative density (%)
Bi0	$Bi_2VO_{5.5-\delta}$	α_f(orth)	α_f(mono)	800 °C, 24 hr	94
Ti5	$Bi_2(V_{0.95}Ti_{0.05})O_{5.475-\delta}$	α_f(orth)	α_f(orth)	800 °C, 24 hr	95
Ti10	$Bi_2(V_{0.9}Ti_{0.1})O_{5.45-\delta}$	α_f(orth)	α_f(orth)	800 °C, 12 hr	97
Ti15	$Bi_2(V_{0.85}Ti_{0.15})O_{5.425-\delta}$	γ_f(tetra)	γ_f(tetra)	800 °C, 12 hr	97
Zr5	$Bi_2(V_{0.95}Zr_{0.05})O_{5.475-\delta}$	α_f(orth)	α_f(orth)	850 °C, 24 hr	94
Zr10	$Bi_2(V_{0.9}Zr_{0.1})O_{5.45-\delta}$	β_f(orth)	β_f(orth) +sp**	850 °C, 24 hr	96
Zr15	$Bi_2(V_{0.85}Zr_{0.15})O_{5.425-\delta}$	β_f(tetra)	β_f(orth) + sp**	850 °C, 24 hr	95
Hf5	$Bi_2(V_{0.95}Hf_{0.05})O_{5.475-\delta}$	α_f(orth)	α_f(orth)	850 °C, 24 hr	95
Hf10	$Bi_2(V_{0.9}Hf_{0.1})O_{5.45-\delta}$	β_f(orth)	β_f(orth) + sp**	850 °C, 24 hr	95
Hf15	$Bi_2(V_{0.85}Hf_{0.15})O_{5.425-\delta}$	β_f(tetra)	β_f(orth) + sp**	850 °C, 24 hr	94

* (symmetry of subcell) "mono", "orth", and "tetra" refer to monoclinic, orthorhombic, and tetragonal, respectively.

** "sp" refers to the secondary phase due to decomposition of the BIMEVOX phase. The secondary phase was estimated to be $Bi_{3.5}V_{1.2}O_{8.25}$ phase.

Figure 7.2 shows the XRD patterns of powders slowly cooled at 1 K min^{-1} from 800 °C or 850 °C (only in Zr15 and Hf15) in logarithmic intensity scale, and obtained phases are also listed in Table 7.2. Despite the cooling, orthorhombic α_f was obtained in Ti5, Ti10, Zr5, and Hf5, and tetragonal γ_f was obtained in Ti15. On the other hands, slowly cooled Zr10, Zr15, Hf10, and Hf15 contained secondary phase owing to the partial decomposition of the BIMEVOX phase. Appeared secondary phase was estimated to be $Bi_{3.5}V_{1.2}O_{8.25}$ phase. This indicates the poor phase stabilities of Zr- and Hf-doped $Bi_2VO_{5.5-\delta}$ at intermediate temperatures, which is further investigated in Section 7.5.

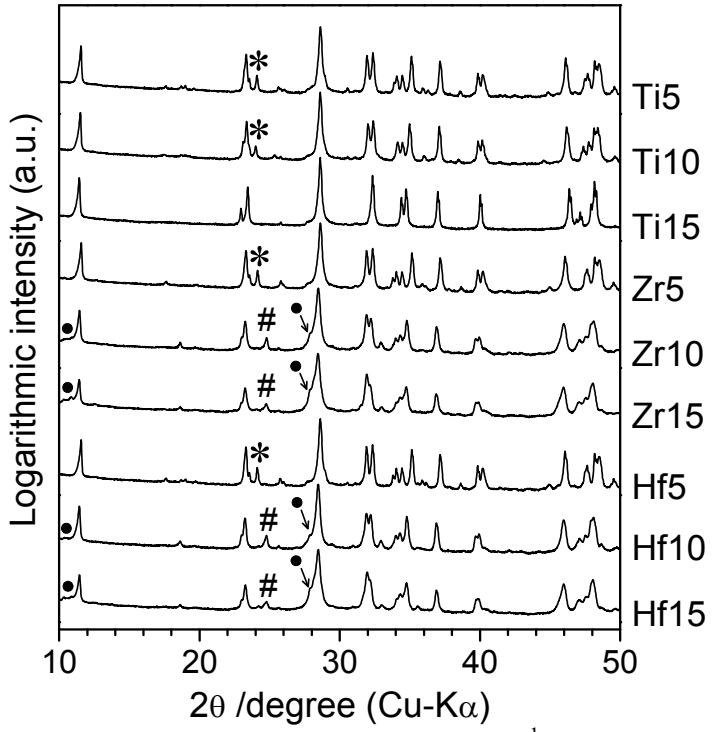

Figure 7.2 XRD patterns of powders cooled at 1 K min^{-1} from 800 °C or 850 °C (only in Zr15 and Hf15) in logarithmic intensity scale. Asterisks (∗) and hashes (#) indicate typical superlattice diffractions of α_f and β_f, respectively. Closed circles (•) indicate the typical peaks of the secondary phase estimated to be $Bi_{3.5}V_{1.2}O_{8.25}$, which was caused by thermal decomposition of the BIMEVOX phase.

7.4. Temperature dependence of electrical conductivities determined by AC impedance spectroscopy

Figure 7.3 shows the Arrhenius plots of electrical conductivities on heating in air. Conductivities of Cu10, YSZ [94Her], and LSGMC [99Ish] are also shown as references. As shown in Figure 7.3(a), Ti10 exhibited two conductivity jumps at 260 and 445 °C that correspond to α_f/β_f transition and β_f/γ_f transition, respectively. Meanwhile, Ti15 showed no conductivity jump, although the slope of conductivity, *i.e.*, E_a changed at around 450 °C (E_a from 200 to 400 °C is 0.71 eV, and E_a from 500 to 730 °C is 0.46 eV as listed in Table 7.3. This slope change corresponds to the slight structural modification in γ_f from lowly

conductive to highly conductive state. As shown in Figures 7.3(b) and (c), Zr10, Zr15, Hf10, and Hf15 exhibited slow conductivity jumps from 425 to 500 °C, from 415 to 470 °C, from 450 to 500 °C, and from 400 to 460 °C, respectively. These jumps correspond to β_f/γ_f transitions. Additionally, Zr10, Zr15, and Hf10 exhibited small changes in conductivity slope at around 700 °C, which are probably explained by the partial decomposition and/or recomposition of the BIMEVOX phase.

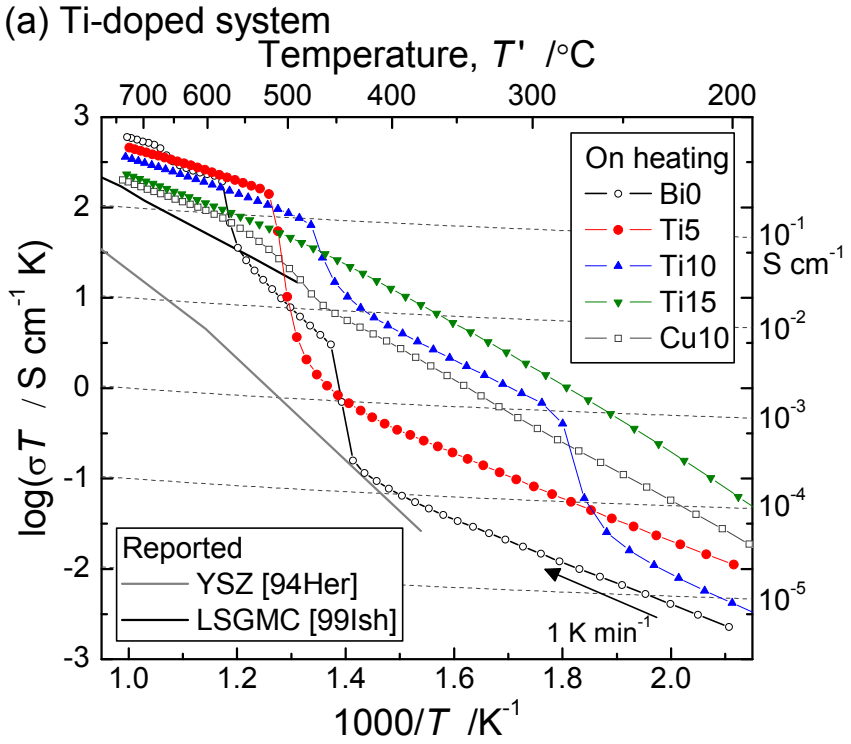

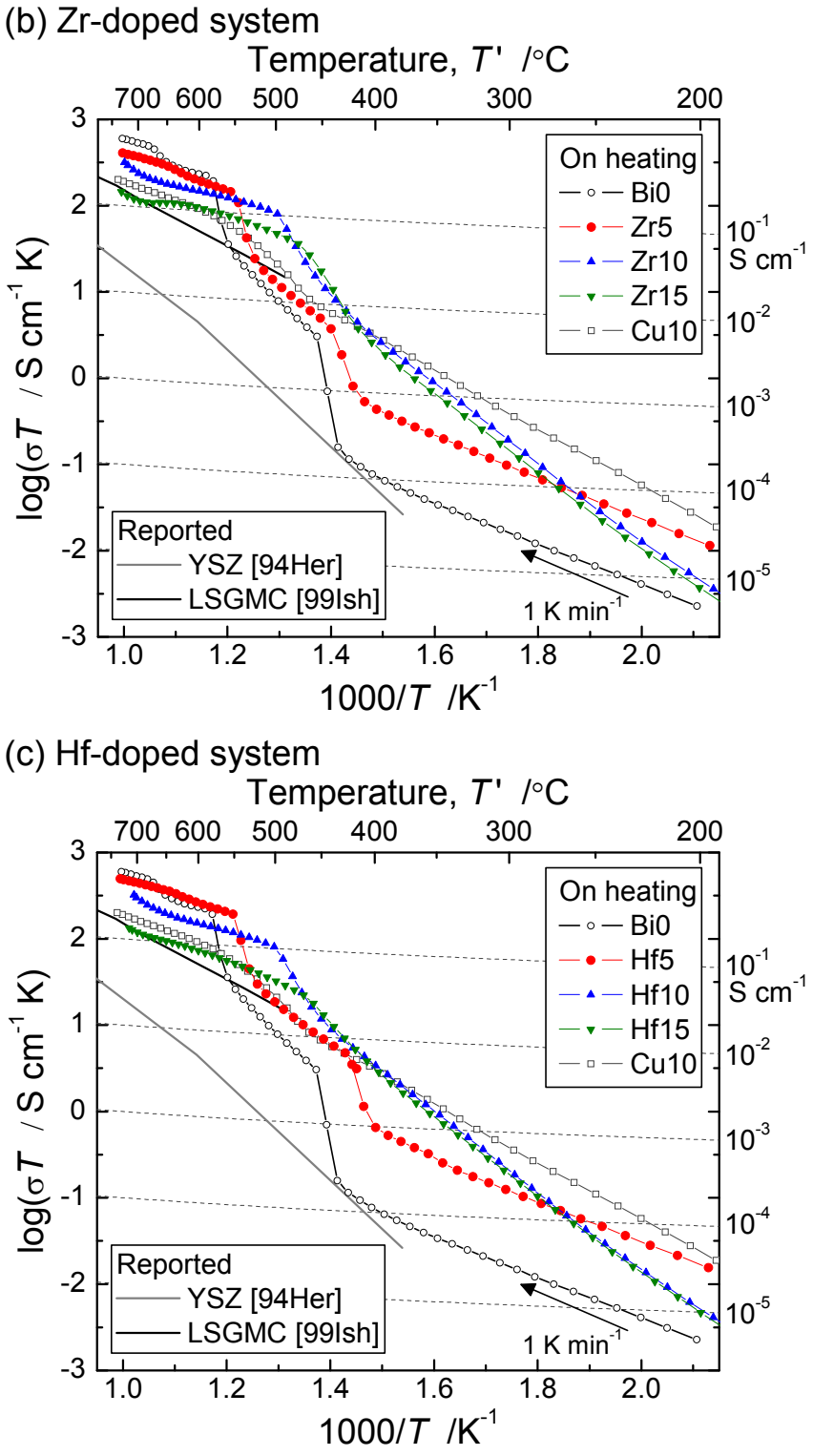

Figure 7.3 Arrhenius plots of electrical conductivities in air at a heating rate of 1 K min^{-1}. (a) Ti-doped system, (b) Zr-doped system, and (c) Hf-doped system. Just before measurements, pellets with Au electrodes were quenched from 800 °C or 850 °C (only in Zr15 and Hf15). Conductivities of Cu10, YSZ [94Her], and LSGMC [99Ish] are also shown as references.

Table 7.3 Activation energies (E_a), and pre-exponential terms (A) of the electrical conductivities in γ_f. We employed $\sigma T = A\exp[-(E_a/kT)]$, where k is the Boltzmann constant.

	E_a (eV)	A (S cm^{-1} K)	Temperature range (°C)
Bi0	0.43 (±0.03)	7.1 (±0.4) ×10^4	580–650
	0.38 (±0.03)	5.0 (±0.2) ×10^4	670–730
Ti5	0.38 (±0.01)	4.0 (±0.3) ×10^4	525–730
Ti10	0.41 (±0.01)	4.3 (±0.3) ×10^4	525–730
Ti15	0.71 (±0.01)	2.7 (±0.4) ×10^6	200–400
	0.46 (±0.01)	4.6 (±0.2) ×10^4	500–730

Conductivities at 500 and 700 °C are re-plotted in Figure 7.4. When an ideal Aurivillius structure for γ_f is assumed, the oxygen vacancy concentration, which should increase with dopant concentration, can be expressed by v in $Bi_2(V_{1-x}TM_x)O_{6-v}\square_v$. At 700 °C, all samples belong to γ_f, and the conductivities decrease with an increase in dopant concentration. For Ti-doped samples, E_a at around 700 °C increased with an increase in dopant concentration as shown in Table 7.3. This fact suggests the dopants associate with oxygen vacancies. When we compare the conductivity at the given dopant concentration, the conductivity of Zr15 and Hf15 was significantly lower than that of Ti15 at 700 °C. This is probably explained by the partial decomposition of BIMEVOX phase in Zr15 and Hf15.

At 500 °C, 10 and 15 mol% doped samples exhibited high conductivities of 0.6×10^{-1} and 1×10^{-1} S cm^{-1}, respectively, because γ_f was stabilized. The conductivities of 10 and 15 mol% doped samples do not depend on dopants at 500 °C. In Figure 7.5, we plot the temperatures at the end of conductivity jumps of α_f/β_f and β_f/γ_f transitions. For Ti5, the end temperature of the conductivity jump of the α_f/β_f transition is not shown because the β_f region was not clearly

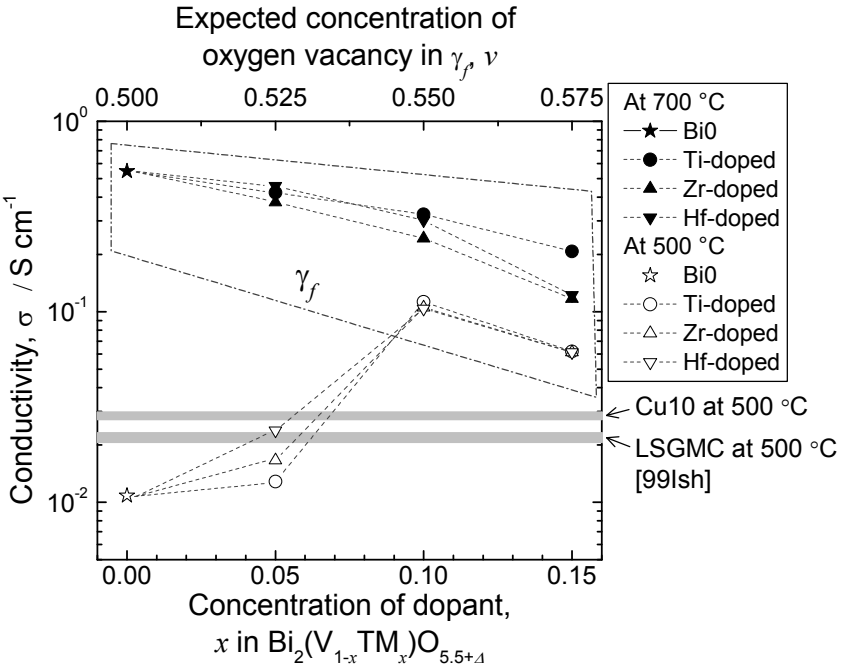

Figure 7.4 Oxide-ion conductivities at 500 and 700 °C. Concentration of oxygen vacancies in γ_f, *i.e.*, v in $Bi_2(V_{1-x}TM_x)O_{6-v}\square_v$, was evaluated assuming ideal Aurivillius structure (V-O layer consists of VO_6 octahedron including TM and oxygen vacancies) and by preserving electroneutrality via oxygen content. Gray lines indicate the conductivities of Cu10 and LSGMC [99Ish] at 500 °C.

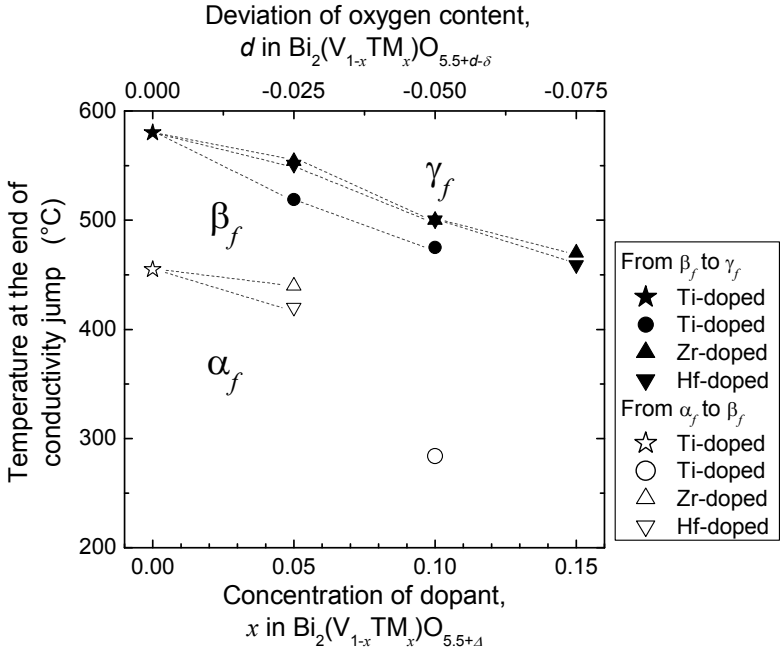

Figure 7.5 Temperatures at the end of conductivity jumps of α_f/β_f and β_f/γ_f transitions.

observed on heating. At a given dopant concentration, Ti doping stabilized γ_f phase at the lowest temperatures among three tetravalent dopants. Zr- and Hf-doped samples exhibit almost the same polymorphs at the same dopant concentration and oxygen content, but the Ti-doped sample shows different polymorphs.

To confirm the oxide-ion conduction in prepared samples, the conductivities were measured with varying oxygen partial pressures (pO_2). Figure 7.6 shows the electrical conductivities of Ti10, Ti15, Zr10, and Zr15 at pO_2 of 1, 0.21, and 8×10^{-4} atm, which were evaluated on cooling from 720 °C. Ti10, Ti15, Zr10, and Zr15 belong to γ_f at both 500 and 700 °C. The electrical conductivities of γ_f were almost unchanged in the pO_2 range from 1 to 8×10^{-4} atm. This indicates that the γ_f phases of Ti-, Zr, and Hf-doped $Bi_2VO_{5.5-\delta}$ are primary oxide-ion conductors, as described in Chapter 1.

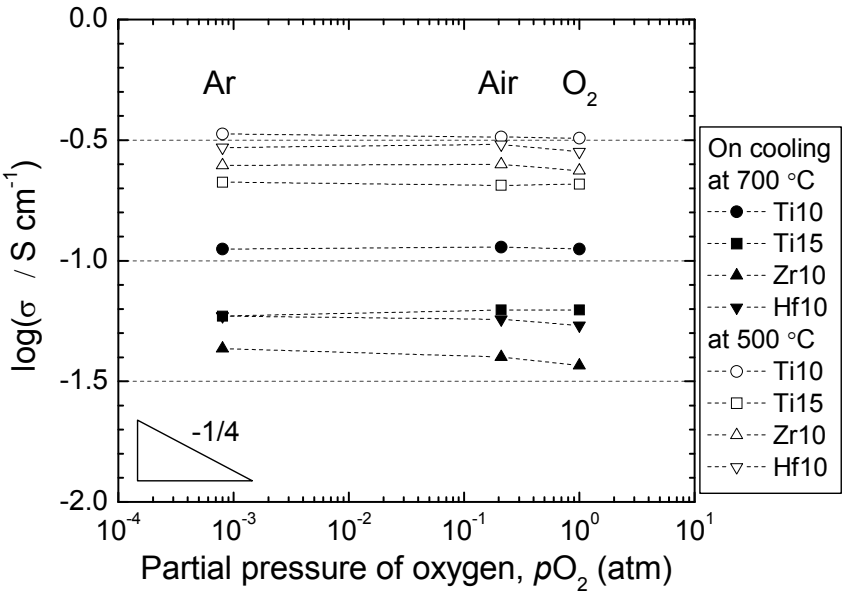

Figure 7.6 Electrical conductivities of Ti10, Ti15, Zr10, and Zr15 at various pO_2. Data were collected on cooling at 1 K min^{-1} from 720 °C. Electron conductivity is expected to be proportional to $pO_2^{-1/4}$, as described in Chapter 1.

7.5. Long-term phase stabilities and phase diagrams determined by XRD analysis, AC impedance spectroscopy, and DTA

Figure 7.7 shows the XRD patterns of powders after annealing at 500 and 600 °C for 200 hr in air. Diffraction intensities are plotted in logarithmic scale. At an annealing temperature of 500 °C, all Ti-doped samples were stable, as shown in Figure 7.7(a). In contrast, thermal decomposition proceeded in Zr- and Hf-doped samples, although BIMEVOX remained as the main phase. At an annealing temperature of 600 °C, only Ti10 and Ti15 were stable and other samples partially decomposed, as shown in Figure 7.7(b). Ti5 annealed at 600 °C, Zr5 annealed at 500 and 600 °C, and Hf5 annealed at 500 and 600 °C contained $BiVO_4$ and $Bi_{3.5}V_{1.2}O_{8.25}$ phases besides BIMEVOX phase. Meanwhile, XRD patterns of annealed Zr10,

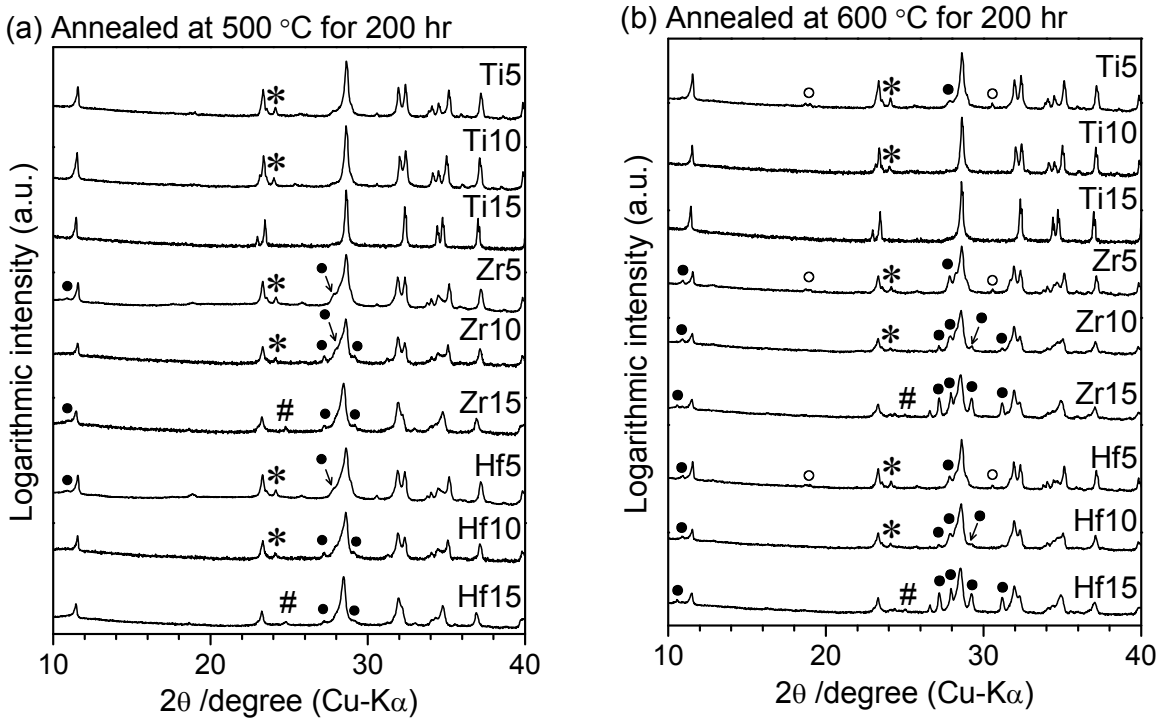

Figure 7.7 XRD patterns after annealing for 200 hr in air at (a) 500 °C and (b) 600 °C. Diffraction intensities are shown in logarithmic scale. Open circles (○) and closed circles (●) indicate diffraction peaks of decomposition products of $BiVO_4$ and $Bi_{3.5}V_{1.2}O_{8.25}$ phases, respectively. Asterisks (∗) and hashes (#) indicate typical superlattice diffractions of α_f and β_f, respectively.

Zr15, Hf10, and Hf15 indicate that BIMEVOX and $Bi_{3.5}V_{1.2}O_{8.25}$ phases were present without $BiVO_4$ phase. This suggests that phase equilibrium changes with Zr and Hf content in samples. It is also notable that the order phase of α_f appeared in annealed Zr10 and Hf10, although only β_f phase was exhibited before annealing. Figures 7.8(a) and (b) show the conductivities of Ti10, Zr10, and Hf10 after annealing for 200 hr at 500 and 600 °C, respectively. The data of Bi0 obtained in Chapter 3 are also shown as references. Ti10 kept high oxide-ion conductivity for 200 hr at 500 and 600 °C. This fact further confirms the high phase stability of Ti-doped $Bi_2VO_{5.5}$. Meanwhile, the conductivities of Zr10 and Hf10 decreased by prolonged annealing for 200 hr, because the partial decomposition and ordering of BIMEVOX phase proceeded.

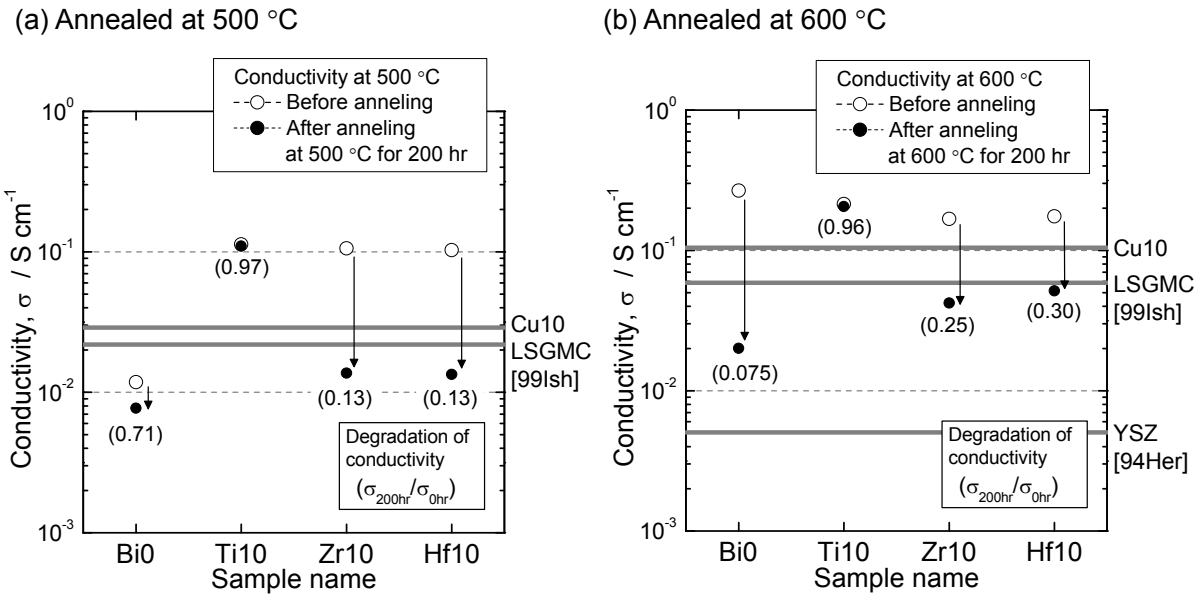

Figure 7.8 Time dependence of electrical conductivities at (a) 500 and (b) 600 °C. Conductivities of Bi0, Ti10, Zr10, and Hf10 obtained before and after annealing in air for 200 hr are plotted. "$\sigma_{200hr}/\sigma_{0hr}$" means the ratio of conductivity after annealing to that before annealing. Gray lines indicate the conductivities of Cu10, YSZ [94Her], and LSGMC [99Ish] without prolonged annealing.

The results of XRD analysis of powders annealed for 200 hr are summarized as pseudo-binary phase diagrams in Figure 7.9(a) for Ti-doped system, Figure 7.10(a) for Zr-doped system, and Figure 7.11(a) for Hf-doped system. The upper limit of the stable region of the BIMEVOX phase was evaluated by DTA on heating until the liquid phase appeared, as shown in Figure 7.9(b) for Ti-doped system, Figure 7.10(b) for Zr-doped system, and Figure 7.11(b) for Hf-doped system. In DTA profiles, large endothermic reaction started at T_1 and ended T_2, corresponding to the formation of liquid phase. Thus, the estimated phases in regions (i) and (ii) of Figures 7.9–11 are as follows: (i) solid + liquid between T_1 and T_2, (ii) liquid above T_3. We show the thermodynamically stable region for γ_f phase as shaded areas in pseudo-binary phase diagrams, considering the changes in electrical conductivity with temperature. The thermodynamically stable region of γ_f is effectively expanded by Ti doping, but is reduced by Zr and Hf doping.

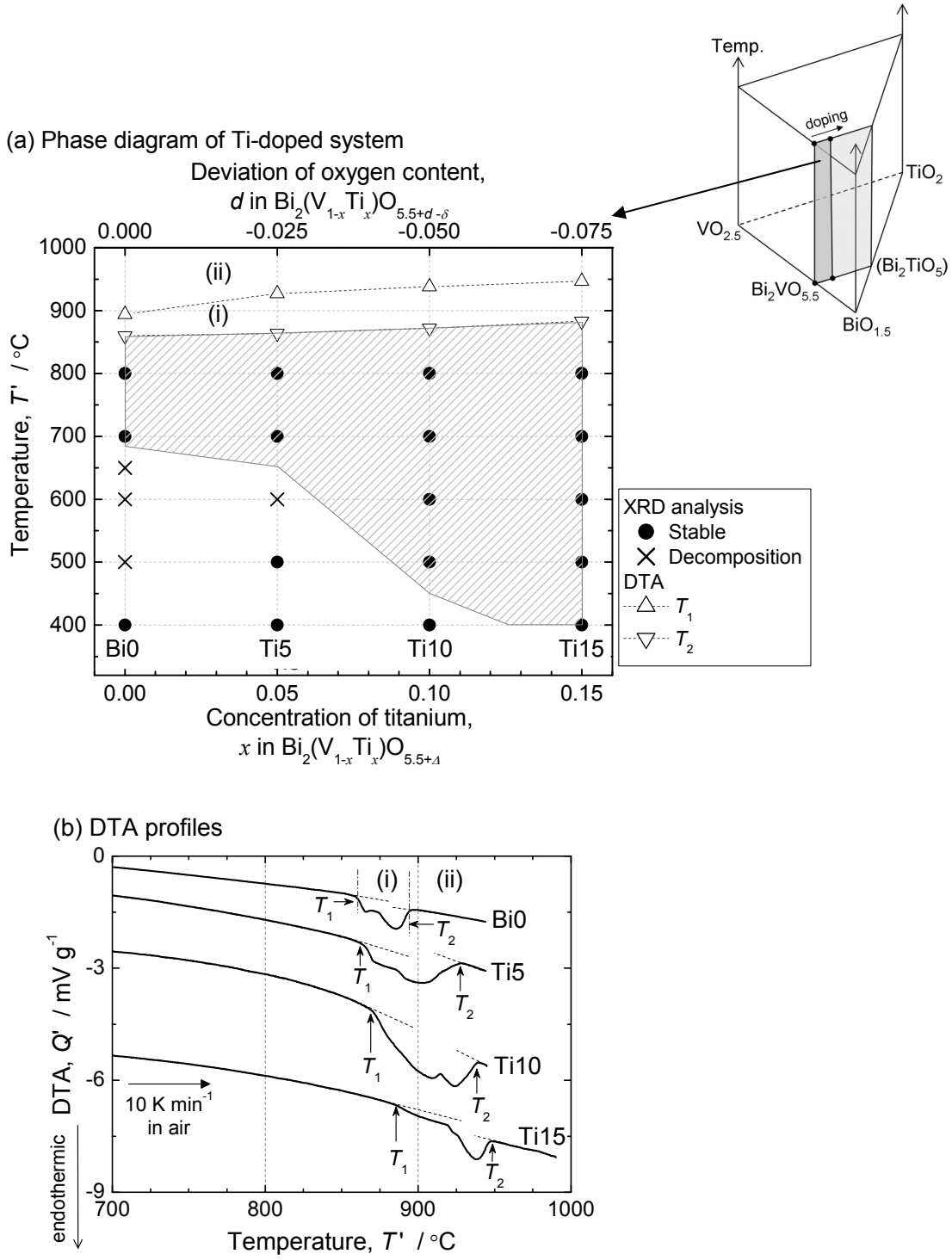

Figure 7.9 (a) Pseudo-binary phase diagram of $Bi_2(V_{1-x}Ti_x)O_{5.5+\Delta}$ generated by conductivity measurements, XRD analysis, and DTA. The shaded area indicates the thermodynamically stable region of γ_f. (b) DTA profiles obtained at a heating rate of 10 K min^{-1} in air. The following phases are estimated: (i) solid + liquid, from T_1 to T_2, (ii) liquid, above T_2.

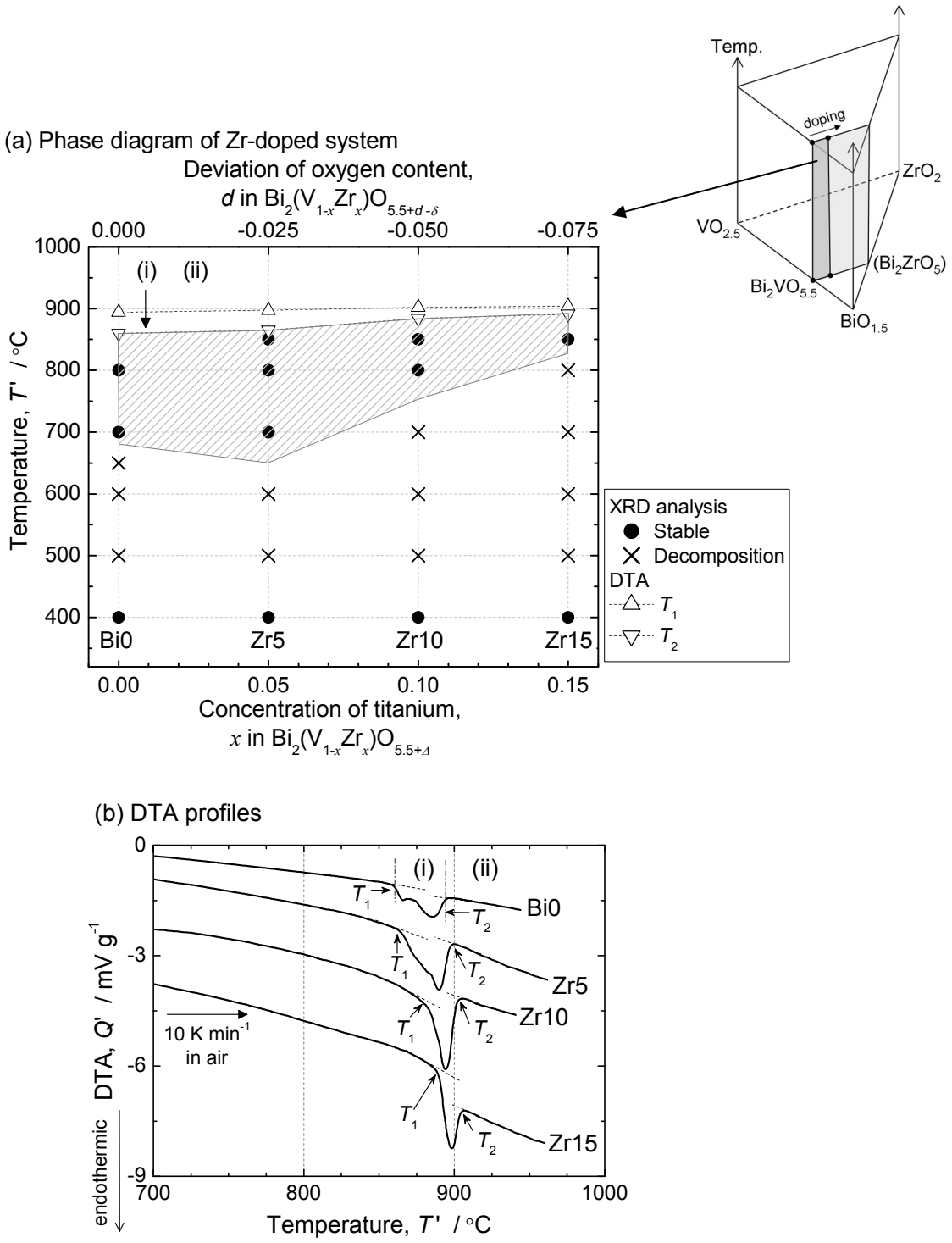

Figure 7.10 (a) Pseudo-binary phase diagram of $Bi_2(V_{1-x}Zr_x)O_{5.5+\Delta}$ generated by conductivity measurements, XRD analysis, and DTA. The shaded area indicates the thermodynamically stable region of γ_f. (b) DTA profiles obtained at a heating rate of 10 K min^{-1} in air. The following phases are estimated: (i) solid + liquid, from T_1 to T_2, (ii) liquid, above T_2.

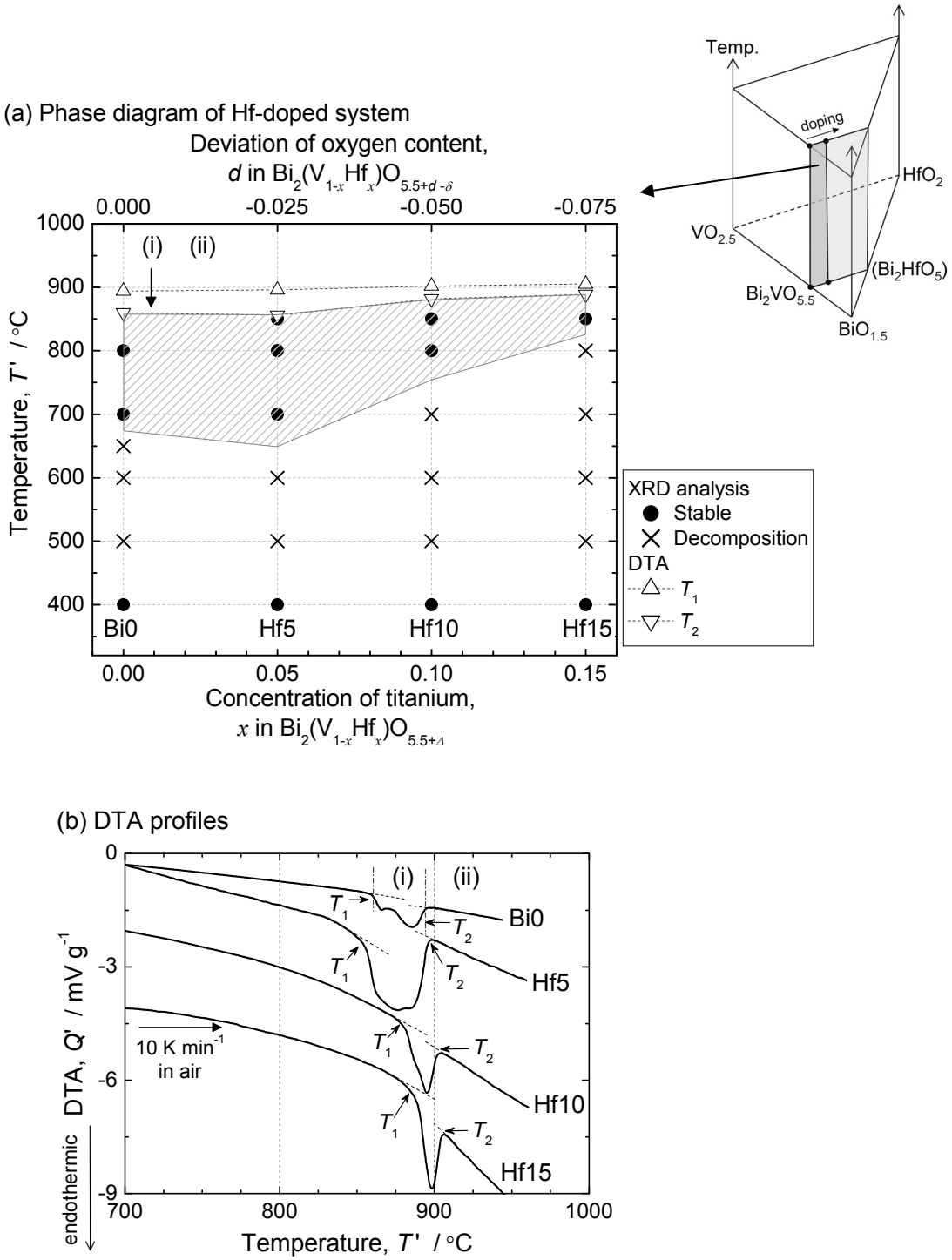

Figure 7.11 (a) Pseudo-binary phase diagram of $Bi_2(V_{1-x}Hf_x)O_{5.5+\Delta}$ generated by conductivity measurements, XRD analysis, and DTA. The shaded area indicates the thermodynamically stable region of γ_f. (b) DTA profiles obtained at a heating rate of 10 K min^{-1} in air. The following phases are estimated: (i) solid + liquid, from T_1 to T_2, (ii) liquid, above T_2.

7.6. Empirical knowledge about doping effects

This section briefly describes the effects of tetravalent-metal-doping on oxide-ion conductivity in γ_f, phase stability of γ_f against β_f and α_f (widening of temperature region for γ_f at low temperatures), and phase stability against thermal decomposition. Table 7.4 lists some characters of dopants with those of V, *i.e.*, valences, ionic radius in 6-fold coordination, lattice energies of binary oxide "*Q*" (trend of affinity with oxide ion in BIMEVOX), and preferable oxygen coordinations. The difference in size between Ti and V is relatively small, although Zr and Hf have much larger size than V. Lattice energy *Q* increases in the following order of Zr, Hf, and Ti. Only for Ti, the preferable oxygen coordination is octahedrally 6-fold (the V-O layer of γ_f is composed of VO_6 octahedron).

Table 7.4 Valences, Shannon ionic radii in 6-fold coordination [76Sha], lattice energies of binary oxide "*Q*" (trend of affinity with oxide-ion in BIMEVOX), and preferable oxygen coordinations of Ti, Zr, Hf, and V. Doping with tetravalent metal increases the amount of oxygen vacancies. As described in Chapter 1, lattice energy *Q* is the negative value of the enthalpy change of following reaction: $ME^{4+}(g) + 2O^{2-}(g) \rightarrow ME_1O_2(s)$, where ME^{4+} is Ti^{4+}, Zr^{4+}, and Hf^{4+}. Comparing at the same valence of dopant, dopant with larger *Q* is expected to bind more strongly with oxide-ion in BIMEVOX. Oxygen coordinations in TiO_2 (rutile structure), ZrO_2 (fluorite structure), HfO_2 (fluorite structure), and V_2O_5 (ReO_3-related one-dimensional shear structure) [76Hul,86Enj] are regarded as preferable.

	Valence	Ionic radius (nm)	Lattice energy, *Q* (MJ mol^{-1})	Preferable oxygen coordination
Ti	+4	0.0605	12.009	6-fold (octahedron)
Zr	+4	0.072	9.811	8-fold (hexahedron)
Hf	+4	0.071	11.113	8-fold (hexahedron)
V	+5	0.054	–	5-fold (square pyramid)

Oxide-ion conductivity in γ_f

Oxide-ion conductivity in γ_f decreases with an increase in dopant concentration although doping with tetravalent metal should increase the amount of oxygen vacancies. As shown in Table 7.3, E_a of γ_f of Ti10 and Ti15 is larger than that of Bi0. This suggests that dopants associate with oxygen vacancies, *i.e.*, association areas (disarray in local structure) disturb the diffusion of oxide ions, and some oxygen vacancies can not diffuse independently and freely.

Phase stability of γ_f against β_f and α_f

γ_f become stabilized against β_f and α_f with an increase in Ti, Zr, and Hf concentration, as summarized in Figure 7.5. As discussed in Chapters 3 and 4, oxygen vacancies induced by aliovalent doping tends to destabilize β_f and α_f (the enthalpy of β_f and α_f was largely increased). Additionally, the presence of dopant and oxygen vacancy might increase the configurational entropy of disorder γ_f phase, which has an advantage to thermodynamically stabilize γ_f against β_f and α_f and retard the ordering from γ_f to β_f and α_f. Ti most effectively stabilized γ_f among three dopants, and Zr- and Hf-doped samples exhibited almost same transition behavior. This suggests that the preferable oxygen coordination of Ti, *i.e.*, octahedrally 6-fold, also plays an important role to stabilize γ_f (whose V-O layer is composed of VO_6 octahedron containing oxygen vacancies) against β_f and α_f.

Phase stability against thermal decomposition

Ti-doping markedly improves the phase stability against thermal decomposition and expands the stable region of γ_f towards room temperature. On the other hand, thermal decomposition proceeds in Zr- and Hf-doped samples at intermediate temperatures. The size difference from V is small for Ti but is large for Zr and Hf. These facts further indicate that lattice distortions around dopants tend to destabilize BMEVOX against thermal decomposition. That is, the dopant, whose size largely deviates from that of V, has a disadvantage to suppress thermal

decomposition in terms of strain energy. Additionally, Ti has relatively strong affinity with oxide ion among three dopants, which might also play an important role to stabilize BIMEVOX. Strong affinity with oxide ion tends to decrease the diffusion rate of dopant in BIMEVOX. When decomposition reaction required sufficient diffusion of dopants, dopant with strong affinity for oxide ion might retard the thermal decomposition effectively.

7.7. Conclusion

In this chapter, the electrical conductivities, phase transitions, and long-term phase stabilities of $Bi_2(V_{1-x}TM_x)O_{5.5+\Delta}$ (TM = Ti^{4+}, Zr^{4+}, and Hf^{4+}, $0 \leq x \leq 0.15$) have been determined. The findings are summarized as follows:

(1) Among three dopants, Ti doping stabilized γ_f at the lowest temperatures. In particular, γ_f of $Bi_2(V_{0.9}Ti_{0.15})O_{5.45-\delta}$ was stabilized down to room temperature. At around 700 °C, the oxide-ion conductivities in γ_f decreased with an increase in dopant concentration. Regardless of the dopants, 10 and 15 mol% doped $Bi_2VO_{5.5-\delta}$ exhibited high oxide-ion conductivities of 10^{-1} and 0.6×10^{-1} S cm^{-1} at 500 °C, respectively.

(2) $Bi_2(V_{0.9}Ti_{0.1})O_{5.45-\delta}$ and $Bi_2(V_{0.9}Ti_{0.15})O_{5.45-\delta}$ were stable during prolonged annealing at intermediate temperatures between 400 and 800 °C for 200 hr. Meanwhile, thermal decomposition proceeded in Zr- and Hf-doped samples.

(3) The pseudo-binary phase diagrams of $Bi_2(V_{1-x}Ti_x)O_{5.5+\Delta}$, $Bi_2(V_{1-x}Zr_x)O_{5.5+\Delta}$, and $Bi_2(V_{1-x}Hf_x)O_{5.5+\Delta}$ were generated. Ti doping expands the thermodynamically stable region of γ_f. In contrast, Zr and Hf doping reduce the size of the stable region.

References

[76Hul] F. Hulliger, *Structural chemistry of layer-type phases*, D. Reidel Publishing Company, Boston (1976).

[76Sha] R.D. Shannon, Acta Crystallogr. A 32 (1976) 767.

[86Enj] R. Enjalbert and J. Galy, Acta Cryst. C42 (1986) 1467.

[92Sha] V. Sharma, A.K. Shukla, and J. Gopalakrishnan, Solid State Ionics 58 (1992) 359.

[92Goo] J.B. Goodenough, A. Manthiram, M. Paranthaman and Y.S. Zhen, Mater. Sci. Eng. B12 (1992) 357.

[94Her] J. Van Herle, A.J. Mcevoy, and K.R. Thampi, J. Mater. Sci. 29 (1994) 3691.

[95Yan] J. Yan and M. Greenblatt, Solid State Ionics 81 (1995) 225.

[96Laz] S. Lazure, Ch. Vernochet, R.N. Vannier, G. Nowogrocki, and G. Mairesse, Solid State Ionics 90 (1996) 117.

[99Ish] T. Ishihara, H. Furutani, M. Honda, T. Yamada. T. Shibayama, T. Akbay. N. Sakai, H. Yokokawa, and Y. Takita, Chem. Mater. 11 (1999) 2081.

[02Kro] F. Krok, I. Abrahams, W. Wrobel, S.C.M. Chan, M. Malys, W. Bogusz, and J.R. Dygas, Solid State Ionics 154-155 (2002) 511.

[05Wro] W. Wrobel, I. Abrahams, F. Krok, A. Kozanecka, S.C.M. Chan, M. Malys, W. Bogusz, and J.R. Dygas, Solid State Ionics 176 (2005) 1731.

[09Beg1] S. Beg, N.A.S. Al-Areqi, and A. Al-Alas, J. Alloys Compd. 479 (2009) 107.

[09Beg2] S. Beg, N.A.S. Al-Areqi, A. Al-Alas, and S. Hafeez, Physica B 404 (2009) 2072.

Chapter 8

Co-doping with monovalent metal and Ti:

"Oxide-Ion Conductivity and Phase Stability of $Bi_2(V_{0.9}MM_{1-x}Ti_x)O_{5.5+\Delta}$ (MM = Li and Ag, x = 0.04 and 0.06)"

8.1. Introduction

Figure 8.1 summarizes the temperatures at the end of conductivity jumps from β_f to γ_f, which were evaluated from the conductivity changes of various $Bi_2(V_{0.95}ME_{0.05})O_{5.5+\Delta}$ ($\Delta \equiv d - \delta$, Δ: total deviation of oxygen content, d: oxygen deviation due to aliovalent doping, δ: oxygen loss due to partial reduction). Data in Figure 8.1 were obtained in Chapters 3–5. Among various dopants investigated in this thesis, monovalent metals of Li and Ag were most effective dopants to stabilize γ_f against β_f and α_f. As described in Chapter 4, γ_f was stabilized down to room temperature in $Bi_2(V_{0.9}Li_{0.1})O_{5.3-\delta}$ and $Bi_2(V_{0.9}Ag_{0.1})O_{5.3-\delta}$. The γ_f of $Bi_2(V_{1-x}MM_x)O_{5.5+\Delta}$ (MM = Li and Ag, x = 0.05 and 0.1) exhibited high oxide-ion conductivity at around 500 °C but showed poor phase stability against thermal decomposition. High oxide-ion conduction of $Bi_2(V_{1-x}MM_x)O_{5.5+\Delta}$ at intermediate temperatures markedly degraded with time. In Figure 8.1, doping with tetravalent Ti also stabilized γ_f against β_f and α_f, although it was less effective than doping with Li and Ag. Ti is the most effective dopant to stabilize γ_f against thermal decomposition, as described in Chapters 5 and 7. In this chapter, therefore, co-doping with monovalent metal and Ti is employed to further improve the oxide-ion conductivity and phase stability of γ_f at intermediate temperatures.

There has been no study about the co-doping with Li and Ti (Li-Ti) as well as Ag and Ti

(Ag-Ti). However, a few properties of co-doped BIMEVOX phases have been reported (Cu-Ni, Cu-Zn, Ni-Zn, Cu-Mo [94Van], Co-Cu [97Kro], Ti-Cu [01Pay], and Nb-Cu [05Alg]).

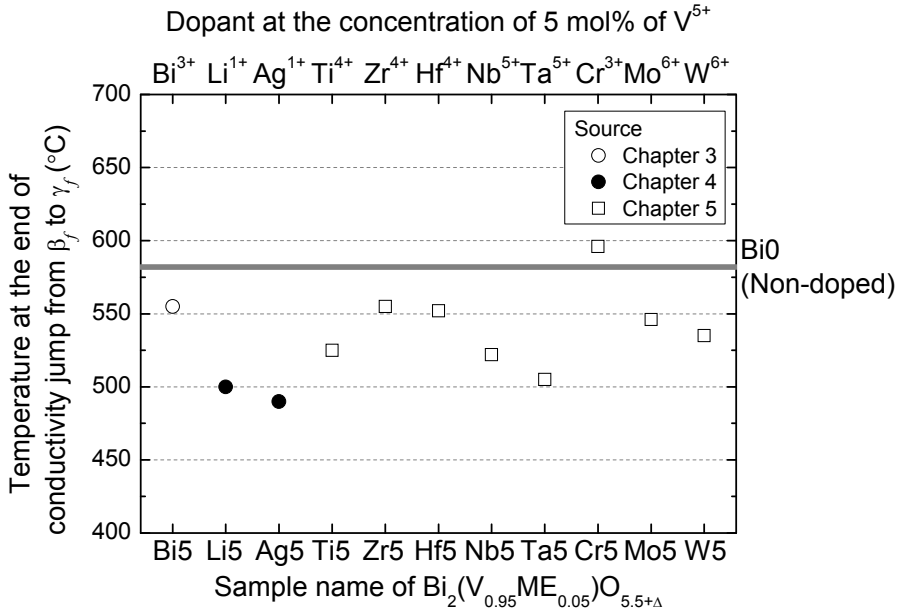

Figure 8.1 Temperatures at the end of conductivity jumps from β_f to γ_f. The conductivity changes shown in Chapters 3–5 were used for evaluation. The concentration of dopants was fixed at 5 mol%.

8.2. Sample preparation

Table 8.1 shows the abbreviations and compositions of prepared samples. The total concentration of dopant was fixed at 10 mol% of vanadium sites. We denote Li10, LiTi, and Ti10 as the (Li,Ti)-doped system, and Ag10, AgTi, and Ag10 as the (Ag,Ti)-doped system. Powder samples of LiTi and AgTi were synthesized by solid-state reaction in air using platinum crucibles. Table 8.2 lists the starting materials and Figure 8.2 shows the flowchart for sample preparation. As shown in Figure 8.2(a), the mixtures of appropriate amounts of constituents were heated at 600 °C for 12 hr. The ground powders were pelletized at 0.2 ton cm^{-2}, heated again at 700 °C for 12 hr, and then grinded. The synthesized powders were pressed uniaxially at 3 ton cm^{-2} for 15 min and then sintered at 700 °C for 12 hr in air, as

shown in Figure 8.2(b). The preparation processes of Li10 and Ag10 are given in Chapter 4, and that of Ti10 is given in Chapter 7.

Table 8.1. Abbreviations and compositions of prepared samples

Abbreviation		Composition	Synthesized
LiTi	Li6Ti4	$Bi_2(V_{0.9}Li_{0.06}Ti_{0.04})O_{5.36-\delta}$	This study
	Li4Ti6	$Bi_2(V_{0.9}Li_{0.04}Ti_{0.06})O_{5.39-\delta}$	
AgTi	Ag6Ti4	$Bi_2(V_{0.9}Ag_{0.06}Ti_{0.04})O_{5.36-\delta}$	This study
	Ag4Ti6	$Bi_2(V_{0.9}Ag_{0.04}Ti_{0.06})O_{5.39-\delta}$	
Li10		$Bi_2(V_{0.9}Li_{0.1})O_{5.3-\delta}$	Chapter 4
Ag10		$Bi_2(V_{0.9}Ag_{0.1})O_{5.3-\delta}$	Chapter 4
Ti10		$Bi_2(V_{0.9}Ti_{0.1})O_{5.45-\delta}$	Chapter 7

Table 8.2 Purity and source of starting materials.

Starting material	Chemical formula	Purity (mass %)	Source
Bismuth oxide	Bi_2O_3	99.99	Furuuchi Chemical
Vanadium oxide	V_2O_5	99.9	Furuuchi Chemical
Lithium carbonate	Li_2CO_3	99.9	Furuuchi Chemical
Silver oxide	Ag_2O	99 +	Wako
Titanium oxide	TiO_2	99.9	Wako

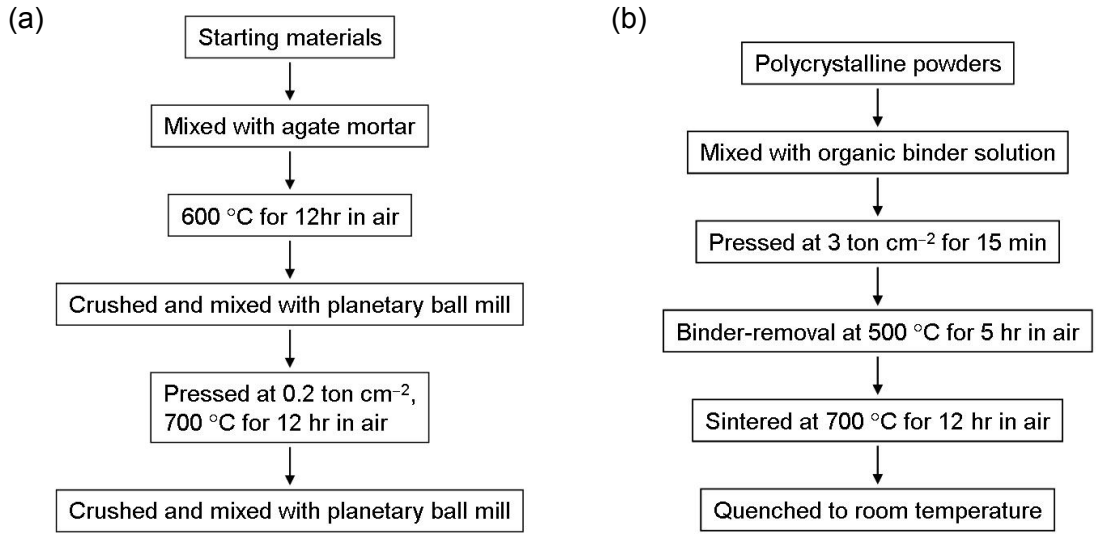

Figure 8.2 Flowchart for (a) preparing of polycrystalline powder and (b) sintering of pellet.

8.3. Phases at room temperature identified by XRD analysis

Figure 8.3 shows the XRD patterns of powders quenched from 700 °C (LiTi, AgTi, and Li10), 750 °C (Ag10), or 800 °C (Ti10) in a logarithmic intensity scale. Figure 8.4 shows the lattice constants of a_m, b_m, and c_m. Tetragonal γ_f was stabilized in Li10 and Ag10. Meanwhile, orthorhombic α_f with a small amount of $BiVO_4$ was obtained in Ti10. In Figure 8.3(a), a single phase of γ_f was successfully stabilized in both Li6Ti4 and Li4Ti6. As shown in Figure 8.4(a), Li6Ti4 had a tetragonal subcell. Meanwhile, Li4Ti6 had an orthorhombic subcell and exhibited quite a small trace of 1/3 1 3 diffraction, which is a typical superlattice diffraction of α_f, as indicated by an arrow in Figure 8.3(a). In both Ag6Ti4 and Ag4Ti6, tetragonal γ_f was stabilized without any secondary phases, as shown in Figures 8.3(b) and 8.4(b).

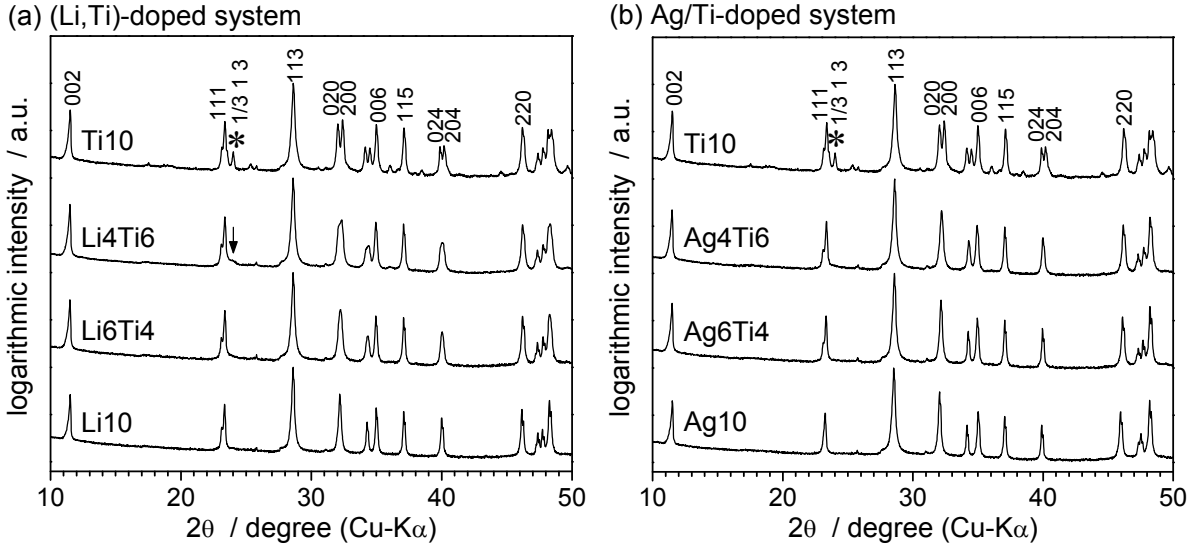

Figure 8.3 XRD patterns of powders quenched from 700 °C (LiTi, AgTi, and Li10), 750 °C (Ag10), or 800 °C (Ti10) in a logarithmic intensity scale. (a) (Li,Ti)-doped system. (b) (Ag,Ti)-doped system. The plane indices are marked assuming the orthorhombic subcell of a_m, b_m, and c_m. Asterisks (∗) indicate typical superlattice diffraction peaks of α_f. Arrow indicates the small trace of the 1/3 1 3 peak.

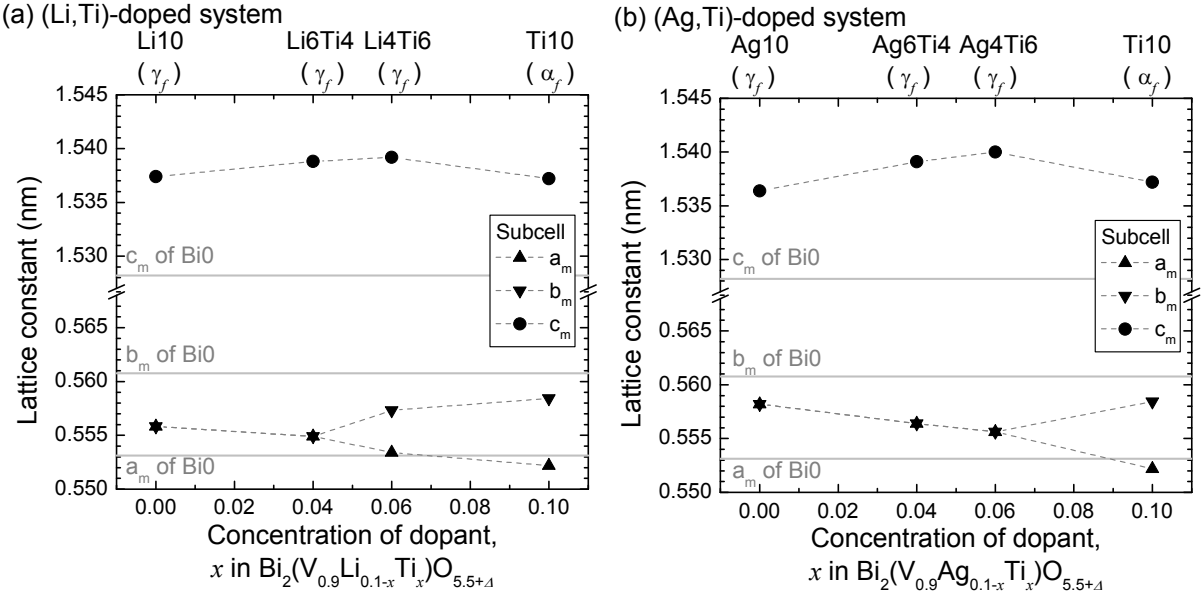

Figure 8.4 Lattice constants of a_m, b_m, and c_m as a function of Ti concentration. (a) (Li,Ti)-doped system. (b) (Ag,Ti)-doped system. Gray lines indicate the lattice constant in quenched Bi0 powder.

Figure 8.5 shows the XRD patterns of powders slowly cooled at 1 K min^{-1} from 700 °C (LiTi, AgTi, and Li10), 750 °C (Ag10), or 800 °C (Ti10) in a logarithmic intensity scale. Despite slow cooling, orthorhombic α_f with a small amount of $BiVO_4$ was obtained in Ti10. Meanwhile, slowly cooled Li10 powder exhibited a 1/3 1 3 peak and contained a small amount of secondary phase. Thermal decomposition largely progressed in slowly cooled Ag10 powder. In LiTi and AgTi, thermal decomposition did not progress during slow cooling, which means that phase stabilities were improved by doping with Ti. However, ordering from γ_f somewhat proceeded in LiTi and AgTi, as verified by the slight trace of a 1/2 1 3 peak in Li6Ti4, a small 1/3 1 3 peak, the slight trace of 1/2 1 3 peaks in Li4Ti6, and small 1/3 1 3 peaks in Ag6Ti4 and Ag4Ti6. This ordering behavior corresponds to the fact that γ_f of LiTi and AgTi are transformed to α_f by prolonged annealing at 400 °C. Phase stability against

thermal decomposition as well as ordering behavior by long-term annealing is further investigated in Section 8.8.

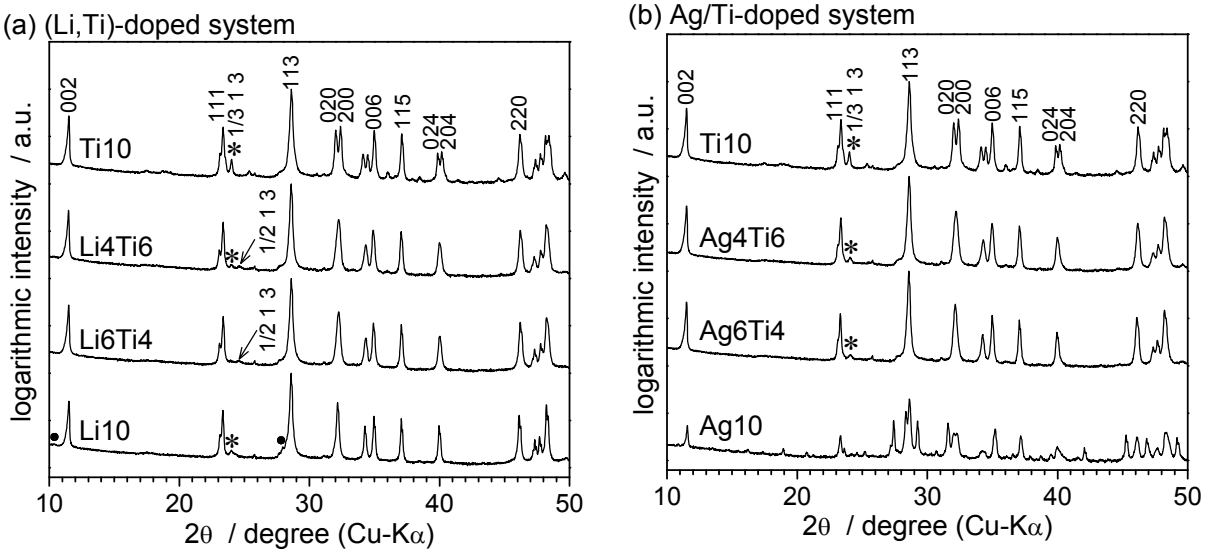

Figure 8.5 XRD patterns of powders slowly cooled at 1 K min^{-1} from 700 °C (LiTi, AgTi, and Li10), 750 °C (Ag10), or 800 °C (Ti10) in a logarithmic intensity scale. (a) (Li,Ti)-doped system. (b) (Ag,Ti)-doped system. Asterisks (∗) indicate typical superlattice diffraction peaks of α_f. Arrows indicate slight traces of 1/2 1 3 diffraction, which are typical superlattice diffraction peaks of β_f. Thermal decomposition slightly proceeds in Li10, and the peaks of the secondary phase are indicated by closed circles (•). Ag10 largely decomposes during slow cooling.

8.4. Phase transitions determined by DSC and HT-XRD

Figure 8.6(a) shows the DSC profiles of Li10, Li6Ti4, Li4Ti6, and Ti10. Quenched powders were heated and cooled at 10 K min^{-1} in flowing air. Li10 shows two broad endothermic peaks on heating from 300 to 420 °C, which corresponds to a gradual conductivity jump in γ_f. In addition, the pair of endothermic and exothermic peaks at around 680 °C corresponds to the partial melting of Li10. On heating, Ti10 exhibits a large endothermic peak at 263 °C, corresponding to the transition from α_f to β_f (α_f/β_f transition),

and a small endothermic peak at 433 °C, corresponding to the transition from β_f to γ_f (β_f/γ_f transition). DSC profiles of Li6Ti4 and Li4Ti6 did not exhibit clear peaks except for a very broad and small endothermic peak from 315 to 400 °C in Li6Ti4 and from 310 to 438 °C in Li4Ti6. Figure 8.6(b) shows the DSC profiles of Ag10, Ag6Ti4, Ag4Ti6, and Ti10. Ag6Ti4 and Ag4Ti6 showed no endothermic and exothermic peaks, like Ag10.

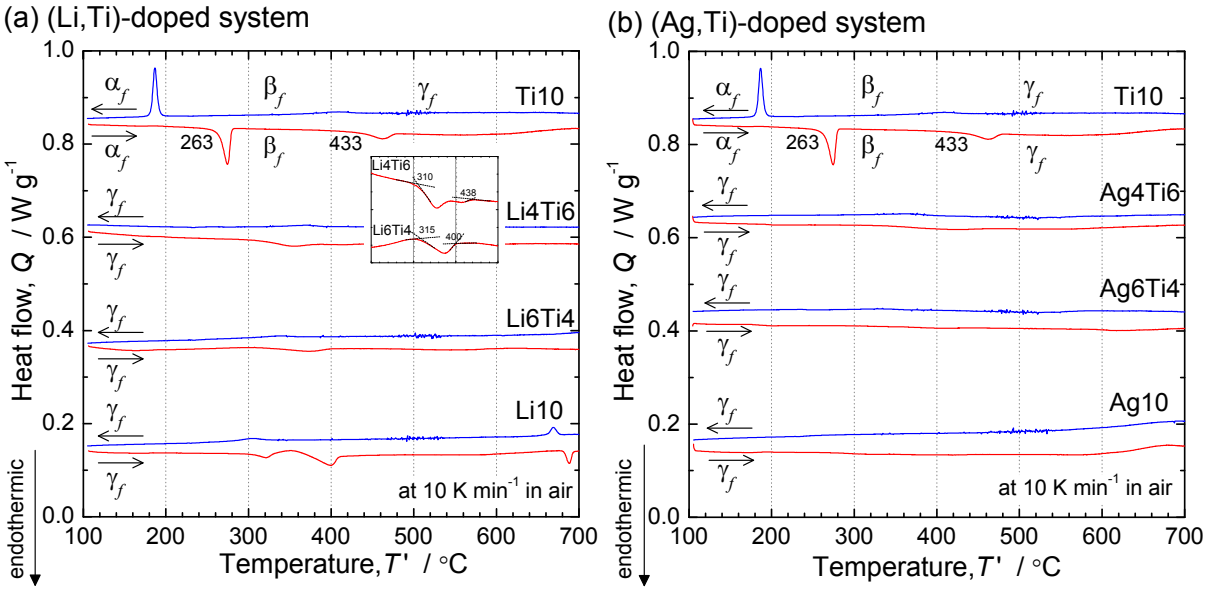

Figure 8.6 DSC profiles collected in flowing air at a scan rate of 10 K min^{-1}. (a) (Li,Ti)-doped system. Inset shows magnified profiles on heating. (b) (Ag,Ti)-doped system.

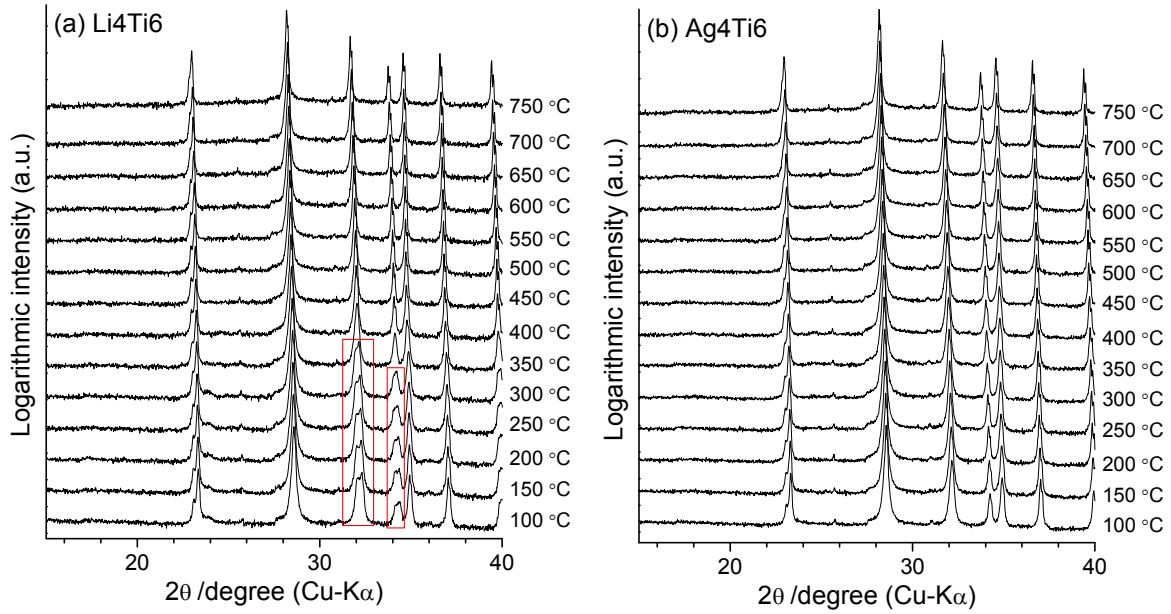

Figure 8.7 HT-XRD profiles of quenched powders of (a) Li4Ti6 and (b) Ag4Ti6. In γ_f of Li4Ti6, the symmetry of the subcell changed from orthorhombic to tetragonal between 300 and 350 °C. In Ag4Ti6, tetragonal γ_f was obtained from 100 to 700 °C.

Figure 8.7 shows the HT-XRD patterns of quenched powders of Li4Ti6 and Ag4Ti6 in a logarithmic intensity scale. The scan rate of the sample temperature was 10 K min^{-1}. The sample temperatures were maintained for 5 min at 50 °C intervals, and diffraction patterns were collected within 10 min at each temperature. γ_f of Li4Ti6 was obtained from 100 to 750 °C. However, the symmetry of the subcell became tetragonal and a slight trace of 1/3 1 3 diffraction disappeared above 350 °C. In Ag4Ti6, tetragonal γ_f was observed up to 750 °C without notable structural changes.

8.5. Microstructures and relative densities of sintered pellets

Figure 8.8 shows the cross-sectional FE-SEM images of sintered pellets after thermal etching. Large grains exceeding 5 μm were observed in all pellets. For LiTi and AgTi pellets, EDX did not indicate compositional inhomogeneity. Comparing the grain size among Li10, Li6Ti4, and Ti4Ti6, we can see the trend that the grain size decreases with an increase in Ti concentration. A similar trend is also observed among Ag10, Ag6Ti4, and Ag4Ti6.

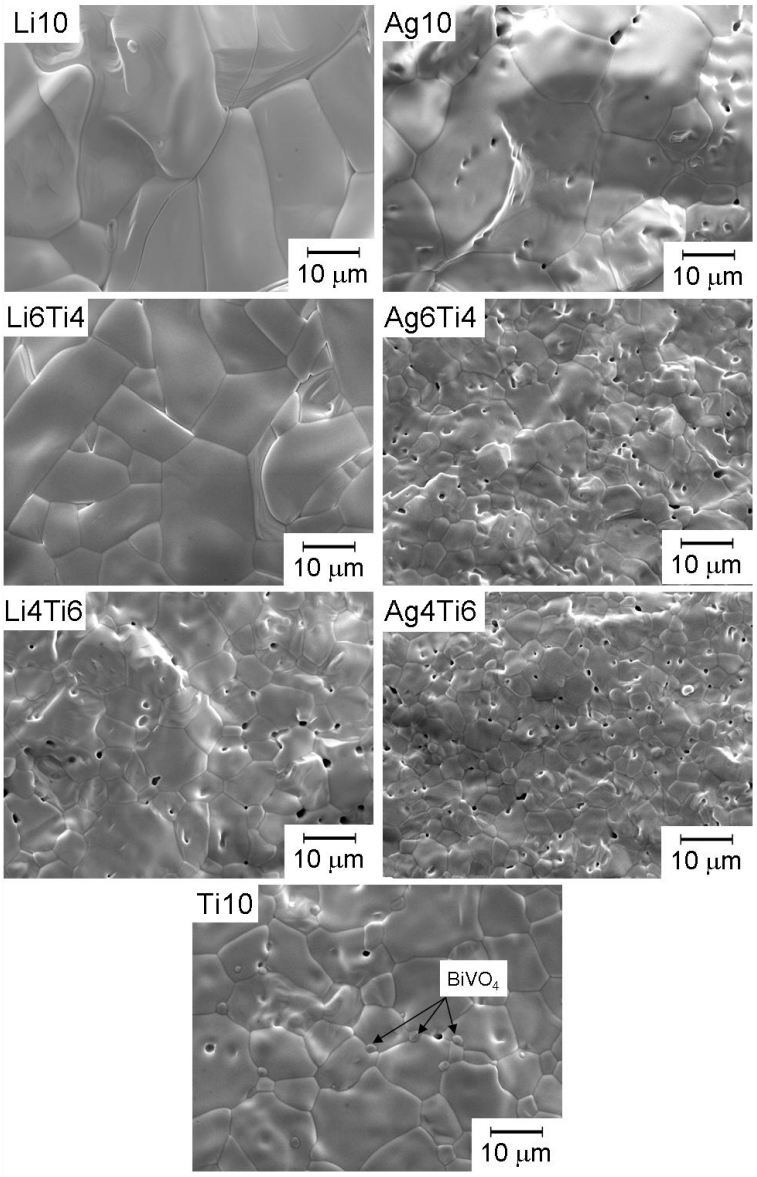

Figure 8.8 Cross-sectional FE-SEM images of sintered pellets after thermal etching at sintering temperatures for 3 hr. Ti10 contains a small amount of $BiVO_4$.

Table 8.2 Sintering conditions and relative densities of pellet samples. Compositions and phases identified in quenched powders are also listed.

	Composition	Phase in quenched sample	Pellet	
			Sintering condition	Relative density (%)
Li6Ti4	$Bi_2(V_{0.9}Li_{0.06}Ti_{0.04})O_{5.36-\delta}$	γ_f (tetragonal)	700 °C, 12 hr	94
Li4Ti6	$Bi_2(V_{0.9}Li_{0.04}Ti_{0.06})O_{5.39-\delta}$	γ_f (orthorhombic)	700 °C, 12 hr	95
Ag6Ti4	$Bi_2(V_{0.9}Ag_{0.06}Ti_{0.04})O_{5.36-\delta}$	γ_f (tetragonal)	700 °C, 12 hr	94
Ag4Ti6	$Bi_2(V_{0.9}Ag_{0.04}Ti_{0.06})O_{5.39-\delta}$	γ_f (tetragonal)	700 °C, 12 hr	93
Li10	$Bi_2(V_{0.9}Li_{0.1})O_{5.3-\delta}$	γ_f (tetragonal)	700 °C, 12 hr	93
Ag10	$Bi_2(V_{0.9}Ag_{0.1})O_{5.3-\delta}$	γ_f (tetragonal)	750 °C, 12 hr	95
Ti10	$Bi_2(V_{0.9}Ti_{0.1})O_{5.45-\delta}$	α_f (orthorhombic)	800 °C, 12 hr	95

Table 8.2 shows the relative densities of sintered pellets with the sintering conditions. The relative densities were evaluated using the theoretical densities, which were calculated from the nominal composition and the cell volume derived from XRD analysis. LiTi and AgTi pellets show high relative densities of 93–95%.

8.6. Temperature dependence of electrical conductivities determined by AC impedance spectroscopy

Au electrodes were attached using gold paint, and then AC impedance spectroscopy was performed for LiTi and AgTi pellets on heating at 1 K min^{-1} in air. Just before measurement, pellets with Au electrodes were quenched from sintering temperatures. Figure 8.9 shows the typical impedance spectra of Li6Ti4 and Ag6Ti4 obtained at (a) ~250 °C and (b) ~700 °C. At around 250 °C, an arc and almost straight line inclined at an angle of ~45° appeared at higher- and lower-frequency regions, respectively. The arc at the higher-frequency region comes from the total of bulk and grain-boundary conductions, and the almost straight line can be

explained by the ionic diffusion-limited process in the electrode reaction, *i.e.*, Warburg impedance [97Jia]. The resistivity of the electrolyte was evaluated by the intersection between the arc and the straight line, as indicated in Figure 8.9(a).Meanwhile, spectra at around 700 °C showed only a straight line, which can be explained by the ionic diffusion-limited process in the electrode reaction. The resistivity of the electrolyte was evaluated by the intercept of the line spectra with the real axis, as shown in Figure 8.9(b). From impedance spectra, dominant charge carriers are estimated to be oxide ions. Pure oxide-ion conduction in LiTi and AgTi is further confirmed in Section 8.7.

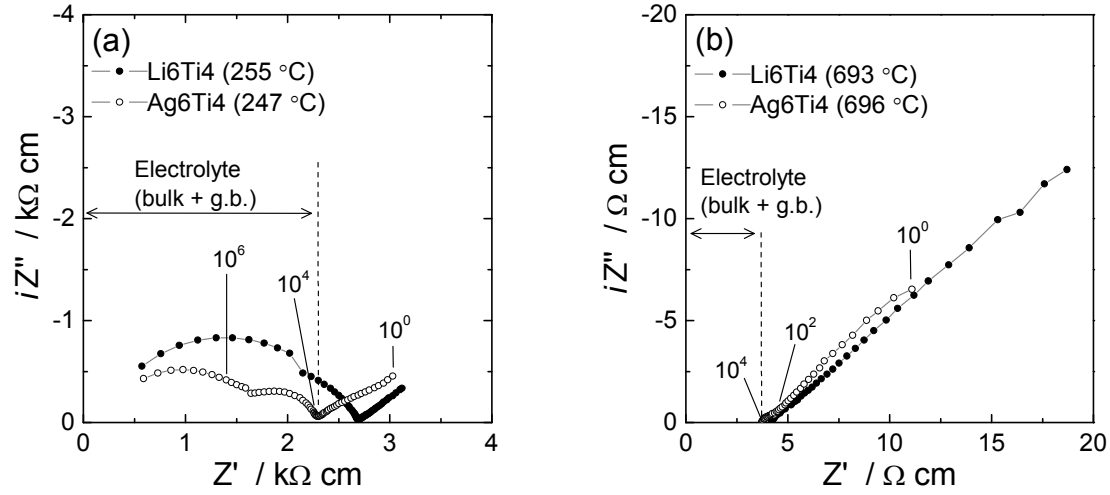

Figure 8.9 Typical impedance spectra of Li6Ti4 and Ag6Ti4 (a) at around 250 °C and (b) at around 700 °C. Data are collected during heating at 1 K min^{-1} in air.

Figure 8.10(a) shows the Arrhenius plots of the oxide-ion conductivities of LiTi. Distinct increases in conductivity were observed from 400 to 470 °C in Li6Ti4 and from 430 to 490 °C in Li4Ti6, although γ_f was stabilized down to room temperature. An endothermic peak as well as structural change was not confirmed in DSC and HT-XRD analysis at the corresponding temperatures, as shown in Figures 8.6(a) and 8.7(a). Through these conductivity jumps, highly conductive states of LiTi were realized and the conductivities approached 10^{-1} S cm^{-1}. The activation energies (E_a) of LiTi in the highly conductive state of γ_f were as low as that in γ_f of

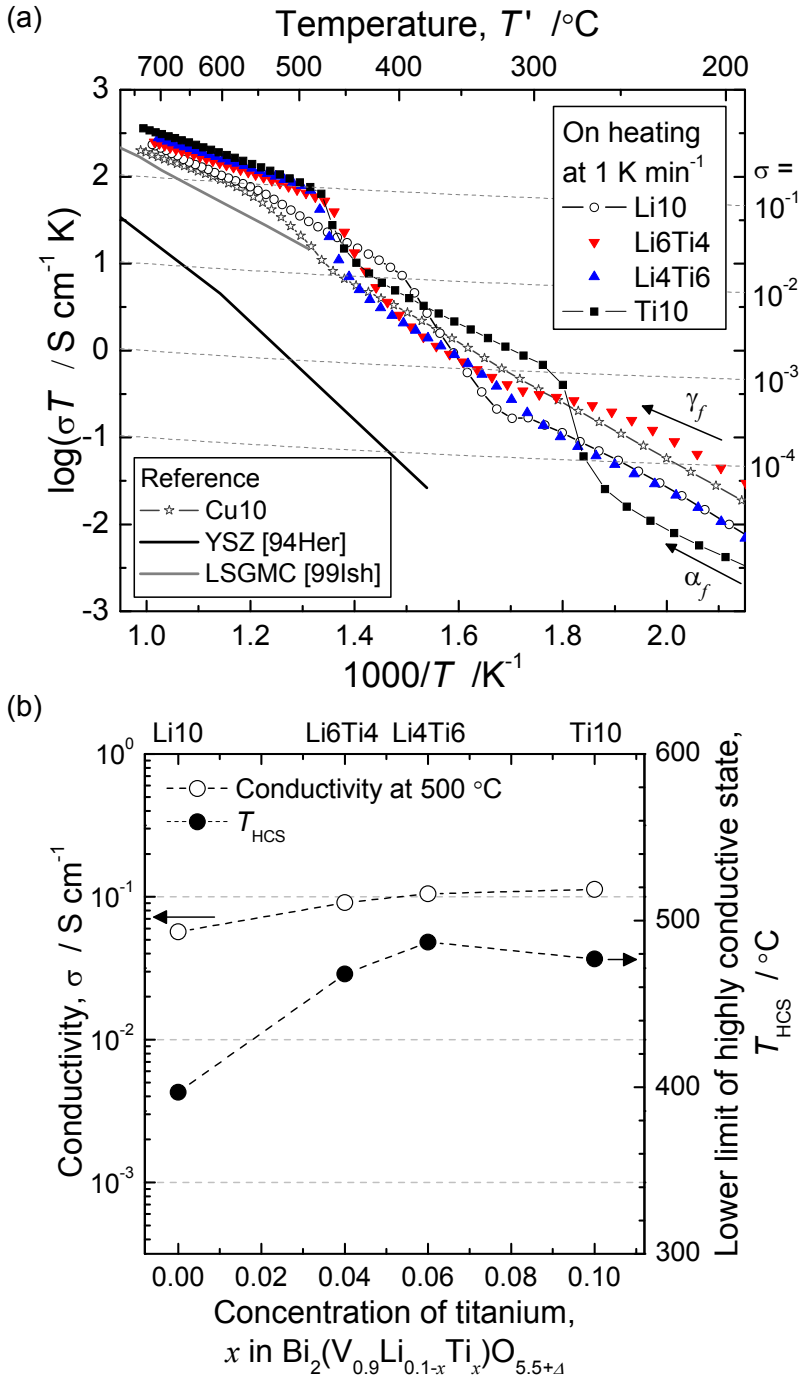

Figure 8.10 (a) Temperature dependence of total conductivities of the (Li,Ti)-doped system in air. Just before measurement, pellets with Au electrodes were quenched from sintering temperatures. The conductivity of Cu10 measured at the same condition and reported conductivities of YSZ [94Her] and LSGMC [99Ish] are also shown. (b) Oxide-ion conductivity at 500 °C and temperature of the lower limit for the highly conductive state of γ_f, T_{HCS}.

Ti10, as listed in Table 8.4. The distinct conductivity jumps in γ_f at around 450 °C should be related with the slight modification of atomic arrangement in the V-O layer which contains oxygen vacancies and dopants. Additionally, the conductivity slope of Li6Ti4 became small at 270–320 °C. This slope change probably corresponds to the small endothermic peak from 315 to 400 °C shown in Figure 8.6(a). Li4Ti6 showed a slight change in the conductivity slope at around 305 °C, which should correspond to the small endothermic peak shown in Figure 8.6(a) and is explained by the change in subcell symmetry shown in Figure 8.7(a).

Table 8.4 Activation energies (E_a) and pre-exponential terms (A) of the oxide-ion conductivities in γ_f.

	E_a (eV)	A (S cm^{-1} K)	Temperature range (°C)
Li10	0.60 (±0.02)	3.2 (±0.4) ×10^5	410–720
Li6Ti4	0.40 (±0.01)	2.9 (±0.2) ×10^4	470–700
Li4Ti6	0.39 (±0.01)	2.9 (±0.1) ×10^4	480–700
Ag10	0.47 (±0.02)	4.5 (±0.5) ×10^4	430–750*
Ag6Ti4	0.44 (±0.01)	5.0 (±0.3) ×10^4	430–700
Ag4Ti6	0.44 (±0.01)	4.8 (±0.4) ×10^4	430–700
Ti10	0.41 (±0.01)	4.3 (±0.3) ×10^4	480–720

* The data between 540 and 730 °C were not used.

In Figure 8.10(a), the conductivities of Li10 and Ti10 are also represented. Li10 exhibits high oxide-ion conductivity above 400 °C through a slow conductivity jump from 320 to 400 °C, as described in Chapter 4. Ti10 exhibits two conductivity jumps at 260 and 445 °C corresponding to an α_f/β_f transition and a β_f/γ_f transition, respectively. Figure 8.10(b) plots the oxide-ion conductivities at 500 °C as well as end temperatures of conductivity jumps to a highly conductive state (T_{HCS}), *i.e.*, end temperatures of distinct conductivity jumps in γ_f for Li10, Li6Ti4, and Li4Ti6. For Ti10, the end temperature of the conductivity jump for the β_f/γ_f

transition is plotted as T_{HCS}. At 500 °C, the oxide-ion conductivities of LiTi were as high as 10^{-1} S cm^{-1}, which is about 1.6 times higher than that of Li10 and the same as that of Ti10. The oxide-ion conductivity of 10^{-1} S cm^{-1} is almost the same order of conductivity of $(ZrO_2)_{0.92}(Y_2O_3)_{0.08}$ at around 930 °C, of $(CeO_2)_{0.85}(SmO_{1.5})_{0.15}$ at around 850 °C, of $La_{0.8}Sr_{0.2}Ga_{0.8}Mg_{0.115}Co_{0.085}O_3$ at around 670 °C, of $(Bi_2O_3)_{0.8}(Er_2O_3)_{0.2}$ at around 570 °C, and of $Bi_2(V_{0.9}Cu_{0.1})O_{5.35-\delta}$ at around 600 °C. However, the region of the highly conductive state in γ_f was largely reduced by doping with Ti.

Figure 8.11(a) shows the Arrhenius plots of electrical conductivities of the (Ag,Ti)-doped system. As described in Chapter 4, Ag10 shows a slow conductivity jump from 320 to 430 °C and an unusual conductivity drop between 540 and 730 °C due to thermal decomposition. γ_f of Ag6Ti4 and Ag4Ti6 also exhibited a slow conductivity jump from 360 to 430 °C, although DSC and HT-XRD analysis did not indicate an endothermic reaction and structural change, respectively. Above 430 °C, highly conductive states with E_a of 0.44 eV, as listed in Table 8.4, are achieved. The difference between highly conductive and lowly conductive γ_f probably derives from the small difference in local structure around dopants (association state between dopant and oxygen vacancies). AgTi exhibited a higher conductivity than Ag10 over the whole temperature range. The oxide-ion conductivity at 500 °C and T_{HCS} are plotted in Figure 8.11(b). At 500 °C, AgTi exhibited a high oxide-ion conductivity of about 10^{-1} S cm^{-1}, which is about 2 times higher than that of Ag10 and the same as that of Ti10. T_{HCS} of AgTi was as low as that of Ag10 despite doping with Ti.

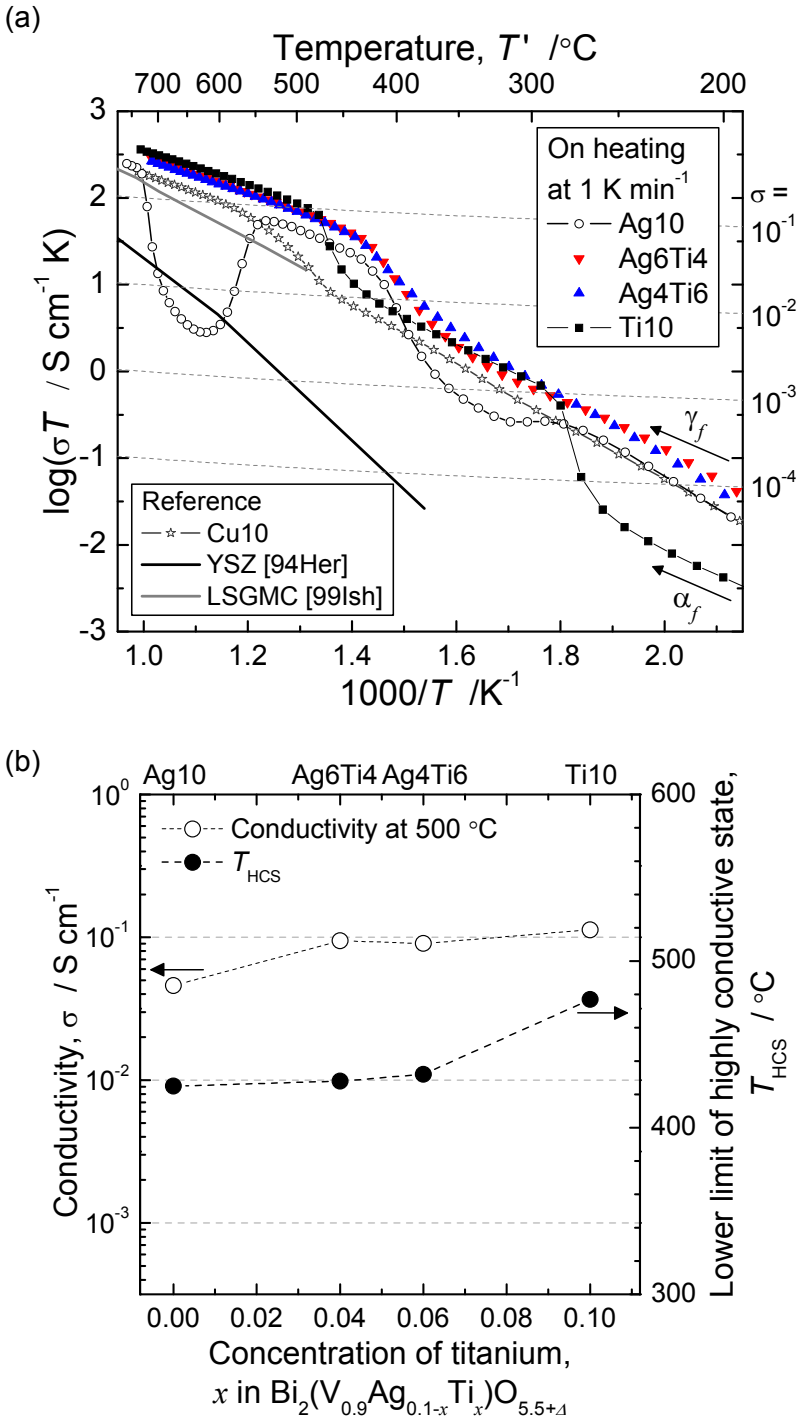

Figure 8.11 (a) Temperature dependence of total conductivities of (Ag,Ti)-doped system in air. Just before measurement, pellets with Au electrodes were quenched from sintering temperatures. The conductivity of Cu10 measured at the same condition and reported conductivities of YSZ [94Her] and LSGMC [99Ish] are also shown. (b) Oxide-ion conductivity at 500 °C and temperature of the lower limit for the highly conductive state of γ_f, T_{HCS}.

8.7. Charge carriers determined by AC impedance spectroscopy and DC polarization measurement

Figure 8.12 shows the conductivities of Li4Ti6 and Ag4Ti6 at various pO_2 values of 1, 0.21, and 8×10^{-4} atm. The data were determined by AC impedance spectroscopy on cooling from 700 °C at 1 K min^{-1}. In general, electron conductivity decreases with pO_2, hole conductivity increases with pO_2, and oxide-ion conductivity is independent of pO_2, as described in Chapter 1. The conductivity did not vary with pO_2 between 500 and 700 °C for Li4Ti6 and between 400 and 700 °C for Ag4Ti6. Consequently, the dominant charge carriers in Li4Ti6 and Ag4Ti6 are oxide ions at intermediate temperatures.

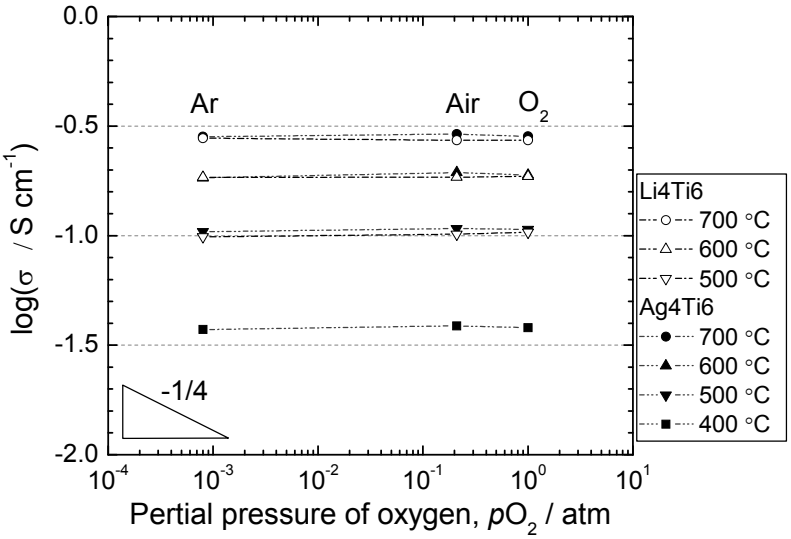

Figure 8.12 Electrical conductivities of Li4Ti6 and Ag4Ti6 as a function of pO_2. The data were collected on cooling from 700 °C at 1 K min^{-1}. Electron conductivity is expected to be proportional to $pO_2^{-1/4}$, as described in Chapter 1.

The oxide-ion conduction was further confirmed by DC polarization measurements, which were performed in air for the pellets with vacuum-deposited Au electrodes. As a blocking electrode was used, the current in a steady state was derived from only electron/hole diffusion. Table 8.5 shows the evaluated transference numbers of electrons/holes (t_e) and

oxide ions (t_O) by comparing with the conductivities evaluated by AC impedance spectroscopy. σ_e was evidently quite small compared with the oxide-ion conductivities in Li4Ti6 and Ag4Ti6.

Table 8.5 Electron/hole conductivities in air (σ_e), and calculated transference numbers of oxide-ion conduction (t_O) and electron/hole conduction (t_e). The transference numbers are preliminary because we employed a simplified version of the Habb-Wagner method [52Heb,56Wag].

	Temperature (°C)	σ_e (S cm^{-1})	t_O	t_e
Li4Ti6	504	4.07×10^{-4}	1.00	0.00
	605	9.37×10^{-4}	1.00	0.00
	705	1.58×10^{-2}	0.95	0.05
Ag4Ti6	399	1.03×10^{-4}	0.99	0.01
	503	2.65×10^{-4}	1.00	0.00
	606	1.23×10^{-3}	0.99	0.01
	706	8.95×10^{-3}	0.97	0.03

8.8. Long-term phase stabilities

8.8.1. Phase stabilities and phase diagrams determined by XRD analysis of annealed powders and DTA

Figure 8.13 shows the XRD patterns after annealing in a logarithmic intensity scale. Li10 and Ag10 are largely decomposed during annealing at 500 °C, although Ti10 is stable. In LiTi and AgTi, the progress of thermal decomposition was suppressed almost completely. A very small amount of secondary phase was detected in Li6Ti4, Ag6Ti4, and Ag4Ti6, as indicated in Figure 8.13. At 400 °C, thermal decomposition did not progress in LiTi and AgTi, but α_f appeared after annealing. Ag4Ti6 after annealing at 400 °C was markedly inhomogeneous, as verified by the broadening of the 0 0 6 peak at ~35°. There is a possibility that AgTi is a

mixture of α_f and γ_f after annealing at 400 °C. The ordering behavior from γ_f to α_f will be further investigated from the viewpoint of conductivity change in Section 8.8.2.

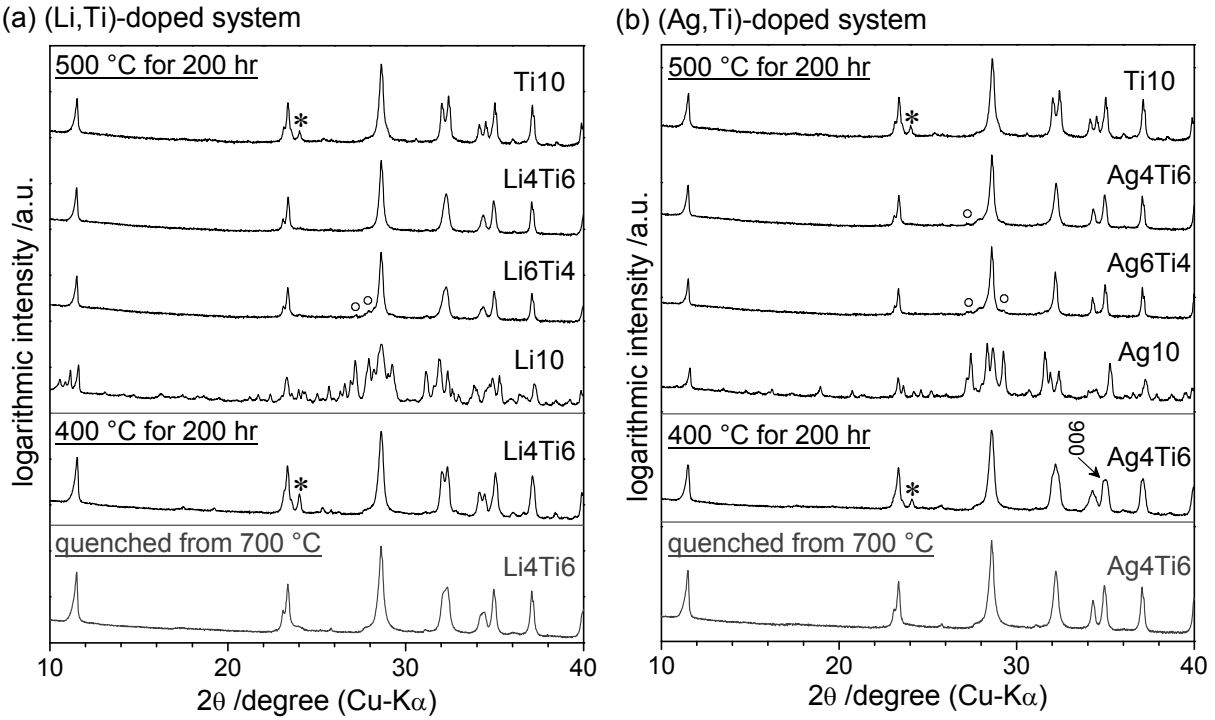

Figure 8.13 XRD patterns of powders annealed at 500 and 400 °C for 200 hr in a logarithmic intensity scale. (a) (Li,Ti)-doped system and (b) (Ag,Ti)-doped system. Typical peaks of secondary phases are indicated by open circles "○". Asterisks "∗" indicate the typical superlattice diffraction peaks of α_f. The patterns of Li4Ti6 and Ag4Ti6 quenched from 700 °C are also shown for reference.

The results of XRD analysis after annealing are summarized as pseudo-binary phase diagrams of $Bi_2(V_{0.9}Li_{1-x}Ti_x)O_{5.5+\Delta}$ and $Bi_2(V_{0.9}Ag_{1-x}Ti_x)O_{5.5+\Delta}$ in Figures 8.14(a) and (b), respectively. The upper limit of the stable region of the BIMEVOX was evaluated by DTA at a heating rate of 10 K min^{-1} in air. Figure 8.14(c) shows the DTA profiles of Li10, Li6Ti4, Ag10, and Ag6Ti4, as examples. As described in Chapter 4, the estimated phases in region (i–iii) of the phase diagrams and DTA profiles are as follows: (i) BIMEVOX phase + small amount of liquid between T_1 and T_2, (ii) solid + liquid between T_2 and T_3, and (iii) liquid

above T_3. The shaded areas in Figures 8.14(a) and (b) indicate the thermodynamically stable region for single phase of γ_f. For both (Li,Ti)-doped and (Ag,Ti)-doped system, the thermodynamically stable region of γ_f expands with an increase in Ti concentration. In particular, stable region of γ_f is significantly large for LiTi.

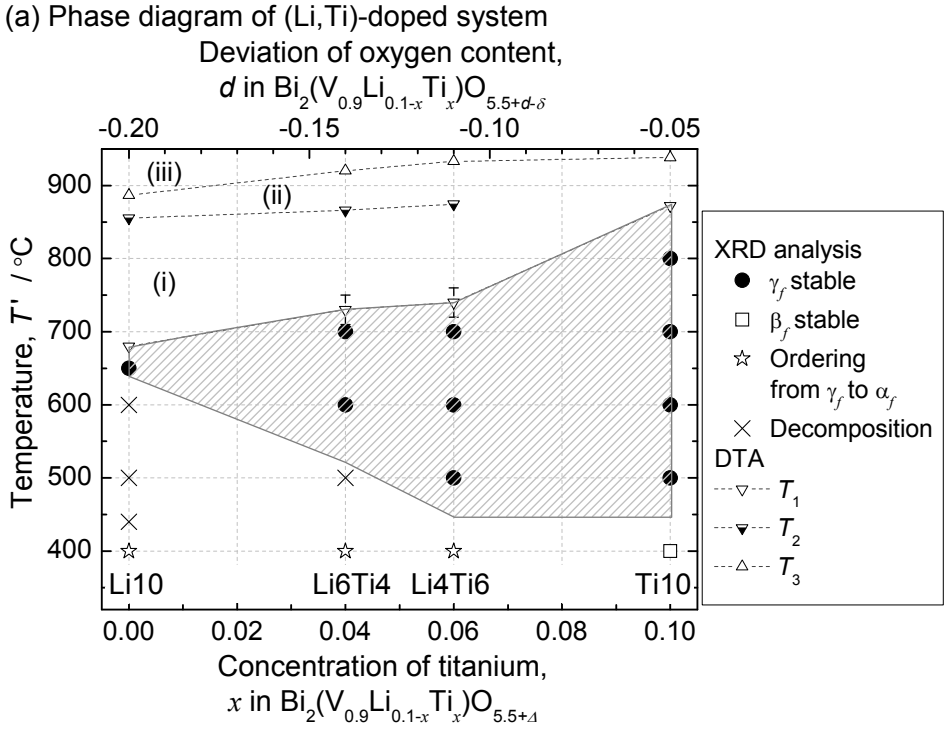

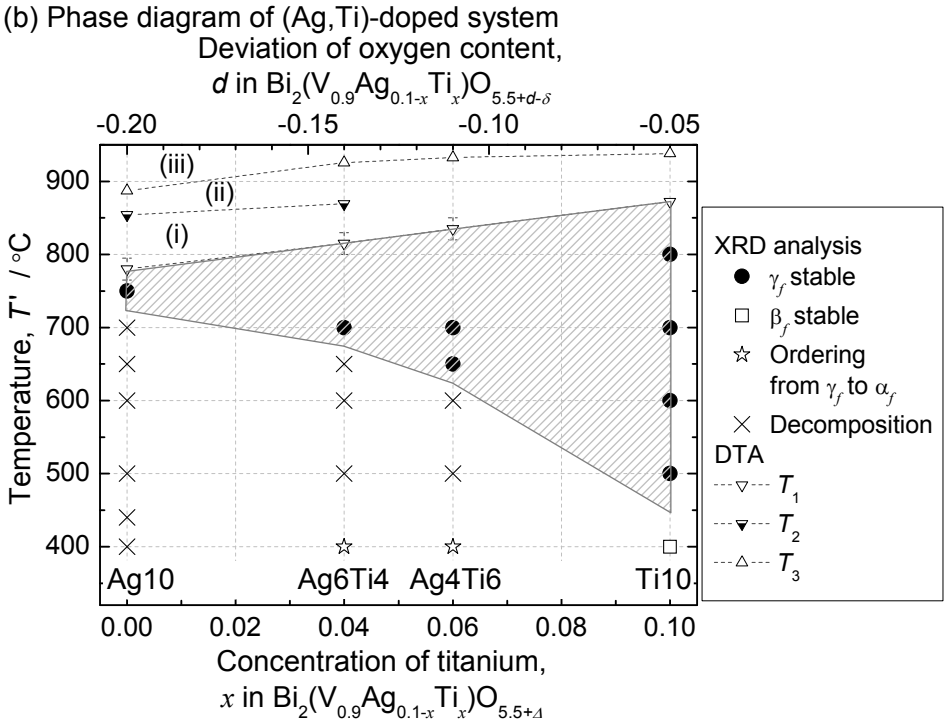

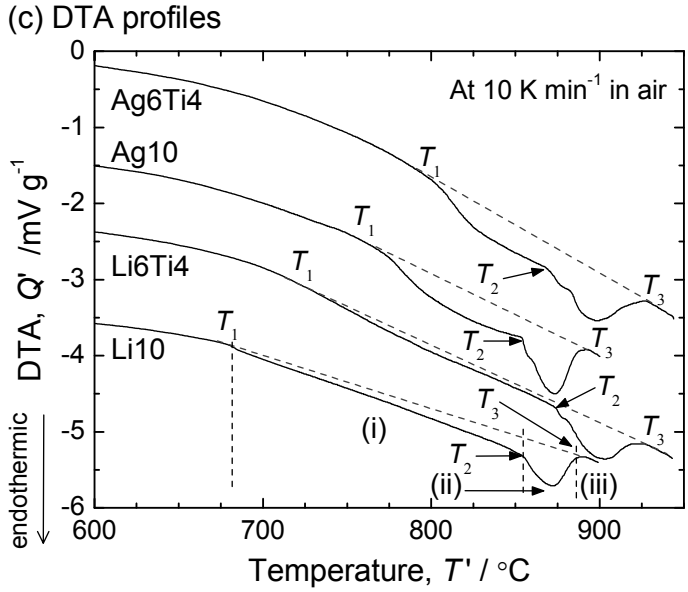

Figure 8.14 Pseudo-binary phase diagram of (a) (Li,Ti)-doped system and (b) (Ag,Ti)-doped system. The shaded areas indicate the thermodynamically stable region of γ_f. (c) DTA profiles of Li10, Li6Ti4, Ag10, and Ag6Ti4. The following phases were estimated in each region: (i) BIMEVOX phase + small amount of liquid, from T_1 to T_2, (ii) solid + liquid, from T_2 to T_3, and (iii) liquid, above T_3.

8.8.2. Time dependence of electrical conductivities determined by AC impedance spectroscopy

Figure 8.15 shows the conductivities after annealing at 500 °C for 200 and 400 hr with those before annealing. "$\sigma_{n\mathrm{hr}}/\sigma_{0\mathrm{hr}}$" denotes the ratio of conductivity after annealing for *n* hr to that before annealing. Degradation of conductivity became small by doping with Ti, which agrees with the results of XRD analysis for annealed powders. LiTi kept high conductivities of ~10^{-1} S cm^{-1} for 400 hr. Prolonged annealing for 400 hr slightly decreased the conductivities of AgTi. However, AgTi exhibited high oxide-ion conductivity above 3×10^{-1} S cm^{-1} after annealing for 400 hr. These results further indicate that γ_f of LiTi and AgTi, particularly γ_f of LiTi, have high phase stability against thermal decomposition.

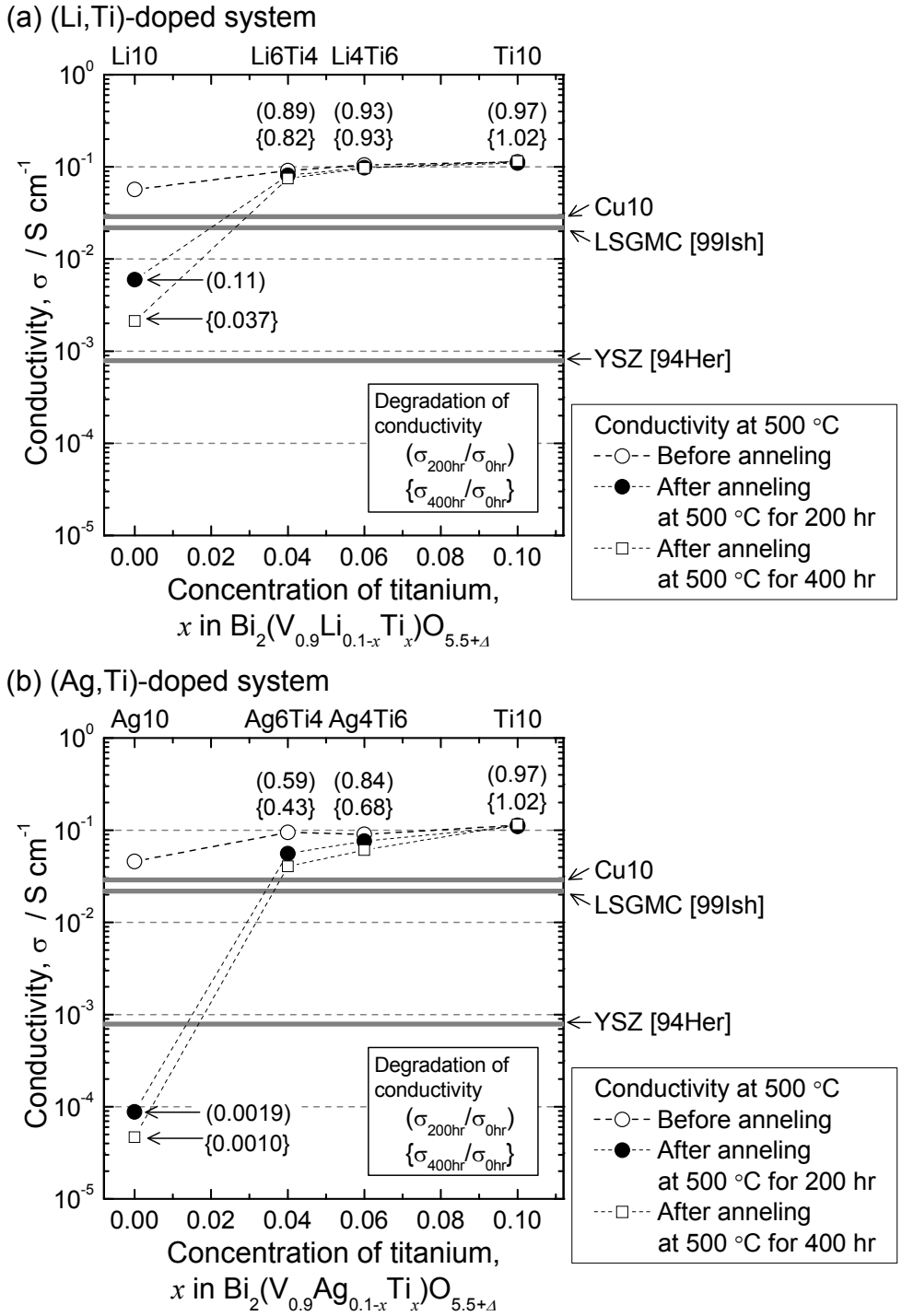

Figure 8.15 Electrical conductivities at 500 °C before and after annealing at 500 °C for 200 and 400 hr in air. (a) (Li,Ti)-doped system and (b) (Ag,Ti)-doped system. "$\sigma_{n\text{hr}}/\sigma_{0\text{hr}}$" denotes the ratio of conductivity after annealing for *n* hr to that before annealing. Gray lines indicate the conductivities of Cu10, YSZ [94Her], and LSGMC [99Ish] at 500 °C without prolonged annealing.

Figure 8.16(a) shows the conductivities of Li4Ti6 and Ag4Ti6 at 400 °C as a function of time. As shown in Figure 8.13, ordering from γ_f to α_f proceeded at 400 °C. In Li4Ti6, ordering to α_f was completed for ~25 hr. On the other hand, ordering to α_f was not completed even after 200 hr in Ag4Ti6. Figures 8.16(b) and (c) shows the temperature dependence of the electrical conductivities of Li4Ti6 and Ag4Ti6 pellets after annealing at 400 °C for 200 hr. The data were collected in air at heating and cooling rates of 1 K min^{-1}. As shown in Figure 8.16(b), α_f in the annealed Li4Ti6 was transformed to γ_f at 450 °C. After the transition to γ_f, the annealed Li4Ti6 pellet exhibited the same conductivity change as the quenched Li4Ti6 pellet. Similar to the annealed Li4Ti6 pellet, α_f in the annealed Ag4Ti6 pellet was transformed to γ_f at 445 °C, as shown in Figure 8.16(b). Thus, γ_f of Li4Ti6 and Ag4Ti6 is kinetically stabilized against α_f below 450 and 445 °C, respectively. Similar ordering phenomena were reported for γ_f of $Bi_2(V_{0.9}Cu_{0.1})O_{5.35-\delta}$ (Cu10) and $Bi_2(V_{0.9}Co_{0.1})O_{5.35-\delta}$ (Co10). Watanabe and Das reported that prolonged annealing at 450 °C for several hundreds of hours caused γ_f of Cu10 and Co10 to change to α_f [02Wat]. In addition, α_f of Cu10 and Co10 changed to γ_f on heating at ~485 and ~535 °C, respectively. LiTi, AgTi, Cu10, and Co10 have the same dopant concentration of 10 mol% of vanadium sites. The oxygen contents in LiTi and AgTi, *i.e.*, 5.36–5.39, are close to those in Cu10 and Co10, *i.e.*, 5.35, where the slight oxygen loss due to partial reduction δ was ignored. The contents of dopant and oxygen might be important to determine the polymorphs of BIMEVOX.

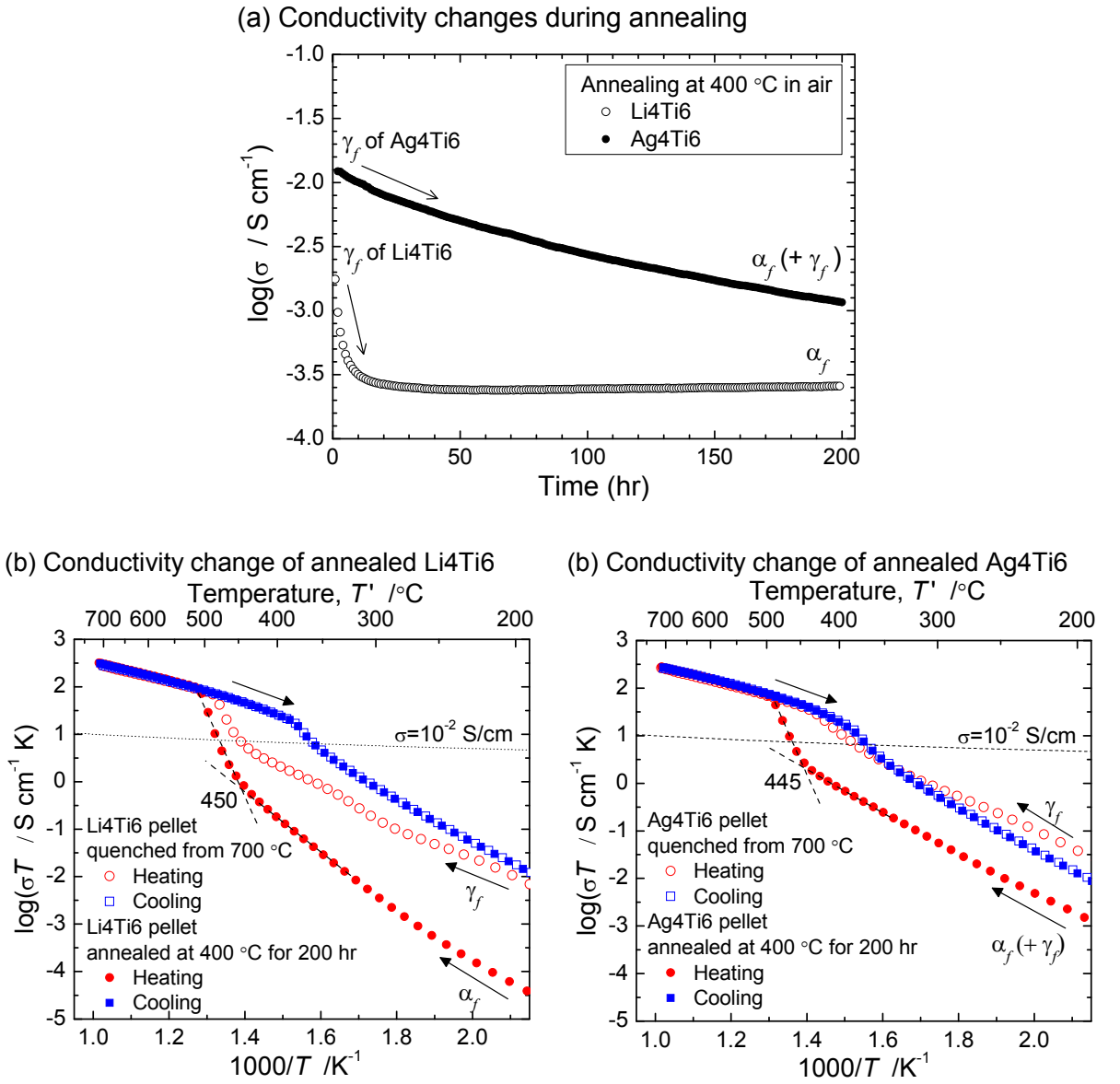

Figure 8.16 (a) Time dependence of total conductivity of Li4Ti6 and Ag4Ti6 at 400 °C in air. Ordering from γ_f to α_f proceeded with time. Temperature dependence of conductivity of (b) Li4Ti6 and (c) Ag4Ti6 after annealing at 400 °C for 200 hr. Conductivities were measured in air on heating and cooling at 1 K min^{-1}. Data of pellets quenched from 700 °C are also shown. α_f in annealed Li4Ti6 and Ag4Ti6 transformed to γ_f at ~450 and ~445 °C, respectively.

8.9. Conclusion

In this chapter, the electrical conductivities, phase transitions, and long-term phase stabilities of $Bi_2(V_{0.9}MM_{1-x}Ti_x)O_{5.5+\Delta}$ (MM = Li and Ag, x = 0.04 and 0.06) has been determined. Co-doping based on empirical knowledge was demonstrated as effective way to further improve the performance at intermediate temperatures. The findings are summarized as follows:

(1) The γ_f of $Bi_2(V_{0.9}MM_{1-x}Ti_x)O_{5.5+\Delta}$ was successfully obtained at room temperature. Distinct conductivity jumps from lowly conductive γ_f to highly conductive γ_f appeared without clear endothermic reaction and structural change.

(2) The γ_f of $Bi_2(V_{0.9}MM_{1-x}Ti_x)O_{5.5+\Delta}$ exhibited oxide-ion conductivities as high as 10^{-1} S cm^{-1} at 500 °C. In $Bi_2(V_{0.9}Li_{1-x}Ti_x)O_{5.5+\Delta}$, the temperature region for highly conductive γ_f was reduced by doping with Ti. On the other hand, $Bi_2(V_{0.9}Ag_{1-x}Ti_x)O_{5.5+\Delta}$ maintained a large temperature region of highly conductive γ_f.

(3) In γ_f of $Bi_2(V_{0.9}MM_{1-x}Ti_x)O_{5.5+\Delta}$, the progress of thermal decomposition was markedly suppressed at around 500 °C by doping with Ti. Degradation of conductivity was small even after annealing for 400 hr. In particular, γ_f of $Bi_2(V_{0.9}Li_{1-x}Ti_x)O_{5.5+\Delta}$ exhibited high long-term stability. Meanwhile, prolonged annealing at 400 °C leaded to ordering from γ_f to α_f.

(4) The pseudo-binary phase diagrams for $Bi_2(V_{0.9}MM_{1-x}Ti_x)O_{5.5+\Delta}$ was generated as a function of Ti concentration. The thermodynamically stable region of γ_f expands with an increase in Ti concentration. $Bi_2(V_{0.9}Li_{1-x}Ti_x)O_{5.5+\Delta}$ exhibited larger stable region of γ_f compared with $Bi_2(V_{0.9}Ag_{1-x}Ti_x)O_{5.5+\Delta}$.

References

[52Heb] M. Hebb, J. Chem. Phys. 20 (1952) 185.

[56Wag] C. Wagner, Electrochemistry 60 (1956) 4.

[84Sub] E.C. Subbarao and H.S. Maiti, Solid State Ionics 11 (1984) 317.

[94Her] J. Van Herle, A.J. Mcevoy, and K.R. Thampi, J. Mater. Sci. 29 (1994) 3691.

[94Van] R.N. Vannier, G. Mairesse, F. Abraham, and G. Nowogrocki, Solid State Ionics 70-71 (1994) 248.

[97Jia] S.P. Jiang, J.G. Love, and S.P.S. Badwal, Key Eng. Mater. 125-126 (1997) 81.

[97Kro] F. Krok, I. Abrahams, M. Malys, W. Bogusz, and J.A.G. Nelstrop, Ionics 3 (1997) 235.

[99Ish] T. Ishihara, H. Furutani, M. Honda, T. Yamada. T. Shibayama, T. Akbay. N. Sakai, H. Yokokawa, and Y. Takita, Chem. Mater. 11 (1999) 2081.

[01Pay] M.H. Paydar, A.M. Hadian, and G. Fafilek, J. Eur. Ceram. Soc. 21 (2001) 1821.

[02Wat] A. Watanabe and K. Das, J. Solid State Chem. 163 (2002) 224.

[05Alg] M. Alga, A. Ammar, B. Tanouti, A. Outzourhit, F. Mauvy, and R. Decourt, J. Solid State Chem. 178 (2005) 2873.

Chapter 9

Summary

Doped bismuth vanadate $Bi_2(V_{1-x}ME_x)O_{5.5+\Delta}$ (ME: dopant metal, x: dopant concentration, and $\Delta \equiv d - \delta$, where Δ is total oxygen deviation, d is oxygen deviation due to aliovalent doping, and δ is oxygen loss due to partial reduction), *i.e.*, BIMEVOX, exhibits complicated phase transition behavior and is a strong candidate for oxide-ion conductive membrane of oxygen pump operating at intermediate temperatures between 400 and 600 °C. This thesis has established new concept of phase classification for BIMEVOX and has uncovered the effects of doping with each dopant on electrical conductivity and phase stability depending on temperature and time. Furthermore, higher-performance BIMEVOX has been designed based on the empirical knowledge. The findings are summarized as follows.

Chapter 2

The practical phase classification system for BIMEVOX has been established in terms of the network structures in the layer containing vanadium, dopant, and oxygen. Besides three main phases of α, β, and γ, $Bi_2VO_{5.5-\delta}$ and BIMEVOX exhibit several phases that deviate from three main phases depending on the composition, temperature, and thermal history. These complex phases were classified into the three groups of α_f, β_f, and γ_f on the basis of characteristic superlattice diffractions and trends of oxide-ion conductivities in each group, without strictly determining crystalline symmetries.

Chapter 9

Chapter 3

The electrical conductivities, phase transitions, and long-term phase stabilities of $Bi_2(V_{1-x}Bi_x)O_{5.5+\Delta}$ (ME = Bi^{3+}) have been determined. The solid solution of $Bi_2(V_{1-x}Bi_x)O_{5.5+\Delta}$ was $0 < x < 8$ at 800 °C. The Bi-doping reduced the transition temperature from β_f to γ_f, although γ_f was not stabilized below 530 °C. The Bi-doping did not improve the long phase stability against thermal decomposition. At intermediate temperatures, thermal decomposition of $Bi_2(V_{1-x}Bi_x)O_{5.5+\Delta}$ into $BiVO_4$ and $Bi_{3.5}V_{1.2}O_{8.25}$ proceeded by prolonged annealing The generated phase diagram indicates that the thermodynamically stable region of the BIMEVOX was reduced by Bi-doping.

Chapter 4

The electrical conductivities, phase transitions, and long-term phase stabilities of $Bi_2(V_{1-x}MM_x)O_{5.5+\Delta}$ (MM = Li^+ and Ag^+, x = 0.05 and 0.1) have been determined. The Li- and Ag-doping markedly stabilized γ_f against β_f and α_f. In particular, the γ_f of $Bi_2(V_{0.9}Li_{0.1})O_{5.3-\delta}$ and $Bi_2(V_{0.9}Ag_{0.1})O_{5.3-\delta}$ was stabilized down to room temperature and showed transformation from lowly conductive to highly conductive state at about 300–400 °C. γ_f of $Bi_2(V_{1-x}MM_x)O_{5.5+\Delta}$ exhibited the oxide-ion conductivities as high as $0.5–1 \times 10^{-1}$ S cm^{-1} at around 500 °C. However, the Li- and Ag-doping did not improve the long-term phase stability against thermal decomposition and prolonged annealing notably reduced the oxide-ion conductivities at intermediate temperatures. Poor phase stability was prominent for $Bi_2(V_{0.9}Ag_{0.1})O_{5.3-\delta}$. The generated phase diagrams indicate that the thermodynamically stable region of the BIMEVOX was reduced by Li- and Ag-doping.

Chapter 9

Chapter 5

The electrical conductivities, phase transitions, and long-term phase stabilities of $Bi_2(V_{0.95}TM_{0.05})O_{5.5+\Delta}$ (TM = Ti^{4+}, Zr^{4+}, Hf^{4+}, Nb^{5+}, Ta^{5+}, Cr^{3+}, Mo^{6+}, and W^{6+}, x was fixed as 0.05) have been determined. The electrical conductivities of α_f, as well as the transition behavior among α_f, β_f, and γ_f, varied significantly with not only the dopant but also the thermal history of a sample. This becomes prominent in Ti- and Nb-doped samples. The 5 mol% doping with TM, except for Cr, decreased the transition temperature from β_f to γ_f, although γ_f was not stabilized below ~500 °C. Despite doping with various transition metals, the γ_f of $Bi_2(V_{0.95}TM_{0.05})O_{5.5+\Delta}$ maintained a high oxide-ion conductivity above 3×10^{-1} S cm^{-1} at 700 °C. The 5 mol% doping with TM tended to improve long-term phase stability against thermal decomposition. In particular, Ti doping effectively suppressed thermal decomposition.

Chapter 6

This chapter revealed the wide variation in phase transition behavior of $Bi_2(V_{0.95}Ti_{0.05})O_{5.475-\delta}$ derived from the difference in thermal history and physical form of samples as well as heating rate. The oxygen content (oxygen vacancy concentration) varied with the applied thermal treatment ($0 \leq \delta \leq 0.005$), although significant difference was not confirmed in average structure (XRD analysis). The phase transition behavior from α_f to β_f and from β_f to γ_f, observed at a heating rate of 10 K min^{-1}, were markedly affected by the sample preparation. The trend of the transition temperatures can be qualitatively explained as follows: $Bi_2(V_{0.95}Ti_{0.05})O_{5.475-\delta}$ with less oxygen content (more oxygen vacancy concentration) exhibits the transition from α_f to β_f at a higher temperature and the transition

from β_f to γ_f at a lower temperature. Two types of phase transition behavior from α_f to β_f are confirmed depending on heating rate. α_f directly transformed to β_f at fast rates of 10 and 40 K min^{-1}. Meanwhile, at a slower heating rate of 2 K min^{-1}, β_f continuously precipitated and the co-existence of α_f and β_f was confirmed. This phenomenon is qualitatively explained in terms of the positions of dopant and oxygen vacancies in the V-O layer. That is, during slow heating, the rearrangement of Ti and oxygen vacancies progressed to take more preferential sites, and different types of α_f appeared in samples.

Chapter 7

The electrical conductivities, phase transitions, and long-term phase stabilities of $Bi_2(V_{1-x}TM_x)O_{5.5+\Delta}$ (TM = Ti^{4+}, Zr^{4+}, and Hf^{4+}, $0 \le x \le 0.15$) have been determined. Among three dopants, doping with Ti most effectively stabilize γ_f against β_f and α_f. At a given temperature, the oxide-ion conductivities in γ_f decreased with an increase in dopant concentration. Despite of dopants, 10 and 15 mol% doped samples exhibited high oxide-ion conductivities of 10^{-1} and 0.6×10^{-1} S cm^{-1} at 500 °C, respectively. The Ti-doping notably improved long-term phase stability against thermal decomposition. γ_f of $Bi_2(V_{0.9}Ti_{0.1})O_{5.45-\delta}$ and $Bi_2(V_{0.9}Ti_{0.15})O_{5.45-\delta}$ were stable during prolonged annealing at intermediate temperatures for 200 hr. Meanwhile, thermal decomposition proceeded in Zr- and Hf-doped samples. The generated phase diagrams indicate that Ti-doping expanded the thermodynamically stable region of γ_f, but Zr- and Hf-doping reduced.

Chapter 8

The electrical conductivities, phase transitions, and long-term phase stabilities of $Bi_2(V_{0.9}MM_{1-x}Ti_x)O_{5.5+\Delta}$ (MM = Li and Ag, x = 0.04 and 0.06) has been determined, and

Co-doping based on empirical knowledge (doping with Li and Ag most effectively stabilizes γ_f against β_f and α_f, and doping with Ti most effectively suppresses thermal decomposition of BIMEVOX) was demonstrated as an effective way to further improve the performance. The γ_f of $Bi_2(V_{0.9}MM_{1-x}Ti_x)O_{5.5+\Delta}$ was successfully stabilized down to room temperature, although it showed transformation from lowly conductive to highly conductive state. In $Bi_2(V_{0.9}Li_{1-x}Ti_x)O_{5.5+\Delta}$, the temperature region for highly conductive γ_f was reduced by doping with Ti. On the other hand, $Bi_2(V_{0.9}Ag_{1-x}Ti_x)O_{5.5+\Delta}$ maintained a large temperature region of highly conductive γ_f. At 500 °C, high conductive γ_f of $Bi_2(V_{0.9}MM_{1-x}Ti_x)O_{5.5+\Delta}$ exhibited the quite high oxide-ion conductivities of 10^{-1} S cm^{-1} (almost the same order of oxide-ion conductivity of $(ZrO_2)_{0.92}(Y_2O_3)_{0.08}$ at around 930 °C, of $(CeO_2)_{0.85}(SmO_{1.5})_{0.15}$ at around 850 °C, of $La_{0.8}Sr_{0.2}Ga_{0.8}Mg_{0.115}Co_{0.085}O_3$ at around 670 °C, of $(Bi_2O_3)_{0.8}(Er_2O_3)_{0.2}$ at around 570 °C, and of $Bi_2(V_{0.9}Cu_{0.1})O_{5.35-\delta}$ at around 600 °C). The γ_f of $Bi_2(V_{0.9}MM_{1-x}Ti_x)O_{5.5+\Delta}$, particularly γ_f of $Bi_2(V_{0.9}Li_{1-x}Ti_x)O_{5.5+\Delta}$, exhibited good stability against thermal decomposition, and degradation of conductivity was sufficiently small even after annealing at 500 °C for 400 hr. In addition, it was found that prolonged annealing at 400 °C leaded to gradual ordering from γ_f to α_f. Generated phase diagrams indicate that the thermodynamically stable region of γ_f expanded with an increase in Ti concentration.

Empirical knowledge about oxide-ion conductivity in γ_f and stabilization of γ_f

Oxide-ion conductivity in γ_f

Oxide-ion conductivity in γ_f tends to decreases with an increase in dopant concentration and oxygen vacancy concentration. This suggests that dopant somewhat associates with oxygen vacancies in the V-O layer of γ_f, which induces local structural defects and disturb oxide-ion

conduction. The γ_f of $Bi_2(V_{0.9}MM_{0.1})O_{5.3-\delta}$, $Bi_2(V_{0.9}Ti_{0.15})O_{5.45-\delta}$, and $Bi_2(V_{0.9}MM_{1-x}Ti_x)O_{5.5+\Delta}$ exhibited the highly conductive and lowly conductive state depending on temperature. This is probably related with the small difference in local structures around dopant (difference in association state).

Phase stability of γ_f against β_f and α_f

Increase in oxygen vacancy concentration and dopant concentration tends to stabilize γ_f against β_f and α_f. The large amounts of oxygen vacancies probably destabilize β_f and α_f because oxygen atoms bind stronger with V in β_f and α_f rather than in γ_f. The presence of structural defects, such as dopant and oxygen vacancy, might increase the configurational entropy of disorder γ_f phase, which has an advantage to thermodynamically stabilize γ_f against β_f and α_f and retard the ordering from γ_f to β_f and α_f. In this thesis, Li- and Ag-doping stabilized γ_f most effectively.

Phase stability against thermal decomposition

Doping with element, whose size largely deviates from that of V, tends to destabilize BIMEVOX phases against thermal decomposition. The large deviation in size between dopant and V should cause notable lattice distortions, which increases the strain energy of BIMEVOX phases. This suggests that the effect of lattice distortion is one of the important parameters to suppress thermal decomposition. In this thesis, Ti-doping most effectively improved the stability against thermal decomposition.

The author has clarified the effects of various dopants on oxide-ion conductivity and phase stability. Some qualitative insight how to design more favorable BIMEVOX was provided based on careful investigation on physical properties. In this research, local structures around

dopant, which can not be identified by XRD and HT-XRD analyses, are suggested to be important for further understanding of oxide-ion conduction and polymorphs. For example, results in Chapter 6 strongly suggests dopant and oxygen vacancies have the preferential crystallographic sites in the V-O layer of α_f and β_f, and the small difference in atomic arrangement notably changes the transition behavior between α_f and β_f. Thus, the author believes that the local structural analysis with considering the physical properties is one of the important researches to further understand BIMEVOX.

List of publications

Bismuth vanadate (oxide-ion conductor)

Papers

- "Phase Stability of $Bi_2(V_{1-x}ME_x)O_{5.5+\delta}$ (ME = Li and Ag, x = 0.05 and 0.1)"

  Y. Taninouchi, T. Uda, T. Ichitsubo, Y. Awakura, and E. Matsubara,

  Accepted for publication in Mater. Trans.

- "High Oxide-ion Conductivities of Monovalent-metal-doped Bismuth Vanadate at Intermediate Temperatures"

  Y. Taninouchi, T. Uda, T. Ichitsubo, Y. Awakura, and E. Matsubara,

  (submitted to Solid State Ionics).

- "Phase Classification, Electrical Conductivities, and Thermal Properties of $Bi_2(V_{0.95}TM_{0.05})O_{5.5+\delta}$ (TM: transition metals)"

  Y. Taninouchi, T. Uda, T. Ichitsubo, Y. Awakura, and E. Matsubara,

  (submitted to Solid State Ionics).

- "Effects of Oxygen Content and Heating Rate on phase transition behavior in $Bi_2(V_{0.95}Ti_{0.05})O_{5.475-x}$"

  Y. Taninouchi, T. Uda, T. Ichitsubo, Y. Awakura, and E. Matsubara,

  (in preparation).

- "Effects of Tetravalent Dopants on Electrical Conductivity and Phase Stability of Bismuth Vanadate"

  Y. Taninouchi, T. Uda, T. Ichitsubo, Y. Awakura, and E. Matsubara,

  (in preparation).

- "Improvement of Oxide-Ion Conductivity and Phase Stability of Bismuth Vanadate by Co-doping with Ag and Ti"

  Y. Taninouchi, T. Uda, T. Ichitsubo, Y. Awakura, and E. Matsubara,

  (in preparation).

- "Oxide-Ion Conductivity and Phase Transition of Li-Ti Double Doped $Bi_2VO_{5.5}$"

  Y. Taninouchi, T. Uda, T. Ichitsubo, Y. Awakura, and E. Matsubara,

  (in preparation).

Cesium dihydrogen phosphate (proton conductor)

Papers

- "Dehydration Behavior of the Superprotonic Conductor CsH_2PO_4 at Moderate Temperatures: 230 to 260 °C"

  Y. Taninouchi, T. Uda, Y. Awakura, A. Ikeda, and S. M. Haile,

  J. Mater. Chem. 17 (2007) 3182.

- "Dehydration Pathway of CsH_2PO_4 at Higher Temperature than 260 °C and the Ionic Conductivity of Liquid Phase"

  Y. Taninouchi, T. Uda, and Y. Awakura,

  Solid State Ionics 178 (2008) 1648.

- "Phase Relationship of CsH_2PO_4-$CsPO_3$ System and Electrical Properties of $CsPO_3$"

  Y. Taninouchi, N. Hatada, T. Uda, and Y. Awakura,

  J. Electrochem. Soc. 156(5) (2009) B572.

Proceedings

- "Chemical Stabilities of Superprotonic Solid Acid Electrolyte: Cesium Hydrogen Sulfate and Cesium Dihydrogen Phosphate"

T. Uda, Y. Taninouchi, and Y. Awakura

16th Iketani Conference 2006, Electrochemistry and Thermodynamics on Materials Processing for Sustainable Production: Masuko Symposium, (2006) 409.

Au nanocontact and multi-walled carbon nanotube (electron conductor)

Papers

- "Effective Temperature of Au Nanocontacts under High Biases"

  M. Tsutsui, Y. Taninouchi, S. Kurokawa, and A. Sakai,

  Jpn. J. Appl. Phys. 44(7A) (2005) 5188.

- "BiasInduced Local Heating Effects on MultiWalled Carbon Nanotube-Au Contacts"

  M. Tsutsui, Y. Taninouchi, S. Kurokawa, and A. Sakai,

  Jpn. J. Appl. Phys. 45(1A) (2006) 341.

- "Electrical Breakdown of Short Multi-walled Carbon Nanotubes"

  M. Tsutsui, Y. Taninouchi, S. Kurokawa, and A. Sakai,

  J. Appl. Phys. 100 (2006) 094302.

Other

Papers

- "Synthesis of Spinel-Type Magnesium Cobalt Oxide and Its Electrical Conductivity"

  N. Kamioka, T. Ichitsubo, T. Uda, S. Imashuku, Y. Taninouchi, and E. Matsubara,

  Mater. Trans. 49(4) (2008) 824.

Acknowledgments

This work was financially supported by a Grant-in-Aid for JSPS fellows.

I would like to express my deep gratitude to Professor Eiichiro Matsubara and Professor Tetsuya Uda, Department of Materials Science and Engineering, Kyoto University, for offering a precious opportunity to complete the course of this study and invaluable discussions and suggestions.

I am grateful to Professor Yasuhiro Awakura and Professor Tetsu Ichitsubo, Department of Materials Science and Engineering, Kyoto University, for their kind advices. I also would like to thank Mr. Tokuji Tanaka for his assistance in experimental work.

I am grateful to Dr. Makusu Tsutsui, Osaka University, and Professor Sossina M. Haile, California Institute of Technology, and Professor Isao Tanaka, Kyoto University, for their kind encouragements.

I would like to express my special thanks to Mr. Naoyuki Hatada, Mr. Kousuke Hirai, Mr. Kouhei Hosokawa, Ms. Natsumi Kamioka, and Mr. Shogo Takashima for their pleasant assistance and useful discussions. Also, I would like to express my gratitude to all other members of Professor Matsubara's and Professor Awakura's research groups.

Finally, I would like to express my deep acknowledgement to my parents, Kentarou Taninouchi and Yoshimi Taninouchi, for their support throughout my academic career. I thank my brother, Toshiki Taninouchi, my grandfathers, Tokushige Taninouchi and Minoru Matsuura (Minoru Matsuura died on March 20, 2007), and my grandmothers, Kinue Taninouchi and Tsuru Matsuura, for continuous encouragements.